Magnetic Resonance Thermometry for Image-Guided Thermal Therapy

by

Robert D. Peters

A thesis submitted in conformity with the requirements
for the degree of Doctor of Philosophy
Graduate Department of Medical Biophysics
University of Toronto

Magnetic Resonance Thermometry for Image-Guided Thermal Therapy

Robert D. Peters

Doctor of Philosophy, 2000

Department of Medical Biophysics

University of Toronto

The integration of medical-image guidance in medicine can enable the adaption of novel minimally-invasive surgeries and therapies. Thermal-coagulation therapy is a procedure that will benefit from image guidance and have clinical significance as an alternative to conventional treatments such as resective surgery or radiation therapy. The goal of this thermal therapy is to elevate diseased tissue temperature to induce necrosis while ensuring that the thermal treatment to surrounding healthy tissue is below toxic levels. The spatial-temporal delivery of heat energy requires control which is ideally provided through mapping of the three dimensional distribution of temperature in tissue.

This thesis explores the use of real-time magnetic resonance imaging (MRI) for monitoring and guiding thermal-coagulation therapy. Specifically, a method of spatially-resolving the temperature distribution is described that incorporates the temperature-sensitivity of the proton-resonance frequency (PRF). This thermal-imaging method is implemented by measuring temperature-dependent phase shifts from a gradient-echo pulse sequence. Thermal calibration results are presented which show the temperature dependent PRF-shift to be independent of *ex vivo* tissue type, within an experimental precision of 4%. The PRF-shift method of MR thermometry is shown to be capable of quantitatively accurate temperature measurements. However, it is identified that attention is required to several considerations, such as temperature-induced changes in the volume-magnetic susceptibility and electrical conductivity of tissue.

The ability for real-time prediction of the spatial extent of thermal-coagulation necrosis is demonstrated with results obtained in an *in vivo* canine prostate model. In this experiment, laser heating of the prostate gland was performed simultaneously with MR-thermal mapping. Using his-

tological sections of the prostate gland to indicate the boundary of necrosis, a discriminant analysis revealed the onset of thermal-coagulative necrosis to be characterized by a critical temperature of approximately 51°C, or equivalently with an Arrhenius t_{43} period of approximately 200 minutes. It is concluded that real-time quantitative MR-thermal mapping is a visualization tool that can be used effectively for delivery and control of thermal-coagulation therapy.

Acknowledgements

This thesis is dedicated to my wife, Diana, without whose love and support this work could not have been possible. Thanks for putting up with all of my late-night hours and experiments that seem to go on forever.

I wish to thank my supervisor, Dr. Mark Henkelman, for his insight and guidance and for explaining to me the conscience of a scientist. I am also grateful to my supervisory committee, Drs. Stuart Foster and Mike Sherar for their direction and critical review. A special thanks to Dr. Scott Hinks for co-supervising me for a period during his sojourn at Sunnybrook.

There were many people who also helped make this work easier, if not possible. I'd like to thank Dr. Walter Kucharczyk for his vision of interventional MRI and Dr. John Trachtenberg for his enthusiasm in urological surgery. Carrie Purcell should be commended for her dedication to animal care and her help in the canine model studies.

Finally, I would like to thank my parents, Don and Lydia, for frequently telling me that they were proud of me. Here is a something you can show when people ask what I've been studying.

Contents

List of Figures

List of Tables

List of Abbreviations and Symbols

3D ..... three dimensional

BPH ..... benign prostatic hyperplasia

CT ..... computed tomography

ILC ..... interstitial laser coagulation

FOV ..... field-of-view

Gd ..... gadolinium

MKS ..... meter, kilogram, second convention of units

MRI ..... magnetic resonance imaging

NMR ..... nuclear magnetic resonance

PRF ..... proton-resonance frequency

ppm ..... parts-per-million

ROI ..... region-of-interest

RF ..... radiofrequency

SAR ..... specific-absorption rate

sd ..... standard deviation

se ..... standard error

sem ..... standard error in the mean

SPGR ..... spoiled gradient recalled echo

TURP ..... transurethral radical prostatectomy

US ..... ultrasound

α ..... proton-resonance frequency thermal coefficient

α ..... tip angle

χ ..... volume-magnetic susceptibility

χ_m ..... mass-magnetic susceptibility

$\Delta\phi$ ..... phase shift

$\Delta\phi/\Delta T$ ..... phase-shift thermal coefficient

$\Delta\psi$ ..... phase-shift offset

ΔT ..... temperature change

ϵ ..... electrical permittivity

γ ..... gyromagnetic ratio

μ ..... magnetic permeability

ρ ..... density

σ ..... intermolecular electron screening constant

σ ..... electrical conductivity

σ_0 ..... intramolecular screening constant

σ_E ..... magnetic-susceptibility effect

$\boldsymbol{B}_{mac}$ ..... macroscopic-magnetic field

$\boldsymbol{B}_{nuc}$ ..... magnetic field at the nucleus

B_o ..... main-magnetic field strength

f ..... proton-resonance frequency

Im ..... imaginary component

k ..... wavenumber

M_o ..... equilibrium magnetization

T ..... temperature

t ..... time

$T1$ ..... spin-lattice relaxation time

$T2$ ..... spin-spin relaxation time

t_{43} ..... equivalent period at 43°C

TE ..... echo time

TR ..... repetition time

TTP ..... temperature-time product

r ..... spatial position

Re ..... real component

Chapter 1

Introduction

1.1 The Role of Image Guidance in Surgery and Therapy

One of the first documented examples of an image-guided surgery took place when an x-radiograph was used to assist in the removal of a needle lodged in a woman's hand[1]. This landmark event occurred shortly after the discovery of the x-ray by Roentgen in 1895 and, besides helping to establish the basic utility of x-radiography, set in motion a means of augmenting and enhancing the performance of conventional surgery with a new source of information. While this happens to be a straight-forward example of how medical images can be used in surgery, the general motivation for image guidance in medicine is two-fold: direct visualization during surgery or therapy is incomplete and limited to the exposed surface of the tissue, and image guidance can provide increased visibility and allow for *minimally-invasive* practices which can lessen the morbidity of conventional surgery.

Since 1896, many developments have shown that image guidance can take on different roles in assisting surgery and therapy. This is mostly a result of technological advances in computer-aided imagery. Some of these roles are currently believed to be:

(*i*) *surgical planning*, where pre-acquired images are used to define the safest and most expedient approach with the least damage to normal tissue

(*ii*) *intra-operative guidance*, where the surgery is guided by real-time or frequent imaging

(*iii*) *computer-assisted surgery*, in which computerized image information is used to help automate or assist in the procedure

[1]This was on January 13, 1896. The two radiologists were Ratcliffe and Hall-Edwards from Birmingham, UK. The surgeon was J.H. Clayton who performed the procedure at the General & Queen's Hospital [1].

(*iv*) *post-operative monitoring*, where medical imaging is used to provide post-treatment evaluation and assessment of the success of the surgery or therapy

There are several medical imaging modalities that are in use for image guidance in surgery and therapy, ranging in complexity and accessibility. These include x-ray imaging devices such as computed tomography (CT), fluoroscopy, and plain film, as well as ultrasound (US), magnetic resonance imaging (MRI), and optical devices like endoscopy and laparoscopy. Each of these has particular attributes that make it useful in certain procedures. For example the real-time capability inherent to medical ultrasound has made this modality indispensable for guiding needle drainage, biopsy, and catheterization [2]. Similarly, the much simpler video laparoscope has changed the way cholecystectomy is performed [3].

The practise of image-guided surgery and therapy represents cross-disciplinary medicine and as such has seen its share of "turf issues" in the medical community [4–7]. This usually results when radiologists and surgeons overlap into each others respective traditional areas. *Interventional radiology*, for example, is also an established specialty that occasionally resembles image-guided surgery and at times the distinction between the two is not always obvious. Consequently, this discussion is purposely restricted to situations where a radiologist and surgeon are both necessary and where their expertise compliment each other. In these cases, the radiologist works with and is seen to be in constant communication with the surgeon to provide feedback when necessary, as the radiologist is experienced at interpreting the images and familiar with the relevant anatomical depictions [8].

In short, image guidance in medicine provides a surgeon with an enhanced visibility and thus wider range of treatment options. Medical image guidance also makes possible new procedures that could not previously have been done. Attention is now turned to intra-operative image guidance which allows for the adaption of minimally-invasive approaches.

1.2 Minimally-Invasive Approaches

Intra-operative image guidance can help reduce the need for large incisions and reduce surgical morbidity. Thus, image guidance can be viewed as a tool for reducing the inherent invasiveness of the surgical or therapeutic procedure. Minimally-invasive medicine is a growing trend in health care, and has become synonymous with percutaneous, interstitial, or intraluminal approaches. The benefits of minimally-invasive approaches are generally recognized as:

- a reduction of trauma inflicted on the patient, including blood loss, infections, and scar formation
- a lessening of sterility requirements or need of a conventional operating room, depending on the level of invasiveness
- a quicker recovery time and shorter hospital stay following surgery
- a potential lower cost of treatment
- less lost wages, a faster return to work, and a reduced impact on society

There are many forms that image-guided minimally-invasive procedures can take. Many interstitial approaches to the treatment of benign and malignant disease are being realized clinically including ethanol injection, cryoablation, radioactive-seed implantation, and the deposition of heat energy or *thermal therapy*, which is the particular interest of this thesis.

As the following sections will explain, thermal therapy is a general term which consists of two distinct treatment regimes: the first incorporates the use of relatively low temperatures for a prolonged period of time and is referred to as *hyperthermia*. The second regime of thermal therapy uses higher temperatures for a shorter period and can be implemented in an image-guided minimally-invasive approach.

A review of the history of the therapeutic use of heat is needed to fully appreciate how thermal therapy has developed in modern medicine. In doing this, some aspects of clinical hyperthermia are first described. The following section is not intended as an extensive overview of hyperthermia, but to draw the distinction between hyperthermia and the high-temperature thermal therapy regime. There are, however, some common features between the two, such as the method of heat delivery and the rationale for thermal therapy as an alternative to conventional treatments, such as surgery, radiation, and chemotherapy.

1.3 Thermal Therapy

1.3.1 Review of Hyperthermia

Heat has been employed as a therapeutic agent for centuries, if not millennia[2]. Early use consisted of a variety of methods, ranging from inducing artificial fever to using heated metals for cautery.

[2] "Give me power to produce fever and I will cure all disease." - Hippocrates [9].

Even though the precise understanding of the bioeffect of heat hasn't always been understood, the observed benefit has usually been quite clear.

Clinical hyperthermia is a field that has had its roots in these early observations and has been under investigation for over 30 years, primarily for the treatment of cancer. This is, in part, a response to the past limitations of conventional approaches, such as surgery, chemotherapy and radiation therapy. Further, there is growing evidence that hyperthermia may be a useful adjunct to surgery, either pre- or post-operatively. Elevations in temperature with hyperthermia may also enhance the radiosensitivity of cancer cells and be useful in radiation therapy. Finally, hyperthermia may be beneficial in certain chemotherapies by improving the uptake and biological effect of drugs.

A complete review of the biophysical mechanisms of hyperthermia is beyond the scope of this introductory chapter and some of the more salient features are now briefly summarized. These can be grouped as either biological or physiological observations.

Biological Effects [10–14]:

- cells can be killed when temperatures are elevated beyond 41°C
- the sensitivity to heat exposure is markedly increased at approximately 42 – 43°C
- different cell lines *in vitro* show variations to heat sensitivity
- cancer cells are not necessarily more sensitive to heat than normal cells, for a given cell type and given environment
- cellular damage from radiation and chemotherapy is enhanced at elevated temperatures
- cellular damage at elevated temperatures can be enhanced by hypoxia or other environmental conditions, such as reduced pH and nutrient depletion, which are often characteristic of tumor environments

Physiological Effects

Clinical hyperthermia requires uniform temperature distributions in the diseased tissue or organ, generally in the range 40 – 45°C, which may be applied for tens of minutes to hours. During this time, there are related physiological responses that are also significant to the efficacy of this therapy [10, 14, 15]:

- blood flow can be significantly lower in tumors than in surrounding normal tissue

- temperature elevation can increase blood flow in normal tissue and cause reduction in tumor blood flow
- heat is dissipated more effectively in normal tissue and more poorly in the tumor, leading to preferential heating in the tumor and thus greater therapeutic effect

Mechanisms of Cellular Inactivation in Hyperthermia

Given these observations, derived from both *in vitro* and *in vivo* studies, the mechanism of heat inactivation in hyperthermia is understood to involve one or more of the following [11]:

1. heat affects the cellular membrane and causes changes in its permeability, composition, and fluidity,
2. disintegration of lysosome vesicles and release of digestive enzymes,
3. thermal damage to proteins, which affects DNA, RNA, and protein synthesis as well as repair from radiation damage.

Heat Delivery for Hyperthermia

At present, depending on such factors as the size and anatomical location of the tumor, heat can be administered through a variety of methods, such as microwave radiation, RF currents (inductive and capacitive), and ultrasound diathermy. Whole-body hyperthermia for more systemic disease is also possible with hot water or wax baths, heated blankets, hot air, and extracorporeal heating of the blood [16].

1.3.2 Rationale for Hyperthermia as an Alternative Therapy

The methods for the management of patients with cancer have traditionally been surgery, radiation therapy, and chemotherapy. Surgery may be indicated in situations when the tumor can be removed. When surgery is not indicated because of the location of the tumor and potential surgical side effects, radiation therapy may be preferable. Finally, chemotherapy is generally applicable for the treatment of more extensive systemic and metastatic disease, such as leukemia and breast cancer. The well-known limitations of these traditional methods have provided the rationale for alternative therapies such as hyperthermia as a standalone or adjuvant to radiation and chemotherapy and are now summarized [13].

Surgery

As surgery consists of the physical removal of diseased tissue, one obvious drawback includes difficulty in surgically removing a tumor due to its proximity to vital tissues and vasculature as well as incompletely removing the gross tumor and inadequately resecting the tumor extensions, which can lead to local recurrence. Also, there is evidence that when a tumor is manipulated there can be a correspondingly greater number of tumor cells circulating in the peripheral vasculature which can lead to potential systemic metastasis. Finally, anatomical deformity and physical impairment may result from more radical surgical procedures.

Radiation Therapy

As with surgery, radiation therapy physically targets tumor masses and thus has similar deficiencies as described above. However, the limitation of radiation therapy also includes the technical challenge of delivering the necessary radiation dose to the entire tumor volume and adequate irradiation of extensions or metastases. Often there is difficulty in localization of the tumor and an inability to define the margin of the tumor volume which, with inadequate treatment planning, may result in an inhomogeneous dose distribution and potential radiation damage to surrounding healthy tissue. Aside from the difficulty in delivering adequate dose to the treatment volume, it is also realized that hypoxic cell subpopulations have a lower radiation sensitivity and require higher doses of radiation than well-oxygenated cells for the same level of cell kill. Also, cells in late G_o or S cell-cycle phase have an increased resistance to radiation.

Chemotherapy

The efficacy of chemotherapy is strongly dependent on pharmaco-dynamic factors such as drug diffusion from the vasculature and the eventual incorporation of the drug within the cell. As such, the limitations of chemotherapy are mainly biological and consist of two main items: variation of cell sensitivity to chemotherapeutic agents throughout the proliferative cell cycle and inherent or acquired drug resistance.

1.3.3 Thermal-Coagulation Therapy

In the hyperthermia regime, elevation to temperatures in the range of 42 – 45°C gives cells an increased sensitivity to radiation and chemotherapeutic agents. However, as an adjuvant or stan-

dalone therapeutic modality, even prolonged heating in this range gives rise to non-specific cellular damage within the treatment volume, which generally requires a latency period to become manifest.

Lately, there has been a growing interest in the use of more direct heat-induced injuries for the treatment of localized disease. Applying higher temperatures ($> 45°C$) for much shorter durations (seconds – minutes) causes thermal damage that is more coincident with treatment. Furthermore, such rapid and high-temperature exposure can be done using localized heating devices that can be used in a minimally-invasive manner. Consequently, this regime of thermal therapy has a more physical volume-targeting attribute than conventional hyperthermia, and its immediacy, or lack of a long latency period, gives it more resemblance to surgical resection.

Understanding the mechanisms of injuries from high-temperature exposure requires an appreciation of the pathological effects of the interaction of heat with living tissue. In general, this interaction is complex and requires consideration of (a) the anatomy and physiology of the target tissue, (b) the repair, regeneration, and healing responses, and (c) the exposure temperature, time history, and latency period at which evaluation is done [17, 18]. Regardless of the source of heat energy, there are many different thermal-injury processes, some of which are summarized in Table 1.1, in relation to the temperature range and approximate durations at which they are believed to occur. However, these are mainly anecdotal observations, and significant variations are expected over a broad range of tissue types and treatment conditions. For a more extensive description the reader is referred to [17].

There is a growing effort towards qualitative and quantitative pathologic techniques for mapping thermal injury and comparing treatment effects. A detailed review can be found elsewhere [18]. Using current histopathological techniques, certain thermal-injury processes can be easily identified and serve as markers for thermal treatment.

Beginning at the center of the thermal-injury site and progressing to the cooler periphery, concentric damage zones may include:

1. tissue ablation, or physical removal of tissue, such as tissue vaporization or combustion
2. carbonization, recognized by formation of black residue
3. water vaporization-based thermal damage, such as steam vacuole formation, explosive fragmentation, and tissue desiccation
4. structural-protein denaturation or thermal coagulation
5. vital enzyme protein denaturation

Table 1.1: Pathologic Effects from Thermal Applications.

Temperature at onset	Pathologic Effect
40 - 45°C	(hyperthermia) deactivation of enzymes? reversible cell injury
46°C for 60 min. or 50–52°C for 4–6 min.	irreversible cell damage [19]
60–100°C	near instantaneous induction of protein coagulation leading to irreversible cell death
>100°C	tissue boiling, vaporization, carbonization, extracellular vacuole formation and rupture

6. cellular membrane rupture
7. hemorrhage, hemostasis, hyperhemia
8. wound healing

Some of these zones can be seen during and immediately after heating in either excised or *in vivo* tissue (**1–6**), whereas others can only develop in living tissue (**7–8**) and then only after a sufficient survival period (**8**). In particular, we focus on structural protein denaturation, which is often referred to as *thermal coagulation.*

Thermal coagulation is a therapeutic and experimental biological endpoint that is believed to be of primary importance for minimally-invasive high-temperature thermal therapy. Visible whitening of tissue is a hallmark sign of this damage process and can usually be seen with the naked eye[3]. More specifically, thermal coagulation is defined as an irreversible alteration of proteins as well as organelles, membranes, cells, and extracellular components. Many of these alterations are due to thermal denaturation of structural proteins, however, membrane rupture can result from such alterations in lipids. Given this rather broad definition, it is seen that thermal coagulation differs markedly from hyperthermia in that it *always* implies lethality, can be readily observed, and occurs immediately following heating.

[3]With the exception of fatty tissues and collagenous tissues, such as tendon, which become translucent.

The full extent of lethal thermal injury in tissue, however, cannot be precisely determined with current histopathological techniques until all injured cells undergo necrosis. Depending on the tissue type, the extent of lethal thermal damage may require 1 – 5 days to develop. *Thermal-coagulative necrosis* is one of the mechanisms[4] and is the most immediate necrosis which occurs within the zone of structural-protein denaturation or thermal coagulation. It is significant to note that, immediately following a thermal treatment that produces thermal coagulation, cells may appear intact but are necrotic. These cells will usually not undergo cellular and nuclear disintegration because their enzymes have been rendered useless through thermal denaturation, and thus may appear viable under the light microscope. Also, there is no blood flow that would normally bring the inflammatory cells to release proteases and lipases to digest the dead cells, and generally in long-term survival the coagulum will persist until new blood vessels and inflammatory cells invade the necrotic tissue.

1.3.4 Minimally-Invasive Delivery of Thermal-Coagulation Therapy

It has been incitefully stated that "When considering thermal lesions, an important maxim to remember is that once generated within the tissue, heat is heat."[5]. However, while this attitude simplifies the patho-biological perspective of the therapeutic endpoint, the delivery of heat energy for thermal-coagulation therapy is not a trivial issue and is an important consideration in a clinical implementation. Minimally-invasive heat delivery devices for thermal-coagulation therapy must be:

- capable of achieving high temperatures (>50°C) for a period of time ranging from a few seconds to several minutes
- able to heat a variety of tissue types with a range of optical, electric, or mechanical properties
- able to reach deep-seated tissues in a minimally-invasive manner, such as through a small gauge interstitial device
- compatible with accessory physiological monitoring equipment, thermal measurement instruments, and image-guidance methods

At present, minimally-invasive thermal-coagulation therapy is usually done using heat energy produced from either microwave radiation, RF currents, focused ultrasound, or laser light. Each heating modality has unique characteristics with respect to their heating patterns and level of

[4]Other mechanisms of interest with respect to thermal injury are lytic necrosis, ischemic necrosis, and apoptosis which are more extensively discussed in [18].

[5]S.L. Thomsen, an anatomic pathologist with expertise in thermal injury at University of Texas, M.D. Anderson Cancer Center [18].

invasiveness, and much of their development has originated in the context of applications for hyperthermia [20, 21]. The following is a brief description of some typical devices that can be used for thermal-coagulation therapy.

Microwave Applicators

Microwave heating is done through the use of oscillatory electric fields [6]. This causes polar molecules in tissue, like water molecules and proteins, to rotate in place generating frictional heating [22–25]. Power sources for microwave antennas or applicators must operate at the ISM (Industrial, Scientific and Medical) band frequencies of 433, 915, or 2450 MHz. Minimally-invasive microwave heating is done with interstitial antennas, which are generally of helical or dipole design [26–31].

RF Currents

Radiofrequency (RF) current heating can actually imply one of three distinct modes of use: (*i*) capacitively-coupled (dielectric) heating, (*ii*) inductive (magnetic) heating, or (*iii*) heating from resistive losses [16, 23, 32]. With RF current heating, where frequencies ranging from 1 – 30 MHz are used, tissue completes the electrical circuit pathway and heating is achieved through the translational motion of dissolved ions in tissue, such as Na^+, Cl^-, K^+, and Ca^{+2}. With interstitial RF devices, the current is emitted from an exposed (non-insulated) electrode implanted in the target tissue which returns to a grounding plate located externally [33–36].

Focused Ultrasound

The delivery of heat energy with focused ultrasound can be done with transducers placed either externally or percutaneously, although the non-invasiveness of external beam ultrasound has been one of the key motivations for development of this heating modality. Ultrasound is a pressure wave that causes motion of particles within the medium. As an ultrasound wave propagates through tissue, part of the energy is absorbed and converted into thermal energy. As such, and unlike other heating modalities, ultrasound energy can be focused to distal spots of the order of a few millimeters in diameter. Further, focused ultrasound is capable of extremely fast energy delivery, such that coagulated tissue volumes can be produced that are relatively insensitive to blood perfusion variations. However, as it propagates as a pressure wave, ultrasound is blocked by bone and

[6] Primarily, as most tissues are non-magnetic.

air, making external focused ultrasound unsuitable for applications without an adequate acoustic window [37–40].

Interstitial Laser Fibres

Laser light energy can be easily delivered to deep-seated tissue through a flexible quartz fibre that is inserted percutaneously [41–43]. Generally, the optimal laser light wavelength for thermal coagulation is in the near infrared, with wavelengths ranging from 800 nm (for diode lasers) to 1064 nm (with Nd-YAG lasers). The absorption of laser energy depends on the specific tissue characteristics and on laser wavelength. Early applications of laser thermal therapy used bare fibres which created spherical point-like heating patterns, and ultimately led to charring of the fibres [44]. But presently, interstitial laser thermal-coagulation therapy is one of the most rapidly developing areas in minimally-invasive thermal therapy, particularly for its ability to treat a wide range of tissue types in various anatomical locations.

1.4 Image Guidance for Thermal-Coagulation Therapy

1.4.1 Four Roles of Image Guidance

Image guidance for thermal-coagulation therapy demands that imaging must fulfill four separate roles. These roles need not necessary be filled by a single imaging modality, and consist of:

(*i*) *pre-treatment determination* of the margins of diseased tissue volume.

(*ii*) *device localization* or targeting of the heat-delivery source within the tissue to be treated,

(*iii*) *real-time monitoring* of the delivery of heat energy during the therapy, and

(*iv*) *post-treatment assessment* of the thermally-treated volume.

1.4.2 Real-Time Monitoring of Thermal-Coagulation Therapy

The goal of real-time monitoring in thermal-coagulation therapy is to provide a physician with a means of controlling the therapy. Ideally, this entails providing some predictive value on the spatial extent of the thermally-coagulated volume of tissue through some form of image display. Thus, there are two approaches for real-time control: either image the *tissue damage* directly, or image the *temperature distribution.*

To date, there are no imaging techniques that are able to easily distinguish between a necrotic volume within normal, healthy tissue. This inability is further confounded by the fact that thermal-coagulation is an irreversible process that will eventually lead to the host response of thermal-coagulative necrosis, after a latency period which may range from a few hours to several days. Research into this capability is ongoing on many imaging-modality fronts, such as ultrasound, MRI, and x-ray [45, 46].

1.4.3 Temperature Measurements

Because heat energy is the applied necrotizing agent used in thermal-coagulation therapy, knowledge of the 3D distribution of temperature within tissue is crucial for monitoring the extent of thermal damage and thus controlling the heat delivery. Tracking the temperature distribution in the target and surrounding tissue would be a simple way of determining the temperature-elevation margin and thus be used to protect healthy tissue from receiving any thermal exposure. Additionally, high-temperature thermal therapy, like thermal-coagulation, is likely to be governed by quantitative thermal dosimetry laws [47, 48]. Therefore, a knowledge of the real-time temperature distribution within tissue, would allow the physician to predict the ultimate necrotic volume and to better match this to the diseased-tissue volume. In short, temperature measurements during thermal-coagulation therapy can provide both a protective measure for healthy tissue and help ensure adequate thermal treatment of diseased tissue.

1.4.4 Approaches to *In Vivo* Temperature Measurement

Measuring temperatures within living tissue is a technically difficult problem that has been considered over the past several decades, since the origin of clinical hyperthermia. There are three general approaches to temperature measurements in tissue:

(*i*) *discrete, invasive measurements* from interstitial probes, which can be used alone or with

(*ii*) *thermal modelling*, to spatially interpolate between the discrete measurements, or

(*iii*) *noninvasive thermal mapping*, where temperature distributions are spatially resolved or imaged.

Discrete and invasive measurements of temperature can be obtained with interstitial thermal probes, such as thermocouples and thermistors. Such measurements, by their nature, add to the

overall invasiveness of the thermal therapy and consequently, are not consistent with a minimally-invasive approach. Also, such measurements provide only a spatially-discrete set of measurements which necessitates heat-transfer modelling to interpolate between these measurements [49–52]. This approach must often make assumptions that neglects the inhomogeneous nature of tissue, the time-varying thermal properties, and the nonuniform deposition of heat energy. Additionally, invasive thermal probes may be prone to artifacts and may perturb the SAR (specific absorption rate) pattern in tissue.

1.4.5 Spatially-Resolving Temperatures

The ability to noninvasively spatially resolve temperatures should make reliance on theoretical models of heat transport much less essential. A method of thermal mapping for guidance in thermal-coagulation therapy would obviously have to meet certain design criteria for it to be clinically useful which are usually in the form of resolution specifications. Considering the physical property of high-temperature thermal-coagulation therapy and the brief period in which relatively small volumes can be coagulated, the usual consensus on resolution guidelines are:

(*i*) *spatial* resolution of structures within 1 mm^3,

(*ii*) *temporal* or image updating approximately once every few seconds,

(*iii*) *temperature* resolution of 1^oC,

and it is quite foreseeable these will vary according to the specific application.

Temperature is a parameter that a so-called thermometer measures to characterize the thermodynamic property of a system. By definition, this property is the variation of the density of states with energy and is related to the entropy of the system [53]. Thus, temperature is really an environmental state and can be quantified through a surrogate measurement of a physical material property, such as the volume-coefficient of expansion as in a simple mercury thermometer. Consequently, a method of spatially-resolving temperatures, or thermal mapping, must be based on some temperature-sensitive property.

Further, this property must be amenable to being easily measured through an imaging method to provide the above resolution criteria. There are some preferred attributes of a temperature-sensitive property which may include:

- a variation in temperature that is linear or one-to-one
- an insensitivity to pathologic effects in tissue from the thermal treatment

- a means of measurement that is easy to make and interpret, has a non-perturbative effect on the therapeutic delivery of heat, and has a negligible sensitivity to other influencing factors

1.4.6 Previous Methods of Thermal Mapping

Several methods have been proposed in the past for thermal mapping during thermal therapy. However, at present, none have demonstrated the necessary resolution properties, as discussed in the previous section. The following is a brief review of some thermal-mapping methods that have been previously examined, such as radiometric techniques, ultrasound, and x-ray computed tomography.

Microwave Radiometry

Radiometry for thermal measurement is one of the earliest methods to be developed [54–56] and originated with the observation that the thermometry of *in vivo* tissues is similar in principle to radiometric determination of temperature profiles in the atmosphere and in free space. According to Planck's law, any object with an absolute temperature above zero Kelvin gives off radiation over a spectrum of frequencies as a consequence of thermal motions.

Radiometry in the both the infrared and microwave-frequency range has been extensively investigated since the late 1970's as a method of noninvasive thermometry. At the long wavelengths, associated with microwave radiometers, the radiated energy is small compared to thermal energy and Planck's law reduces to an expression where the power received by the radiometer is directly proportional to absolute temperature of the object. With an increase in the temperature of an object, the spectral radiation distribution that is emitted increases (over all frequencies), with the peak of the distribution proportional to the absolute temperature. For example a perfect black-body radiator at 37°C will emit radiation over a spectrum that is peaked at approximately 32 THz, which lies in the infrared.

There are a number of concerns with microwave radiometry techniques such as depth of penetration and hence the ability to map thermal distributions deep within tissue [55]. The penetration depth for microwave radiation ranges from 1 to 10 cm in tissues, depending on the frequency. Higher frequencies possess better spatial resolution properties, however at the expense of shallower depths of sensitivity [54]. Also, it is realized that the net signal received by the detecting antenna

is really an integrated average of the radiation emitted within the near-field cone of the antenna. Cross-correlation techniques for microwave radiometry have attempted to circumvent the depth of penetration problem and provide volume localization by employing multiple antennas with overlapping regions [56]. However, there seems to have been very little development in microwave radiometry, most likely because of the difficulty in providing the spatial resolution properties that are demanded in thermal therapies.

Ultrasound

Since the mid-1970's ultrasound imaging has been considered a promising modality for monitoring temperatures either for hyperthermia or high-temperature therapy [54, 57–59]. This is in part, due to its well-known attractive diagnostic imaging attributes, such as its real-time capability, high-spatial resolution, as well as portability, low cost, and general accessibility.

There are several temperature-sensitive properties that have been investigated for ultrasound thermal mapping, such as backscattered power [58], velocity of sound [56, 60], and attenuation coefficient [45]. However, the thermal coefficient of these properties has been shown to be very dependent on the tissue type and composition and consequently require an *a priori* calibration and careful classification of the tissue. Fatty tissues, for example, can show positive or negative thermal coefficients of the backscatter coefficient and velocity of sound. Also, the thermal coefficient of ultrasound attenuation can be positive or negative for the same tissue depending on the temperature range and structural changes that may have resulted from coagulation [45].

There are also some technical challenges with ultrasound measurements of the temperature-sensitive property. Temperature measurements based on the speed of sound may require a tomographic approach which can be quite restrictive [56]. Other limitations to this approach have been recently described [57]. As with diagnostic ultrasound imaging, bone and gaseous cavities, such as lung, will prevent measurements in certain anatomical regions. Nevertheless, ultrasound thermometry continues to be a source of considerable interest in the field of thermal-therapy monitoring.

Computed Tomography

Computed tomography (CT) is an x-ray imaging device that was proposed as a means of thermal mapping in the early 1980's. The attenuation of x-rays is dependent on the local electron density, which is dependent on the bulk density of the material. As the density of most biological tissues

is a function of temperature, intensity changes in CT images can be used to estimate temperature changes [61]. Over the range of temperatures commonly used in hyperthermia, a linear relationship between the CT number and temperature has been observed in water and excised tissues. The CT-number in a reconstructed image reflects the density of tissue, where one Hounsfield unit (HU) corresponds to a fractional change in water density of approximately 0.1%. The CT-number thermal coefficient is approximately -0.4 – -0.45 HU/^{o}C for water and muscle tissue [61].

Although CT-thermal mapping is one of the most simplest methods, it remains largely uninvestigated due to the need for extremely high signal-to-noise ratio (SNR) for temperature resolution, which in turn requires longer scanning time and unreasonable patient radiation doses. For example, in one report, the standard deviation in the CT-number measurement was 0.6 HU (averaged over an in-plane area of 0.5 cm^2) using a typical body-scan setting that delivered 0.6 cGy per scan [61]. This measurement precision translates to a temperature precision of approximately 1.5^{o}C.

One area that CT appears to be gaining acceptance is for monitoring cryosurgery [62]. This is because there is a large change in the CT number from unfrozen to completely frozen tissue of approximately 86 HU, which makes it promising for monitoring the growth of iceballs within tissue.

1.5 MR Image-Guided Thermal-Coagulation Therapy

1.5.1 Interventional MRI

The temperature sensitivity of MRI has been a significant factor in the development of the field of *interventional MRI* [63–68]. Interventional MRI began in the early 1990's and MRI has been a well-established diagnostic modality since the mid-1980's for such reasons as its capability of multi-parametric tissue characterization, excellent soft-tissue contrast, sensitivity to blood flow, multi-planar and high-spatial resolution, capability of functional imaging, and lack of ionizing radiation.

Initially, obstacles to interventional or MR image-guided practices were readily identified such as the closed-magnet design which restricts physician-patient access, MR incompatibility of surgical devices, slow image acquisition, and the expense of MRI. In response, recent technological breakthroughs have included the development of more open-access magnet systems, MR compatible instruments, and rapid or near real-time imaging techniques [69–74].

Currently, interventional MRI practices primarily consist of image-guided biopsy and thermal-coagulation therapy, the latter of which is still in a developmental stage [64, 65, 70]. Other applications, such as cyst aspiration, drainage procedures, and some intra-operative surgeries are also gaining acceptance. It can be argued that the temperature-sensitivity of certain nuclear-magnetic resonance (NMR) properties in fact stimulated the development of interventional MRI, as evidenced in one review article:

> "... recognition of the potential of MR imaging in monitoring and controlling thermal ablations and other percutaneous therapies really initiated this new direction in interventional radiology." Ferenc Jolesz, Radiology **204**: 601–612 (1997).

This opinion is also shared by other developers of the field.

Because of the multi-parametric contrast abilities, MRI can fill all four roles for monitoring thermal-coagulation therapy which are: (*i*) pre-treatment determination of the diseased tissue volume, (*ii*) pre-treatment heat device localization, (*iii*) thermal-mapping during therapy, and (*iv*) post-treatment lesion assessment.

1.5.2 MR Thermometry

At present, there are four main NMR properties that show temperature sensitivity and can be implemented for constructing thermal maps; these are the spin-lattice relaxation time (*T1*), self-diffusion coefficient of water, equilibrium magnetization, and proton-resonance frequency (PRF). These methods for MR thermometry are now discussed briefly, with a more in-depth description of PRF-shift thermometry deferred to Chapter 2.

T1 Relaxation

The earliest known NMR properties to exhibit an easily measurable temperature dependence were the nuclear relaxation times. These time constants are the primary sources of contrast in MR images as they reflect the microscopic and molecular environment of the nuclei of interest, which is the ^{1}H proton in most of clinical MRI [75–77]. Specifically, the longitudinal or spin-lattice relaxation time constant, *T1*, was first empirically shown in 1980 by Lewa and Majewska to exhibit complex and irreversible change with temperature, and was initially used by the authors to examine the thermal denaturation of proteins [78, 79]. A few years later the application of constructing thermal maps based on the *T1*-temperature sensitivity was suggested by Parker, in the context of hyperthermia

monitoring [80, 81]. Since that time, temperature has been recognized as being an important variable when measuring and reporting *T1* values for tissue characterization [77,82–85].

There are several models that have been used to describe the mechanism for the temperature dependence of *T1* relaxation [86,87], which include models incorporating molecular motion and fast-exchange between two states. Either approach reduces to the same approximation, which is that over the narrow range of temperatures used in thermal therapy, *T1* varies approximately linearly with temperature; despite the complex and irreversible behavior that is often observed in biological tissues. In water, the *T1* increases with temperature by approximately 20 ms/^{o}C or approximately 2%/^{o}C, relative to room temperature. Empirical evidence shows the temperature sensitivity of various tissue types to be in the range of 0.5% – 1.5%/^{o}C [78,80,81,88].

Current approaches to implementing *T1*-based MR thermometry attempt either to directly map the *T1* distribution [89] or the *T1*-weighted signal strength in tissue simultaneous with the applied heating [88,90–93]. However, there are several disadvantages to *T1*-based MR thermometry, beginning with the initial observation that *T1* may exhibit a complex and non-linear response to temperature [78, 79, 84, 94, 95]. It is realized that this linear calibration may be of further limited value as it is dependent on tissue type and will therefore require an *a priori* calibration [80, 81]. Finally, the generally preferred method of measurement is through *T1*-weighted signal changes, rather than the more time consuming direct *T1* measurements. These temperature-induced signal changes actually contain other influencing effects, such as those due to changes in the equilibrium magnetization and volume expansion of tissue. In light of the above, some researchers believe that a simple thermal calibration of *T1* or weighted-signal change is just not attainable [94,95].

For many of these reasons, *T1*-based MR thermometry will probably be used in a *qualitative* rather than quantitative role and in situations where other methods of MR thermometry do not perform well, such as at low-magnetic field strengths. Also, because *T1*-weighted images can be acquired rapidly, they can be used to localize the heat-delivery region. For example, *T1*-weighted images acquired with short and non-lethal bursts of ultrasound can be used to localize and steer the focus towards the diseased tissue [96].

Self-Diffusion Coefficient of Water

Another method of MR thermometry makes use of the temperature dependence of the self-diffusion coefficient of water in tissue. The translational-diffusion coefficient quantifies the thermal Brownian

motion of water molecules and is described through the Stokes-Einstein relation [97]. Spatial mapping of the diffusion coefficient of water for MR thermometry was first demonstrated by LeBihan in 1989, where data obtained from a gel heating experiment showed the self-diffusion coefficient of water to vary approximately linearly with temperature by 2.4%/°C [98]. The diffusion coefficient of water in gel at room temperature is approximately $2 \times 10^{-9} m^2/s$.

Brownian motion of water causes protons to move randomly and in an applied magnetic-field gradient (discussed in Chapter 2) the nuclear spins to lose phase coherence which leads to attenuation of the MR signal [99]. Such diffusion-weighted field gradients can be added to most standard MR imaging techniques.

The main issue with using the self-diffusion coefficient of water for thermometry is the phenomenon of *restricted diffusion* in tissues. The Einstein model of Brownian motion normally assumes that water molecules undergo self-diffusive motion in an unrestricted and isotropic medium, such that its mean square displacement is proportional to time. However, most water molecules in biological tissues are transiently bound to macromolecules, membranes, and ions and are hindered by the microenvironment of tissue. As such, water molecules in tissue may travel an average distance of only a few microns, which is roughly the diameter of a cell, during the millisecond MR imaging time scale. The rate of diffusion of tissue water is roughly 2–3 times slower than that of free water. It can therefore be argued that the self-diffusion coefficient of tissue water is really an intrinsic probe for the investigation of the structural changes in tissue, such as those that occur from elevated temperatures.

Some studies have used the self-diffusion coefficient to investigate the extent and mechanism of thermal damage *in vivo* [46]. In one particular study, it was found that the restricted diffusion ranges in tissue increase after a thermal treatment, ie. the tissue shows a less hindered environment for the diffusion of water after thermal damage and the self-diffusive behavior of tissue water approaches that of free water. Consequently, this indicates that the self-diffusion coefficient of water will change irreversibly with temperature. However, it is realized that these restricted diffusion effects result from the use of long diffusion times in the NMR experiment (eg. 150 ms). If shorter diffusion times are used (eg. <30 ms), water molecules will cover a shorter distance and thus fail to show changes in the structural hinderance of tissue [46].

Another important consequence of restricted diffusion are *anisotropic* diffusion effects which must also be considered when using diffusion as a thermometer. Many tissues, such as muscle fibres,

display an inherent anisotropy where the diffusion of water depends on the orientation of the tissue with respect to the applied diffusion magnetic-field gradients [100]. Tissue anisotropy thus adds a complication to the general use of diffusion in MR thermometry. This is because both *a priori* knowledge of the thermal coefficient of the diffusion coefficient is required for each tissue type as well the orientation of the tissue.

Finally, involuntary bulk tissue motions, such as those originating from vascular pulsatility and respiration, can present significant difficulties in accurately measuring the self-diffusion coefficient. This is because bulk motion of the water molecules diminishes the ability to detect the small Brownian diffusive motion that is desired [100–103].

Fortunately, many of these above problems have been in part rectified by the use of faster diffusion imaging sequences [104–106]. Rapid imaging techniques, with commensurate shorter diffusion times, should help reduce the effect of restricted diffusion and bulk tissue motion.

Equilibrium Magnetization

In any material, the ^{1}H nuclear protons or "spins" are normally randomly oriented and, when placed in an MR scanner, will tend to align with the direction of the applied-magnetic field. This produces an equilibrium magnetization that, in the absence of NMR relaxation phenomena, determines the strength of the MR signal used to construct images[7].

The tendency for a material to interact with an applied magnetic field is quantified through the magnetic susceptibility [107]. Nuclear paramagnetism obeys a Curie-law behavior, such that susceptibility is inversely dependent on the absolute temperature [108]. Consequently, the equilibrium magnetization available has an inherent temperature sensitivity that is approximately -0.3%/°C at room temperature and is reflected by changes in the MR signal intensity.

The temperature dependence of equilibrium magnetization has been known since the 1950's and has received very little attention as a method for MR thermometry [109,110]. The reason for this is likely due to its low temperature sensitivity, compared to other methods such as thermometry based on *T1* and the self-diffusion coefficient of water. Also, temperature-induced changes in the equilibrium magnetization manifests as a change in the magnitude of the MR signal and can be difficult to distinguish from other effects, such as changes in the *T1* [95].

One favorable aspect of equilibrium magnetization is that temperature changes do *not* reflect

[7]The equilibrium or net magnetization is also sometimes referred to as Boltzmann magnetization.

the structural changes in biological tissue that were discussed in the context of *T1* and diffusion coefficient. This means that a single, universal temperature sensitivity is expected for all tissues which does not necessitate any form of an *a priori* calibration.

The Proton-Resonance Frequency

One of the most recent methods to be implemented for MR thermometry is based on the temperature sensitivity of the proton-resonance frequency (PRF) of the ^{1}H nuclear protons. The observation that the PRF varies with temperature was actually first observed in 1958 by Schneider [111] and further described by Hindman in 1966 [112] through NMR spectroscopy experiments on liquid water. A method of incorporating the temperature dependence of the PRF for spatial-thermal mapping was first described by Ishihara in 1992 [113]. A description of the physical mechanism of temperature sensitivity of the PRF is given in Chapter 2.

At present, the PRF-shift method is considered the most promising quantitative method of MR thermometry compared to those previously discussed [105, 114–116]. This is mainly due to its proven linearity, reversibility with temperature, and the ease with which measurements can be made. There is also growing evidence to suggest that the PRF-shift method is not affected by thermal damage to tissues.

1.5.3 An Overview of MR Thermometry

A literature search can easily demonstrate the predominant interest in PRF-shift thermometry for monitoring thermal therapy, as shown in Figure 1.1. It is evident from the survey that the interest in *T1*-based thermometry, starting in 1983, has been sparse up until the last few years. This is due to its use in low-field applications, where the PRF-shift method suffers from poor SNR. Use of the self-diffusion coefficient has never really amounted to more than a few publications per year. Notice that the number of publications on the PRF-shift method of MR thermometry has more than doubled those that include *T1* and diffusion combined, since 1995.

What the above literature survey does not describe is how the various methods of MR thermometry are being used. Prior to around 1996, publications on *T1* or the self-diffusion coefficient were mostly qualitative descriptions of tissue-heating effects seen in MR images. Those reports that incorporate PRF-shift thermometry are noticeably more quantitative and generally contain more discussion on using the thermal maps actively in the decision-making processes of thermal therapy.

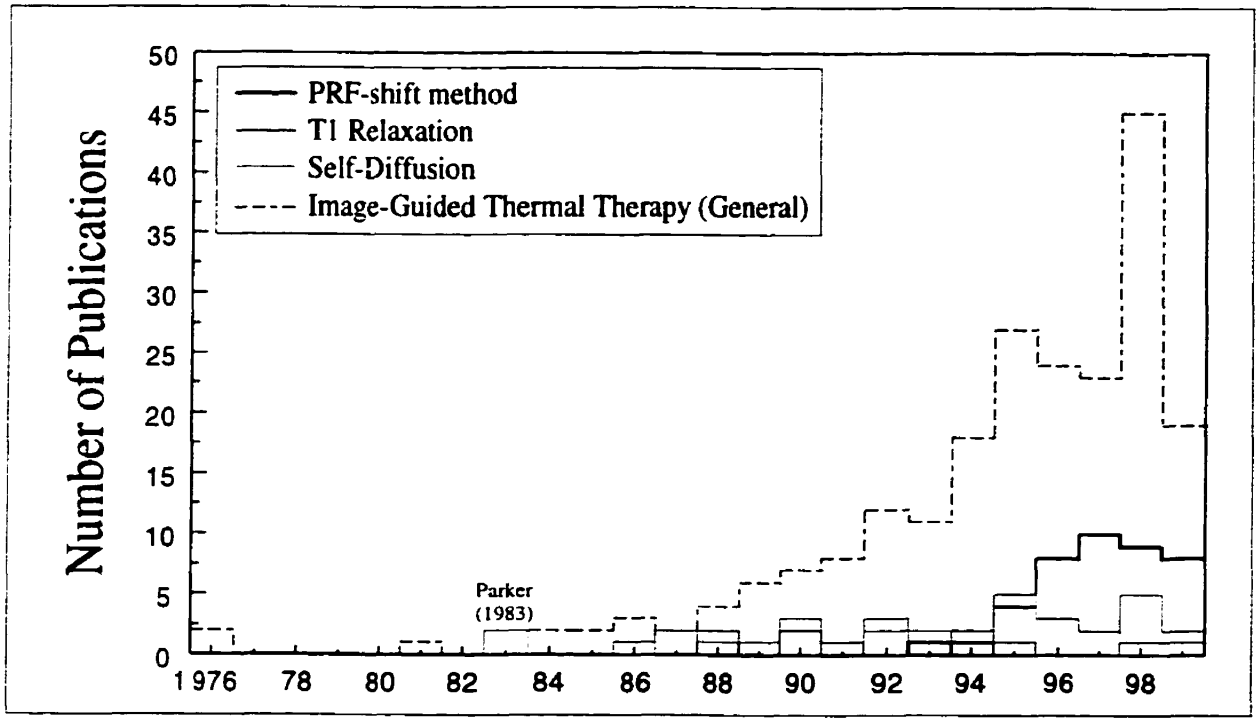

Figure 1.1: A survey of the number of related publications. The survey includes full-length publications that describe the use of a method of MR thermometry, either in a calibration experiment or for monitoring in a thermal-therapy. The dotted line shows a more general survey of the number of publications that describe high-temperature thermal therapy with any form of image guidance, eg. MRI, ultrasound, or CT, and not necessarily with thermal mapping. This excludes topics such as conventional hyperthermia, cryotherapy, dermatology, opthamology, dentistry, and photodynamic therapy. The entries for 1999 are based on the publications that have been indexed in MedLine as of October.

Also, these publications provide more insight into such concepts of thermal dose from both animal and human studies.

Finally, from the survey in Figure 1.1, it is worth noting that although the interest in image-guided thermal therapy has climbed rapidly over the past few years, there is actually a decreasing proportion of publications that make use of MR thermometry. This trend will hopefully reverse itself once the quantitative ability of MR thermometry has been more fully accepted in clinical applications and supplies even greater motivation for further developments.

1.6 Summary and Overview of Thesis

It is evident that image-guidance of therapy is becoming integrated into modern medicine. This adoption of technology can allow procedures that could not otherwise be performed without the

improved visualization. Image-guidance has also enabled the adaption of minimally-invasive approaches to surgery and therapy which have several well-known benefits, such as reduced trauma to the patient. High-temperature thermal-coagulation therapy is one such procedure that is expected to have a growing clinical importance. However, the primary hinderance to thermal-coagulation therapy has been the inability to monitor and control the heat delivery to the diseased tissue. Although several methods of thermal mapping have been proposed in the past, MR-thermal mapping has many favorable advantages for this application. In particular, the temperature dependence of the PRF seems to be the most promising basis for MR-thermal monitoring during thermal-coagulation therapy, and is the subject of this thesis.

This thesis demonstrates the quantitative nature of PRF-shift MR thermometry and thus much of the work presented focuses on a numerical evaluation of the PRF-shift thermal coefficient, ie. the amount that the PRF changes per unit change in temperature. This is done primarily through the use of thermal-calibration experiments, where MR measurements are made on tissue or tissue-equivalent material as a function of the applied temperature with careful attention paid to the details of the experimental design.

Finally, image-guided thermal therapy and interventional MRI practices are, by nature, *hands on* and technique oriented. Although the physicist and engineer play crucial roles in the initial development of these tools, like MR thermometry, they must also play an active role in facilitating these tools to the physician and surgeon who will ultimately be the ones using them in the clinic. Unfortunately, sometimes the acceptance of a new technological development is met with reluctance and hesitation. This is particularly true when a surgical or therapeutic procedure can already be done without the new tool. For example, certain high-temperature therapies are already routine and have been done without sophisticated thermal mapping. However, it is possible that these same procedures could be done with greater effectiveness and confidence with simultaneous thermal mapping. Additionally, it is disconcerting when a potentially useful therapeutic procedure, like thermal-coagulation therapy, is simply dismissed for lack of a necessary technical component like thermal mapping.

The outline of the thesis is as follows: **Chapter 2** contains some introductory material on MR imaging and provides some background physics on the temperature dependence of the PRF. The following chapters answer some simple, fundamental questions concerning the quantization

of PRF-shift thermometry. In **Chapter 3**, a calibration experiment is described to show that the PRF-thermal coefficient is independent of the *ex vivo* tissue type. While the importance of this study may seem obvious, it was an investigation that had not been previously satisfactorily completed. The consequences of the finding are far reaching and show the PRF-shift method to be much simpler than previously thought.

Chapters 4 and 5 deal with practical issues and they identify some physical properties that could impose limitations on the quantitative ability of PRF-shift thermometry. **Chapter 4** examines how temperature-induced changes in the volume-magnetic susceptibility of tissue leads to a unique orientation and geometry dependence on the heat source that is used in the delivery of the therapeutic temperatures. This dependence is shown to cause errors in thermal mapping if not accounted for. **Chapter 5** identifies the temperature sensitivity of the electrical conductivity of tissue as another confounding factor in PRF-shift thermometry.

An actual MR image-guided thermal-coagulation treatment is described in **Chapter 6** where the methodology is demonstrated in an *in vivo* canine prostate model. This study shows the capability of MR thermometry and illustrates the potential predictive value of thermal mapping for estimating the spatial extent of thermal damage in living tissue. A summary of the conclusions are given in **Chapter 7** along with some remarks about the future of PRF-shift thermometry and its role in clinical thermal therapy.

Chapter 2

The Physics of PRF-Shift MR Thermometry

2.1 Principles of MRI

The phenomenon of nuclear magnetic resonance (NMR) was first discovered independently by Bloch and Purcell[1] in 1946, for which they later shared the Nobel Prize in Physics in 1952. This was soon followed by the discovery of the *chemical-shift effect* that allows nuclei in different chemical environments to be identified by an offset in their resonant frequency, which laid the foundations for NMR spectroscopy and now routinely used to study the conformation of molecules and chemical processes. Magnetic resonance imaging (MRI)[2] is an application of NMR physics which came to realization around 1973, when Lauterbur described a method of spatially encoding the NMR signal to construct images [120].

Many atomic nuclei have an angular momentum that arises from their inherent property of rotation or spin. These nuclei can be considered as spinning charged spheres which then generate a small magnetic field. Thus, nuclei with a non-zero spin have an associated magnetic dipole moment, and only atoms with an odd number of nucleons, ie. protons or neutrons like the ^{1}H nuclei, exhibit an NMR phenomenon. In biological tissue, the ^{1}H proton is the most abundant and is the source for most clinical MRI as the body consists of 70 - 80% water. As such, the following discussion

[1] Felix Bloch of Stanford University and Edward M. Purcell of Harvard University [117,118].

[2] Material in this section is drawn extensively from "Introduction to Magnetic Resonance Imaging" by Nishimura [119].

deals exclusively with ^{1}H proton MRI.

In the absence of an external magnetic field, the net magnetization of a material is zero because the nuclear spins are randomly oriented. When an applied polarizing magnetic field (B_o) is imposed two effects occur[3]. The first, is that a fraction of the nuclear spins become aligned with the applied magnetic field, creating a net or equilibrium magnetization (M_o) that is directed along the z-axis or longitudinal direction. In most clinical MRI systems, the applied magnetic-field strength is between 0.1 and 2.0 Telsa (1 Tesla (T) = 10^4 Gauss (G)). The second effect is that the nuclear spins behave as spinning gyroscopes such that if perturbed from the longitudinal axis they will precess about the longitudinal direction with a well-defined resonance or Larmor frequency.

The Larmor frequency of the nuclear spins is related to the strength of the magnetic field through:

$$f = \frac{\gamma}{2\pi} B_{nuc} \tag{2.1}$$

where γ is the gyromagnetic ratio for the nuclei of interest (for ^{1}H, $\frac{\gamma}{2\pi}$ = 42.57 MHz/T) and B_{nuc} is the magnetic field that the nucleus experiences. Generally, B_{nuc} is slightly different from the externally-applied magnetic-field strength, B_o, due to electronic shielding of the nucleus and variations in the bulk magnetic susceptibility of the object. This will be discussed at greater length in Section 2.2. At a field strength of 1.5 T, the Larmor frequency for ^{1}H protons is approximately 63.87 MHz, which is in the radio-frequency (RF) band of the electromagnetic spectrum.

In order to observe or measure the NMR signal, the longitudinal magnetization (M_z) must be tipped into the transverse (x-y) plane, which gives rise to transverse magnetization (M_{xy}). This is achieved with a pulsed electromagnetic field (B_1) that is applied at the resonant frequency of the nuclear spins (see Figure 2.1). In effect, the B_1 field provides a torque which rotates the longitudinal magnetization by a prescribed angle (α) that is dependent on the strength and duration of the applied B_1 field pulse.

The transverse magnetization is often conveniently represented as a complex number[4], and

[3]Most physics textbooks use the symbol B to denote the magnetic flux density or induction and H to identify the applied "magnetizing force". However, as discussed by Schenck [107], the use of B and H to describe magnetic fields in MRI is essentially redundant. The convention of B is used throughout this thesis, as it more correctly applies to the magnetic field within an object, whereas H usually does not have this interpretation. To avoid confusion, externally applied magnetic fields are denoted as B fields, such as B_o and B_1.

[4]A complex number can be expressed as $c = a + ib$ where a and b are real values and $i = \sqrt{-1}$. a and b represent the real (Real$\{c\}$) and imaginary (Imag$\{c\}$) components of c, respectively. c can also be expressed as a complex-exponential; $Ae^{i\theta} = A(\cos\theta + i\sin\theta)$, where the magnitude $A = \sqrt{(a^2+b^2)}$, and the phase angle $\theta = \arctan(\frac{b}{a})$.

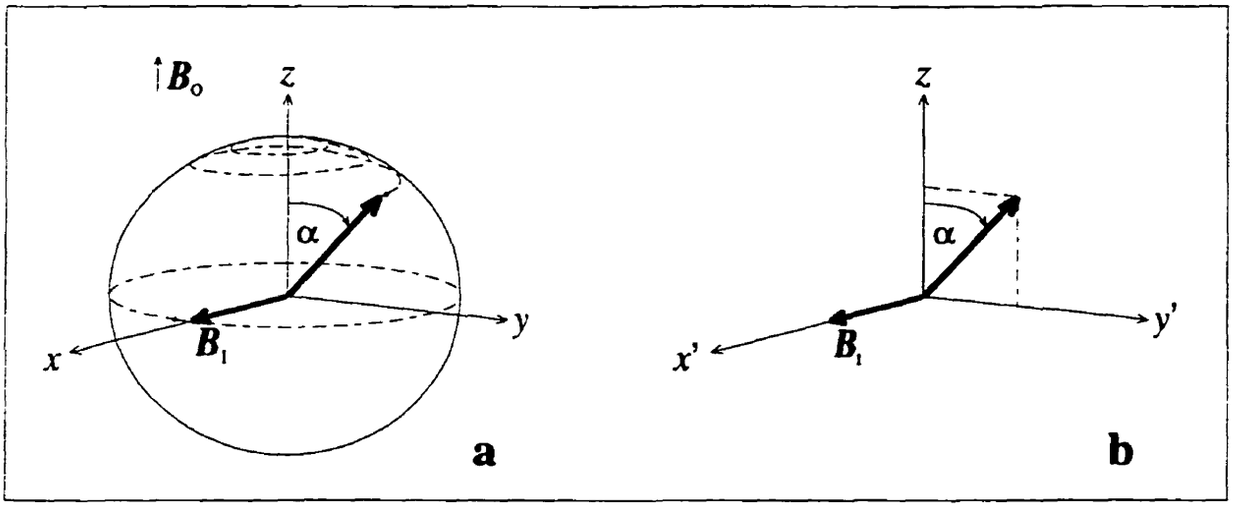

Figure 2.1: Application of a B_1 field to produce transverse magnetization. (a) The applied B_1 magnetic field rotates at the resonant frequency in the transverse plane causing the longitudinal magnetization vector to tip from the z-axis into the (x-y) plane, while precessing at the Larmor frequency. (b) In the rotating frame of reference, where the (x'-y') plane rotates clockwise at the Larmor frequency, the B_1 field and magnetization vectors are stationary.

thus can be described as:

$$M_{xy} = M_x + iM_y \tag{2.2}$$

where M_x and M_y are components of the transverse magnetization along the x- and y-axis, respectively. As M_{xy} rotates at the Larmor frequency within the transverse plane, it generates a time-varying magnetic field that can be detected as an induced voltage in a tuned RF (receiver) coil. Often, the coil used to detect the transverse magnetization is also used to generate the initial B_1 field (transmit mode).

Upon cessation of the B_1 field pulse, the longitudinal magnetization will recover with a time constant of *T1* or spin-lattice relaxation time. The *T1* reflects the effects of random fluctuating magnetic fields that are caused by motion of nearby magnetic dipoles. Similarly, the spin-spin relaxation time constant or *T2* characterizes the decay of the transverse magnetization. The *T2* describes the non-reversible dephasing of transverse magnetization. In biological tissue, *T1* values range from 100 – 1500 ms, while *T2* values are usually between 20 – 300 ms. In addition to *T2*, inhomogeneities in the main-magnetic field, B_o, can lead to a further destructive phase dispersion of the transverse magnetization and thus an effective reduced time constant known as $T2^*$ ($< T2$).

2.1.1 Spatial Encoding

The objective in MR imaging is to spatially map the three-dimensional (3D) distribution of transverse magnetization, $M_{xy}(\vec{r})$ (where $\vec{r} = (x,y,z)$). This distribution includes contributions from tissue characterization properties such as physical density of nuclear spins and the relaxation times *T1*, *T2*, or *T2**. However, within the static main-magnetic field, B_o, all of the nuclear spins will precess with the same frequency such that the received signal following a B_1 pulse would be:

$$S(t) = \int\int\int_{vol} M_{xy}(\vec{r}) e^{-i\omega_o t}\, d^3\vec{r} \tag{2.3}$$

where $\omega_o = \gamma B_o$ is the Larmor frequency[5] (neglecting the small discrepancy between B_o and B_{nuc} and relaxation effects for the moment). Consequently, it is not possible to distinguish the NMR signals originating from different locations within the imaging volume or patient.

Spatial encoding of the transverse magnetization is achieved with the use of linear magnetic-field gradients ($\vec{G}$) that are transiently superimposed on the main-magnetic field, B_o. Gradient fields cause the nuclear spins to precess with different frequencies, depending on their spatial position, $\vec{r}$, according to:

$$\omega(\vec{r}) = \omega_o + \gamma\vec{G}\cdot\vec{r} \tag{2.4}$$

and linear gradient fields can be applied along the x, y and z directions ($\vec{G} = (G_x, G_y, G_z)$) with different strengths or durations in time. Thus, with the application of magnetic-field gradients, the detected MR signal takes the form (again, neglecting relaxation effects):

$$S(t) = \int\int\int_{vol} M_{xy}(\vec{r})\; e^{-i(\omega_o t\; +\; \gamma \int_0^t \vec{G}(t')\cdot\vec{r}\; dt')}\; d^3\vec{r} \tag{2.5}$$

Often it is convenient to define the MR spatial-encoding parameter to be:

$$\vec{k} = \frac{\gamma}{2\pi}\int_0^t \vec{G}(t')\, dt' \tag{2.6}$$

which has the units of spatial frequency (cycles/m). If the spatial position of the nuclear spins is

[5]Precessional frequency can be expressed either in units of radians/second (angular frequency, ω) or cycles/second (f). The two quantities are related through $\omega = 2\pi f$.

constant in time, ie. $\vec{r} \neq \vec{r}(t)$ then Equation 2.5 becomes:

$$S(\vec{k}) = \int\int\int_{vol} M_{xy}(\vec{r})\ e^{-i2\pi\vec{k}\cdot\vec{r}}\ d^3\vec{r} \tag{2.7}$$

where the exponential term $e^{-i\omega_o t}$ is understood to have been removed through base-band frequency demodulation.

The above use of linear magnetic-field gradients describes Fourier encoding in which discrete samples of $S(\vec{k})$ are obtained, known as the filling of the object's k-space matrix. The k-space represents the discrete Fourier transform of the transverse magnetization, $M_{xy}(\vec{r})$ with respect to $\vec{k}$. Image reconstruction is achieved by performing an inverse Fourier transform on $S(\vec{k})$.

By varying the strength and duration of the magnetic-field gradients, different values of $\vec{k}$ can be obtained (Equation 2.6). Filling of a 3D k-space can be time consuming, because k-space is usually filled one line at a time. However, in practice, most clinical situations require only a limited number of 2D images which necessitates the filling of a 2D k-space (k_x,k_y).

The detected MR signals are usually detected in the form of resonant echoes, which are produced through techniques known as gradient reversal (gradient echo) or by the application of a second B_1 pulse known as an inversion or 180^o pulse (spin echo). These echo signals are digitally sampled in time with the simultaneous application of a readout or frequency-encoding gradient, usually denoted as G_x. The frequency encoding of an echo fills one line in k-space and thus resolves one spatial dimension, x. To fill the 2D k-space, this process of echo formation and frequency encoding must be repeated. On each repetition, the gradient G_y is applied and incremented, prior to the signal acquisition, in a procedure known as phase encoding. For 2D MR imaging the third spatial dimension is resolved by tipping only the nuclear spins that lie within a thin slab or slice, usually 3 - 10 mm in width, known as slice selection.

An example of the formation of a gradient echo is given in Figures 2.2 and 2.3. Figure 2.2 describes a pulse-timing diagram, which shows the relative timing and duration of the B_1 pulse, the applied frequency-encoding gradient G_x, and the resultant MR signal $S(t)$, representing the transverse magnetization. The temporal evolution of the magnetization during the formation of a gradient echo is illustrated in Figure 2.3. Using the timing diagram of Figure 2.2, before the application of the B_1 pulse (t<0), all of the magnetization is directed along the longitudinal or z-axis. When the B_1 pulse is applied along the rotating x-axis, the longitudinal magnetization is

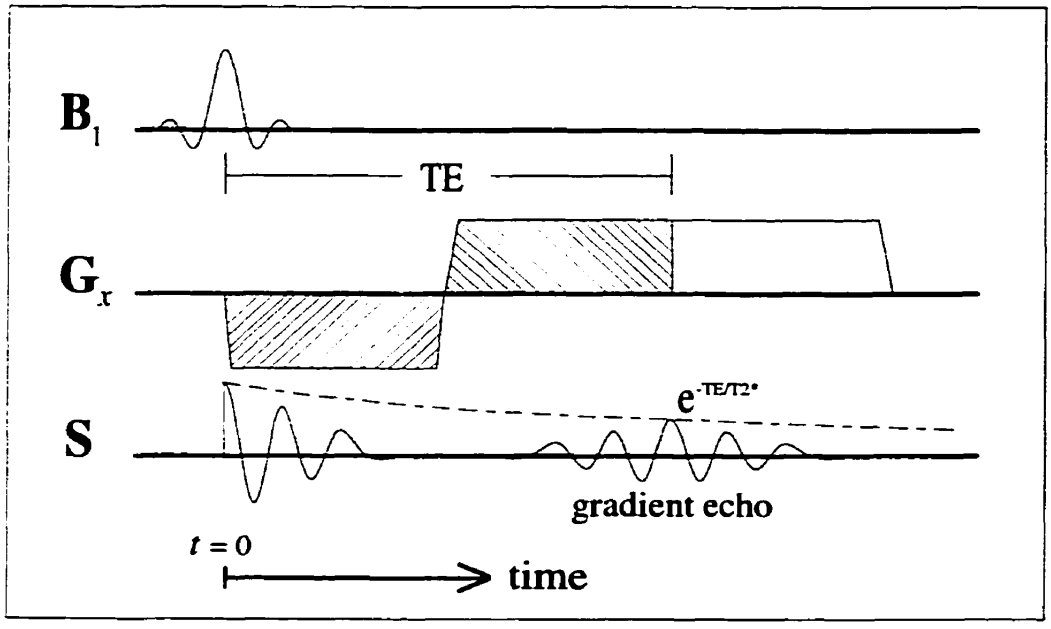

Figure 2.2: Pulse-timing diagram showing frequency encoding of a gradient echo. Shown are the B_1 pulse, the frequency-encoding gradient (G_x), and the resultant MR signal (S) over time. The B_1 pulse produces transverse magnetization which quickly dephases with the application of the magnetic-field gradient. A gradient echo is produced when the G_x gradient is reversed and the area of the positive duration equals the negative (cross-hatched areas). At this time, the MR signal has been attenuated to $e^{-TE/T2*}$, relative to when transverse magnetization was first produced (t=0).

tipped into the transverse (x-y) plane by an angle α, and is initially directed along the y or y'-axis.

The transverse magnetization begins to dephase as indicated by the numerated vectors in Figure 2.3 at t=0, primarily as a result of the application of the applied linear gradient, G_x (Figure 2.2). The nuclear spins that precessed slower, when G_x was negative, precess faster when G_x is positive. The nuclear spins are rephased and form a gradient echo at t = TE, when the area under the negative and positive gradients become equal. If there is an off-resonance condition, there will be a net phase accumulation at the time of the gradient echo, denoted as ϕ.

2.1.2 Off-Resonance Conditions

Unlike MR imaging pulse sequences that detect signals based on a spin echo, techniques that employ a gradient echo are sensitive to sources of off resonance. In the absence of applied linear magnetic-field gradients, the Larmor frequency is not uniform across the object due to three main sources:

(i) *inhomogeneities* in the main-magnetic field, B_o,

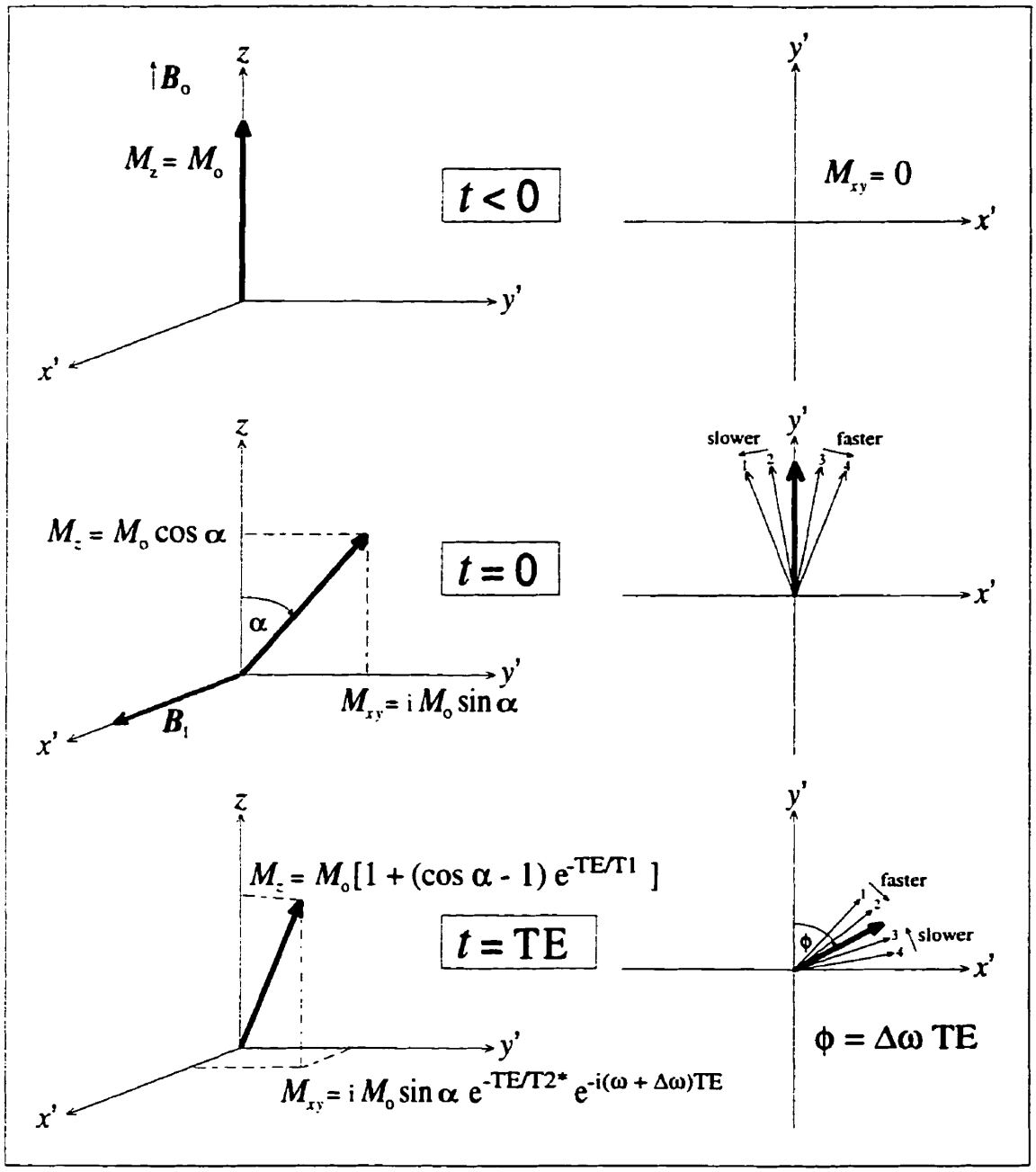

Figure 2.3: Representation of the formation of a gradient echo. Shown are the longitudinal and transverse magnetization (in the rotating frame of reference). Before the B_1 pulse ($t<0$), all of the magnetization is directed along the z-axis. When the B_1 pulse is applied on resonance, transverse magnetization (M_{xy}) is produced which is initially directed along the y'-axis and begins to dephase. At $t=TE$, the transverse magnetization is brought back into coherence and a gradient echo is formed (Figure 2.2). If an off-resonance condition exists ($\Delta\omega$), there will be some phase accumulation, denoted by ϕ.

(*ii*) variations in the *magnetic susceptibility* of the object, and

(*iii*) *chemical shift* due to differences in the microenvironment of the ^{1}H proton.

As all of these sources cause variations in the resonant frequency, they are referred to as off-resonance conditions.

All modern high-field magnets used in MRI systems have some degree of non-uniformity or inhomogeneity in the B_o field over the volume used in imaging. Additional "shim" coils are then used to improve this overall uniformity. Such inhomogeneities are usually expressed in terms of parts-per-million (ppm) of the main-magnetic field strength, over a specified spherical volume. For example, an inhomogeneity of 1 ppm over a 40 cm diameter spherical volume in a 1.5 T main-magnetic field would correspond to a maximum field excursion of 1.5 μT (0.015 G) which implies a maximum frequency offset ($\Delta\omega$) of approximately 64 Hz for ^{1}H protons.

There will be variations in the macroscopic-magnetic field, B_{mac}, in the object or patient due to differences in the bulk or volume-magnetic susceptibility, χ_v, even within a perfectly uniform main-magnetic field . The volume-magnetic susceptibility is a dimensionless quantity that can vary by as much as 10^{-6} - 10^{-5} in soft tissues. Inhomogeneity in B_{mac} is most severe at boundaries between materials with different volume-magnetic susceptibilities, such as at air-tissue interfaces where there are large differences in χ_v.

The macroscopic-magnetic field, B_{mac}, can derived from applying Maxwell's equations in matter [121] given the volume-magnetic susceptibility distribution and the geometry of the object relative to the applied-magnetic field. If the object can be approximated as an ellipsoid with a uniform susceptibility, then B_{mac} will be parallel with the applied-magnetic field if it is aligned along one of the object's principal axes. Some useful expressions for B_{mac} are listed in Table 2.1 for a sphere and circular cylinder [107, 122].

An off-resonance condition can also originate from the chemical-shift effect. Whereas variations in the volume-susceptibility represent a macroscopic effect to perturb the main-magnetic field, the chemical-shift can be regarded as a microscopic effect on the nuclear spins. The magnetic field that the nuclear spin experiences is altered from the macroscopic-magnetic field due to electronic shielding and can be written as:

$$B_{nuc} = (1 - \sigma)\, B_{mac} \tag{2.8}$$

where σ is generically referred to as a shielding or screening constant. Consequently, the resonant frequency can vary among different electronic configurations and chemical environments. For ex-

Table 2.1: The macroscopic-magnetic field inside a uniform sphere or cylinder. The objects are of uniform susceptibility and are placed in a uniform external magnetic field, B_o. This is a first-order approximation, where $|\chi| \ll 1$ and assuming the cylinders are sufficiently long with an aspect ratio ≥ 5. χ and χ_e represent the volume-magnetic susceptibility of the object and the outer environment, respectively ($\chi_{air} \approx 0$).

Object	B_{mac}
sphere	$(1 + \frac{2}{3}(\chi - \chi_e))B_o$
circular cylinder, $\parallel B_o$	$(1 + (\chi - \chi_e))B_o$
circular cylinder, $\perp B_o$	$(1 + \frac{1}{2}(\chi - \chi_e))B_o$

ample, the ^{1}H nuclei in fat (largely from CH_2 groups) has a chemical shift of approximately -3.5 ppm relative to water. At 1.5 T, this means that the resonant frequency of nuclear spins in fat is 220 Hz lower than those in water.

2.2 The Physics of PRF-Shift MR Thermometry

A practical implementation of PRF-shift method of MR thermometry was first described in 1992; however, the basic physics for the temperature sensitivity of the PRF has been known for quite some time. The temperature dependence of the PRF in hydride molecules, such as water, was first observed by Schneider in 1958 [111] and further elucidated by Hindman in 1966 [112]. These studies consisted of NMR experiments and were primarily aimed at investigating the structure of water, as MR imaging had not yet been established.

2.2.1 A Model of B_{nuc} in Water

A complete understanding of the temperature dependence of the PRF begins with a consideration of the various contributions to the chemical shift of the ^{1}H nucleus, first at a fixed temperature. Chemical shift arises because nuclei are not simply isolated, but are contained in atoms, ions, or molecules. Consequently, the magnetic field at the nucleus[6], B_{nuc}, is different from the macroscopic-magnetic field, B_{mac}. The following discussion focuses on water which is the primary source of the ^{1}H NMR signal.

[6]It is understood that B_{nuc} represents a time *average* value of the magnetic field at the nucleus, which is averaged over a sufficiently long time interval, ie. longer than the molecular configuration time of the water molecule [123].

The chemical shift in water arises from both *intramolecular* and *intermolecular* effects and the screening constant in Equation 2.8 can be written as the sum of three separate screening effects[7] [112, 122–125]:

$$\sigma_T = \sigma_0 + \sigma_\chi + \sigma_E \tag{2.9}$$

where the subscripts refer to the contributions to the total screening of the isolated or gaseous molecule (σ_0), the volume-susceptibility of the surrounding medium (σ_χ), and variations in the electron configuration of the hydrogen atom due to the electric field of neighboring water molecules (σ_E).

Intramolecular Screening, σ_0

In an isolated water molecule, σ_0 represents an intramolecular shielding constant that (in the absence of solvent effects) leads to the generalized interpretation of the nuclei's chemical shift [112, 123, 124]. This component to the total screening constant results from differences in the effective electron distribution about the nuclei. For example, intramolecular screening accounts for the chemical shift between water and fat.

Magnetic-Susceptibility Effect, σ_χ

In NMR spectroscopy, it is known that the chemical shift is dependent on the volume-magnetic susceptibility, χ_v, as well as on the shape and orientation of the sample holder which are usually glass cylinders or spheres. It is understood that χ_v contributes to the chemical shift through two separate, but similar, effects: variations in the B_{mac} field and through a "Lorentz" cavity field which is described by a screening constant σ_χ. For an arbitrarily-shaped object and orientation, B_{mac} will not generally be parallel to B_o and for this reason, Equation 2.8 is cast as a screening of the spatially-variable B_{mac} rather than B_o, thus leaving σ_χ effectively decoupled from B_{mac}.

The macroscopic-magnetic field, B_{mac}, represents the bulk effect of magnetic susceptibility from the entire object. Now consider susceptibility on the geometric scale of the individual water molecules. Every nuclear spin can be conceptualized to diffuse about the compartment in a hypothetical spherical bubble or "sphere of Lorentz" of zero magnetic susceptibility, ie. vacuum cavity [122–124, 126]. The radius of the sphere is small compared to the dimensions of the object,

[7] An alternative convention is to describe B_{nuc} directly as a superposition of the various magnetic fields associated with the individual chemical-shift effects, as done in references [122–124].

but large compared to the microscopic dimensions of the water molecules. In this construct, the surrounding uniform water medium produces an effect on the surface of this sphere called a cavity field.

Using the result for a sphere in Table 2.1, if a sphere of zero susceptibility is placed in a medium with a uniform susceptibility, χ, and magnetic field, B_{mac} (uniform on a geometric scale of the Lorentz sphere), the magnetic field within the sphere will be given by $(1 - \frac{2}{3}\chi)B_{mac}$. This can be viewed as an effective screening of B_{mac} where $\sigma_\chi \equiv \frac{2}{3}\chi$, with χ being the susceptibility of water[8]. Pure water is diamagnetic, and has a volume-magnetic susceptibility of -9.03 $\times$ 10^{-6} (MKS) at room temperature[9].

Intermolecular Electric-Field Effect, σ_E

Intermolecular effects between water molecules are characterized by the screening constant σ_E. One intermolecular effect that is particularly relevant in liquid water occurs from hydrogen-bonding among water molecules. Schneider in 1958 first described an apparent "association shift" when measuring the chemical shift in liquid hydride molecules. The postulation was that hydrogen bonding caused a change in the electronic configuration and hence shielding of the ^{1}H proton, and that disturbances in hydrogen bonding could cause observable chemical shifts from variations due to changes in sample temperature for example. As the intermolecular screening effects in liquid water are dominated by hydrogen bonding, some review of the hydrogen bond may be beneficial at this point.

The Hydrogen Bond and Considerations of the Structure of Water

Understanding the structure of water, and in particular the hydrogen bond, has been a primary concern in many fields of pure and applied science. For instance, this understanding has crucial relevance to many other structures, such as DNA and proteins [127].

A hydrogen bond is a weak association between an electronegative atom or *acceptor* and a hydrogen atom that is covalently bonded to another atom, or *donor*, as illustrated in Figure 2.4.

---

[8]To exclude the effects of volume-magnetic susceptibility on the chemical shift, some NMR spectroscopy experiments use spherical sample holders, where $B_{mac} = (1 + \frac{2}{3}\chi)B_o$ and thus Equation 2.8 becomes (in the absence of other chemical-shift effects): $B_{nuc} = (1 - \sigma_\chi)B_{mac} = (1 - \frac{2}{3}\chi)(1 + \frac{2}{3}\chi)B_o \cong B_o$, neglecting terms of χ^2. Therefore, chemical-shift measurements using a spherical sample holder contain no contributions from magnetic susceptibility.

[9]The reader is reminded that several papers referenced in this thesis use the older CGS (centimeter, gram, second) convention, rather than the more current MKS (meter, kilogram, second) convention, where the magnetic susceptibilities are related through: $\chi_{(MKS)} = 4\pi\chi_{(CGS)}$.

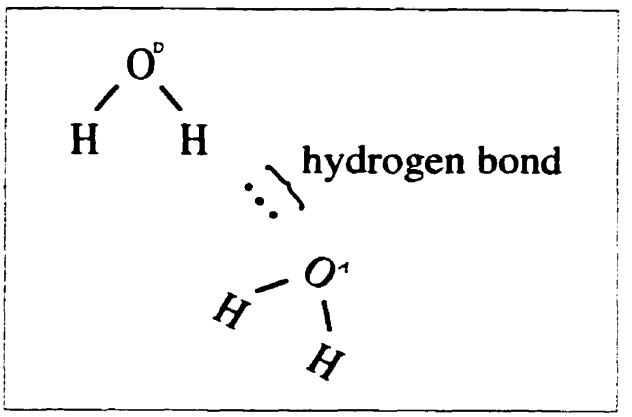

Figure 2.4: Representation of a hydrogen bond between two water molecules. The hydrogen bond among water molecules is approximately 0.27 nm in length and 0.22 eV (5 kcal/mol) in strength. The donor (D) and acceptor (A) oxygen atoms are indicated.

In water molecules, the covalent bond between the donor oxygen and hydrogen atom is dipolar and the hydrogen atom in one molecule is attracted to a pair of electrons in the outer shell of the acceptor oxygen atom in an adjacent molecule. Between water molecules, the hydrogen bond is approximately 0.22 eV in strength and much weaker than the covalent H-O bond (4.77 eV). For reference, thermal energy at room temperature (kT) is 0.025 eV.

Hydrogen bonds possess a strong directionality, such that the donor oxygen, the hydrogen, and the acceptor oxygen atom lie in a straight line. The length of this bond (between the H atom and acceptor O) is approximately 0.27 nm and roughly twice the length of the covalent H-O bond. In fact, the covalent bond length between the donor oxygen and hydrogen atom can increase slightly when there is a hydrogen bond because the acceptor oxygen atom effectively *pulls* the hydrogen atom away from the donor oxygen atom.

Ordinary ice is a crystal in which each oxygen atom forms two covalent bonds with two hydrogen atoms and two hydrogen bonds with hydrogen atoms of adjacent molecules[10]. While the detailed structure of liquid water is a topic of debate, it is generally agreed that it may consist of "ice-like" hydrogen-bonded networks that are transient such that a crystal does not form. The number of hydrogen bonds per water molecule may also range from 3 - 6, with an average of 4.5 [127]. With increasing temperature, the kinetic energy of water molecules approaches the hydrogen-bond strength and water molecules spend less time, on average, in a hydrogen-bonded

[10]There is mounting evidence to suggest that there is a covalent nature to hydrogen bonds in ice [128], a prediction originally put forward by Linus Pauling in 1935.

state. The correlation time constant (or diffusional time constant) which characterizes the time for a water molecule to diffuse a length of its own diameter is approximately 10^{-5} s in ice and 10^{-11}–10^{-12} s in liquid water [129].

Previous models have assumed liquid water to be a mixture of two species: (*i*) a hydrogen bonded ice-like fraction, and (*ii*) a non-hydrogen bonded monomeric fraction. With this simplified model the fraction of non-hydrogen bonded molecules is estimated to increase linearly from 0.16 at 0°C to 0.29 at 100°C, as compiled by Hindman [112].

Having discussed the various screening effects, Equations 2.8 and 2.9 can be used to write an expression for the magnetic field at the nucleus:

$$B_{nuc} = \left(1 - \sigma_0 - \frac{2}{3}\chi - \sigma_E\right) B_{mac} \tag{2.10}$$

If the macroscopic-magnetic field is approximated as $B_{mac} \approx B_o + \boldsymbol{O}(\chi B_o)$, with $\boldsymbol{O}(\chi B_o)$ representing terms linear with and of the order of χB_o, then Equation 2.10 can be rewritten as:

$$B_{nuc} = B_{mac} - \left(\sigma_0 + \frac{2}{3}\chi + \sigma_E\right) B_o \tag{2.11}$$

Attention is now turned to how B_{nuc} varies with temperature. Because the intramolecular screening constant, σ_0, is usually considered a static contribution, examination of the temperature sensitivity of B_{nuc} reduces to looking at the temperature sensitivity of the volume-magnetic susceptibility, χ and the intermolecular screening constant, σ_E.

2.2.2 The Temperature Dependence of χ_v in Water

The magnetic susceptibility has been examined in the past as a means of probing the structure of water, as well as providing valuable reference data [130–138]. The quantity of interest is the volume-magnetic susceptibility (χ_v) which is equal to the product of the physical density (ρ) with the mass-magnetic susceptibility (χ_m). Generally, the quantity that is experimentally measured is χ_m. Figures 2.5 and 2.6 show the temperature dependence of the physical density and mass-magnetic susceptibility of water, respectively. From initial experimental evidence, it was believed that χ_m had a complicated temperature dependence [130, 131]. However, measurements have since been considerably improved to show an approximate linear behavior with temperature [133, 137, 138]. It is currently thought that the diamagnetism of liquid water, much like the intermolecular screening

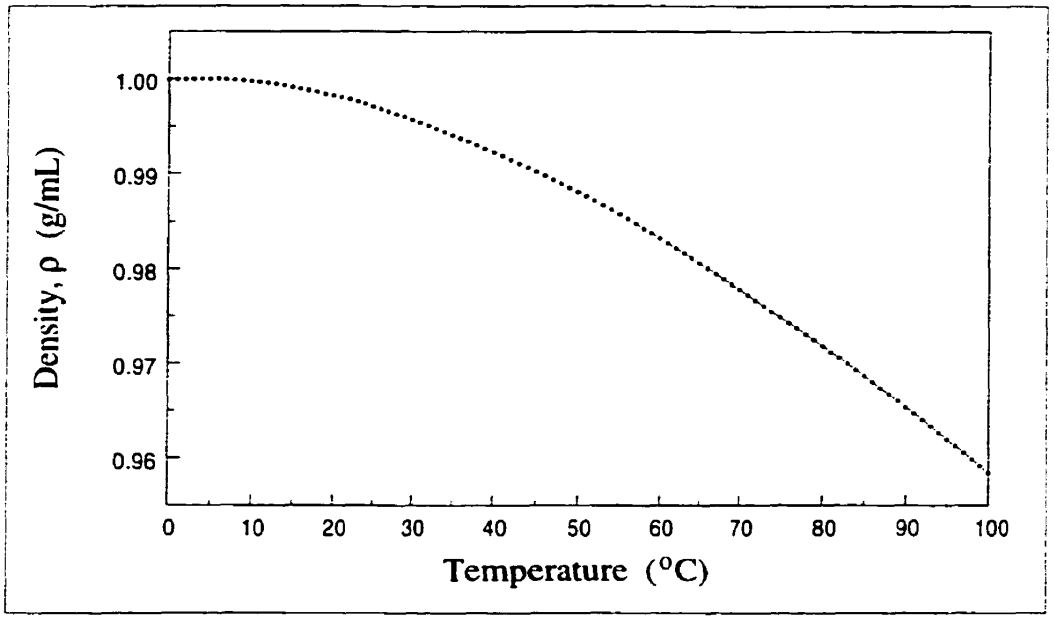

Figure 2.5: The density of water as a function of temperature. The above data was obtained from the CRC Handbook of Chemistry and Physics [139].

constant σ_E, is altered by weak intermolecular interactions of hydrogen bonds such as changes in the average number, strength, and orientation. The mass-magnetic susceptibility, χ_m, increases roughly linearly with temperature as shown in Figure 2.6.

Using the χ_m data provided by Philo and Fairbank [137] along with tabulated values for the density of water [139], the volume-magnetic susceptibility, χ_v, is seen to exhibit a quadratic behavior with temperature, as shown in Figure 2.7. This non-linear behavior is primarily due to the variation of the density of water with temperature. At 37°C, the volume-magnetic susceptibility of water increases (becomes less diamagnetic) with temperature by approximately $+0.003\times10^{-6}$/°C.

2.2.3 The Temperature Dependence of σ_E in Water

Variations in hydrogen bonding among water molecules is a major contributor to the temperature dependence of the intermolecular screening constant σ_E. As temperature increases, water molecules have more kinetic energy and spend less time on average in a hydrogen-bonded configuration. There is a so-called "association" shift in water, defined by Schneider as the difference between the chemical shift of liquid water at a temperature just above the melting point (of maximum association) and that of gas (with unassociated molecules or monomers) [111]. Further insight into hydrogen bonding among water molecules as a function of temperature was provided by Muller,

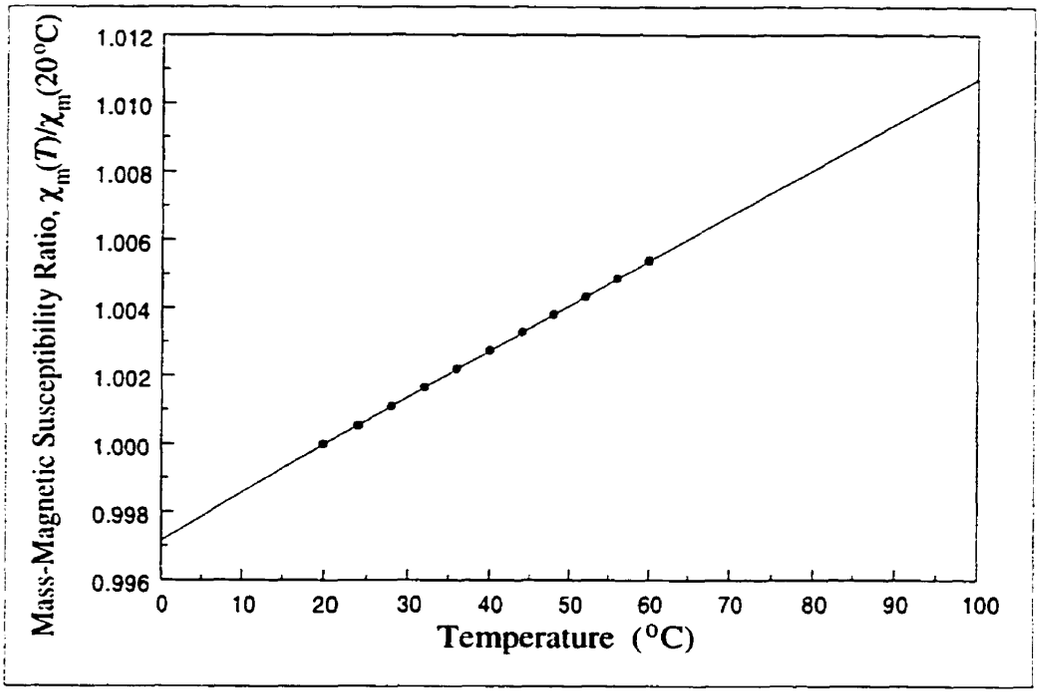

Figure 2.6: The mass-magnetic susceptibility ratio of water as a function of temperature. Shown is the susceptibility ratio relative to 20°C ($\chi_m(T)/\chi_m(20°C)$) listed in [137]. The solid line represents the reported fitted curve to the data $\chi_m(T)/\chi_m(20°C) = 1 + 1.38810\times10^{-4}(T\text{-}20) - 1.2685\times10^{-7}(T\text{-}20)^2 + 8.09\times10^{-10}(T\text{-}20)^3$.

who used chemical-shift measurements to specifically probe the structure of water [140, 141].

A good working understanding of the temperature dependence of σ_E can be gained by considering the following three points:

(*i*) The B_{nuc} field of a ^{1}H proton in a free water molecule (monomer) is screened *more effectively* by the electron cloud than when hydrogen bonded to another water molecule. This is because the ^{1}H proton in a hydrogen bond is drawn away from its own bonding electrons, which are not able to circulate as freely about the nucleus.

(*ii*) As temperature increases, there is an *increasing* degree of dissociation among water molecules, as hydrogen bonds are more readily broken and there is an increasing fraction of monomers[11].

(*iii*) Consequently, as temperature increases the ^{1}H proton experiences a (time averaged) greater electron screening and hence a *lower* B_{nuc} field.

As shown by Hindman[12] (see Figure 2.8), the intermolecular screening constant exhibits an

[11] Changes in the effective length of the hydrogen bond, such as stretching and vibrations, may also be significant [112, 140, 141].

[12] This report tabulated the chemical shift as a function of temperature in Table II where δ(obs) denotes the raw chemical-shift measurements [112]. The magnetic-susceptibility corrected data δ(corr) more accurately reflects the temperature dependence of σ_E as shown in Figure 2.8. There is likely a mistake in the 50°C entry, which should read 0.285 rather than 0.235.

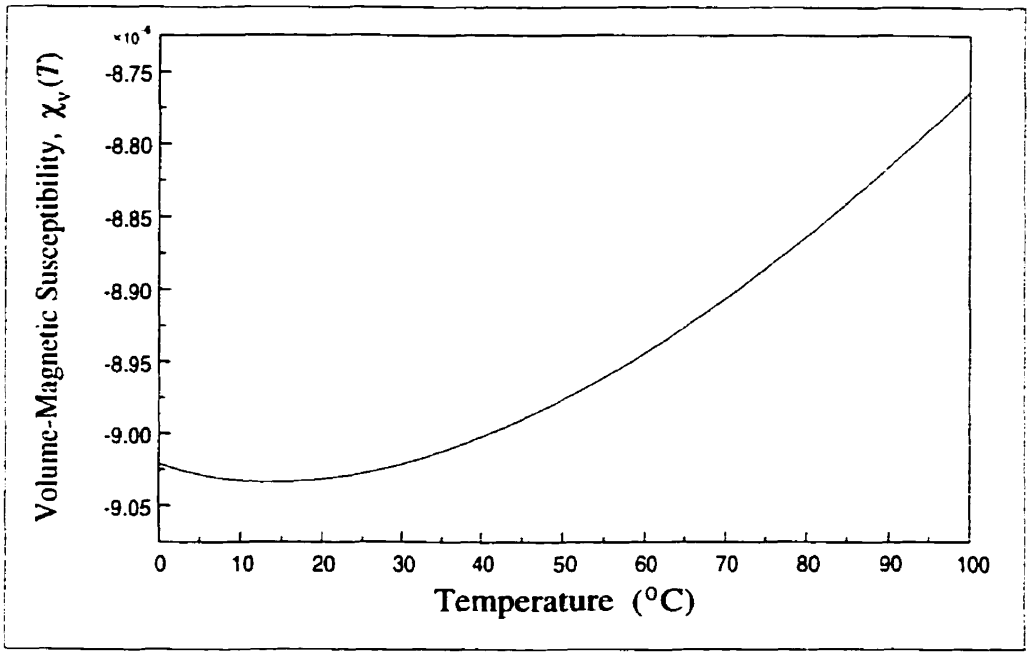

Figure 2.7: The volume-magnetic susceptibility of water as a function of temperature. The above data was calculated through $\chi_v(T) = \chi_m(20°C) \cdot [\chi_m(T)/\chi_m(20°C)] \cdot \rho(T)$, using the density and mass-magnetic susceptibility data as shown in Figures 2.5 and 2.6 respectively. A reference value of $\chi_m(20°C)$ = -9.05×10^{-6}mL/g was used as suggested in [107].

approximate linear dependence with temperature with a thermal coefficient of roughly +0.0103×10^{-6}/°C [112].

2.2.4 The Temperature Dependence of the PRF

With Equation 2.11 and the Larmor relationship (Equation 2.1), temperature-induced changes in the PRF can be modelled as:

$$\Delta f = \frac{\gamma}{2\pi}\left(\Delta B_{mac} - \left(\frac{2}{3}\Delta\chi + \Delta\sigma_E\right) B_o\right) \tag{2.12}$$

where temperature-induced changes in the macroscopic-magnetic field, volume-magnetic susceptibility, and intermolecular screening constant are indicated. Although the temperature sensitivity of the PRF is dictated by that of B_{mac}, χ, and σ_E, changes in the intermolecular screening constant dominates and the temperature dependence of the PRF is usually described by a linear thermal coefficient (generally in units of ppm/°C). In pure water, the PRF-thermal coefficient is approximately -0.01 ppm/°C; however, it is realized that significant changes in the spatial distribution of

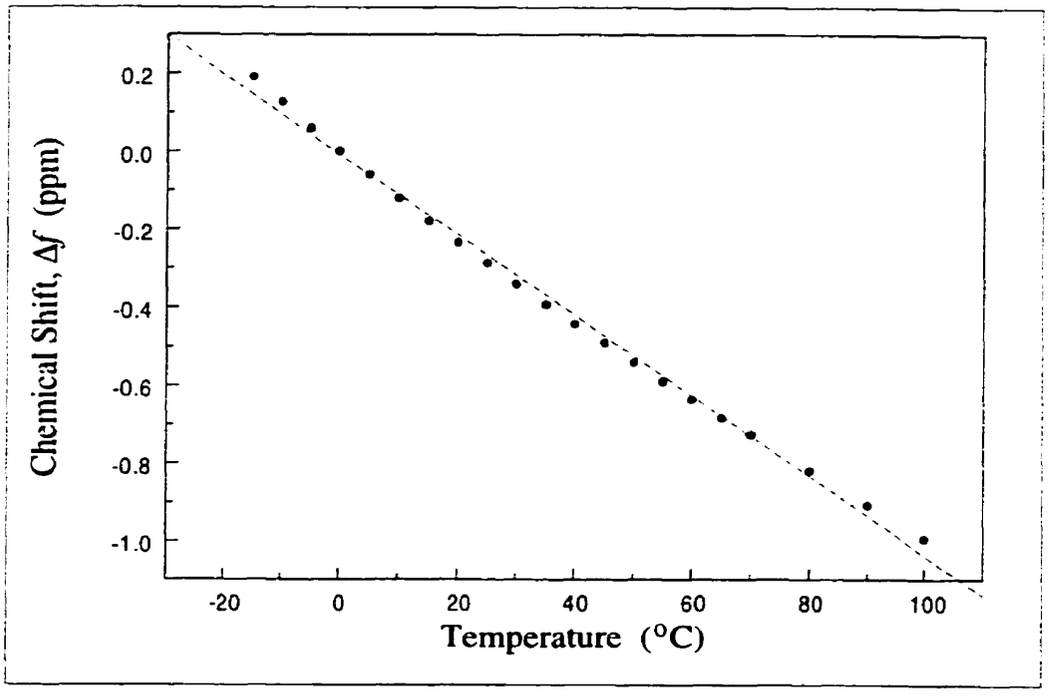

Figure 2.8: The intermolecular screening contribution to the chemical shift in water as a function of temperature. Shown is the chemical shift data corrected for changes in the magnetic susceptibility, as reported by Hindman (Table II, δ(corr)) [112]. A zero chemical shift has been assigned at T = 0°C. A linear fit gives $\Delta f/\Delta T$ = -0.0103 $\pm$ 0.0002 (sd) ppm/°C.

B_{mac} may result and violate this simple linear approximation.

2.3 Practical Implementations of PRF-Shift MR Thermometry

The overall goal of PRF-shift thermometry is to spatially resolve the temperatures within tissue with adequate resolution that is necessary for guiding the thermal therapy. Currently, there are three main ways that PRF-shift thermometry can be implemented: (*i*) *chemical-shift imaging*, (*ii*) chemical-shift imaging with *temperature-sensitive contrast agents*, and (*iii*) *phase-shift mapping*.

2.3.1 Chemical-Shift Imaging

One of the most direct methods of spatially-resolving a temperature distribution using the temperature sensitivity of the PRF is through a method referred to as chemical-shift imaging (CSI) or MR spectroscopic imaging. This method differs from usual MRI, in that each volume element (voxel) is represented by a ^{1}H NMR spectrum rather than a signal intensity. Chemical-shift imaging for thermometry was first reported in 1985 by Hall and Talagala who demonstrated the technique in

a tissue-equivalent material [142].

The general approach with CSI methods is to measure the water chemical-shift relative to a reference frequency. One commonly-used reference peak is fat or lipid which is separated from the water peak by approximately 3.5 ppm (220 Hz at 1.5 T). As fat contains relatively few hydrogen bonds, its PRF-thermal coefficient is dictated primarily by its volume-magnetic susceptibility. Other reference peaks of metabolites have been investigated, such as pyruvate, acetate, lactate and choline-containing compounds such as choline, creatine, and N-acetylaspartate [143–145].

With the use of a suitable reference peak, one major advantage of CSI methods is the ability to provide an *absolute* temperature measurement, rather than a temperature change from some baseline value. This could prove useful in situations other than for monitoring thermal therapy, such as in estimating local brain temperatures [144], and metabolic abnormalities or even blood-circulation disorders.

Despite the simplicity and ability to map absolute temperatures, CSI methods are not extensively used for thermal-therapy applications. The major reasons for this is the poor spatial resolution and long imaging acquisition times that are required. For example, in one recent implementation of CSI using PRF-shift thermometry, the image update time was 2.5 minutes and the voxel size was $3\times3\times3$ mm^3 [145].

2.3.2 Temperature-Sensitive Contrast Agents

To address the relatively low temperature sensitivity of the PRF in water (approximately -0.01 ppm/°C) there has been considerable development in the use of temperature-sensitive contrast agents with CSI techniques. This method involves measuring the chemical shift of non-water proton resonances that originate from specially-designed molecules. Several contrast agents have been described for use in monitoring thermal therapy, such as encapsulated liquid crystals [146], ^{59}Co complexes [147–149] and paramagnetic lanthanide-ion chelated complexes [150–154].

Recently, much attention has turned to the temperature sensitivity of lanthanide complexes. These contrast agents consist of large molecules which have a paramagnetic ion at the center of a chelate complex, such as praseodymium, thulium, and ytterbium. The NMR signal comes from a methoxy side chain contained within the chelate. Small conformational changes result from temperature elevations which alter the distance between the protons and the paramagnetic center. This results in a large chemical shift that can be as much as 10 - 100 times more than that of pure

water.

Along with the advantages of using CSI techniques, exogenous contrast agents are used primarily for their marked increase in the chemical shift with temperature and thus potentially allow for superior temperature resolution. However, the disadvantages of CSI continue to hold with the use of contrast agents, notably the poor spatial resolution and long acquisition periods. Exogenous contrast agents may also require relatively large concentrations to be useful in temperature mapping and have related toxicity. Further, some agents have a limited temperature range, above which they show decomposition which could preclude their use in high-temperature thermal coagulation therapies.

2.3.3 Phase-Shift Mapping

An alternative to CSI techniques for PRF-shift thermometry was introduced by Ishihara in 1992 [113], and consisted of spatially mapping temperature-induced phase shifts and is the method exclusively employed in this thesis. As will be described in the following chapters, this technique is based on the acquisition of phase images obtained from gradient-echo imaging sequences. As illustrated in Figure 2.3, if there is an off-resonance condition there will be a phase accumulation upon gradient reversal and signal detection. The PRF manifests as a temperature-dependent off-resonance condition (Equation 2.12) and, consequently, a temperature distribution, $\Delta T(\vec{r})$, results in a temperature-dependent phase shift:

$$\Delta\phi(\vec{r}) \;=\; \Delta f(\vec{r}) \cdot (360^o/cycle) \cdot TE \tag{2.13}$$

or more explicitly,

$$\Delta\phi(\vec{r}) \;=\; \frac{\gamma}{2\pi}\left(\frac{\Delta B_{mac}}{\Delta T} \;-\; \left(\frac{2}{3}\,\frac{\Delta\chi}{\Delta T} \;+\; \frac{\Delta\sigma_E}{\Delta T}\right) B_o\right) \cdot (360^o/cycle) \cdot TE \cdot \Delta T(\vec{r}) \tag{2.14}$$

relative to a baseline or reference temperature distribution. In the above equation, linear temperature dependencies for B_{mac}, χ, and σ_E are explicitly shown and the temperature-induced phase shift, $\Delta\phi$, is seen to be directly proportional to the echo-time period, TE, as indicated in Figure 2.2. In experimental conditions where temperature-induced changes in the macroscopic-magnetic

field are negligible, Equation 2.14 can be reduced to a much simpler form:

$$\Delta\phi(\vec{r}) \;=\; \alpha \cdot \frac{\gamma}{2\pi} \cdot B_o \cdot (360^o/cycle) \cdot TE \cdot \Delta T(\vec{r}) \tag{2.15}$$

where $\alpha = \frac{2}{3}\frac{\Delta\chi}{\Delta T} + \frac{\Delta\sigma_E}{\Delta T}$ is a spatially independent constant.

The main advantages of using the phase-shift mapping technique is that it provides spatial and temporal resolution equivalent to standard diagnostic quality MR images and is easy to implement. However, one obvious drawback is that it allows only for measurements of temperature *change*, relative to a reference temperature distribution, whereas CSI methods could ideally provide measures of absolute temperature. Also, as a "preheating" reference image is necessary, the phase-shift mapping technique is sensitive to motion during the thermal-monitoring course, whereas each voxel in the CSI method contained its own intrinsic reference in the form of a temperature-insensitive reference peak. Other limitations and correction schemes that are necessary with the phase-shift mapping technique are described in the following chapters.

2.3.4 Summary

It seems reasonable that spatial mapping of temperatures could provide a means of monitoring and controlling the delivery heat energy during a thermal therapy. Magnetic resonance imaging has been recently proposed as a method for *in vivo* thermometry and possesses many desireable attributes that make it well suited for this clinical application.

The basic physics of nuclear magnetic resonance have been reviewed, with an emphasis on the temperature sensitivity of the proton resonance frequency (PRF). In water, it has been shown that this dependence is due to temperature-induced changes in the volume-magnetic susceptibility (χ_v) and the intermolecular electric-field effect (σ_E), the latter of which is highly dependent on hydrogen bonding among water molecules.

Practical implementations of PRF-shift thermometry have been described, based on either chemical-shift or phase-shift imaging techniques. In particular, phase-shift imaging is identified to provide the spatial, temporal, and temperature resolution that is required for thermal-coagulation therapy monitoring. The following chapters describe studies on PRF-shift thermometry that encorporate the phase-shift imaging technique. However, a full appreciation of the methods, results, and implications of these studies will require a good understanding of the physics, definitions, and nomenclature introduced in this present chapter.

Chapter 3

Ex Vivo Tissue-Type Independence in PRF-Shift MR Thermometry

adapted from:
Robert D. Peters, R. Scott Hinks, R. Mark Henkelman,
Ex Vivo Tissue-Type Independence in Proton-Resonance Frequency Shift MR Thermometry.
Magnetic Resonance in Medicine **40**: 454-459 (1998).

3.1 Abstract

The temperature-sensitivity of the proton-resonance frequency (PRF) has proven valuable for the monitoring of MR image-guided thermal coagulation therapy. However, there is significant inconsistency in reported values of the PRF-thermal coefficient, as measured from experiments encompassing a range of *in vivo* and *ex vivo* tissue types and experimental conditions. A method of calibrating the temperature dependence of the PRF is described and results are presented which indicate a tissue-type independence. To this end, other possible mechanisms for variations in the PRF-thermal coefficient are suggested including physiological perturbations and volume magnetic susceptibility effects from geometry and orientation.

3.2 Introduction

Minimally-invasive surgery and therapy of benign and malignant diseases are seen to benefit from near-real time MR image-guidance [66,67,69,70]. This is, in part, due to the well-known attractive properties of MRI such as its noninvasiveness, lack of ionizing radiation, and ability to produce images in any orientation with good resolution. However, it is the ability of MRI to construct maps of *in vivo* body temperature which makes it particularly well suited for monitoring and guiding minimally-invasive thermal therapy [80,88].

Thermal therapy is a broad term spanning two regimes. The first is conventional low-temperature hyperthermia, where relatively precise temperatures in the range of 43 – 45°C are required for tens of minutes to kill cancer cells directly or to sensitize the cells to cytotoxic agents and/or radiation [155]. The second is a high-temperature regime, called thermal coagulation, where temperatures in the range of 50 – 80°C are used to rapidly induce necrosis through processes such as protein denaturation [17, 156]. Regardless of the therapeutic regime, the cautious theme of thermal therapy is two-fold: (*i*) to ensure that the diseased tissue has been exposed to an adequate temperature-time treatment to induce necrosis over the entire diseased volume, and (*ii*) to ensure that the surrounding healthy tissue is spared excess thermal treatment [47]. Consequently, the role of MR thermometry is to quantify and visualize the deposition of heat energy in the treated and surrounding tissue, and to do so with good spatial and temporal resolution.

Presently, MR image-guided thermal-coagulation therapy is used in a number of diseases such as the treatment of unresectable tumors in the head and neck [42, 68], liver [91], prostate [157], breast [96], and other non-life threatening conditions such as the ablation of herniated discs [158]. Heat may be delivered using minimally-invasive interstitial laser fibres, microwave and RF antennas, or high-intensity focused ultrasound transducers. While the specific requirements of MR thermometry will be dependent on the exact application, the general consensus is that a temporal resolution between 1 and 10 seconds, spatial resolution of approximately 1 mm, and a temperature resolution less than 2°C would be quite sufficient.

There are several NMR properties that exhibit temperature dependence which have been used in MR thermometry such as *T1* relaxation time [81, 92, 94, 95], the diffusion coefficient of water [98,159], and the proton-resonance frequency (PRF) [113,145,160–165]. Some concerns with the currently available MR thermometric methods include low temperature sensitivity, irreversible behaviour between heating and cooling, difficulty of measurement and interpretation, and need for

a priori thermal calibrations. For example, *T1* relaxation times and *T1*-weighted signal changes are known to be dependent on tissue-type and to exhibit irreversible behavior with heating *in vivo* [94,95]. Likewise, diffusion coefficient measurements may require specialized hardware, long imaging times, and can be difficult to interpret due to restricted diffusion [98]. However, MR thermometry based on the temperature dependence of the PRF appears most promising, particularly for its linear behaviour and ease of measurement.

Recent reports in the literature demonstrate large variations in the reported value of the PRF-thermal coefficient (ie. PRF change per degree Centigrade - usually reported in units of ppm/^{o}C) for various animal species, *in vivo* and *ex vivo* tissue types, and experimental conditions. For example, values as small as -0.0067 ppm/^{o}C have been reported from RF heating on *in vivo* canine muscle [161] and as large as -0.0146 ppm/^{o}C for *in vivo* rat muscle, using a heated water bag in contact with the rat thigh [145] (see Figure 3.1). Generally, better agreement is achieved for PRF-thermal calibration experiments done on gels, solutions, and excised tissues; however significant discrepancies remain.

Uncertainty in the PRF-thermal coefficient could have a critical impact on the success of thermal therapy, particularly when large temperature changes are used. An incorrect PRF-thermal coefficient could lead to underestimates or overestimates of the magnitude and extent of the temperature distribution, thus potentially destroying healthy tissue or leaving diseased tissue cells viable, respectively.

Some sources that may account for the discrepancies in the PRF-thermal coefficient include volume-magnetic susceptibility effects from geometry and orientation of the object [164], the inherent physical temperature dependence of the volume-magnetic susceptibility [107,137], physiological responses to heat [162], and tissue-type and thermal history dependencies. Another important consideration is that calibration experiments using interstitial heating devices (eg. laser fibres, focused ultrasound) which can quite rapidly produce small point-like temperature distributions. While necessary clinically, this experimental design is not well suited to PRF-thermal calibration as there can be large thermal gradients, both spatially and temporally. This leads to difficulty in choosing regions-of-interest (ROI) to correlate phase changes with direct *in situ* temperature measurements, usually obtained from interstitial thermal probes.

Thus we chose to measure the PRF-thermal coefficient of a variety of different tissue types to establish or eliminate tissue type as a contributor to the observed variance in previously reported

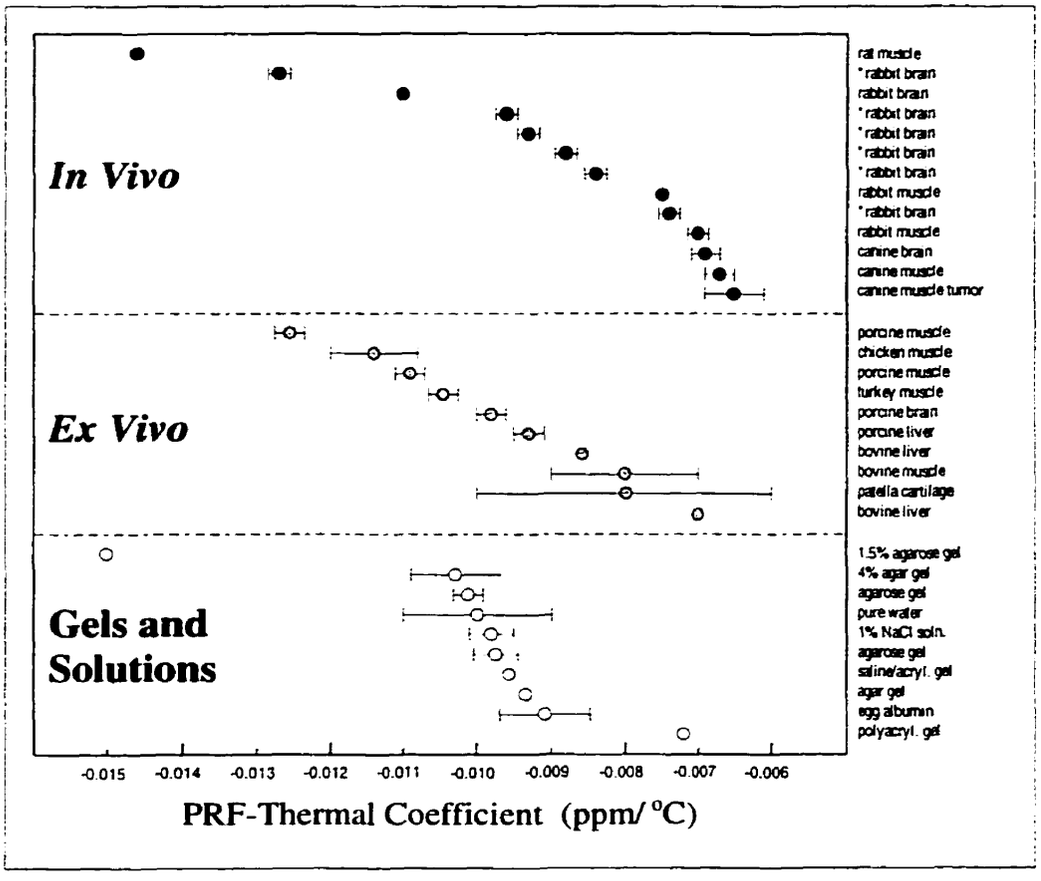

Figure 3.1: Recent literature survey of reported PRF-thermal coefficient values for *in vivo* and *ex vivo* tissues and various gels and solutions. The above plot shows a wide distribution ranging from -0.0067 ppm/°C (*in vivo* canine muscle) to -0.0146 ppm/°C (*in vivo* rat muscle). The asterisk (*) denotes unpublished calibration results that were obtained from *in vivo* rabbit brain heating experiments conducted in 1996–97 at Sunnybrook & Women's College Health Sciences Center. This survey included published articles from 1995–99 [114, 115, 145, 160, 161, 163, 166–173].

results. We report on PRF-thermal calibration measurements on freshly excised animal tissues under an experimental design incorporating a temperature range of 20 to 80°C, using large, uniformly heated volumes, and a slow-heating rate. Within the level of experimental precision, we show that there is no tissue-type dependence of the PRF-thermal coefficient and only a slight dependence on thermal history.

3.3 Method and Materials

3.3.1 Theoretical Basis

The temperature sensitivity of the PRF was first observed by Hindman in 1966 [112], and only recently adapted for MR-temperature monitoring by Ishihara et al [113]. Briefly, the PRF of hydrogen nuclei (^{1}H) in pure water changes by approximately -0.01 ppm/°C and can be modelled as:

$$f(T) = \frac{\gamma}{2\pi} \cdot \left(1 - \frac{2}{3}\chi(T) - \sigma_E(T)\right) \cdot B_o \tag{3.1}$$

where the temperature dependencies are indicated explicitly for the volume-magnetic susceptibility (χ) and the electronic-screening constant of the ^{1}H nucleus (σ_E). In the above equation, γ is the gyromagnetic ratio for ^{1}H nuclei, and B_o is the main-magnetic field strength.

The primary source of temperature dependence of the PRF in water is change in the electron-screening constant of the ^{1}H nuclei. While more detailed descriptions can be found elsewhere [111, 112], a general understanding can be gained by considering that a ^{1}H nuclei in a free H_2O molecule is screened more effectively by the electron cloud than if the H_2O molecule is hydrogen bonded to another molecule. As temperature increases, the hydrogen bonds stretch, bend, and break; the H_2O molecules spend less time on average in a hydrogen-bonded state. Consequently, as temperature increases, there is more electron screening of the ^{1}H nucleus, and thus a lower local magnetic field and Larmor frequency.

Pure water is diamagnetic and at room temperature has a volume magnetic susceptibility of -9.05×10^{-6} (MKS) which increases (becomes less diamagnetic) with temperature by approximately $+0.003 \times 10^{-6}/^oC$, primarily due to a decrease in the density of water [107, 137]. In solutions containing paramagnetic ions, the magnetic susceptibility is described by the Curie Law [121], and at high ion concentrations the temperature sensitivity can be comparable to that of the screening constant [164].

Recently, DePoorter has identified a complex source of variation in the PRF-thermal coefficient arising from the macroscopic-magnetic field, B_{mac} [164]. The macroscopic field derives from the strength of the applied magnetic field and from volume and surface integral that involve the size, shape, orientation, and susceptibility constituents of the object.

Ishihara et al. demonstrated that MR-derived thermal maps can be constructed using a gradient-recalled echo imaging sequence [113]. Spatial- and temporal-temperature distributions,

$T(r,t)$, result in signal-phase shifts, $\Delta\phi$, that are proportional to the PRF-thermal coefficient, α (units of ppm/^{o}C):

$$\Delta\phi = \alpha \cdot \frac{\gamma}{2\pi} \cdot B_o \cdot (360^o/cycle) \cdot TE \cdot \Delta T \tag{3.2}$$

where TE is the echo time of the gradient-echo pulse sequence. At 1.5 T, a PRF-thermal coefficient of -0.01 ppm/^{o}C would produce a phase shift of 4.6 phase degrees/^{o}C over a TE of 20 ms.

3.3.2 Tissue Preparation and Experimental Setup

Freshly excised brain, muscle, liver, and kidney tissues were obtained from New Zealand white rabbits and New Hampshire pigs within 30 minutes of sacrifice and cut into approximately 80 × 15 × 15 mm^3 sections. The muscle and liver sections were trimmed of visible fat. The samples were carefully inserted into 15 ml centrifuge tubes (14 mm inner diameter) (Sarstedt Inc., Newton, NC) as to leave as little trapped air as possible. The tubes containing the tissue were then spun at 500 rpm for one minute in a centrifuge to further eliminate any trapped air. Agar gel (2% by mass) (Sigma Chemical Co., St. Louis, MO) was prepared with degassed, distilled water and poured into additional centrifuge tubes and served as water-equivalent controls, to avoid convection currents that were observed in liquid water. Tubes containing the excised animal tissue and agar gel were placed in a plexi-glass container as indicated in Figure 3.2. A temperature-controlled water bath and pump (Lauda MT/M20, Konigshofen, Germany) located outside of the MR scanner room circulated $MnCl_2$-doped water at a rate of 1.7 litres/minute through a plexi-glass container (1.85 litre volume), holding the tissue sample tubes (Figure 3.2). The circulating water lines passed through a waveguide into the MR scanner room. To remove ghosting artifacts that might overlap on the sample regions in the MR image, the 20 litres of circulating water had a $MnCl_2$ concentration of 0.02 moles/litre giving the solution a $T2 < 1$ ms [174] and a volume-magnetic susceptibility of approximately -4.0 × 10^{-6} (MKS) at room temperature [139]. The water container was wrapped with styrofoam insulation and four thermally insulated agar-gel reference phantoms were placed around the container.

During the experiment, the circulating water was heated from room temperature to 80°C, over a period of approximately 2 hours as shown in Figure 3.3. This slow heating rate (approximately 0.5^{o}C/minute) ensured homogeneous heating and uniform temperature within the sample. As indicated in Figure 3.2, *in situ* temperature measurements were made in two sample tubes with fluorescent fibre-optic temperature probes (Luxtron 3100, Luxtron Corp., Santa Clara, CA) that

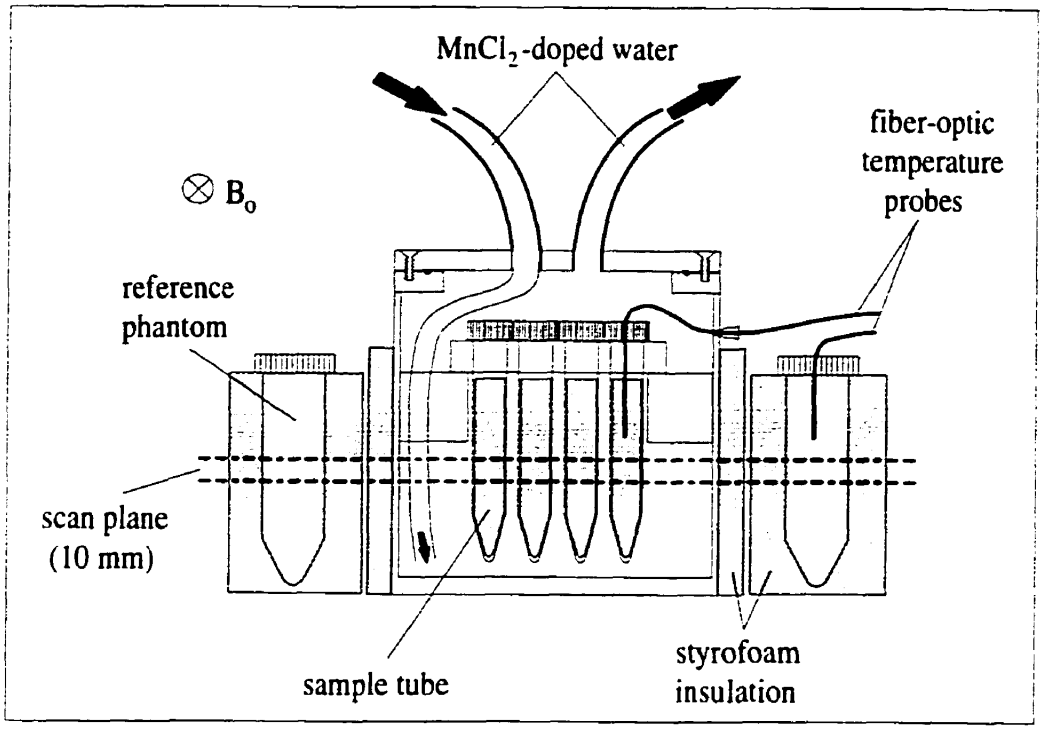

Figure 3.2: Geometry of the experimental apparatus for the PRF-thermal calibration of *ex vivo* tissues. Shown is a cross-section of the experimental setup that was placed inside a standard head coil. A temperature-controlled water pump circulated $MnCl_2$-doped water through the container holding 14 tissue-sample and agar-gel tubes (four shown). The water container and the reference phantoms (two shown) were insulated with styrofoam. Fibre-optic temperature probes were placed in sample tubes and reference phantoms as indicated. The container was oriented with the long axis of the tubes perpendicular to the direction of B_o.

showed less that 1.0°C temperature difference throughout the experiment. The absolute accuracy of the fibre-optic measurements was ±0.3°C (manufacturer's specification) and the precision of each fibre-optic probe was determined to be $\leq$ 0.1°C (sd). Two additional fibre-optic probes were also inserted into two of the four agar-gel reference phantoms placed outside of the water container to aid in a phase-drift correction scheme. The temperatures of the reference phantoms increased by approximately 3°C over two hours, due to their proximity to the water container and possible changes in magnet-room temperature.

To study the effect of thermal history on the PRF-thermal coefficient, in a separate series of experiments, raw tissue samples (in tubes) were placed in 80°C water either for 2 minutes or for 10 minutes and allowed to cool to room temperature prior to performing the calibration experiment as described above. The results with these two sets of pre-cooked tissues were compared to the PRF-thermal coefficient of the previously uncooked tissues.

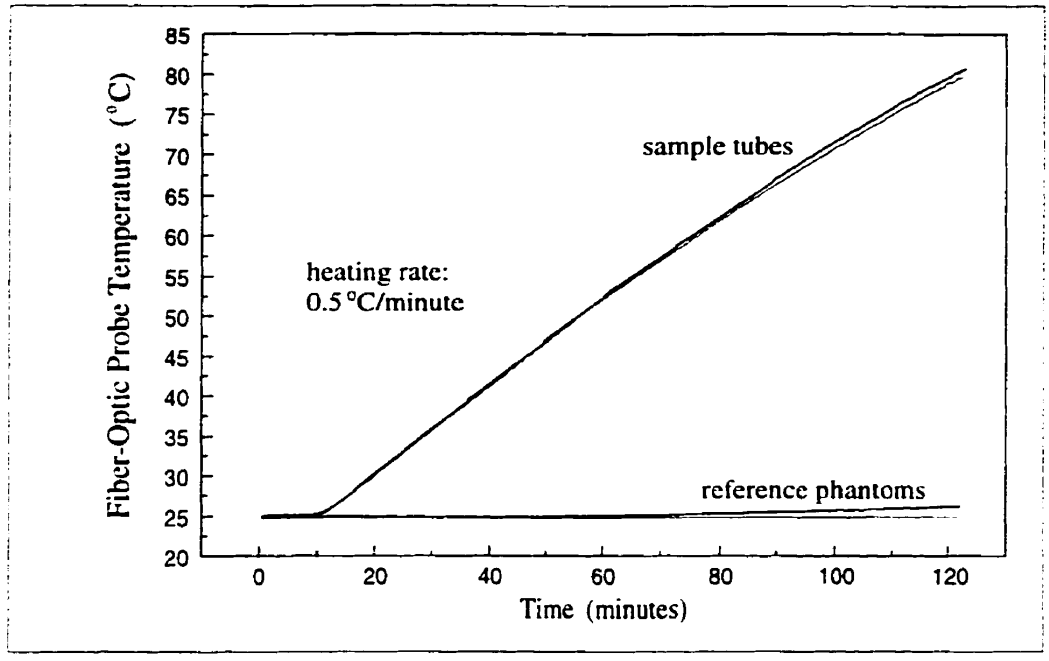

Figure 3.3: Representative temperatures in two sample tubes and two reference phantoms as a function of time for the experimental arrangement in Figure 3.2. There is typically less than a 1°C temperature difference between two sample tubes at any point in the experiment. The temperatures of the reference phantoms increased by approximately 3°C over two hours, due to their proximity to the water container and changes in the magnet room temperature.

3.3.3 MR Imaging

All MR imaging was performed on a standard 1.5 T clinical whole-body MRI system (Signa, GE Medical Systems, Milwaukee, WI). An RF-spoiled gradient recalled-echo (SPGR) sequence was used with the quadrature-head coil. At every 1°C temperature change three images were acquired with *TE* settings of 10, 20, and 30 ms and the following imaging parameters: TR = 50 ms , tip angle = 30°, 10 mm slice thickness, 20 cm field-of-view, 256 × 256 image matrix, 2 averages, for a time of 26 seconds per image. The location of the scan plane was chosen as indicated in Figure 3.2. The multiple *TE* settings allowed for estimates of the *T2** of the tissue samples, and were also found necessary for calculation of the PRF-thermal coefficient. By the time imaging and heating were begun, the tissues had been excised for approximately two hours.

3.3.4 Data Analysis

All MR image reconstruction and processing was performed offline on a Sun SPARC workstation (Sun Microsystems, Mountainview, CA). Phase-reference images were constructed by averaging ten images acquired at room temperature for each *TE* setting. For each image i acquired during the heating cycle, a phase difference image ($\Delta\phi_i$) was constructed using the complex image data:

$$\Delta\phi_i(x,y) = arctan\left(\frac{Re_{REF}(x,y)\cdot Im_i(x,y) - Re_i(x,y)\cdot Im_{REF}(x,y)}{Re_i(x,y)\cdot Re_{REF}(x,y) + Im_i(x,y)\cdot Im_{REF}(x,y)}\right) \tag{3.3}$$

on a pixel-by-pixel basis (x,y), where *Re* and *Im* are the real and imaginary components of the ith and reference (*REF*) image. This complex-phase subtraction procedure avoids problematic phase wrapping and is superior to simply performing the subtraction $\phi_i(x,y)$ - $\phi_{REF}(x,y)$. To avoid phase wrap-around errors that would occur at sufficiently-high temperature, the temporal history of each pixel's phase was examined and compensated when 360° discontinuities were encountered. Circular ROIs 9 mm in diameter were placed over each of the 14 tissue sample tubes in each phase difference image (Figure 3.4). Each ROI contained approximately 100 pixels, from which a mean phase shift and standard error (sem) was computed. The ROI phase-shift measurements were correlated with the fibre-optic probe temperatures.

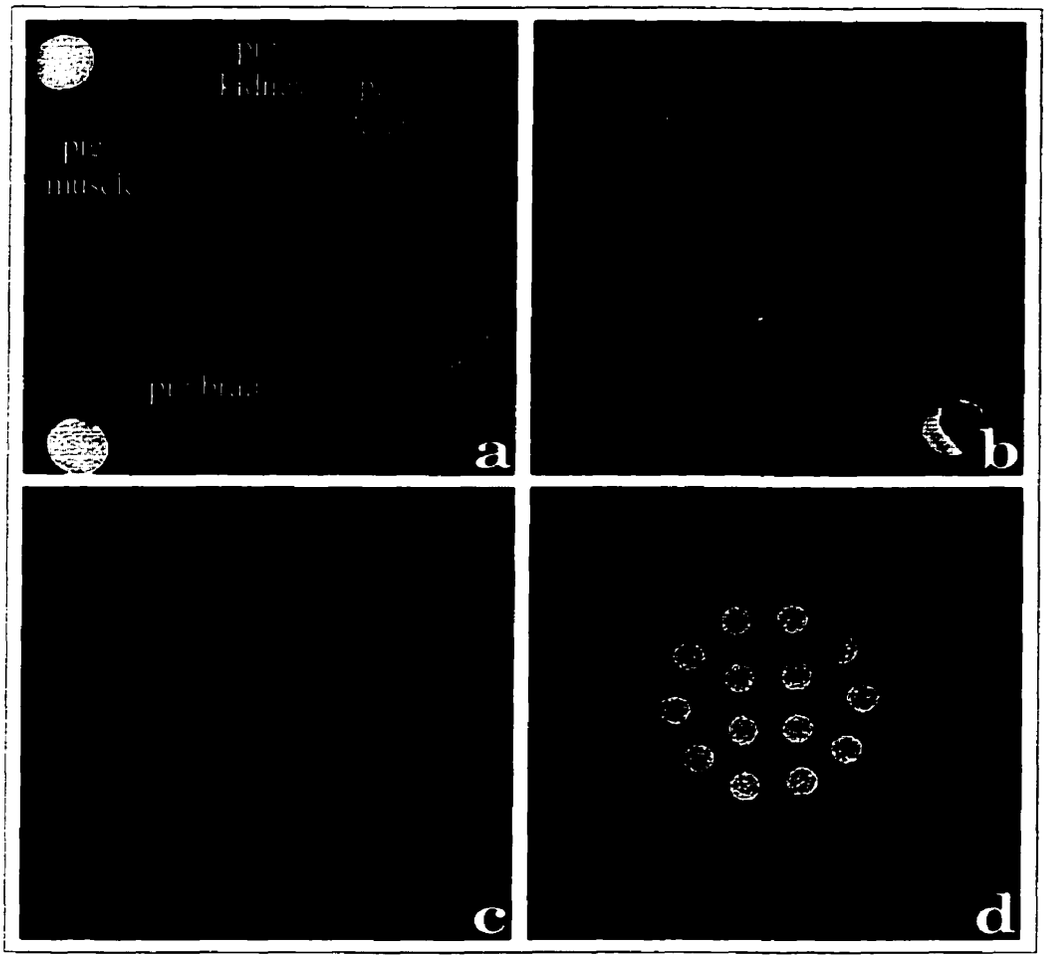

Figure 3.4: MR images of the experimental arrangement. Shown are (*a*) magnitude, (*b*) phase reference, and phase difference images at (*c*) 23°C and (*d*) 25°C. The phase difference images were windowed to 30° in phase. Magnitude thresholding was used to remove background noise in the phase images (*b* - *d*). Reference phantoms appear in the four corners of the images.

3.3.5 Frequency-Drift Sources

During the two hour period of data acquisition, phase drifts were observed attributable to MR-system instability that required correction prior to calculating the PRF-thermal coefficient. The MR-system instability most often manifests as a reference-frequency instability or drift and phase-reference phantoms are a convenient means of establishing the true thermal-induced phase shift, as predicted by Equation 3.2. Known sources of frequency drift include variations in magnet-room temperature, main-magnetic field drift due to cryogen boil off, and shifts in the MR reference frequency. In this experiment, the major source of system drift were the latter two sources. Figure 3.5*a* shows the typical phase-drift behaviour in an unheated reference phantom, observed on the

MR system used in this experiment over a period of 25 minutes. This phase drift showed two distinct components: a slow gradual decline and an oscillation with an approximate 6 minute period. The first component is attributed to a 0.55 ppm/hour B_o field drift, which is within specification of the MRI system of 1.0 ppm/hour. Both increasing and decreasing phase-drift behaviour have been observed. The oscillatory phase-drift component proved to be considerably more interesting. When the phase drift and air temperature in the MRI system's electronics room were monitored simultaneously (Figure 3.5*b*), correlation was found between variations in the room air temperature (2.5°C peak-to-peak) and the phase-drift oscillations (approximately 6° peak-to-peak). The equipment's electronics room temperature varied with a distinct period in response to the air conditioner cycling on and off. From these observations, it was estimated that the MR frequency standard (10 MHz crystal) had a thermal coefficient of 0.01 ppm/°C which is within the manufacturer's specifications of 0.1 ppm/°C. It should be noted that the siting specifications on the temperature of the electronics room include a temperature regulation of ±3°C and a maximum rated temperature change of 3°C/hour which was not realized in our installation.

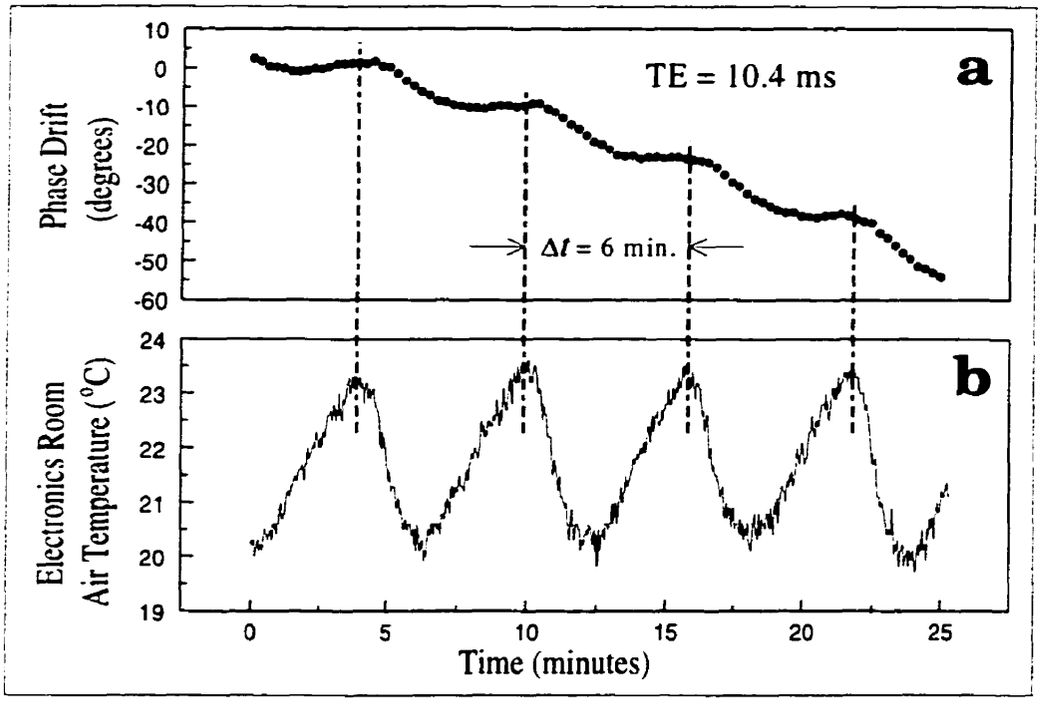

Figure 3.5: (*a*) Phase drift in an unheated reference phantom and (*b*) air temperature in the MR system electronic's room near the frequency reference module as a function of time. Periodic behavior is indicated by the vertical dashed lines.

3.3.6 Phase-Drift Correction

Phase-drift correction is normally accomplished by subtracting the phase of a thermally-insulated reference phantom from each phase-difference image, $\Delta\phi_i(x,y)$ for each image i (Equation 3.3). However, in this experiment the temperature of the reference phantoms changed very slightly because of changes in the air temperature of the magnet room and because of their proximity to the heated-water container (Figures 3.2 and 3.3). By also monitoring the temperature of the reference phantom, the phase drift for image i was thermally compensated for by subtracting a phase of $\alpha \cdot \frac{\gamma}{2\pi} \cdot B_o$ (360°/cycle) $TE \cdot \Delta T_{REF,i}$ from the ROI measurement in the phase-reference phantom, where $T_{REF,i}$ is the temperature change of the reference phantom in image i. The data

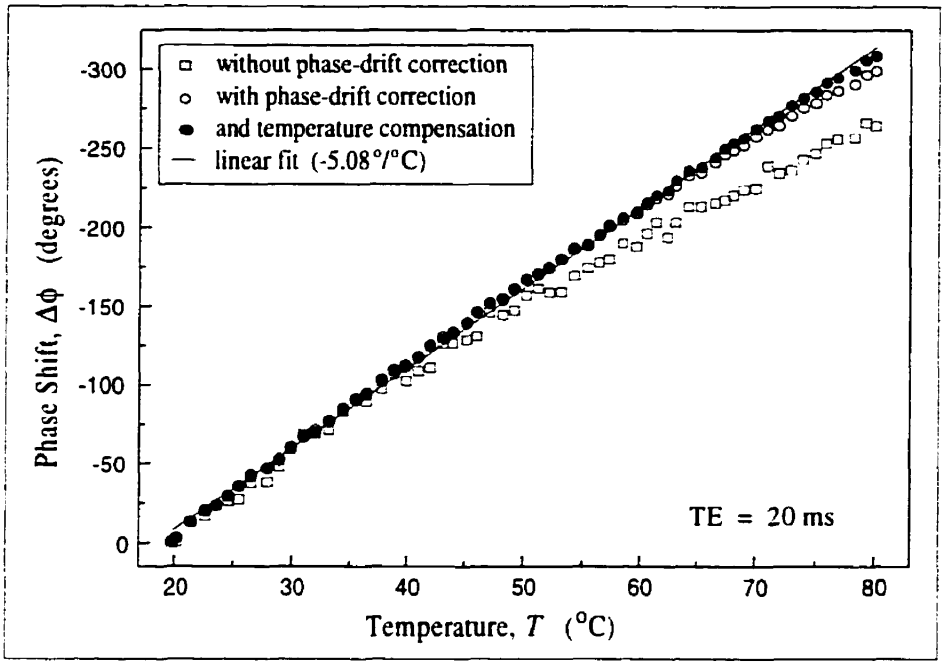

Figure 3.6: The importance of phase-drift correction on the measurement of the PRF-thermal coefficient. Shown is the measured phase shift in *ex vivo* pig brain (TE = 20 ms) as a function of sample temperature: without phase-drift correction, with phase-drift correction, and with thermal-compensated phase-drift correction. A linear fit of the corrected data is indicated with a straight line. In this case, without phase-drift correction, the PRF-thermal coefficient would have been underestimated.

shown in Figure 3.6 is representative of all of the *ex vivo* tissue results, and shows that phase-drift correction improves the quality of the experimental data, reducing systematic fluctuations that can give erroneous results. For example, without phase-drift correction a linear fit of 4.35°/°C with a reduced chi-squared value (χ^2) of 9.1 would have been obtained, whereas the phase-drift correction

gave a linear fit of $4.93^o/^oC$ and an improved χ^2 of 3.3. Finally, the thermally-compensated phase-drift correction yielded a fit of $5.08^o/^oC$ and a χ^2 of 1.3.

3.3.7 Convection Currents in Pure Water

Agar gel was used as a water-equivalent control rather than pure (undoped) water. With the heating apparatus described earlier, convection currents were observed in sample tubes containing pure water, as shown in the velocity-encoded phase contrast images in Figure 3.7. During the heating cycle, water near the edge of the tube flowed from bottom to top and in the center of the tube flowed from top to bottom. These currents changed directions during a cooling cycle, as indicated in Figure 3.7. From the phase-contrast images the velocity of the flow was estimated to be 1 mm/s at the center and 2 mm/s (opposite direction) near the edge of the tube. This convective flow gave a spatially-varying phase shift across the profile of the tubes which confounded the ROI-based phase-shift measurements. Because of these convective effects, agar gel was used as the water-equivalent control.

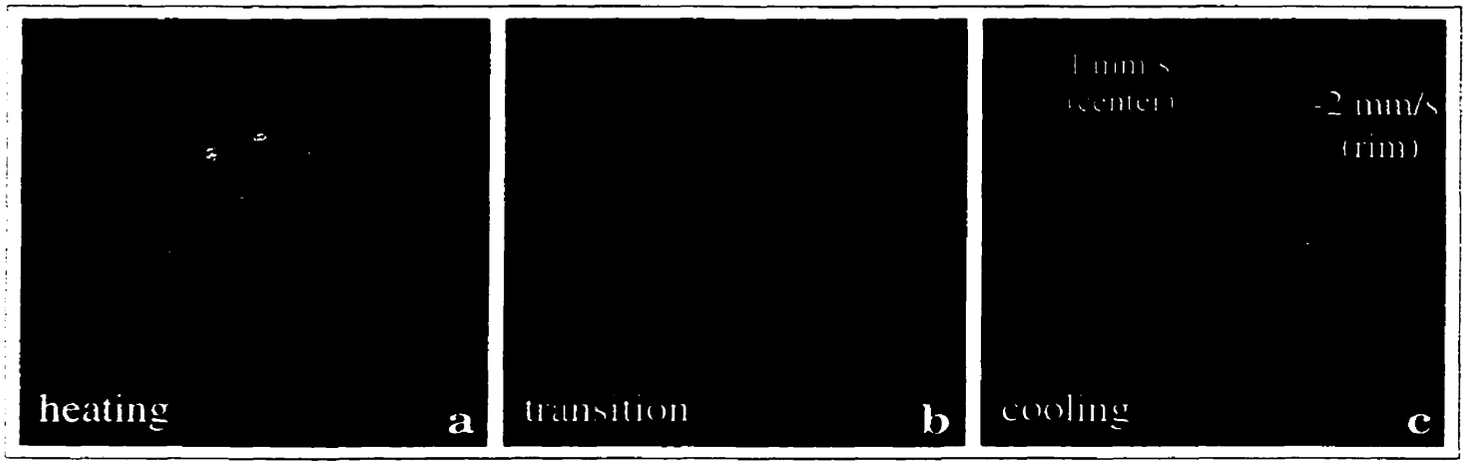

Figure 3.7: Phase-contrast velocity-encoded images showing convection currents in sample tubes containing pure water. Shown are images during the (*a*) heating, (*b*) transition, and (*c*) cooling periods. The circles indicate four tubes containing pieces of paper that disrupt the currents. The velocity-encoding direction is perpendicular to the scan plane and a maximum velocity encoding parameter (venc) of 5 cm/s was used.

3.4 Results

3.4.1 Uncooked Tissue Samples

Between four and eight measurements of the PRF-thermal coefficient were made of each uncooked animal tissue. A summary of these results are reported in Figure 3.8*a*, showing the mean values for each tissue and a 95% confidence interval obtained using the Student's t-distribution [175]. Upon comparing the measurement distributions of the animal tissues to those of the water-equivalent material (2% agar gel), only rabbit liver was found to differ at the 0.05 significance level. The reason for this is unclear. Using the 95% confidence interval as a measure of the precision of the experiment, precision levels range from approximately 2%, as seen in rabbit muscle and pig kidney, up to 8% in rabbit kidney. The relatively large confidence interval for rabbit kidney might also be attributable to variations in the magnetic susceptibility from blood content. In this particular experiment, an average over all of the uncooked tissues was -0.0101 $\pm$ 0.0004 ppm/^{o}C (sd). It is realized, however, that this average value is dependent on the experimental setup and geometry.

3.4.2 Thermally-Treated (Precooked) Samples

The results from the precooked tissue samples are shown in Figure 3.8*b*. At the 0.05 level, all of the pig tissues that were precooked for two minutes and only the pig liver precooked for 10 minutes (at 80^{o}C) differed significantly from 2% agar gel. This observation was contrary to an intuitive expectation that the PRF-thermal coefficients of the tissues precooked for the shorter time (two minutes) would more closely resemble those of the uncooked tissues. Also shown in Figure 3.8*b*, the calculated PRF-thermal coefficients of all tissues precooked for ten minutes were generally larger (absolute value) than those precooked for two minutes. The precision levels of the PRF-thermal coefficients of the precooked tissues ranged from 2%, in the pig liver precooked for two minutes, to 10%, for the pig brain precooked for ten minutes.

3.5 Discussion

A relatively precise method for measuring the PRF-thermal coefficient of *ex vivo* tissues has been demonstrated utilizing a temperature-controlled water bath to slowly and uniformly heat large tissue volumes over a wide temperature range. While this experimental method is clearly restricted to excised tissues, it is advantageous in that the sample temperature is well defined and the image

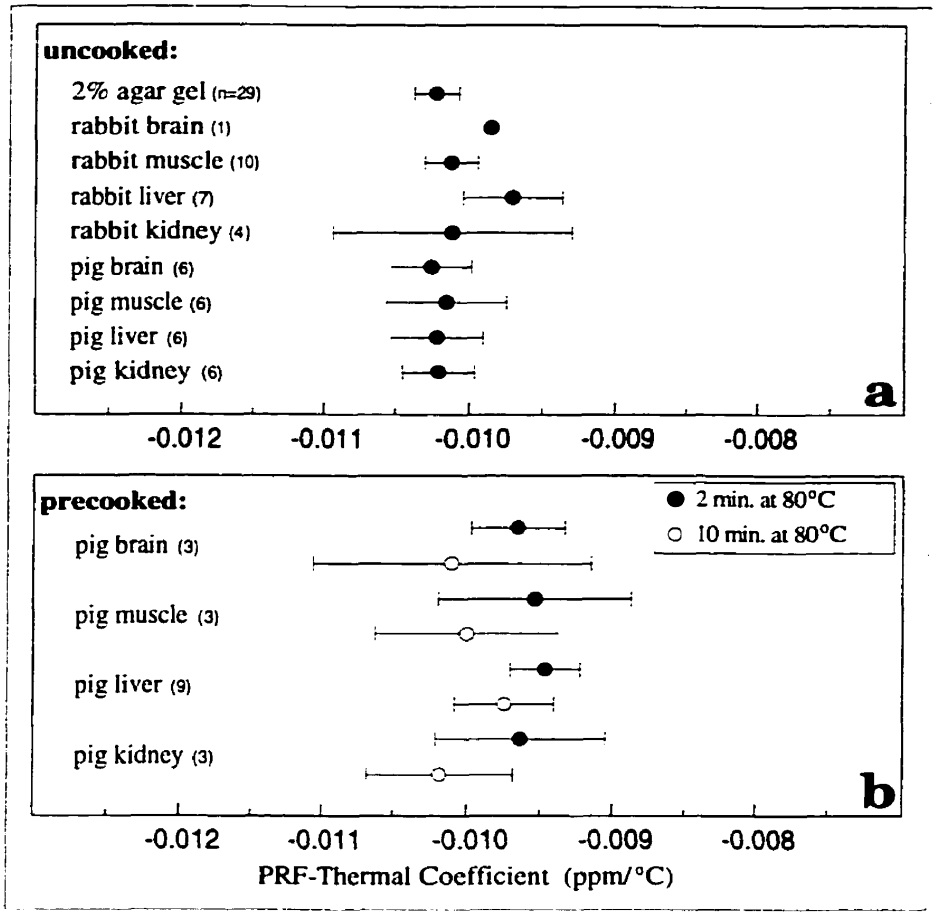

Figure 3.8: PRF-thermal coefficients of (*a*) uncooked and (*b*) precooked *ex vivo* rabbit and pig tissues obtained from this experimental arrangement. The error bars indicate a 95% confidence interval in the mean using the Student's t-distribution. Only one data point was acquired for rabbit brain.

ROI's are large, providing for high phase SNR. Interstitial approaches to tissue heating, such as lasers and microwave antennas produce small, point-like temperature distributions, in which temperatures are usually sampled *in situ* at discrete points in space with thermal probes. From the perspective of calibrating the PRF-shift temperature dependence, such interstitial approaches usually make ROI measurements difficult due to the presence of thermal gradients, both spatially and temporally, which result in significant sources of systematic uncertainty.

There are at least two contributions to uncertainty in estimated temperatures using PRF-shift thermometry. The first is the uncertainty in the measured phase shift, or phase noise, which is inversely proportional to the signal-to-noise ratio from the magnitude images [176]. A second contribution arises from the actual uncertainty in the PRF-thermal coefficient. The following example

may be useful for clarification. In this particular experimental arrangement, if the PRF-thermal coefficient is taken as -0.0101 ppm/°C with an uncertainty (sd) of ± 0.0004 ppm/°C, then a phase shift of 4.64 ± 0.23 °/°C is expected using a TE setting of 20 ms. A mean temperature-induced phase shift of 139.0 ± 0.5° (se), as measured from an ROI, would indicate a mean temperature change of $\Delta T = 139.0^{o}/(4.64^{o}/^{o}\mathrm{C}) = 30.0^{o}\mathrm{C}$. The corresponding uncertainty in the temperature would be $\delta T = 1.6^{o}\mathrm{C}$, if both sources of uncertainty are incorporated. This measure of the minimum resolvable temperature change is significantly larger than $\delta T = 0.5^{o}/(4.64^{o}/^{o}\mathrm{C}) = 0.1^{o}\mathrm{C}$ if only the phase noise were considered. In more practical situations, such as during a thermal therapy, phase noise will likely be larger and contribute more significantly to the estimated temperature uncertainty. Unfortunately, the only available optimization may be to choose TE equal to $T2^{*}$ of the tissue [160], if multiple signal averages are unattainable due to time constraints.

3.6 Conclusion

It has been shown that within the level of precision of the experiment described, there is no significant difference in the PRF-thermal coefficient of freshly-excised rabbit and pig tissues. An approximate linear relationship was observed between the phase shift and temperature throughout the temperature range studied (20 to 80°C). This result suggests that the observed variations of the PRF-thermal coefficient among tissues *in vivo* are likely due to other mechanisms such as the inherent physiology, geometry and orientation effects from the magnetic volume susceptibility, as well as difficulty in the actual calibration procedure itself. These sources of variation should be assessed prior to the reliance on PRF-shift thermometry for guiding interventional thermal coagulation therapy. Further study has been undertaken to evaluate the significance of geometry and orientation of the heat source with respect to the main-magnetic field on the PRF-thermal coefficient as described in Chapter 4.

Chapter 4

Heat-Source Orientation and Geometry Dependence in PRF-Shift Thermometry

adapted from:
Robert D. Peters, R. Scott Hinks, R. Mark Henkelman,
Heat-Source Orientation and Geometry Dependence in Proton-Resonance Frequency Shift MR Thermometry.
Magnetic Resonance in Medicine **41**: 909-918 (1999).

4.1 Abstract

The proton-resonance frequency (PRF) shift method of thermometry has become a promising tool for MR-image guided thermal therapies. Although the PRF-thermal coefficient has recently been shown to be independent of tissue type when measured *ex vivo*, significant discrepancy remains on its value for tissues measured *in vivo* under a variety of experimental conditions. A potential source of variation in the PRF-thermal coefficient is identified that arises from temperature-induced changes in the volume-magnetic susceptibility of tissue and is dependent on the orientation and geometry of the heat-delivery device and its associated heat pattern. This study demonstrates that spatial variations in the apparent PRF-thermal coefficient could lead to errors of up to ±30% in the MR-estimated temperature change if this effect is ignored.

4.2 Introduction

Magnetic-resonance imaging (MRI) for monitoring and guiding minimally-invasive therapeutic interventions and surgeries is an attractive concept that has become more clinically realizable over the last few years [67, 96, 177]. In particular, thermocoagulation therapy represents a new therapeutic regime that may serve as a feasible alternative to conventional resective surgery in the treatment of various malignancies and will likely benefit from MR-image guidance. The intent of this image-guided therapy is to deposit heat energy into a pre-localized diseased tissue volume and induce necrosis while avoiding the destruction of surrounding healthy tissue. The ability to render quantitative 3D maps of *in vivo* temperature makes MR-image guidance particularly suitable for this procedure.

There are several temperature-sensitive NMR properties that could be used for MR thermometry, such as the $T1$-relaxation time [80, 88, 94, 95], diffusion coefficient of water [98, 159], and the proton-resonance frequency (PRF) [113, 145, 161, 163, 164, 178, 179]. The PRF-shift method possesses many attributes that make it suitable for high-temperature thermal therapies, including good temperature sensitivity, linearity and reversibility with temperature, and ease of measurement and interpretation.

Unfortunately, there is much discrepancy in the reported value of the PRF-thermal coefficient from recent articles in the literature. For example, values as small as -0.0067 ppm/^{o}C were reported from RF heating on *in vivo* canine muscle [161], whereas, values as large as -0.0146 ppm/^{o}C have been reported from *in vivo* rat muscle, using a heated water bag in contact with the rat thigh [145]. Some suggested sources of this variation include dependencies on tissue type, *in vivo* physiological responses, and magnetic susceptibility-related errors. Recently, it has been shown that the PRF-thermal coefficient has no dependence on tissue type when measured *ex vivo* [179].

Regardless of the method of thermometry employed to guide the thermal therapy, accurate and precise *in vivo* MR-estimated temperatures is believed to be a prerequisite. This is primarily to ensure that the target tissue volume has been sufficiently exposed to the applied elevated temperatures and, equally important, to spare the surrounding healthy tissue of excess thermal treatment. As a research tool, MR thermometry for monitoring thermal therapies can also aid in the understanding of thermal-dose modelling [47] and the associated tissue injury in response to different thermal treatments [17, 156].

In this study, we identify a source of variation in the PRF-thermal coefficient that arises

from temperature-induced changes in the volume-magnetic susceptibility of water, that is dependent on the orientation and geometry of the heat-delivery device and its associated heat pattern. Based on the findings from a carefully-controlled, simple experimental model that emulates a cylindrically-shaped heat-delivery device, it is proposed that such variations in the apparent PRF-thermal coefficient might help explain the discrepancies found in the literature. Furthermore, once this thermally-induced variation is recognized, its effect can be corrected.

4.3 Methods and Materials

4.3.1 Theoretical Considerations

The PRF is directly proportional to the magnetic field at the nucleus, B_{nuc}, through the Larmor relationship, $f = \frac{\gamma}{2\pi} B_{nuc}$, where γ is the gyromagnetic ratio for ^{1}H nuclei. The temperature dependence of B_{nuc} can be modelled as a shielding of the macroscopic-magnetic field in the object, B_{mac}, by the temperature-dependent volume-magnetic susceptibility (χ) and the electron-screening constant of the ^{1}H nucleus (σ_E) [112, 164]:

$$B_{nuc} = \left(1 - \frac{2}{3}\chi - \sigma_E\right) \cdot B_{mac} \tag{4.1}$$

Changes in the electron-screening constant provides most of the temperature sensitivity for B_{nuc} and has been reported elsewhere [111, 112]. The average electron-screening constant varies approximately linearly with temperature by about $1.03 \pm 0.02 \times 10^{-8}/^oC$ over a wide range in temperatures from -15 to 100°C (as derived from a linear fit of the data listed in Table II of reference [112]). Owing to its physical origins on hydrogen bonding among water molecules, electron screening of the ^{1}H nucleus is considered a microscopic effect, providing a direct relationship between changes in a water molecule's bonding state and B_{nuc}.

Most soft tissues, such as liver, muscle, and brain have magnetic properties that are similar to pure water [107]. Pure water is diamagnetic at room temperature, having a volume-magnetic susceptibility of -9.03×10^{-6} (MKS), which increases (becomes less diamagnetic) with temperature by approximately $+3 \times 10^{-9}/^oC$ at 37°C [137]. This behaviour is largely due to a decrease in the density of water with temperature, as discussed in Chapter 2 [139]. The relationship described in Equation 4.1 is, unfortunately, misleading in suggesting that the volume-magnetic susceptibility has a linear effect on B_{nuc}, as the electron-screening constant does [162, 164, 180]. In general, changes

in χ do not give rise to proportionate changes in B_{nuc} due to the inherent relationship between magnetic susceptibility and the macroscopic-magnetic field, B_{mac}, which is now briefly discussed.

The macroscopic-magnetic field, B_{mac}, in an arbitrary object that is placed in a uniform-external magnetic field, B_o, can be derived from applying Maxwell's equations in matter [121]. However, this derivation is generally difficult as it requires a full description of the object's geometry, orientation relative to the external field, susceptibility distribution, and the evaluation of volume and surface integrals, while usually necessitates the use of computer-coded field modelling. If the object can be approximated by an ellipsoid, such as spheres, cylinders, and flat disks, analytic solutions are well known [107]. In such objects, the B_{mac} field will be uniform and also parallel to B_o when one of the principal axes of the ellipsoid lies parallel to B_o.

An applied-temperature variation, $T(\vec{r})$, arising from a heat-delivery device, will give rise to direct changes in χ and σ_E, thus having a local and proportional effect on B_{nuc}, as described in Equation 4.1. However, such temperature-induced variations in the object's χ distribution will also imply that $B_{mac}(\vec{r})$ is actually determined by the entire spatial distribution of temperature, $T(\vec{r})$, and its orientation with B_o. With non-magnetic or weakly diamagnetic materials in which $|\chi| \ll 1$, the macroscopic-magnetic field can be approximated by $B_{mac} \sim B_o + \boldsymbol{O}(\chi B_o)$, where $\boldsymbol{O}(\chi B_o)$ represents terms that are linear with and of the order of χB_o. Thus Equation 4.1 can be recast to give:

$$B_{nuc}(\vec{r},T) \cong B_{mac}(\vec{r},T) - \left(\frac{2}{3}\chi(T) + \sigma_E(T)\right) \cdot B_o \tag{4.2}$$

where the χ^2, $\chi\sigma_E$, and higher-order terms have been neglected. The quantity B_{mac} is now shown to be explicitly dependent on position and implicitly dependent on the applied temperature distribution, $T(\vec{r})$, and σ_E and χ are only spatially-dependent according to $T(\vec{r})$.

To summarize, the magnetic field at the nucleus has contributions from two distinct effects, one arising from the immediate vicinity of the ^{1}H nucleus (microscopic), the second from the bulk properties of the object and distribution of temperature in the object (macroscopic). Consequently, B_{nuc} and the apparent PRF-thermal coefficient at a position $\vec{r}$ will be determined by the entire spatial distribution of temperature, $T(\vec{r})$, and its orientation with the external magnetic field, B_o.

4.3.2 Experimental Design

To demonstrate the applied-temperature distribution's orientation and geometry dependence on the apparent PRF-thermal coefficient, a phantom was constructed consisting of a hard-plastic sphere

containing agar gel and a long pyrex glass cylinder passing through the center of the sphere. as shown in Figure 4.1. The gel-filled sphere *alone* has no preferred orientation within the external-magnetic field and the macroscopic-magnetic field is uniform and parallel to the external field and equal to $(1\text{-}\frac{2}{3}(\chi_o - \chi_{gel}))B_o$ (Table 1, Chapter 2) [107].

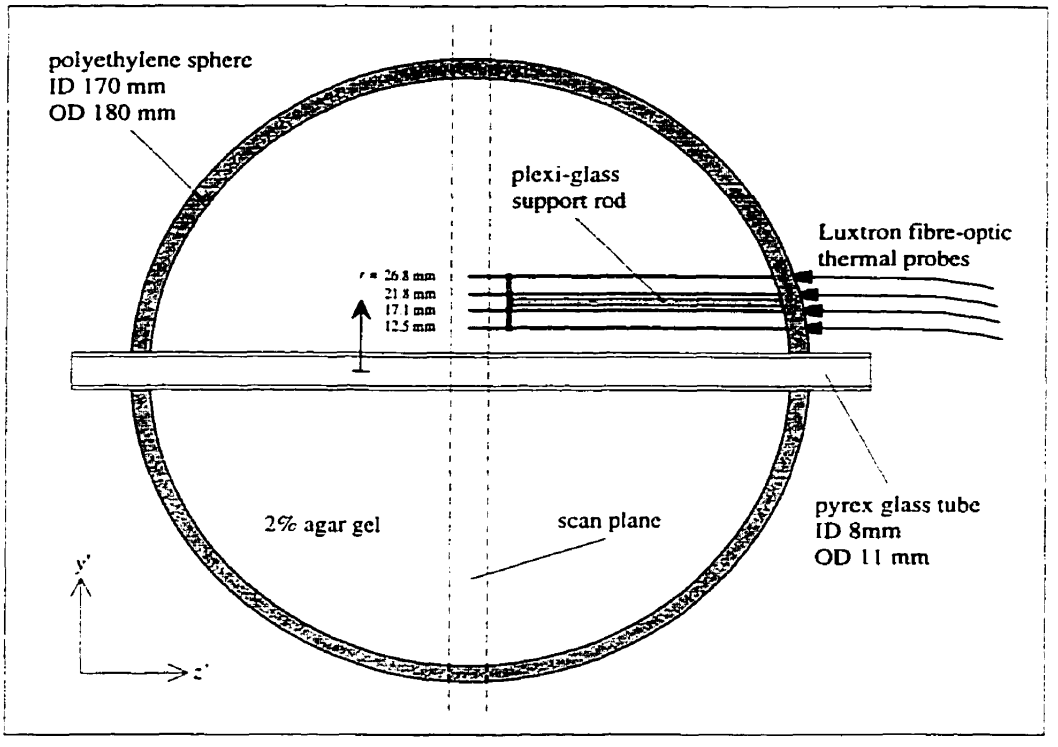

Figure 4.1: Geometry of the experimental apparatus. The phantom consisted of a long pyrex glass cylinder passing through a hollow polyethylene sphere filled with 2% agar gel. Fibre-optic thermal probes were inserted into the sphere to measure the gel temperature at discrete radial distances. The phantom was placed in a 1.5 T whole body MR scanner and orientated either parallel or perpendicular to the direction of the main-magnetic field.

An orientational-dependent temperature distribution was applied to the phantom by pumping 90°C water through the glass cylinder, thus providing a radially-symmetric temperature distribution. The whole arrangement was placed in a 1.5 T whole-body MR scanner with the glass cylinder oriented either parallel or perpendicular to the direction of the main-magnetic field, B_o (z-direction). In this lab frame, the x-direction was chosen to be horizontal and the y-direction to be vertical. Two different perpendicular orientations were examined with the cylinder aligned along the x-direction and differing only by a 90° rotation about the x-direction to exclude any effects that might be caused from intrinsic signal variations in the gel, though none were seen. The perpendicular orientation with the cylinder aligned along the y-direction was not physically

possible due to the space restrictions imposed by the MR imaging coil.

The temperature in the phantom was monitored with four Luxtron fibre-optic probes (Luxtron 3100, Luxtron Corp., Santa Clara, CA) which were placed at 5 mm increments radially from the glass cylinder as indicated in Figure 1. The agar gel (2% by mass) (Sigma Chemical Co., St. Louis, MO) was prepared with degassed, distilled water and poured into the empty sphere containing the cylinder and fibre-optic probe sheaths and support rod.

A temperature-controlled water bath and pump (Lauda MT/M20, Konigshofen, Germany) circulated pure (undoped) water through the glass cylinder at a rate of approximately 1.7 litres/minute. For each orientation, with the phantom initially at uniform-room temperature, the pump was switched on at $t = 0$, sending 90°C water through the glass cylinder. This heating cycle continued for 19.1 minutes at which time the pump was switched off and the phantom was allowed to cool to ambient-room temperature.

Temperature-induced changes in the PRF were spatially resolved through phase-difference images obtained from a gradient-recalled echo imaging sequence. The temperature-induced changes in phase were modelled as $\Delta\phi = \alpha \cdot \frac{\gamma}{2\pi} \cdot B_o \cdot (360^o/\text{cycle}) \cdot TE \cdot \Delta T$, where $\alpha = \Delta B_{nuc}/(B_o \Delta T)$, the experimental estimate of the apparent PRF-thermal coefficient which will reflect spatial variations in B_{mac} as discussed.

4.3.3 MR Imaging

The phantom was positioned in a standard-quadrature head coil of a 1.5 T MRI system (Signa, GE Medical Systems, Milwaukee, WI). A spoiled gradient recalled-echo (SPGR) sequence was used to obtain single-slice images of the phantom during the baseline, heating, and cooling cycles of the experiment. The relevant MR scan settings were: TE=30 ms, TR=50 ms, tip angle = 30°, 10 mm slice thickness, 21 cm field-of-view, 256 × 256 image matrix, 2 averages, and an acquisition time of 26 seconds per image.

4.3.4 Data Analysis

All of the MR image reconstruction and processing was performed offline on a Sun SPARC workstation (Sun Microsystems, Mountainview, CA). A phase-reference image was first constructed by averaging ten images acquired at room temperature ($t < 0$). For each subsequent image, a phase-difference image was calculated using the complex-phase subtraction technique described in

Chapter 3 [179].

Temporal correspondence of the MR images and fibre-optic temperature measurements was achieved by assigning to each image the nearest temperature measurement corresponding to the time at which the center of k-space was filled for that image.

To correct for phase drifts attributable to MR system instability, a three-point (planar) correction was implemented [165]. This phase-drift correction method used a reference phase signal from three non-colinear (thermally-isolated) reference phantoms, placed around the sphere, to construct a planar map that approximates phase-drift spatial variations. This phase-drift map was then subtracted on a pixel-by-pixel basis from each phase-difference image. In comparison, a single-point (scalar) phase-drift correction scheme would subtract only a single reference phase signal from each phase-difference image which was done in the calibration experiments in Chapter 3.

4.4 Results

4.4.1 Temperature Measurements in the Phantom

The temperature-time behaviour of the phantom is shown in Figure 4.2 for the parallel-orientation experiment. As measured from the four fibre-optic probes, the temperatures all increased steadily when heat was applied at $t = 0$. At the $t = 9.7$ minute point, the temperature of probe 1 was increasing by approximately 0.4^{o}C over the MR data acquisition period of 26 seconds. When heating was terminated ($t = 19.1$ minutes), the fibre-optic probe temperature at $r = 12.5$ mm began to decrease while the remaining three probes (located at $r > 12.5$ mm) continued to increase in temperature due to the radial heat diffusion in the phantom. The experimental temperature measurements for the parallel and perpendicular orientations were nearly identical, differing by less than 0.7^{o}C, which was likely due to a difference in ambient temperature. The four arrows in Figure 4.2 indicate time points ($t = 9.7$, 18.9, 28.0, and 68.5 minutes) that are examined in following sections.

4.4.2 MR Phase-Difference Images

Representative phase-difference images of the phantom in the parallel and perpendicular orientations are shown in Figure 4.3. Figures 4.3*a* and 4.3*f* are baseline images, acquired before heat was

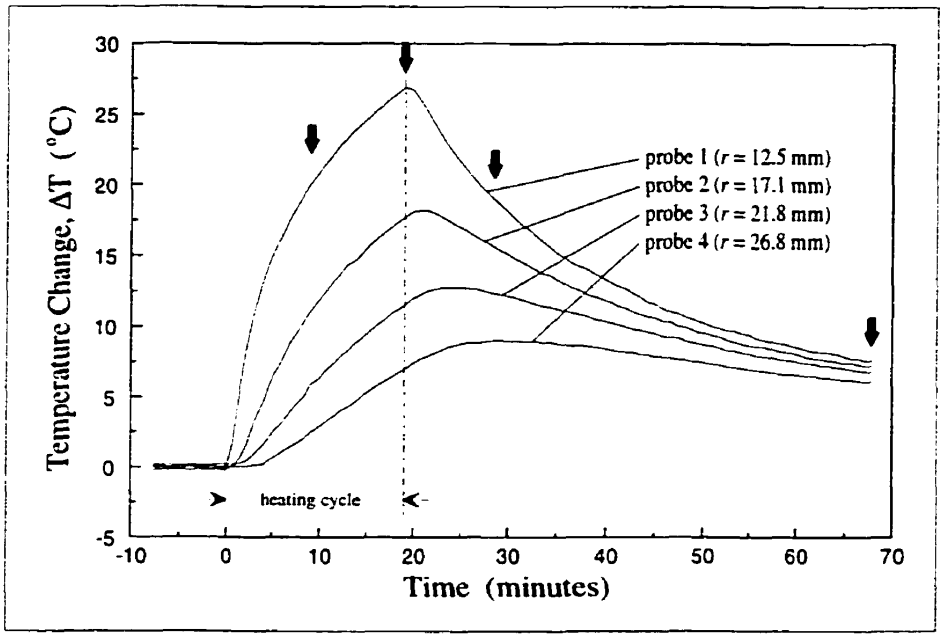

Figure 4.2: Temperature change as a function of time during the experiment for the parallel-orientation experiment as measured from the four fibre-optic probes. The water pump was switched on at $t = 0$ and switched off at $t = 19.1$ minutes. The four arrows indicate time points ($t = 9.7$, 18.9, 28.0, and 68.5 minutes) that are used for further examination.

introduced to the phantom. Qualitatively, there is a noticeable eccentricity in the phase-shift pattern for the perpendicular orientation (Figures 4.3*g* and 4.3*h*), becoming less severe once heating was terminated (t >18.9 minutes), as indicated in Figures 4.3*i* and 4.3*j*. The phase-shift pattern in the parallel orientation appears radially-symmetric at all times.

In examining the eccentricity in the phase-shift patterns of Figure 4.3, attention is now focused to the images of Figures 4.3*c* and 4.3*h*, which were obtained at the $t = 18.9$ minute time point, just prior to the moment the pump and heater were switched off. Phase-shift profiles were obtained from ROI's placed along the x-, y-, and z-directions, averaged from a width of 9 pixels (7 mm) and carefully centered about the central axis of the glass cylinder: as indicated by the rectangular regions shown in Figures 4.3*a* and 4.3*f*. The profiles (Figures 4.4*a* and 4.4*b*) were then subtracted from each other, yielding the phase-shift difference profile, $\delta\{\Delta\phi\}$ (Figure 4.4*c*). In the parallel orientation, there was no difference between the phase-shift profiles along the x- or the y-direction. Significant differences were observed among the profiles along the y- and z-direction in the perpendicular orientation as shown in Figure 4.4*c*.

Phase-shift difference profiles at the $t = 9.7$, 18.9, 28.0, and 68.5 minute time points are

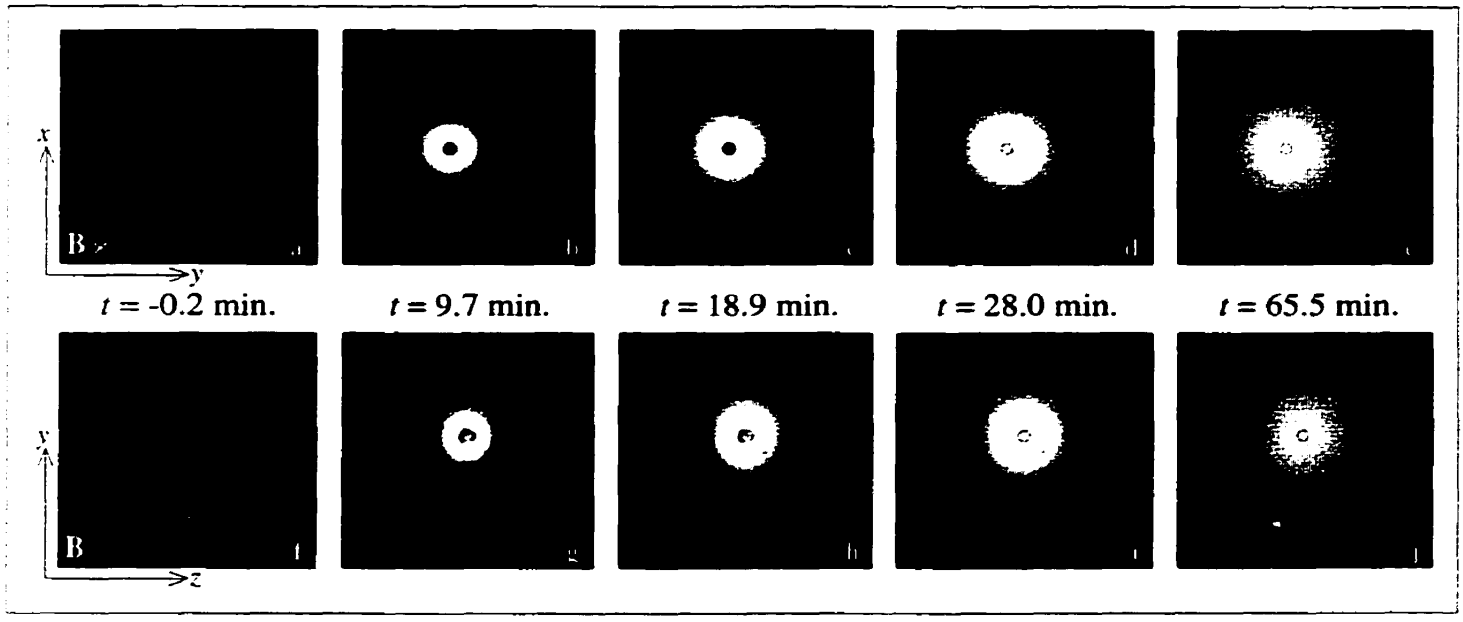

Figure 4.3: Phase-difference images of the phantom in the parallel and perpendicular orientation. The times shown are relative to the moment heat was introduced to the phantom, as indicated in Figure 4.2. Phase-shift profiles were obtained from the four rectangular regions indicated in the baseline phase-difference images, (a) and (f). All of the images were windowed to 100^o and levelled to 0^o. Magnitude thresholding was used to remove noise. The bottom reference phantom in (f) - (j) had low magnitude SNR due to its proximity to the imaging coil and has a broken appearance from subsequent magnitude thresholding.

also shown in Figure 4.5 for the perpendicular orientation. Consistent with the observations of the phase-shift images in Figure 4.3, the eccentricity appears to diminish with time, seemingly with the diffusion of the thermal energy. At the t = 68.5 minute time point, there remains only a minor amount of eccentricity in the phase-shift pattern. A portion of the phase-shift profiles in Figures 4.4 and 4.5 have been removed corresponding to -10 mm $< r <$ 10 mm. This region was not considered reliable for phase-shift measurements, nor considered immediately relevant to the present study, due to the presence of observed local phase artifacts around the pyrex glass cylinder. There are two potential sources for these phase artifacts. First, the artifacts may be due to changes in the magnetic-volume susceptibility of pyrex glass with temperature, as temperature-independent phase artifacts would have been removed through the phase-image subtraction process. Second, it is possible that the phase artifacts may be related to flow effects from agarose gel that has melted close to the pyrex glass cylinder.

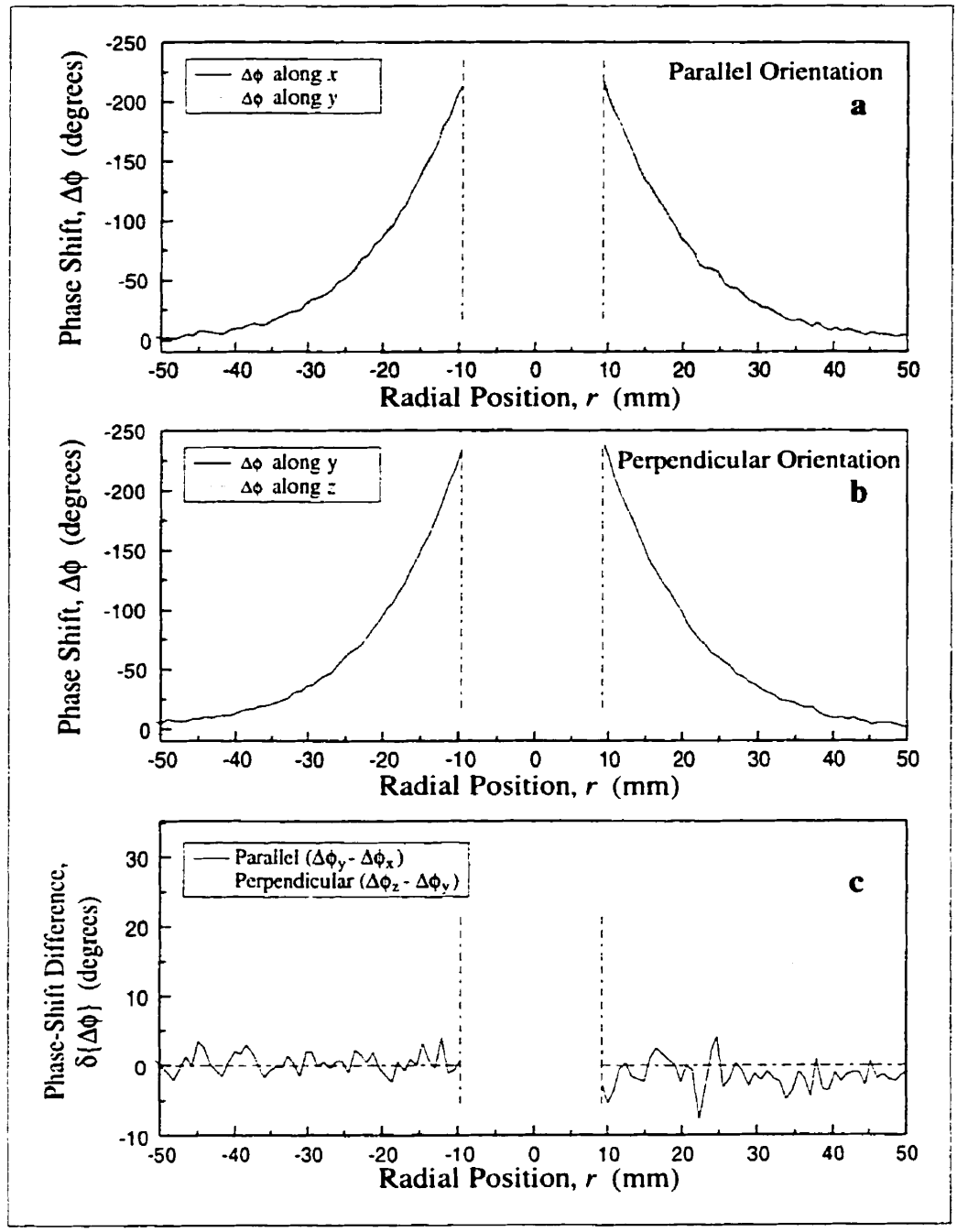

Figure 4.4: Temperature-induced phase-shift profiles for the $t = 18.9$ minute time point. Shown are the profiles for (a) the x- and y-direction in the parallel orientation, (b) the y- and z-direction in the perpendicular orientation, and (c) the differences in the parallel and perpendicular orientations. The profiles were averaged from ROI's of 9 pixels (7 mm) in width and carefully centered about the central axis of the glass cylinder. The region -10 mm $< r <$ 10 mm was not considered reliable for phase-shift measurements due to the presence of some observed local phase artifacts around the pyrex glass cylinder. The above data was derived from the images in Figures 4.3c and 4.3h.

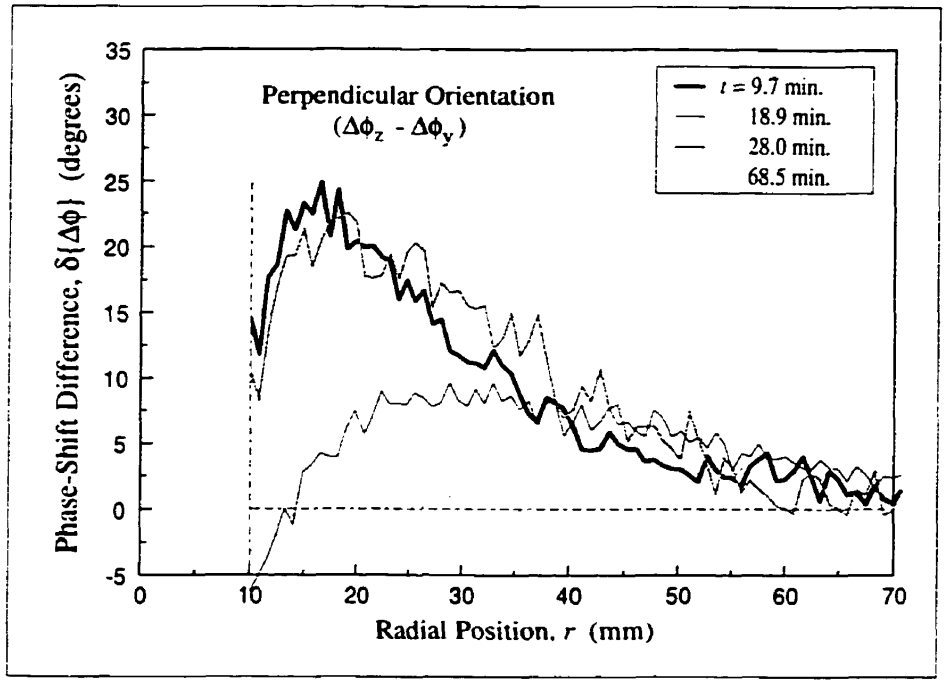

Figure 4.5: Phase-shift difference as a function of radial position for the perpendicular orientation. Shown are difference profiles, $\delta\{\Delta\phi\}$, for each of the four time points, derived from subtracting the $\Delta\phi$ profile along the z-direction from the y-direction. The vertical dotted line represents the edge of the glass cylinder and associated local artifacts.

4.4.3 Experimental Estimates of the Apparent PRF-Thermal Coefficient

Temperature-induced phase shifts at four radii corresponding to the radial positions of the four fibre-optic probes are plotted in Figure 4.6 as a function of temperature change, as measured from the fibre-optic probes. In the parallel orientation (Figure 4.6*a*) the phase-shift varies linearly and reversibly with temperature change at all four radial positions, for both the heating and cooling periods. The results of a linear fit to these phase-shift measurements as a function of temperature are presented in Table 4.1, for each of the four radial positions. There were no significant differences between the fitted values of $\Delta\phi/\Delta T$ obtained from the measurements along the x-direction or the y-direction, suggesting a single, spatially-independent PRF-thermal coefficient. This is consistent with the radially-symmetric phase shift patterns observed in Figure 4.3. As indicated in Table 4.1, the average value of $\Delta\phi/\Delta T$ from all four radial positions was -6.49 $\pm$ 0.04 °/°C which corresponded to an apparent PRF-thermal coefficient of -0.0094 $\pm$ 0.0001 ppm/°C. Notice that this average PRF-thermal coefficient is, in fact, smaller in value than the thermal coefficient of the electron-screening constant ($\Delta\sigma_E/\Delta T$) [112].

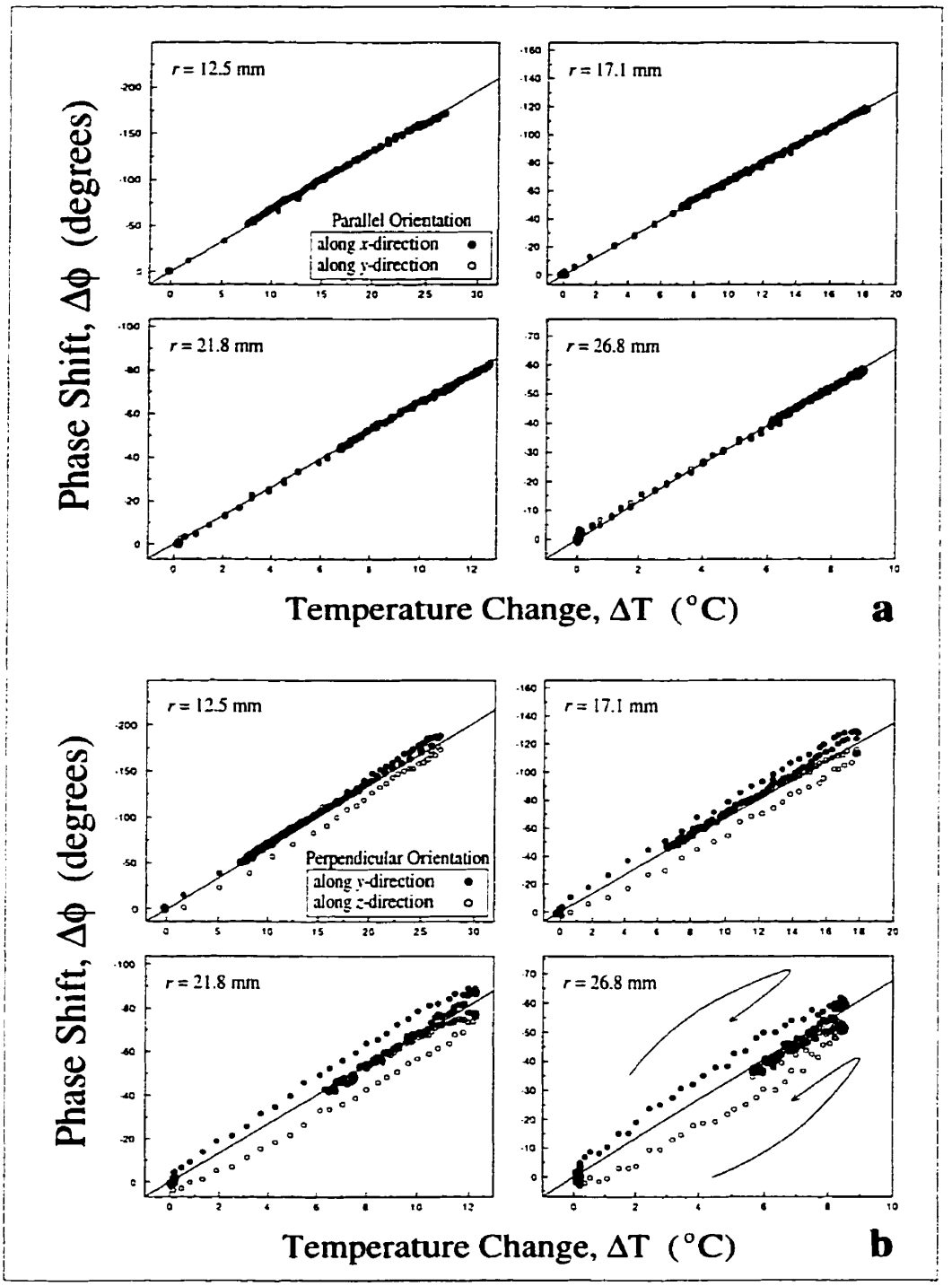

Figure 4.6: Phase-shift as a function of temperature change at four radial positions over the entire course of the experiment for the phantom in the (*a*) parallel and (*b*) perpendicular orientations, along the *x*-, *y*-, and *z*-directions. The straight line represents the derived-average thermal coefficient of -6.49°/°C (-0.0094 ppm/°C) for the parallel orientation in (*a*) and -6.76°/°C (-0.0098 ppm/°C) for the perpendicular orientation in (*b*).

Table 4.1: Experimentally-derived estimates of $\Delta\phi/\Delta T$ at four radial positions for the phantom in the parallel and perpendicular orientation. The values of $\Delta\phi/\Delta T$ were obtained from a linear fit of the results plotted in Figure 4.6, using the entire temporal data set for the parallel orientation and only the last 20 minutes of data (cooling period) for the perpendicular orientation. A sample mean and standard deviation of the eight measurements is given.

	Parallel (^{o}/^{o}C)		**Perpendicular** (^{o}/^{o}C)	
Radius (mm)	x-direction	y-direction	y-direction	z-direction
12.5	-6.48 ± 0.02	-6.51 ± 0.02	-6.83 ± 0.03	-7.10 ± 0.03
17.1	-6.52 ± 0.03	-6.56 ± 0.02	-6.98 ± 0.03	-7.01 ± 0.03
21.8	-6.46 ± 0.03	-6.49 ± 0.02	-6.65 ± 0.03	-6.62 ± 0.03
26.8	-6.43 ± 0.03	-6.47 ± 0.02	-6.60 ± 0.03	-6.31 ± 0.03
Average	-6.49 ± 0.04 (-0.0094 ± 0.0001 ppm/^{o}C)		-6.76 ± 0.27 (-0.0098 ± 0.0004 ppm/^{o}C)	

In the perpendicular orientation (Figure 4.6*b*) a markedly different behaviour is seen. At all four radial positions, the phase shift displays confounding nonlinear and irreversible behaviour with temperature between the heating and cooling periods. Phase-shift differences between the y- and z-direction are also clearly evident, arising from the eccentric phase-shift patterns in Figure 4.3. Some convergence is seen during the cooling period, in which the phase shifts along the y- and z-direction are similar, and both vary approximately linearly with temperature. The apparent PRF-thermal coefficient was estimated to initially range from -0.0055 ppm/^{o}C, as derived from the measurements along the z-direction, to -0.0130 ppm/^{o}C, derived from the measurements along the y-direction, implying a spatial dependence. Listed in Table 4.1 are the results of a linear fit to the data points of the final 20 minutes of the experiment (cooling period). The average apparent PRF-thermal coefficient from all four radial positions was found to be -0.0098 ± 0.0004 ppm/^{o}C, and is represented by a solid line in Figure 4.6*b*.

To summarize the above findings, in the parallel orientation, radially-symmetric phase-shift patterns were observed resulting in spatially-independent, linear, and reversible phase-shifts as a function of temperature. These results lead to the estimations of a single apparent PRF-thermal coefficient that suitably described the experimental results at all points in time. However, in the perpendicular orientation, significantly different behavior was observed, beginning with noticeable eccentricities in the phase-shift pattern. Confounding nonlinear and irreversible behaviour between heating and cooling was observed in the phase-shift measurements as a function of temperature,

suggesting that this apparent PRF-thermal coefficient was spatially- and temporally-dependent.

4.4.4 Numerical Modelling of the Macroscopic-Magnetic Field

In an attempt to resolve the above experimental observations, notably the distinct behaviour in the perpendicular orientation, numerical modelling of the macroscopic-magnetic field was performed. The hypothesis was that the experimental results could be explained by considering the effect of temperature-induced variations in B_{mac}.

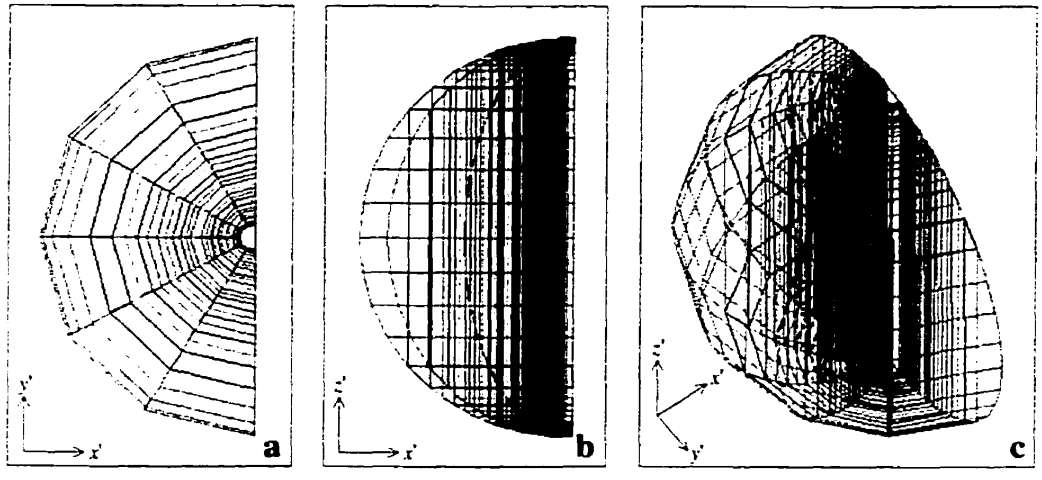

Figure 4.7: Representation of the finite-element numerical model for calculating the macroscopic-magnetic field. Shown are representations of the numerical model in the (*a*) x'-y' plane, (*b*) x'-z' plane, and (*c*) 3D view. The model consisted of 25 cylindrical shells of varying thickness, ranging from 1.5 mm to 4 mm. With the coordinate system defined above, the external magnetic field (boundary condition) was applied either along the z'- or y'-direction, simulating the parallel or perpendicular orientation of the experiment.

A finite-element analysis software package (Maxwell, Ansoft Corp., Pittsburgh, PA) was implemented to model the sphere and glass cylinder phantom (Figure 4.7). To simulate the radially-symmetric temperature distribution and, thus, the volume-magnetic susceptibility distribution, the model was constructed with concentric cylindrical shells (Figure 4.7*a*). The physical dimensions of the model were chosen to match the actual sphere and glass cylinder. A boundary condition was given in which a uniform external-magnetic field was applied either along the z'- or y'-axis of the model, to simulate the parallel or perpendicular orientation, respectively. Because of axial and mirror symmetry in the model, relative to the direction of the external-magnetic field, a half model was used to reduce computing time. Once meshed, only the direction of the external-magnetic field (boundary condition) and volume-magnetic susceptibilities of the cylindrical shells were altered,

keeping the mesh fixed. The volume-magnetic susceptibility of the pyrex glass and inhomogeneity in the external-magnetic field was not included in the model. Also, only the volume-magnetic susceptibility of pure water was used, as precise information for 2% agar gel was unavailable.

To assign volume-magnetic susceptibilities to each cylindrical shell in the numerical model, the radial-temperature distribution in the phantom (r = 0 to 60 mm) was first approximated using the fibre-optic temperature measurements and solutions from the heat-diffusion equation [181]. Given boundary conditions that describe the geometry of the phantom and the duration of heating, solutions to the heat-diffusion equation were obtained at the t = 9.7, 18.9, 28.0, and 68.5 minute time points. These modelled radial-temperature distributions were then independently scaled to match the fibre-optic probe measurements, obtained at the radial positions r = 12.5, 17.1, 21.8, and 26.8 mm, as shown in Figure 4.8. Volume-magnetic susceptibilities were then assigned to each concentric shell according to the shell's radius and the modelled radial-temperature distribution in the phantom. Approximately 30 minutes of computing time on a Sun SPARC Ultra workstation were required to generate a solution to each magnetostatic problem.

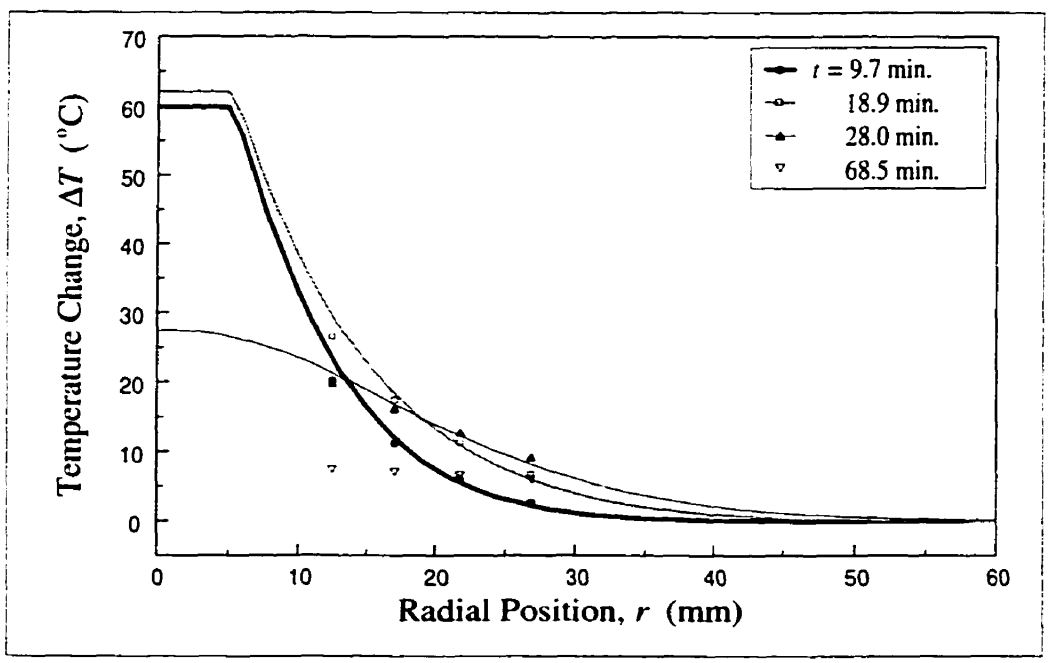

Figure 4.8: Experimentally-measured and modelled radial-temperature distributions in the phantom. Shown are the experimentally-measured temperature changes (symbols) and the modelled temperature distributions (lines) for the t = 9.7, 18.9, 28.0, and 68.5 minute time points. The modelled temperature distributions were incorporated into the numerical-field modelling, using a reference temperature of 24°C.

Some representative macroscopic-magnetic field maps from the finite-element numerical model are shown in Figure 4.9. Shown are the relative change $\Delta B_{mac}(t)/B_o$, where $\Delta B_{mac}(t) = B_{mac}(t)$ - $B_{mac}(t{=}0)$, for t = 9.7, 18.9, 28.0, and 68.5 minute time points. The numerical-modelling results for the parallel orientation (Figures 4.9*a* to 4.9*d*) indicate that $\Delta B_{mac}(t)$ is radially symmetric. Further, in every cylindrical shell at all time points, it was found that $\Delta B_{mac}/B_o = \Delta\chi$, a finding identical to the result for an infinitely long cylinder aligned parallel to an external-magnetic field [107]. To understand the implications of this result, Equation 4.2 is rewritten specifically for the parallel orientation:

$$\Delta B_{nuc,\|}(\vec{r}) \cong \left(\frac{1}{3}\frac{\Delta\chi}{\Delta T} - \frac{\Delta\sigma_E}{\Delta T}\right) \cdot B_o \cdot \Delta T(\vec{r}) \tag{4.3}$$

The experimental findings are consistent with this model in two respects. First, Equation 4.3 suggests that in the parallel orientation, there should be no spatial variations in the PRF-thermal coefficient, ie. changes in temperature should result in direct and local changes in B_{nuc}, which is what was observed experimentally. Second, the numerical-modelling results included in Equation 4.3 predict that the value of the apparent PRF-thermal coefficient will be ($\Delta\sigma_E/\Delta T$ - $\frac{1}{3}\Delta\chi/\Delta T$), which is smaller than the usually expected quantity ($\Delta\sigma_E/\Delta T + \frac{2}{3}\Delta\chi/\Delta T$) suggested in Equation 4.2. This result was also observed experimentally, in which the average apparent PRF-thermal coefficient was -0.0094 $\pm$ 0.0001 ppm/^{o}C, smaller than the accepted value of 0.0103 $\times$ $10^{-6}/^o$C for $\Delta\sigma_E/\Delta T$ of pure water [112]. Using this result, a linear thermal coefficient for the volume-magnetic susceptibility of the agar gel, $\Delta\chi_{gel}/\Delta T$, was estimated to be 0.0027 $\pm$ 0.0002 $\times$ $10^{-6}/^o$C, which is slightly lower than the linear thermal coefficient of 0.0030 $\times$ $10^{-6}/^o$C for pure water [137, 139].

The numerical-modelling results for the perpendicular orientation indicate eccentricity in the $\Delta B_{mac}(t)$ field maps, as shown in Figures 4.9*e* to 4.9*h*, in which the $\Delta B_{mac}(t)$ field is elongated in the direction of the applied-magnetic field (z-direction). There is a positive reinforcement of the macroscopic-magnetic field in the z-direction and a negative enforcement in the y-direction, typical of a magnetic-dipole field.

Figure 4.10 shows simulated values of ΔB_{nuc} as a function of temperature change at four different radial positions and resolves the nonlinear and irreversible behaviour with temperature between the heating and cooling periods that was observed in the experimental results of Figure 4.6*b*. The values of $\Delta B_{nuc}/B_o$ were derived through Equation 4.2, specifically, where changes in the magnetic field at the nucleus were modelled by $\Delta B_{nuc} = \Delta B_{mac}$ - $(\frac{2}{3}\Delta\chi + \Delta\sigma_E)B_o$, relative to

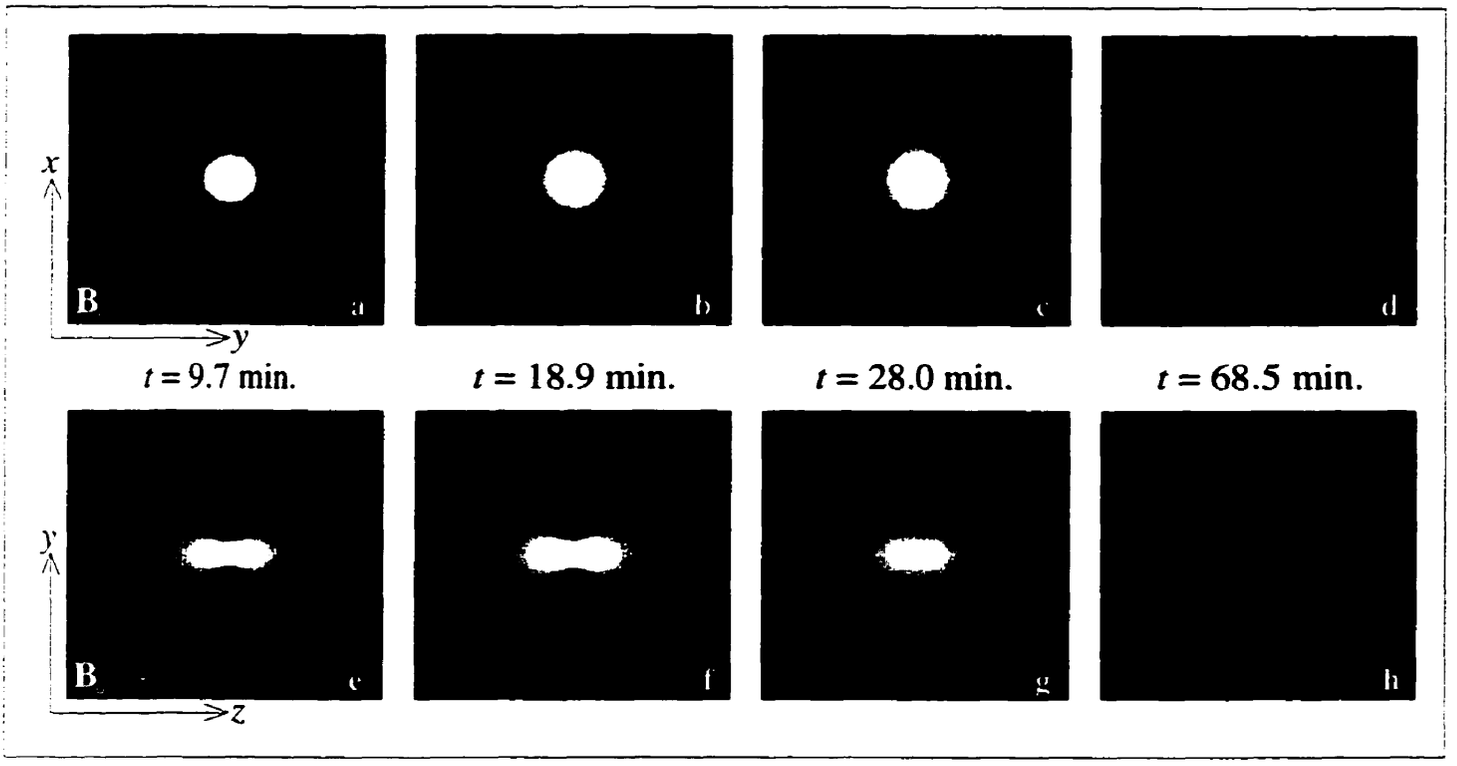

Figure 4.9: Numerically-modelled macroscopic-magnetic field images of the phantom in the parallel and perpendicular orientation. Shown are grey-scale maps of $\Delta B_{mac}(t)/B_o$, where $\Delta B_{mac}(t) = B_{mac}(t)$ - $B_{mac}(t=0)$, for the t = 9.7, 18.9, 28.0, and 68.5 minute time points. The above field maps were constructed by mirroring the half-model result and were windowed and levelled to 0.030 and 0.005 ppm, respectively. The dotted line in (a) and (e) indicates the border of the sphere.

a reference temperature of 24°C. In this simulation, changes in the volume-magnetic susceptibility ($\Delta\chi$) and the electron-screening constant thermal coefficient ($\Delta\sigma_E/\Delta T$) of pure water were used. The numerically modelled values of $\Delta B_{mac}/B_o$ provided the nonlinear and irreversible behaviour seen in Figure 4.10, which originates from the eccentricities in the ΔB_{mac} field maps of Figures 4.9e to 4.9h. To facilitate comparison, the vertical axes in Figure 4.10 correspond with those in Figure 4.6b. Notice how the simulated results in Figure 4.10 show similar behaviour to Figure 4.6b, particularly at larger radial positions. Similar to the experimental results in Figure 4.6b, a convergence is evident in Figure 4.10 during the cooling period which corresponds to the diminishing eccentricity in the ΔB_{mac} field with time.

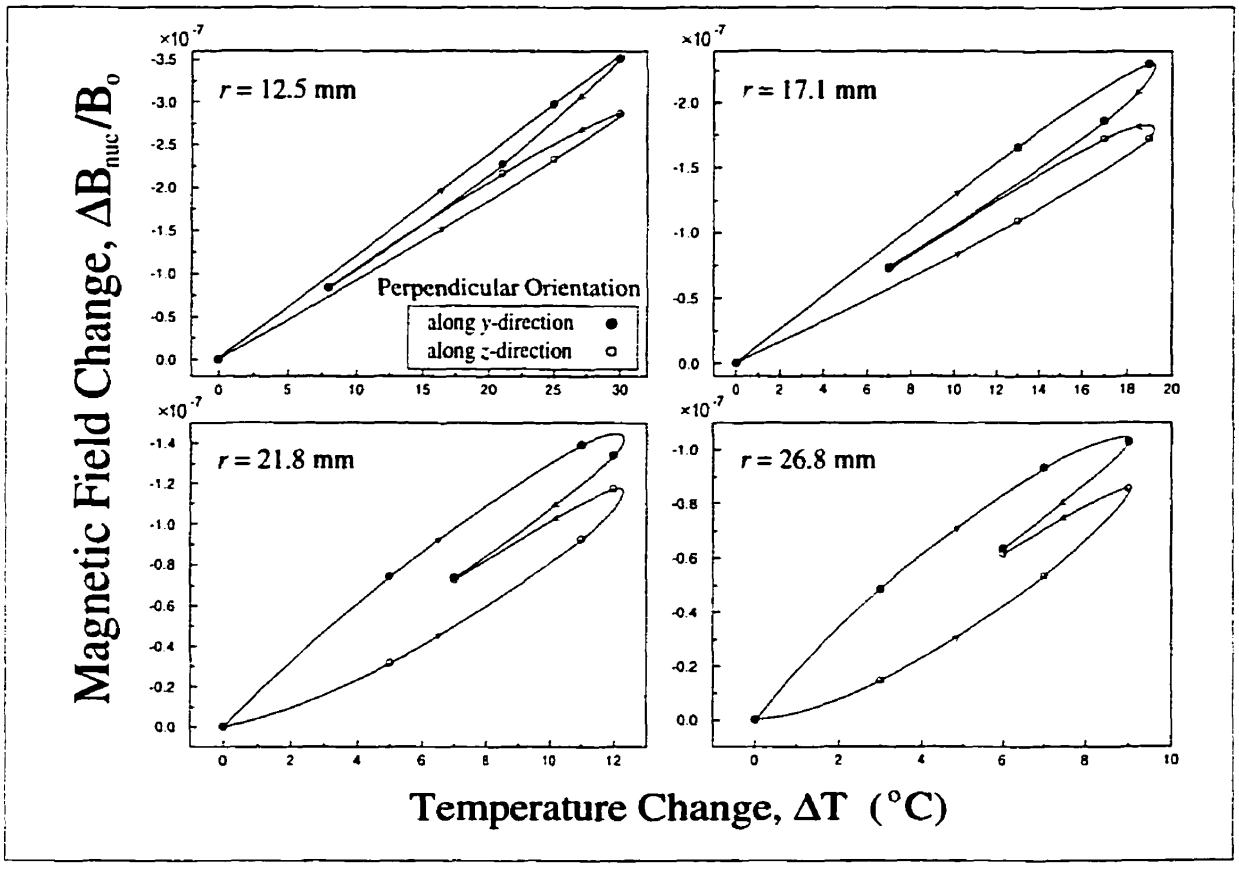

Figure 4.10: Simulated values of $\Delta B_{nuc}/B_o$ as a function of temperature change at four radial positions for the phantom in the perpendicular orientation, along the y- and z-directions. The solid line indicates the progression from heating to cooling.

4.5 Discussion

The results presented here apply specifically to the simple geometry that has been adapted to demonstrate how spatial variations in the macroscopic-magnetic field can influence temperature-induced phase-shift patterns. In this case, the heat-delivery device was modelled with a long, narrow cylinder of constant temperature, thus having a directionality and providing a radially-symmetric temperature distribution to the surrounding gel.

If spatial variations in the macroscopic-magnetic field are neglected, incorrect MR-derived estimates of temperature change may result. For example, in the perpendicular orientation of the experiment described, the difference in the phase-shift observed along the y- and z-direction was approximately 25° (at r = 15 mm, t = 18.9 minutes in Figure 4.5). This difference could have resulted in a temperature error of approximately 4°C, if this effect was not considered. While it

is uncertain of the impact such an error in temperature would have on the outcome of a thermal-coagulation therapy, it is generally agreed that a clinically-useful method of thermometry should be capable of a temperature accuracy of less than 1 or 2°C.

There are several clinically-used heat-delivery devices that have properties that are not dissimilar to this model, making this analysis directly applicable to MR-thermal monitoring of clinical thermal therapies. For example, interstitial microwave antennas have gained some popularity as a heat-delivery device, particularly for the absorptive properties of microwave energy. Such antennas generally have a helical-element, typically 10 to 20 mm in length and a diameter of approximately 1 mm, providing elongated "tear-drop" specific-absorption rate (SAR) patterns. Previous experiments incorporating interstitial microwave heating of polyacrylamide gels have resulted in eccentric temperature-induced phase-shift patterns when the antenna was oriented perpendicular to the main-magnetic field [182]. Further, subsequent experiments have revealed similar eccentric phase-shift patterns from interstitial microwave heating of *in vivo* rabbit brain [183], in which it was assumed that the observed eccentricity was simply a result of *in vivo* anisotropic temperature-diffusion effects, such as those due to blood flow. Other clinically-used heat-delivery devices will potentially give rise to this effect, such as focused ultrasound transducers and interstitial laser fibres. In Chapter 6, evidence is presented to show that this orientation effect is present with a clinical laser heating system.

In light of these findings, it is clear that there are some experimental considerations to be mindful of to better ensure the reliability of the MR-derived temperature measurements. Firstly, heat-delivery devices that emit a spherical SAR pattern are less problematic, as these possess no preferred orientation with the main-magnetic field and their effects can be modelled in a similar manner as described here. Secondly, cylindrically-shaped heat-delivery devices, if oriented parallel with the main-magnetic field, will give rise to a spatially-uniform apparent PRF-thermal coefficient, though expected to be smaller than the standard -0.01 ppm/°C. Finally, it should be noted that this effect arises from spatial gradients of volume-magnetic susceptibility that arise from spatial gradients of temperature. Therefore, depending on the nature of the thermal therapy (eg. thermal coagulation using high temperature for a short duration compared to hyperthermia using relatively low temperatures for longer periods), a slower heating approach should give rise to less eccentric phase-shift patterns, thus yielding more accurate MR-derived estimates of temperature. However, in the case of thermal-coagulation therapy requiring high temperatures only in the small-target

volume, this may not be feasible due to effects such as heat diffusion, blood flow, and/or perfusion.

In principle, it should be possible to correct for heat-source orientation and geometry influences on PRF-shift thermometry through the use of a self-consistent iterative calculation, as outlined below. A first-pass approximation of the 3D applied-temperature distribution, $T(\vec{r})$, is obtained from the raw, temperature-induced phase shift measurements. The volume-magnetic susceptibility distribution, $\chi(\vec{r})$, is then approximated from $T(\vec{r})$, and used as input to numerically solve Maxwell's equations and obtain an estimate of the macroscopic-magnetic field, $B_{mac}(\vec{r})$. An updated version of $T(\vec{r})$ could then be derived from $B_{mac}(\vec{r})$ and the phase-difference images, and so forth until the calculation converges.

4.6 Conclusion

Temperature-induced changes in the magnetic susceptibility cause spatial variations in the macroscopic-magnetic field, and consequently, the apparent PRF-thermal coefficient. These spatial variations may confound PRF-shift MR thermometry if their physical origin is not understood. An experimental model was presented to demonstrate heat-source orientation and geometry dependencies that consisted of a cylindrical heating device in a gel-filled sphere. With the cylinder oriented parallel to the main-magnetic field, radially-symmetric phase-shift patterns were observed. The apparent PRF-thermal coefficient was found to be spatially independent and constant over time. With the phantom in the perpendicular orientation, eccentric phase-shift patterns were found and the estimated apparent PRF-thermal coefficient was spatially dependent, initially ranging between -0.0055 to -0.0130 ppm/^{o}C and converging slowly over time. These experimental findings were resolved by numerical modelling of temperature-induced variations in the macroscopic-magnetic field in the phantom. It is believed that the effect reported here helps explain the discrepancies in recent reported calibrations of the PRF-thermal coefficient.

Chapter 5

PRF-Shift Thermometry is Affected by Changes in the Electrical Conductivity of Tissue

adapted from:
Robert D. Peters and R. Mark Henkelman,
Proton-Resonance Frequency Shift MR Thermometry is Affected by Changes in the Electrical Conductivity of Tissue.
Magnetic Resonance in Medicine **43**: 62-71 (2000).

Abstract

The proton-resonance frequency (PRF) shift method of MR thermometry provides an easy and practical means of quantitatively monitoring *in vivo* temperatures for MR-image guided thermal-coagulation therapy. However, reported discrepancies in the numerical value of the PRF-thermal coefficient persist, when measured in a variety of experimental conditions and in different tissue types, both *ex vivo* and *in vivo*. In this report, a potential source of variation in the PRF-shift method of thermometry is identified that manifests as a constant incremental phase shift per unit change in temperature that is independent of the echo-time setting, when constructing temperature-sensitive phase images from a gradient-echo pulse sequence. It is proposed that this confounding phase-shift offset arises from thermally-induced changes in the electrical conductivity of the material. To this end, it is demonstrated that the MR-derived temperature changes could be in error

by as much as 28%, as measured from a simple calibration experiment on freshly excised cow liver. A simple method of overcoming this phase-shift offset is described.

5.1 Introduction

Quantitative magnetic resonance (MR) thermometry is a relatively new technology that could help bring thermal therapies, such as conventional hyperthermia and thermal-coagulation therapy, to a more complete level of clinical acceptance [67, 96, 177]. Unlike regular diagnostic MR imaging where a radiologist would assess the presence or absence of disease, MR thermometry is a tool that must provide a surgeon with spatially-resolved and real-time quantitative estimations of *in vivo* temperatures. This information is directly used in the decision-making process of the therapy, which generally includes ensuring that healthy surrounding tissue is spared of excessive heat energy and that the diseased tissue has been exposed to adequate temperature-time treatment to induce necrosis. Consequently, the success of MR image-guided thermal therapy rests heavily on the accuracy with which temperatures can be estimated.

5.2 Motivation

5.2.1 PRF-Shift Thermometry through Phase-Shift Mapping

With the PRF-shift method of MR thermometry, thermal maps can be constructed from phase-difference images obtained from a gradient-recalled echo imaging sequence [113, 161, 164, 172, 179, 180, 184]. The generally accepted model of the phase-shift sensitivity or thermal coefficient ($\Delta\phi/\Delta T$) is:

$$\frac{\Delta\phi}{\Delta T} = \alpha \cdot \frac{\gamma}{2\pi} \cdot B_o \cdot (360^o/cycle) \cdot TE \tag{5.1}$$

where $\Delta\phi$ is the temperature-induced phase shift and ΔT is the applied temperature change. In the above equation, α is the apparent PRF-thermal coefficient (units of ppm/^{o}C), γ is the gyromagnetic ratio for ^{1}H nuclei, B_o is the main-magnetic field strength and TE is the echo-time setting. The PRF-thermal coefficient contains contributions from changes in the electron screening constant and magnetic susceptibility and is approximately -0.01 ppm/^{o}C [112, 164, 180, 184].

5.2.2 Identification of a Phase-Shift Offset

To address a fundamental issue as to whether the PRF-thermal coefficient has a dependence on *ex vivo* tissue type, a series of calibration experiments were undertaken as described in Chapter 3 [179]. These results showed there to be no significant difference among animal tissues when measured *ex vivo*, within an experimental precision of approximately 4%. As discussed in the Methods Section in Chapter 3, the calibration experiments involved placing tubes containing freshly excised animal tissues (rabbit and pig brain, muscle, liver, and kidney) and an agar gel control into a container, through which heated water was circulated. The circulating water was doped with $MnCl_2$ (20 mM) to eliminate ghosting artifacts from the flowing solution during MR imaging. Temperature-induced phase shifts in the tissues and agar gel control were measured showing excellent linearity throughout a temperature range of 20–80°C.

However, an inconsistent trend was identified in the phase-shift measurements when using different echo-time settings (not discussed in Chapter 3) and is exemplified in Figure 5.1. These confounding results showed that the phase-shift thermal coefficient did *not* scale with the echo-time setting, as suggested by the model in Equation 5.1. Although the temperature-induced phase shifts for any single TE setting in Figure 5.1*a* appear linear and well-behaved, the derived apparent PRF-thermal coefficient (α) is not a constant but varies with TE, ranging from -0.0098 ppm/°C (TE = 6 ms) to -0.0085 ppm/°C (TE = 15 ms). This inconsistent behaviour is more easily appreciated by plotting the linear fitted phase-shift thermal coefficient ($\Delta\phi/\Delta T$) as a function of the TE setting used in the pulse sequence, as shown in Figure 5.1*b*.

It is plausible and easy to conceptualize that the offset in the data shown in Figure 5.1*b* could have arose from a -1.7 ms offset in the TE setting, which could arguably result from timing errors in the imaging pulse sequence. However, no evidence for such a TE offset was found from examination of the centering of the data in the k-space matrix or by monitoring the pulse sequence on a triggered oscilloscope. An alternative explanation is that the offset in Figure 5.1*b* resulted from a TE-independent phase-shift offset of -0.29°/°C, which is less easy to conceptualize.

If not accounted or corrected for, the presence of this phase-shift offset will hinder the quantitative ability of PRF-shift MR thermometry. Consider the following simple and realistic example of how a phase-shift offset can result in incorrect MR-derived temperatures, using the data in Figure 5.1. Suppose a calibration experiment at 1.5 T was performed using two echo-time settings of 6 ms and 15 ms that resulted in phase-shift thermal coefficients of -1.35 °/°C and -2.93 °/°C,

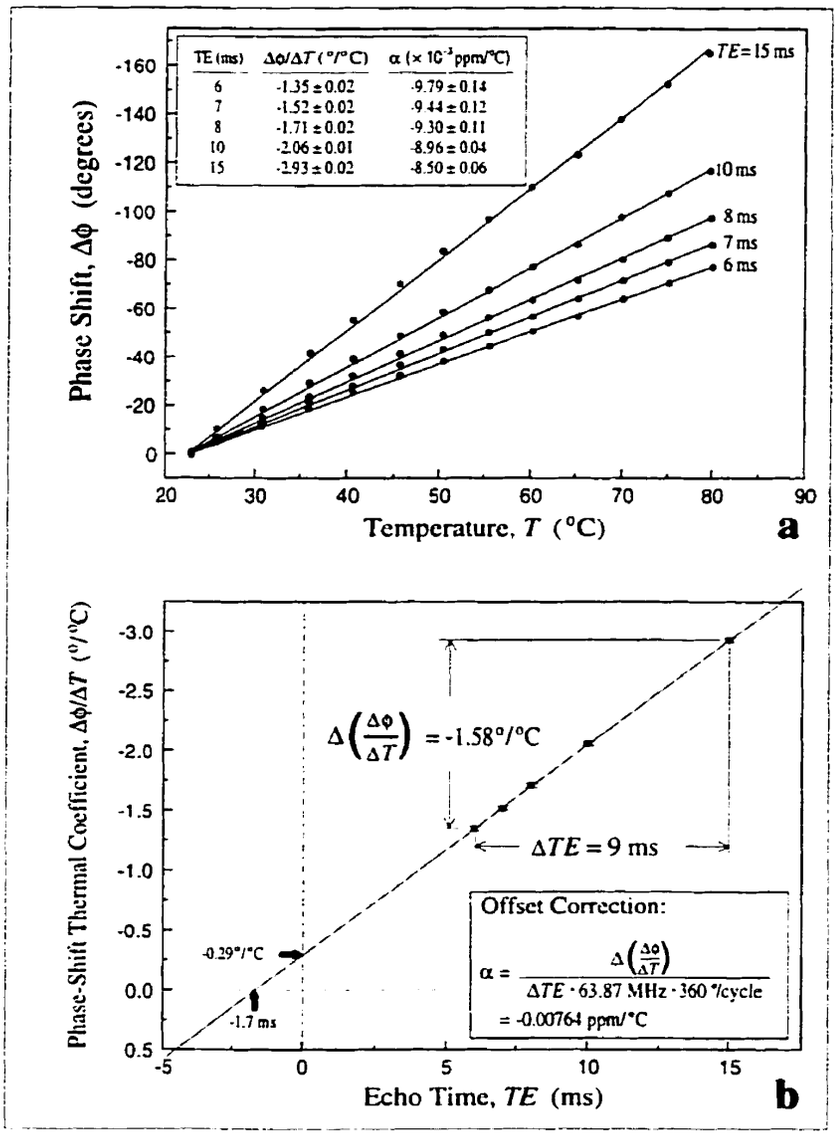

Figure 5.1: Representative data showing an inconsistent trend in PRF-thermal calibration experiments when using different TE settings. Shown are (a) phase shift as a function of temperature in a 2% agar gel-filled tube from five different TE settings, and (b) the phase-shift thermal coefficient ($\Delta\phi/\Delta T$) as a function of the TE setting. These results were obtained using a 20mM $MnCl_2$ circulating solution for heating to eliminate ghosting artifacts and with the gel-filled tubes oriented parallel with the main-magnetic field. In (a) the solid lines represent linear fits to derive the phase-shift thermal coefficients ($\Delta\phi/\Delta T$), which are indicated along with the calculated apparent PRF-thermal coefficients (α) from Equation 5.1. These results were used to construct the plot in (b) which indicates the presence of an offset: a measured phase-shift offset of -0.29°/°C or a TE-setting offset of approximately -1.7 ms. A method of overcoming this apparent offset in determining the PRF-thermal coefficient is shown in (b) using a difference method.

respectively (see Figure 5.1*a*). Using a difference method as outlined in Figure 5.1*b*, these results gave a phase-shift thermal coefficient difference of -1.58 $^o/^o$C over a ΔTE period of 9 ms and allowed a single PRF-thermal coefficient of -0.00764 ppm/^{o}C to be reported, while excluding the phase-shift offset of -0.29$^o/^o$C that was present in the experiment[1]. Given only this *a priori* calibration factor, suppose the goal of a subsequent experiment is to obtain MR-derived temperatures from a similar heating experiment (using identical experimental conditions as the previous calibration experiment), except now with only a single TE setting of 6 ms. If it is assumed that $\Delta\phi/\Delta T$ scales with TE, as suggested in Equation 5.1, then it would seem that a value of $\Delta\phi/\Delta T$ = (-0.00764 ppm/^{o}C)(63.87 MHz)(360^o/cycle)(6 ms) = -1.05$^o/^o$C would be appropriate to convert phase measurements into units of temperature change. However, this value is approximately 28% *smaller* than -1.35$^o/^o$C which was determined in the initial calibration experiment using TE = 6 ms directly (Figure 5.1*a*). With a TE setting of 6 ms, a temperature-induced phase-shift measurement of, say, -55^o would incorrectly indicate a temperature change of ΔT = -55^o/(-1.05$^o/^o$C) = 52^{o}C, whereas the actual temperature change is ΔT = -55^o/(-1.35$^o/^o$C) = 41°C. This potential for overestimating the temperature could conceivably lead to the undertreatment of diseased tissue and have drastic consequences on the outcome of the thermal therapy. Conversely, it is possible to formulate a similar example using the same data in Figure 5.1 where the unaccounted phase-shift offset could lead to underestimates of temperature change, and potentially lead to the destruction of healthy tissue. In light of this potential for error in the MR-derived temperatures, we believe that an understanding of the physical origin of this phase-shift offset is imperative to ensure the quantitative ability of PRF-shift MR thermometry, which is the topic of this chapter.

The PRF-calibration data used in Chapter 3 contained an offset as described above. At the time of that study, the correct explanation for the offset was not understood and an objective interpretation of the results included either an offset in $\Delta\phi/\Delta T$ or in the TE setting. To overcome the effect of the offset, the PRF-thermal coefficients (Chapter 3, Figure 8) were calculated using the difference between two different TE results, as indicated in Figure 5.1*b*.

[1]The reader will recall that in Chapter 3 an average PRF-thermal coefficient value of approximately -0.0101 ppm/°C was obtained from the excised tissue and gel sample tubes when the sample tubes were oriented *perpendicular* to the main-magnetic field (Chapter 3, Figure 2). With an identical experimental setup except with the sample tubes now oriented *parallel* to the main-magnetic field, a significantly smaller PRF-thermal coefficient is observed to be approximately -0.00764 ppm/°C, as indicated in Figure 5.1*b*. This apparent discrepancy is simply an example of an orientation and geometry dependence in PRF-shift thermometry, similar to the one demonstrated in Chapter 4.

5.2.3 Phase-Shift Offsets Observed in Other Reports

The phase-shift offset phenomena has appeared, though inadvertently, in the results of at least two other publications on the use of PRF-shift thermometry for monitoring temperature changes in gel phantoms and in excised and *in vivo* tissues.

MacFall, et al. in 1996, meticulously described simultaneous MR imaging and heating using an RF annular phased array antenna [161]. In a saline-based acrylamide gel ($\epsilon_r = 65$, $\sigma = 1.14$ S/m at 130 MHz) the authors noted differences in the phase-temperature sensitivity when using two different *TE* settings. Their findings from two different regions of interest (ROIs) in the gel are shown in Figure 5.2 and are summarized in Table 5.1, clearly indicating the presence of a phase-shift offset. In particular, the data implies a phase-shift offset of -0.77 ± 0.04 °/°C at the center and -0.37 ± 0.10 °/°C near the edge of the gel phantom.

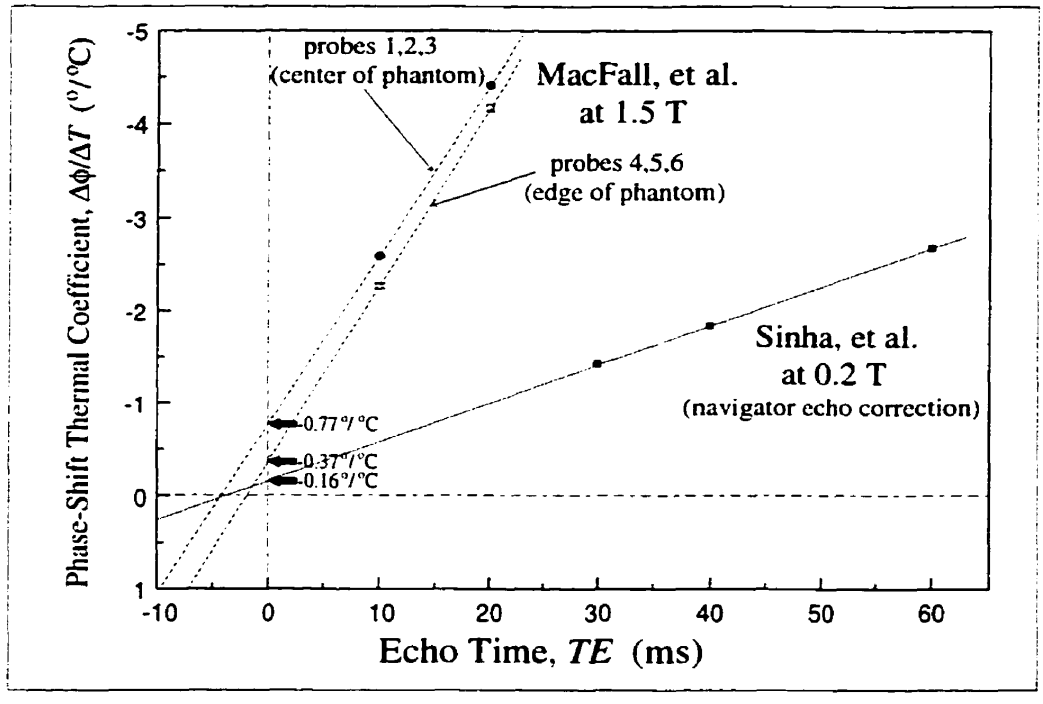

Figure 5.2: Phase-shift temperature sensitivity ($\Delta\phi/\Delta T$) as a function of the *TE* setting as reported from MacFall, et al. [161] and Sinha, et al. [172]. The data from MacFall, et al. show phase-shift offsets at two depths in a phantom of -0.77 ± 0.04 °/°C and -0.37 ± 0.10 °/°C. A similar offset of -0.16 ± 0.11 °/°C was seen in the data reported by Sinha, et al.

At 0.2 T, Sinha, et al. in 1997, have described RF heating of a $NiCl_2$-doped gel phantom (1.5 % agarose, 0.2 mM $NiCl_2$) [172]. Using three different *TE*'s (30, 40, and 60 ms) they reported that the phase-shift temperature sensitivity approximately scaled with *TE*. However, on closer

Table 5.1: Phase-shift offsets observed in other reports. Phase-shift temperature sensitivity as a function of TE from MacFall, et al. [161] and Sinha, et al. [172]. The results of a linear fit for each data set are shown, where $\Delta\phi/\Delta T = A + B \cdot TE$.

	phase-shift temperature sensitivity, $\Delta\phi/\Delta T$ (^{o}/^{o}C)			
	MacFall, et al. at 1.5 T		Sinha, et al. at 0.2 T	
TE (ms)	probes 1–3 (center of phantom)	probes 4–6 (edge of phantom)	navigator echo correction	w/o navigator echo correction
10	-2.59 ± 0.01	-2.27 ± 0.03		
20	-4.41 ± 0.02	-4.17 ± 0.04		
30			-1.42	-1.38
40			-1.84	-1.87
60			-2.68	-2.65
A (^{o}/^{o}C)	-0.77 ± 0.04	-0.37 ± 0.10	-0.16 ± 0.11	-0.15 ± 0.11
B (^{o}/^{o}C · ms)	-0.182 ± 0.003	-0.190 ± 0.007	-0.042 ± 0.003	-0.042 ± 0.003

examination, evidence of a TE-independent phase-shift offset also appears as shown in Figure 5.2 and Table 5.1. It is proposed that these two reports show the same phase-shift offset that has been identified in the data shown in Figure 5.1*b*.

5.3 Methods and Materials

5.3.1 Phase Retardation in a Conductive Material

In an electrically-conductive material, a transmitted time-varying inductive field ($B_1(t)$), such as an RF pulse in an MR imaging sequence, will undergo amplitude attenuation and phase lag or retardation [121, 185, 186]. From the perspective of MR imaging, this gives rise to a non-uniform distribution of tip angles over the spins in the object and a variation of the transverse-magnetization phase with depth [185,186]. The spatial nature of this phase retardation depends on the distribution of the material properties and the imaging coil(s) used to transmit and receive the radiofrequency signal.

To illustrate amplitude attenuation and phase retardation in a simple scenario, consider a linearly-polarized time-varying field of the form $\vec{B}(t) = B_1 e^{i\omega t}\,\hat{z}$. In a semi-infinite conducting

material [121, 185, 186], the field will be modified, such that:

$$\vec{B}(x \geq 0) = B_o e^{-k_i x + i(\omega t - k_r x)} \hat{z} \tag{5.2}$$

and where real wavenumber which describes how the phase retardation varies linearly with depth and is dependent on the material properties:

$$k_r = \omega \sqrt{\frac{1}{2}\epsilon\mu \left(\sqrt{1 + \left(\frac{\sigma}{\epsilon\omega}\right)^2} + 1 \right)} \tag{5.3}$$

In the above equation, ϵ is the electrical permittivity, μ is the magnetic permeability, and σ is the electrical conductivity of the material. The expression for the imaginary wavenumber (k_i) is similar in form to k_r. In a nonconducting material ($\sigma = 0$), Equation 5.3 simplifies to $k_r = \omega(\mu\epsilon)^{\frac{1}{2}}$ and $k_i = 0$.

In more practical situations, such as MR imaging, circularly-polarized induction fields are often used, which along with the appropriate boundary conditions, is not amenable to an analytic solution as in the above example. Although phase retardation will still be dependent on the same material properties as those seen in Equation 5.3, ie. ϵ, μ, and σ, solutions to these problems are usually attainable only through numerical modelling.

5.3.2 The Physical Origin of the Phase-Shift Offset

The PRF-shift method relies on the subtraction of a baseline phase image (acquired before heating) from subsequent phase images that are acquired during the course of the heating experiment. The phase-image subtraction is necessary to exclude non-thermal contributions to phase, such as B_o field inhomogeneities, ideally leaving only the spatially-resolved phase-shifts attributable to temperature-induced shifts in the PRF, as predicted in Equation 5.1.

The electrical conductivity and, to a lesser extent, the permittivity of tissue can change with temperature from the baseline state and thus alter the severity of the phase retardation in the object. If this occurs, the phase-image subtraction will not exclude these changes in phase retardation. Because this phase-shift contribution results from phase retardation of the transmitted and received RF fields, it is independent of the usual spin-evolution waiting period, TE, and will depend only on the spatial distribution of the temperature change, $\Delta T(\vec{r})$. Consequently, a TE-

independent phase shift with change in temperature will result (which we denote now as the phase-shift thermal-coefficient offset, $\Delta\psi/\Delta T$), rendering the simple model of temperature-induced phase shifts (Equation 5.1) incomplete. Furthermore, as phase retardation varies with depth (linearly, as in the above example of a linearly polarized field incident on semi-infinite material) we would expect the severity of the phase-shift offset, $\Delta\psi/\Delta T$, to also vary with depth.

5.3.3 Experimental Design

The experimental setup is identical to that described in Chapter 3 in which temperature-induced phase shifts were measured in 2% agar gel-filled tubes (14 mm inner diameter) (Sarstedt Inc., Newton, NC) [7]. The tubes were immersed in a cylindrical container through which pure water (de-ionized, distilled), 20 mM NaCl, 60 mM NaCl, 150 mM NaCl, 20 mM $MnCl_2$, or 60 mM $MnCl_2$ solutions were heated and circulated (see Figure 5.3). These different solutions were used specifically for their differences in electrical conductivity and permittivity. For reference, physiological saline is 154 mM NaCl. Note that the cylindrical container and tubes were oriented parallel with the main-magnetic field and centered within a standard-quadrature birdcage head coil. Within the container, the agar gel occupied a volume of approximately 0.18 L, the remaining 1.76 L consisting of the heated circulating solution. Although the phase-shift measurements were made in the agar gel, that volume occupied was only 10% of the total capacity of the container, so that any phase-retardation effects would be primarily due to the properties of the surrounding circulating solution. The gel-filled tubes were located at two distinct radii or depths within the container, as shown in Figure 5.3. Measurements from the outer 10 and inner 4 tubes were used to assess the depth dependence of the experimentally-measurement phase-shift offset, $\Delta\psi/\Delta T$.

After measuring how temperature-induced changes in the electrical conductivity affects PRF-shift thermometry in the water, NaCl, and $MnCl_2$ solutions, the same effect was demonstrated through the uniform heating of a large volume of tissue. Approximately 716 g (0.674 L) of freshly excised cow liver was trimmed of excess fat and tendon, and placed in a cylindrical plexiglass container. The container was wrapped with tubing in which water was heated and circulated, allowing the tissue to be slowly and uniformly heated. Luxtron fibre-optic probes (Luxtron Corp., Santa Clara, CA) were placed in the tissue to monitor the temperature and verify that the tissue was being heated uniformly. The whole assembly was placed in a styrofoam box to preserve heat during the experiment.

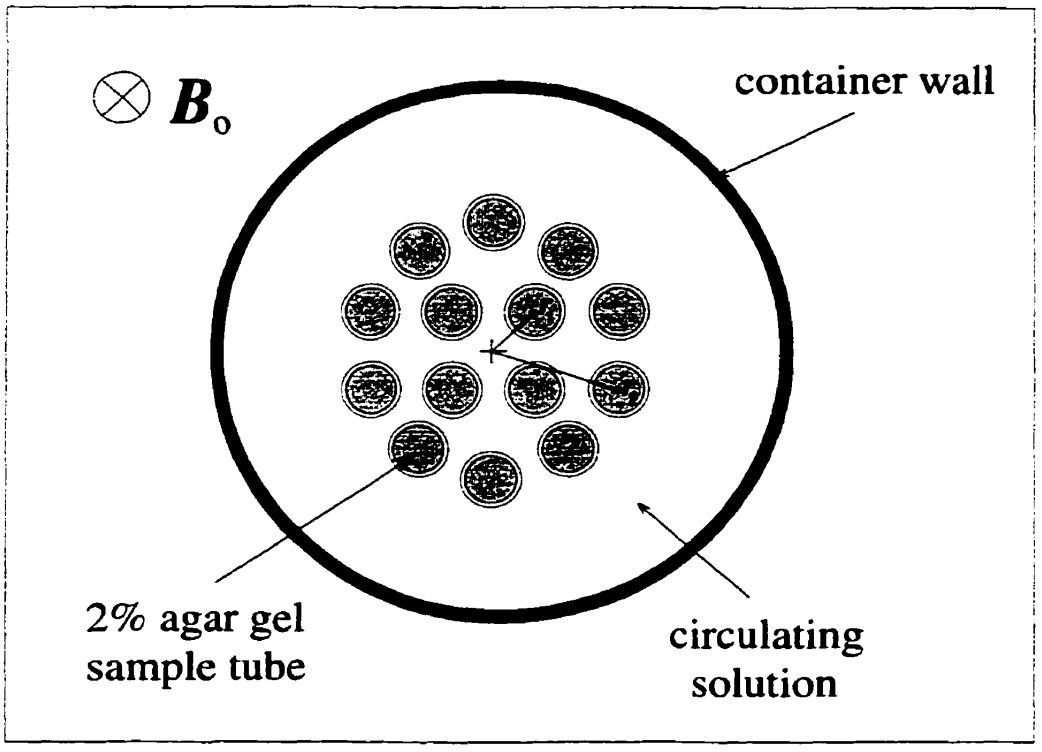

Figure 5.3: Cross section of the cylindrical container used in the PRF-thermal calibration experiments. The container (ID = 138 mm) holds 14 agar-gel sample tubes (ID = 14 mm) arranged as shown. These tubes were immersed in heated circulating solution. The cylindrical container and sample tubes were oriented parallel with the main-magnetic field. Each sample tube was located at a radius of 16 mm or 37 mm or at a depth of 56 mm and 32 mm, respectively.

5.3.4 MR Imaging and Data Analysis

For both experimental setups, involving the pure water, NaCl, and $MnCl_2$ solutions and the excised cow liver, MR imaging was performed using the standard-quadrature head coil of a 1.5 T MRI system (Signa, GE Medical Systems, Milwaukee, WI). A spoiled gradient recalled-echo (SPGR) sequence was used to obtain single-slice images during the baseline and heating segments of the experiment. The relevant MR scan settings were: TE = 6, 7, 8, 10 and 15 ms, TR = 50 ms, tip angle = 30°, 10 mm slice thickness, 18 cm field-of-view, 256 × 256 image matrix, 2 averages, and an acquisition time of 26 seconds per image. A 6 ms TE setting was the minimum that would acquire a full echo on readout with the above sequence. For each TE setting, phase-difference images were constructed by subtracting a phase-reference image that was acquired at room temperature from subsequent phase images acquired during the heating experiment. Measurements from the phase-reference phantoms were used to exclude non-thermal frequency-drift sources in the MR system,

as described in Chapter 3.

Region-of-interest (ROI) measurements were obtained from each TE setting and a linear fit was made to the resultant phase-shift data as a function of temperature, as shown in the representative data in Figure 5.1*a*. The phase-shift offset ($\Delta\psi/\Delta T$) was determined by extrapolating the multi-TE results to the $TE = 0$ intercept, as indicated in Figure 5.1*b*. These experimentally-measured phase-shift offsets were compared with the results from the numerical RF field modelling, for each material and at the two depths within the container.

5.3.5 Numerical Modelling of the RF Magnetic Field

Temperature-induced changes in phase retardation within the cylindrical container were modelled using a 2D finite-difference RF field model as described by Jin [187]. To simulate the experimental conditions, the model consisted of a 16-element birdcage coil containing a cylinder of uniform material, as shown in Figure 5.4. The 14 gel-filled tubes that were present in the experimental setup (see Figure 5.3) were not included in the numerical model for computational simplicity and because they occupied only approximately 10% of the total volume of the cylinder. A 60 cm diameter boundary condition was used for the calculation of the electric field (RF shield). Initially, the electric field within the circular boundary was determined using a self-consistent iterative calculation using the method of finite differences. The magnetic field in this region, was then derived from a numerical curl operation of the electric field. Of particular interest is the radial variation of the phase of the transverse magnetic field throughout the material cylinder. Relating to the B_1 field used in MR imaging, this phase is the arctangent of the modelled B_y/B_x. The circularly polarized field solution was generated from a superposition of vertical and horizontal polarizations. The material cylinder was assigned permittivity, electrical conductivity, and permeability as described in Table 5.2 for pure water, 20 mM NaCl, 60 mM NaCl, 150 mM NaCl, 20 mM $MnCl_2$, 60 mM $MnCl_2$ solutions and excised cow liver. The numerical modelling results from the cow liver material would only be qualitatively compared with the experimental results, due to slight differences in the experimental geometry.

5.3.6 Electrical Conductivity

The electrical conductivity of a material depends on the density of charge carriers as well as the ability of the carriers to move through the material. Consequently, the conductivity of pure (deionized)

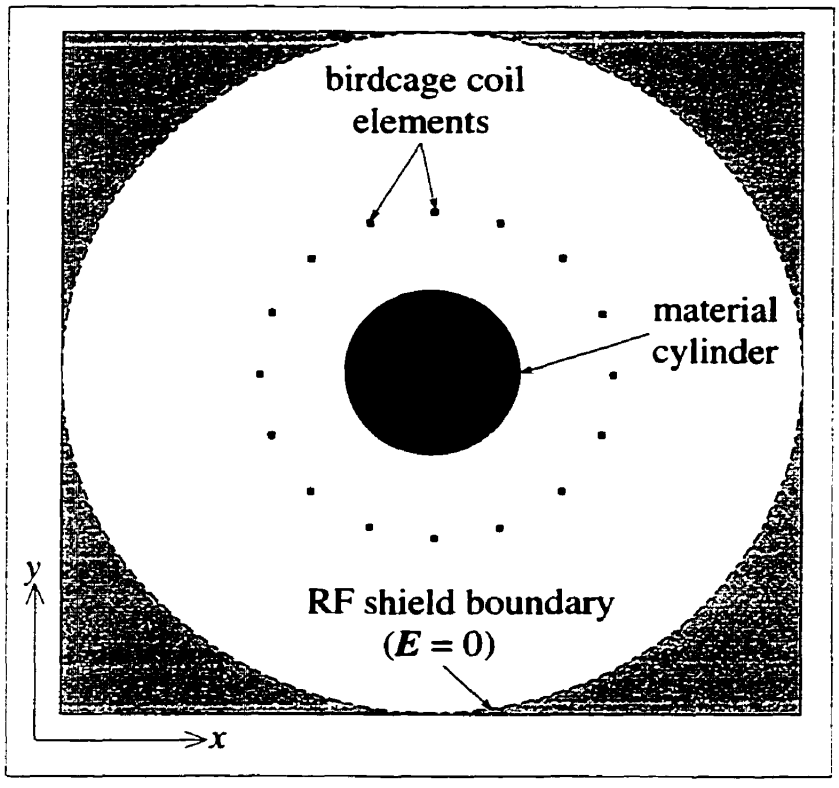

Figure 5.4: Representation of the 2D finite-difference numerical model for calculating the RF magnetic field. Shown are relative size and locations of the central material cylinder (OD = 138 mm), the 16 elements of the birdcage coil (OD = 290 mm) and the boundary condition for the electric field (OD = 600 mm). The model was represented by a 248 × 248 matrix.

water is zero because it contains no charge-carrying ions and remains zero over all temperatures. In an electrolytic solution, the electrical conductivity depends on the concentration of ions in the solution. In saline, the charge carriers are the Na^+ and Cl^- ions whose equivalent-molar conductances are 5.09 and 7.55 (S/m)/(mol/L), respectively at 25°C [139]. The electrical conductivity of a 60 mM NaCl solution is approximately 0.77 S/m at 25°C and increases by approximately 2.3%/°C, at zero frequency. We make the assumption that the conductivity of saline at 64 MHz is similar to that at zero frequency.

Although tissue contains physiologic saline (154 mM NaCl), its electrical conductivity is largely dictated by the presence of cellular membranes [188–192]. At 64 MHz, cell membranes become charged through the intra- and extra-cellular media, leaving the tissue's conductivity approximately 0.54 S/m at 37°C, increasing by approximately 2.6%/°C as measured in excised cow liver [189]. For comparison, the conductivity of 154 mM NaCl solution is approximately 2.50 S/m at 37°C [139], roughly five times the conductivity of the excised tissue. Note that the electrical

Table 5.2: Material properties used in the numerical RF field modelling. The values listed in the table were used to assign relative permittivity (ϵ_r), electrical conductivity (σ), and relative permeability (μ_r) to the material cylinder at temperatures between 10 and 90°C [139, 188–192]. The relative permeability ($\mu_r = 1 + \chi_v$) was assumed to be constant in temperature.

material	ϵ_r (25°C)	$\Delta\epsilon_r/\epsilon_r\Delta T$ (%/°C)	σ (25°C) (S/m)	$\Delta\sigma/\sigma\Delta T$ (%/°C)	χ_v (25°C) $\times 10^{-6}$
water	78	-0.4	0	0	-9.05
NaCl (20 mM)	78	-0.4	0.26	+2.3	-9.06
NaCl (60 mM)	78	-0.4	0.77	+2.3	-9.07
NaCl (150 mM)	78	-0.4	1.93	+2.3	-9.11
$MnCl_2$ (20 mM)	78	-0.4	0.52	+1.9	-5.39
$MnCl_2$ (60 mM)	78	-0.4	1.56	+1.9	+1.93
cow liver (*ex vivo*)	87	+0.3	0.41	+2.6	-9.05
background (air)	1	0	0	0	0

conductivity and its thermal coefficient may vary with tissue type and on the thermal history of the tissue.

5.3.7 Permittivity

At zero frequency, the dielectric constant or relative permittivity of water is approximately 78 at 25°C and decreases with temperature by approximately 0.5%/°C [139]. This is due to the temperature dependence of hydrogen bonding among water molecules [193]. This behaviour was adapted into the numerical model, approximating the permittivity of water and the NaCl and $MnCl_2$ solutions at 64 MHz. In excised cow liver, the relative permittivity is approximately 90 at 37°C, and increases with temperature by approximately 0.3%/°C [189, 191]. While care was taken to closely approximate the relative permittivity of each material, it was found that the numerically-modelled phase retardation was primarily dependent on the electrical conductivity of the material.

5.3.8 Permeability

A complete description of the electromagnetic properties of a material includes the relative permeability (μ_r), describing the material's response to an external magnetic field. Pure water is diamagnetic with a volume magnetic susceptibility (χ_v) of -9.05 $\times 10^{-6}$ (MKS) at room temperature which increases with temperature by approximately +0.003 $\times 10^{-6}$/°C, mostly because of a decrease in the density of water [107, 137]. With the permeability defined as $\mu = (1 + \chi_v)\mu_o$, with

μ_o the permeability of free space, it follows that μ increases by approximately 3×10^{-7} %/°C. Saline and most tissues are also diamagnetic and have volume-magnetic susceptibilities similar to that of pure water. Notice however, that $MnCl_2$ is paramagnetic where χ_v is positive in high-concentration solutions, as shown in the last column of Table 5.2. Due to its weak sensitivity, temperature variations in the relative permeability of the materials had no measurable effect on the numerically-modelled phase retardation.

5.4 Results

5.4.1 Experimentally-Measured Phase-Shift Offsets

Representative phase shifts as a function of temperature are shown for the experiment using 150 mM NaCl circulating solution in Figure 5.5. This solution had the highest conductivity of all the solutions examined and therefore was expected to give the largest phase-shift offset. In the results shown in Figure 5.5*a* there is a clear difference between the phase shifts obtained from gel-filled tubes located at different depths within the cylindrical container. The results shown in Figure 5.5*b* clearly show the presence of a phase-shift offset as well as a variation with depth. The tubes located at a depth of 53 mm gave an average $\Delta\psi/\Delta T$ of -1.03 ± 0.04 (sd) °/°C and those at a depth of 32 mm an average of -0.91 ± 0.04 °/°C. For comparison, a PRF-thermal coefficient of -0.01 ppm/°C would give a phase-shift thermal coefficient ($\Delta\phi/\Delta T$) of approximately -1.38 °/°C using a TE of 6 ms, which underscores the importance in identifying phase-shift offsets. Among the solutions examined (pure water, 20 mM NaCl, 60 mM NaCl, 150 mM NaCl, 20 mM $MnCl_2$, and 60 mM $MnCl_2$) phase-shift offsets ranging from 0 to -1.03 °/°C were observed. Generally, variations of $\Delta\psi/\Delta T$ with depth were more apparent in the higher concentration solutions of 60 mM NaCl, 60 mM $MnCl_2$ and 150 mM NaCl.

No significant phase-shift offset was observed when pure water was examined, likely due to its zero conductivity. This finding was consistent with the underlying hypothesis on the physical origin of phase-shift offsets. The experiment using pure water also provided a useful control which showed that other sources, such as phase errors originating from the imaging pulse sequence, flow-induced phase artifacts, and MR system phase drifts were not giving rise to the observed effect that would also have appeared with the NaCl and $MnCl_2$ solutions.

In the experiment involving uniform-heating of freshly excised cow liver, an average $\Delta\psi/\Delta T$

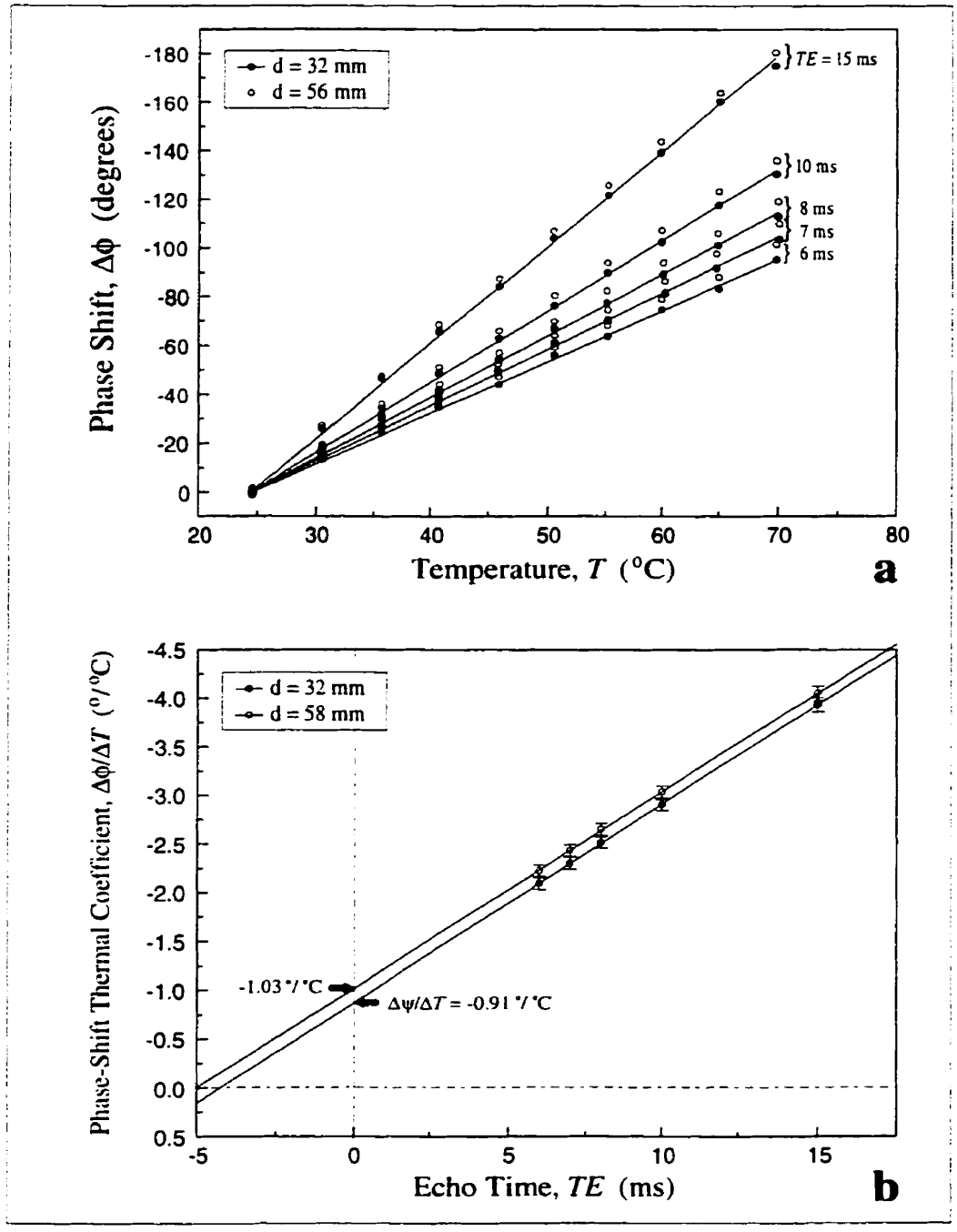

Figure 5.5: Phase-shift offsets in the experiment using 150 mM NaCl circulating solution. Shown are (a) phase shift as a function of temperature from five different TE settings, from ROI measurements in gel-filled tubes at two different depths, and (b) the phase-shift thermal coefficient ($\Delta\phi/\Delta T$) as a function of the TE setting. In (b) there are two distinct phase-shift offsets ($\Delta\phi/\Delta T$), of -0.91 and -1.03 °/°C corresponding to the two different depths within the cylindrical container.

of -0.33 ± 0.02 °/°C was measured and depth variations were not significantly resolved. With this particular experimental arrangement, $\Delta\psi/\Delta T$ was estimated to be approximately 28% of the offset-corrected $\Delta\phi/\Delta T$ at a TE setting of 6 ms and reducing to only 11% at a TE of 15 ms. Consequently, the presence of this phase-shift offset could have lead to corresponding errors in the MR-derived temperatures of 28% and 11% at the TE settings of 6 ms and 15 ms, respectively.

5.4.2 Numerically-Modelled Phase Retardation

Some representative numerically-modelled profiles of the phase-retardation effects are shown in Figure 5.6 for the 20 mM $MnCl_2$ material. These results show the phase of the transverse magnetic field through the material cylinder for various discrete uniform temperature states, relative to the 10°C condition (Figure 5.6*a*). It is clear that the phase varies approximately linearly with temperature and displays a quadratic behaviour with depth. The derived phase-shift offset, $\Delta\psi/\Delta T$, shows a similar variation with depth, reaching a minimum at the center of the cylinder. To compare with the experimental results, values of $\Delta\psi/\Delta T$ were extracted at radial positions of 16 mm and 37 mm, and averaged over a width of 10 mm which was the diameter of the gel-filled tubes. The numerically-modelled values of $\Delta\psi/\Delta T$ ranged from 0 for pure water to -0.79 °/°C for the 150 mM NaCl material properties.

5.4.3 Comparison of Experimental and Numerically-Modelled Results

The hypothesis that temperature-induced changes in phase retardation that originate from changes in the electrical conductivity seems valid in light of the good agreement between the experimentally-measured and numerically-modelled phase-shift offsets as shown in Figure 5.7. In general, good correlation is seen for each of the materials studied and the two depths examined, particularly at the lower-concentration solutions of 20 mM NaCl, 20 mM $MnCl_2$, and 60 mM NaCl.

It is reasonable to suggest that the discrepancy between the experimental and numerically-modelled results at the higher-concentration solutions may be due to the absence of the gel-filled tubes in the numerical model. The gel-filled tubes contained only agar and pure distilled water, such that their absence from the numerical model should make the electrical conductivity of the material cylinder solution in the present numerical model (Figure 5.4) larger than the average electrical conductivity of the cylinder containing the gel-filled tubes and the circulating solution in the experimental setup (Figure 5.3). Consequently, this should cause the numerically-modelled phase-

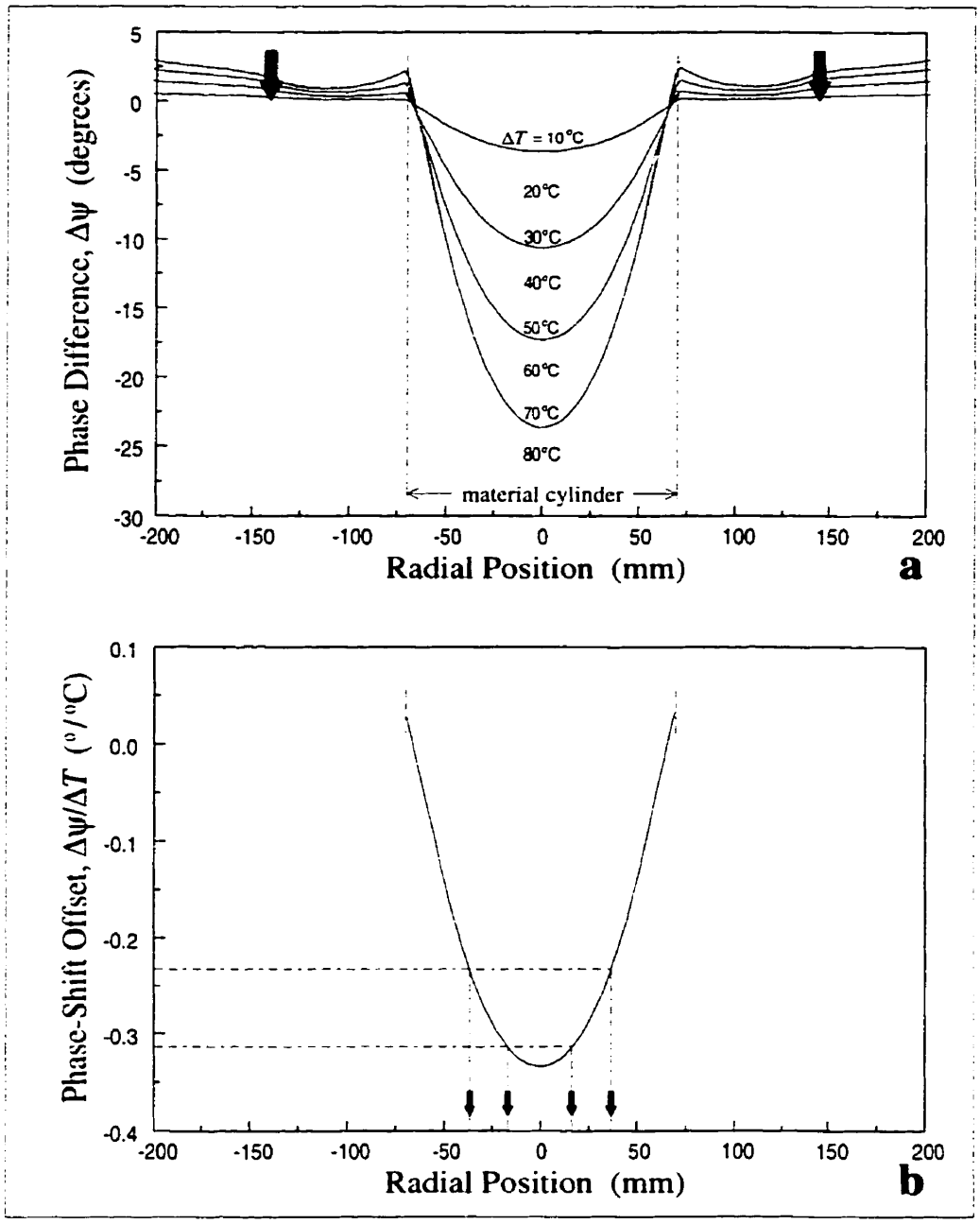

Figure 5.6: Numerically-modelled results of phase retardation in a cylinder using 20 mM $MnCl_2$ material properties. Shown are (a) phase-difference profiles ($\Delta\psi$), relative to the $T = 10°C$ state and (b) the derived phase-shift offset ($\Delta\psi/\Delta T$) through the center of the material cylinder. The arrows in (a) indicate the location of the bird-cage coil elements used in the model and in (b) indicate the locations of the gel-filled tubes. The numerical model predicts $\Delta\psi/\Delta T$ values of -0.31°/°C and -0.23°/°C at radial positions of 16 mm and 37 mm, respectively.

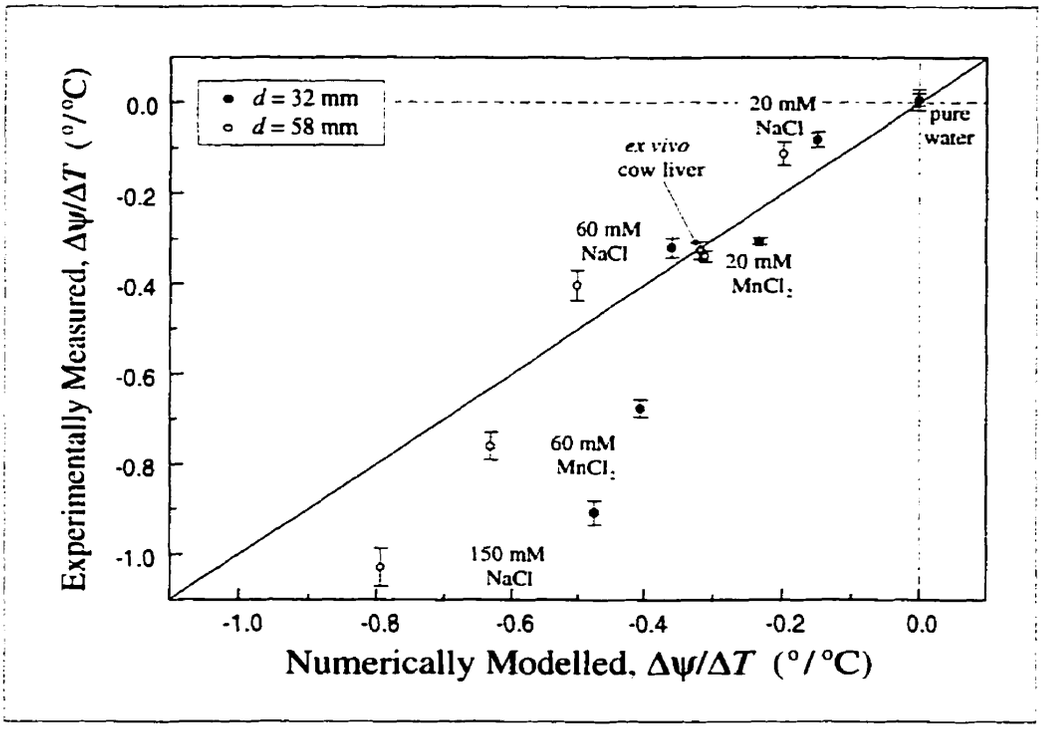

Figure 5.7: The experimentally-measured versus numerically-modelled phase-shift offset, $\Delta\psi/\Delta T$. Two data points are shown for each material studied, corresponding to two depths within the cylinder. The solid line represents the identity. A correlation coefficient of 0.916 (p=4×10^{-6}) was found between the experimental and numerically-modelled results. The vertical error bars represent standard deviations, as derived from multiple ROI measurements.

shift offsets to be larger than the experimental measurements. However, this was not what was observed for the higher-concentration solutions 60 mM $MnCl_2$ and 150 mM NaCl as seen in Figure 5.7 where the numerically-modelled values of $\Delta\psi/\Delta T$ were smaller than the experimental measurements. While the exact source of this discrepancy in the higher-concentration solutions is unclear, other simplifications of the numerical model are not ruled out such as the 2D approximation and the accuracy of the thermal coefficients of the material properties that were used and listed in Table 5.2. However, it is worth noting that most *in vivo* tissues should behave similarly to the excised cow liver and the lower-concentration NaCl and $MnCl_2$ solutions. In this range, there appears very good agreement between the experimentally-measured and numerically-modelled phase-shift offsets.

5.5 Discussion

It has been shown that temperature-induced changes in the electrical conductivity of tissue gives rise to alterations in the phase retardation of RF fields, in particular, the B_1 field used in MR imaging. This effect manifests as a constant phase shift per unit change in temperature that can vary spatially within the object and which is independent of the usual spin-evolution period, *TE*. This confounding phase-shift offset, if present and not corrected for, presents a significant hinderance to the quantitative ability of PRF-shift thermometry through phase-shift mapping. Fortunately, this phase retardation phenomenon does not affect implementations of PRF-shift thermometry using chemical-shift imaging.

Having established that temperature-induced changes in electrical conductivity is the likely physical origin of the observed phase-shift offsets, there are some implications that can be drawn with the use of numerical field modelling with respect to such experimental parameters as main-magnetic field strength and the size of the heated volume. At a main-magnetic field strength (B_o) of 1.5 T, the Larmor frequency is approximately 64 MHz for ^{1}H nuclei. At this frequency, the wavelength in a material with a relative permittivity of 85 and a zero conductivity is approximately 0.5 m. This wavelength is large compared to the object used in the experiment, which was a cylindrical container 13.8 cm in diameter. Using the numerical model described earlier, it was found that the phase-shift offset, $\Delta\psi/\Delta T$, approximately scaled with frequency, and thus B_o. In other words, the modelled value of $\Delta\psi/\Delta T$ at 1.5 T was approximately 10 times that at 0.15 T. Unfortunately, $\Delta\phi/\Delta T$ also scales with B_o (see Equation 5.1) such that the ratio $(\Delta\psi/\Delta T)/(\Delta\phi/\Delta T)$, and hence temperature error, remains constant. Consequently, the phase-shift offset can be equally troublesome at low field strengths also, which are likely to be employed for image-guided thermal-coagulation therapy. Referring to Figure 5.2, it is seen that the $\Delta\psi/\Delta T$ value derived at 0.2 T from Sinha et al. [172] remains a significant fraction of the $\Delta\phi/\Delta T$ values at all of the echo times used.

A markedly different behaviour was found when the wavelength of the RF field approaches the dimensions of the object. For example, at 640 MHz ($\epsilon_r = 85$, $\sigma = 0$) the wavelength is now only 0.05 m and the numerical modelling showed standing wave behaviour in the 13.8 cm diameter cylinder with very complex and rapidly varying phase retardation patterns. It would be an interesting exercise to experimentally assess phase-shift mapping PRF-thermometry at higher field strengths, such as at 4T, though it is unlikely to be used for MR image-guided thermal therapy.

One important aspect to consider is the volume of the tissue to be heated and nature of the heating process. In this experiment, a large volume of material was *uniformly* heated in order to identify and understand the origin of the observed phase-shift offsets. However, in practice high-temperature thermal-coagulation therapies generally use small localized heating sources, such as laser fibres and interstitial microwave antennas. To briefly examine how the above effect manifests itself in cases of localized heating, a variety of radial temperature distributions were given to the material cylinder in the numerical model, as shown in Figure 5.3 (whereas previously a uniform temperature was used). These results are summarized in Figure 5.8. To generate these results, five representative radial temperature distributions were used: one distribution measured from a laser-fibre heating experiment and four distributions that were previously used in Chapter 4 (see Figure 5.8*a*). The phase retardation, $\Delta\psi$, that was numerically modelled from these five temperature distributions is shown in Figure 5.8*b* and are significantly smaller than any of the phase-difference profiles that were seen with the uniform-heating model in Figure 5.6*a*. As a result, the error in determining the temperature with PRF-shift thermometry, as defined by $\delta(\Delta T) = \Delta\psi/(\Delta\phi/\Delta T)$, is seen to be relatively insignificant even with a small TE setting of 6 ms, as shown in Figure 5.8*c*.

Thus, in general, the numerical modelling showed that phase retardation effects only posed significant uncertainties when large volumes were uniformly heated. While this is not believed to affect thermal-coagulation therapy in which smaller heating devices are used, phase retardation effects should be more prevalent in such regimes as hyperthermia. In conventional hyperthermia, very accurate and well-controlled temperatures (43 - 45°C) of relatively large volumes need to be maintained for prolonged periods of time.

As described in this report, phase lag or retardation of the B_1 field used in MR imaging can cause remnant phase variations in the object and lead to a confounding phase-shift offset in PRF-shift thermometry. The severity of this phase-retardation effect has been shown to be dependent on the material properties of the object, particularly the temperature dependence of the electrical conductivity. As such, phase retardation should be viewed as distinct from the coil-dependent phase variations that are described in the so-called "Principle of Reciprocity" [194–198]. This well-established theory simply states that if the same imaging coil is used in the transmit and receive mode then all coil-dependent non-uniform phase-variations, ie. transmit and receive phase-sensitivities, will cancel.

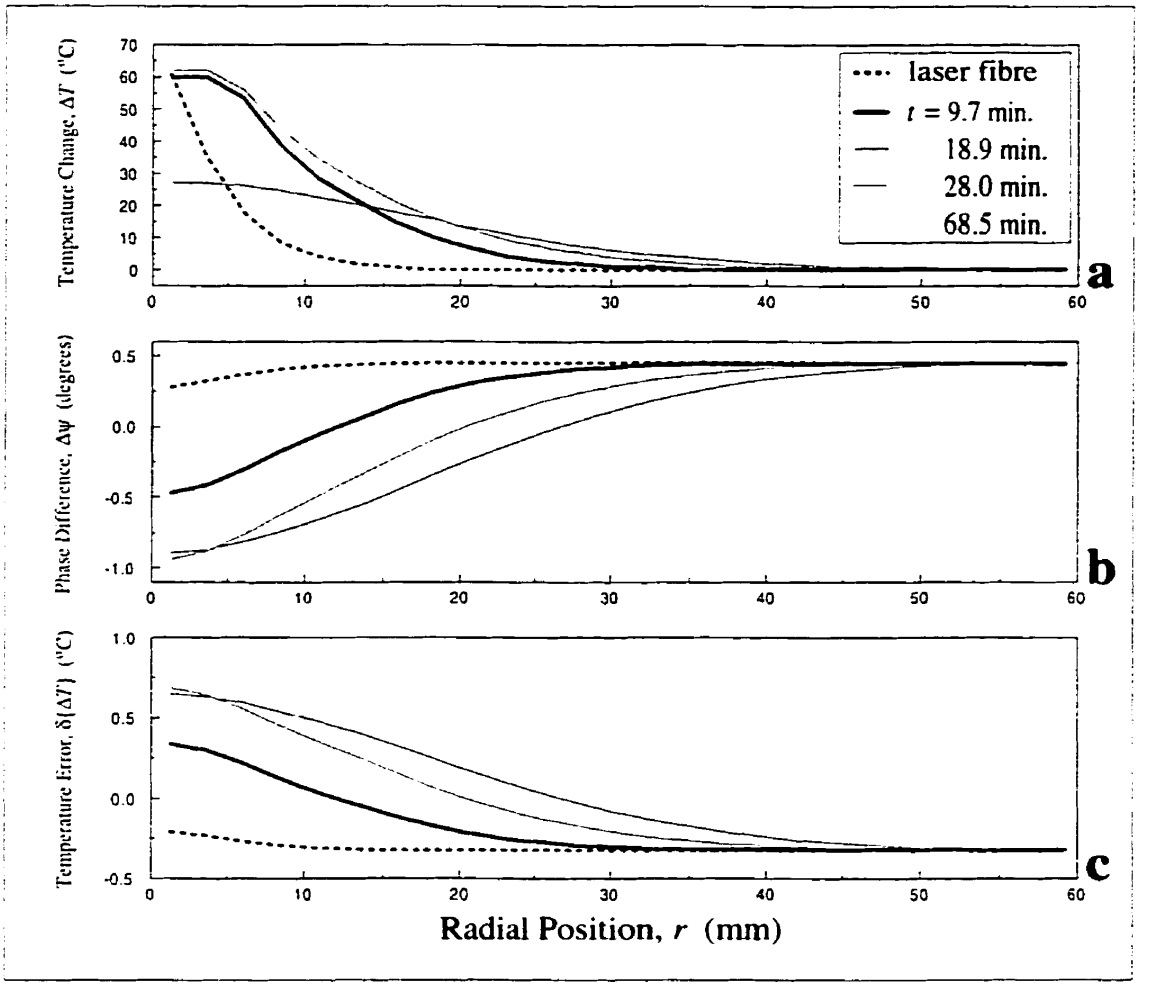

Figure 5.8: Numerically-modelled errors in the MR-derived temperature estimates from phase-retardation effects. Shown are (*a*) five representative radial temperature distributions given to the material cylinder in Figure 5.4, (*b*) the modelled phase retardation, and (*c*) the resultant error in temperature when using a *TE* setting of 6 ms. The radial temperature distributions in (*a*) represent four time points from the experiment described in Chapter 4.

5.6 Conclusion

In a PRF-thermal calibration experiment, a phase-shift offset was identified when monitoring temperature-induced phase shifts in PRF-shift thermometry when using $MnCl_2$ to eliminate ghosting artifacts from a heated circulating solution. This phase-shift offset manifests as a constant phase shift per unit change in temperature that is independent of the *TE*. In this chapter, it has been shown that thermally-induced changes in tissue electrical conductivity alter the phase retardation of the B_1 fields used in MR imaging and are likely responsible for the phase-shift offsets. Though easily correctable, if neglected such phase-shift offsets will give rise to incorrect temperature estimates which could affect the outcome of MR-image guided thermal therapy. It has been demonstrated that an MR-derived temperature error of as much as 28% could have resulted from an unaccounted phase-shift offset in a simple heating experiment of excised cow liver. Numerical modelling results indicate that the above effect will not be problematic for localized heating devices, which are primarily used for high-temperature thermal-coagulation therapy. However, significant errors in the MR-derived temperatures could result when uniformly heating large volumes of tissue, as in clinical hyperthermia. It is suggested that an understanding of this phenomenon may help to resolve the discrepancies in the PRF-thermal coefficient reported in the literature and allow for more accurate MR-derived temperatures.

Chapter 6

MR Thermometry for Predicting Thermal Damage: An Application of Interstitial Laser Coagulation in an *In Vivo* Canine Prostate Model

adapted from:
Robert D. Peters, Eric Chan, John Trachtenberg, Serge Jothy, Linda Kapusta, Walter Kucharczyk, and R. Mark Henkelman,
MR Thermometry for Predicting Thermal Damage: An Application of Interstitial Laser Coagulation in an *In Vivo* Canine Prostate Model.
accepted for publication in *Magnetic Resonance in Medicine* June, 2000.

6.1 Abstract

Magnetic resonance image guidance for interstitial thermal therapy has proven to be a valuable tool for device localization and, more recently, in monitoring heat deposition within tissue. However, a quantitative understanding of how temperature-time exposure relates to thermal damage is crucial if the predictive value of real-time MR thermal-monitoring is to be fully realized. Results are presented on interstitial laser coagulation of two canine prostate models which are shown to provide an opportunity to evaluate three models of thermal damage, based on a threshold maximum temperature, an Arrhenius damage integral, and a temperature-time product. These models were

compared to the resultant lesion margin as derived from post-treatment *T1*- and *T2*-weighted MR images, as well as from direct histological evaluation of the excised canine prostate. Histological evaluation shows that the thermal-injury boundary can be predicted from a threshold-maximum temperature of approximately 51°C or an equivalent Arrhenius t_{43} period of 200 minutes, but not reliably using the temperature-time product. The methods described in this study are expected to have implications for the treatment of benign prostatic hyperplasia and prostate cancer with interstitial laser coagulation, which will be the focus of future human studies.

6.2 Introduction

Magnetic resonance image guidance has recently brought much attention to the prospect of greater clinical acceptance of thermal-coagulation therapy as an alternative to conventional surgical resection [67, 177]. This is due, in part, to both the capability for high-resolution localization of the heat-delivery device and for the ability to render quantitative 3D maps of *in vivo* temperature during the thermal treatment [80, 94, 98, 113, 159, 178]. In this latter role, proton-resonance frequency (PRF) shift MR thermometry appears to be a promising method for thermal mapping largely because of its ease of use, linear behavior with temperature, and independence of tissue type [179].

The basic motivation for MR image-guided thermal therapy is that real-time thermal mapping during the treatment provides more control over the deposition of heat energy in the tissue. This helps to avoid excess heating of surrounding healthy tissue and to ensure sufficient treatment of the diseased tissue volume. While other indirect measures may correlate with the volume of thermal necrosis, such as the total output energy from a focused ultrasound transducer [96], such measures are generally not universal over the variety of interstitial heating methods and experimental conditions. Unfortunately, with such high-temperature coagulation therapy, where treatment times may range from a few seconds to several minutes with temperatures exceeding 80 - 90°C, the relationship between temperature and time and the actual thermal damage is not entirely well evaluated [199–201]. This particular deficiency places demands on thermal-mapping modalities, such as MRI, for predicting the treatment outcome during the course of thermal treatment.

One application of thermal therapy that is expected to have a large significance in health care management is in the treatment of benign prostatic hyperplasia (BPH) and prostate cancer.

The primary motivation for thermal therapy in the prostate is to avoid or reduce the side effects that can accompany the conventional treatments of radical prostatectomy and radiation therapy for prostate cancer and transurethral radical prostatectomy (TURP) for BPH. These side effects may include impotence, incontinence, and painful or difficult urination. In the prostate, interstitial laser coagulation (ILC) has been shown to be a simple method for delivery of heat energy [202–205]. Although ILC provides a mechanism for heat deposition, there remains the issue of thermal dosimetry that is necessary to provide physicians with operating guidelines, such as how long to heat the tissue and at what temperature for thermal coagulation to occur over the desired volume. At present, the choice of these guidelines can be quite subjective.

In this study, we report on an experiment involving ILC in an *in vivo* canine prostate model. Canine prostate has topographical features comparable to the human prostate, and this study represents a logical preliminary stage before designing human prostate protocols [206, 207]. One of the anticipated outcomes of this study was to determine whether quantitative MR-thermal mapping can provide a prediction of thermal damage in the prostate, providing useful operating parameters to conduct future human prostate studies. Thus, the primary objectives of this study were three-fold: (*i*) to characterize laser heating with PRF-shift thermometry in a simple gel-phantom model, (*ii*) to use MR-thermal mapping in the canine prostate over the course of an ILC treatment regime, and (*iii*) to use these results to examine the validity of thermal-damage models through an assessment of the resultant thermal lesions from post-treatment MR images and histology of the extracted canine prostate gland.

6.3 Methods & Materials

6.3.1 Laser System

A diode laser was employed in this study (Indigo 830e, Indigo Medical Inc., Cincinnati, OH) for both the gel-calibration experiments and the ILC of the *in vivo* canine prostate. The laser operates at a median wavelength of 830 nm and has been described previously [203]. A schematic of the applicator fibre is shown in Figure 6.1. The outer diameter of the temperature-resistant teflon sheath is 1.8 mm and the treatment region consists of a 10 mm long quartz-clad diffuser. The laser system also contained a temperature-sensing element that provided a feedback mechanism to regulate the output power level and maintain a constant target temperature at the laser tip, over

the duration of the treatment. To ensure sufficient fibre length, a 6 m extension fibre was used to allow for an overall fibre length of 10 m. The laser system used in this study was specially tuned to compensate for the losses from the extension fibre. The treatment and extension fibre entered the MR scanner room through a metal waveguide.

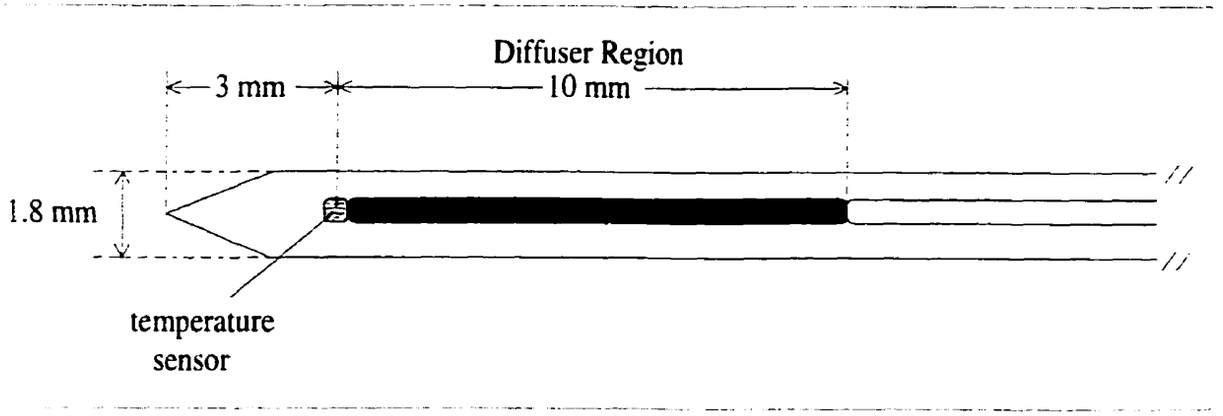

Figure 6.1: Schematic of the Indigo Diffuser-Tip^{TM} laser fibre used in the gel and canine prostate heating experiments. The fibre is enclosed in a teflon sheath approximately 1.8 mm in diameter and the treatment (diffuser) region is approximately 10 mm in length. The laser fibre employed in these experiments also contained a temperature-sensing element at the distal end.

6.3.2 Initial Characterization of Laser Heating in a Gel Phantom with PRF-Shift Thermometry

Experimental Design

Quantification of temperatures with the PRF-shift method of MR thermometry is dependent on several experimental factors including the geometry and orientation of the heat source, an effect originating from the temperature sensitivity of the volume-magnetic susceptibility [162, 164, 184]. Also, as the laser fibre is known to produce a relatively small cylindrically-shaped temperature distribution, a thick imaging slice may cause partial-volume averaging effects. For these reasons, we undertook some gel-phantom experiments to characterize the laser heating in a simple unperfused model system, prior to performing the canine studies.

The phantom consisted of a sphere filled with 2% agarose (Type I-A, Sigma Chemical Co., MO) with an evenly distributed 0.05% concentration of black ink (Black India, RapidoGraph, Bloomsbury, NJ) to increase the absorption of the laser energy [208]. This agarose concentration was found to liquify at temperatures between 85 and 90°C. As shown in Figure 6.2, the agarose

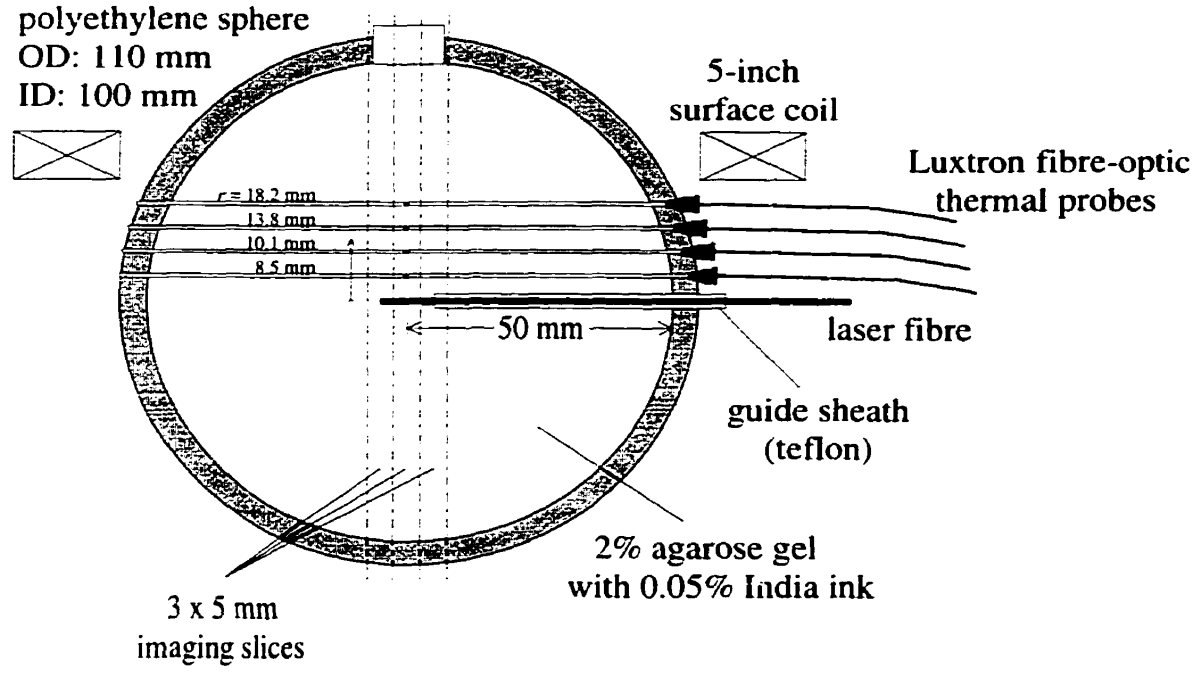

Figure 6.2: Geometry of the experimental apparatus. The phantom consisted of a polyethylene sphere containing 2% agarose gel, with a 0.05% concentration of black ink. Luxtron Fibre-optic thermal probes were inserted into the sphere to measure the gel temperature at the discrete radial distances shown. The phantom was placed in a 1.5 T whole body MR scanner and was oriented with the laser fibre either parallel or perpendicular to the direction of the main-magnetic field.

gel was moulded in the sphere containing guide sheaths for the laser fibre and Luxtron fibre-optic temperature probes (Luxtron 3100, Luxtron Corp., Santa Clara, CA). The Luxtron probes provided discrete temperature measurements at four radial distances from the laser fibre, centred on the 10 mm diffuser region, and allowed for calibration of the MR phase-shift with temperature. This arrangement was placed in a 1.5 T MRI system (Signa, GE Medical Systems, Milwaukee, WI) with the laser fibre oriented either parallel or perpendicular to the main-magnetic field, B_o. The gel sphere itself provided no preferred orientation with B_o. A 5-inch surface coil was used and the MR image scan planes are shown in Figure 6.2.

PRF-Shift Thermometry Pulse Sequence

The PRF-shift method of MR thermometry was used where temperature-dependent phase shifts were obtained from a gradient echo acquisition:

$$\Delta\phi = \alpha \cdot \frac{\gamma}{2\pi} \cdot B_o \cdot (360^o/cycle) \cdot TE \cdot \Delta T \tag{6.1}$$

where γ (= 42.58 MHz/T) is the gyromagnetic ratio for ^{1}H nuclei and α is the apparent PRF-thermal coefficient containing contributions from changes in the electron screening constant and the magnetic susceptibility [111, 112]. A spoiled-gradient recalled (SPGR) echo sequence was used to acquire three contiguous 5mm thick slices sequentially with the following settings: TE=30 ms, TR=50 ms, tip angle=30°, 256 × 128 image matrix for an acquisition period of 6.6 seconds per slice (19.9 seconds for all three slices as indicated in Figure 6.3). Phase-reference maps for each slice were constructed by averaging ten images acquired prior to heating. Phase-difference images were constructed using a complex phase-subtraction technique, as described in Chapter 3 [179] and phase drifts were corrected using a three-point (planar) method, using the phase signal in thermally isolated reference phantoms. As discussed in Chapter 5, in some experimental conditions

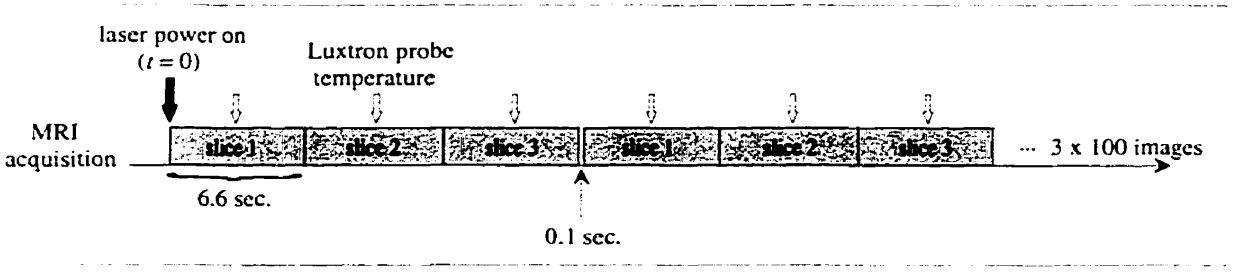

Figure 6.3: Image acquisition sequence for the MR-thermal mapping. Three 5 mm-thick slices were acquired sequentially as indicated to cover 15 mm of the phantom or prostate gland. Prior to laser heating, ten baseline images were acquired. Luxtron and laser-tip temperature measurements were extracted at the center of each of the MR image acquisition periods (6.6 sec.). With this acquisition sequence, each of the three slices was updated every 19.9 sec.

the temperature-induced phase shift may not scale with the TE setting, as suggested in Equation 6.1 [209]. This effect is caused by variations with depth of the phase of the RF B_1 field that originates from temperature-induced changes in the electrical conductivity of tissue and occurs primarily when relatively large volumes are uniformly heated. However, numerical modelling of this effect and gel-phantom experiments have shown this phenomenon to be insignificant when using a moderately long TE setting (30 ms) with small localized heating devices, such as the

interstitial laser fibres used in this study (Chapter 5, Figure 8).

PRF-Shift Calibration and Orientation Dependence

With the laser fibre in the parallel orientation, a calibration was made of the phase shift as a function of temperature, as measured from the Luxtron thermal probes. A linear fit was made to determine the PRF-thermal coefficient for this particular experimental setup. This calibration experiment was repeated using a 10 mm slice thickness centred on the laser fibre. The thicker slice thickness was expected to result in an apparently lower PRF-thermal coefficient due to averaging of the temperature distribution over the wider slice.

As the treatment region of the laser fibre is less than 2 mm in diameter and 10 mm in length, it essentially constitutes as a cylindrically-shaped heat source. As such, the laser fibre will possess an orientation dependence with PRF-shift thermometry, as demonstrated in Chapter 4 [184]. To examine the severity of potential errors in the MR-derived thermal maps, the gel-phantom calibration experiment was repeated with the laser fibre oriented perpendicular to the main-magnetic field.

MR-Temperature Profiles of the Laser Heating in Gel

In an additional series of gel-phantom experiments, MR-thermal maps were acquired of laser heating in the plane of the laser fibre, whereas the previous calibration and orientation experiments used axial images. Using the same SPGR pulse sequence, a 2 mm thick slice was used to reveal the axial temperature distribution of the laser fibre.

This experiment also allowed an opportunity to directly compare the MR-derived temperatures with the temperatures as measured from the laser fibre. As described in Figure 6.1 the temperature sensing element is located approximately 3 mm from the tip of the fibre and could not properly be compared with the axial MR-thermal maps with a 5 mm slice thickness (as in Figure 6.2). In previous experiments, that are not shown here, it was noted that there was considerable discrepancy between the laser-tip temperature readings and the temperatures immediately in the vicinity of the laser fibre tip, as determined by the MR-thermal maps. One belief is that the laser-tip reading is measuring some internal heat building up within the fibre. In this brief experiment, two laser-fibre models were examined: a conventional fibre that is currently sold commercially for treating BPH and a fibre that reportedly has less "self heating", which is being developed by Indigo

Medical Inc. The following canine prostate study was carried out using the conventional laser fibre.

6.3.3 ILC Application in an *In Vivo* Canine Prostate Model

General Overview of Study

Two male Labrador dogs weighing 28 and 32 kg were used in this investigation of interstitial laser coagulation in an *in vivo* prostate model. The animals were between 5 and 6 years of age and were cared for according to the Canadian Council for Animal Care Guidelines. Protocol approval was obtained from the local animal care committee at our institution (S&WCHSC).

Surgical Placement of Fibres

The dogs were initially sedated with a cocktail of acetylbromazine and atrophine. Anesthesia was later induced and maintained with halothane, at which time the dog was intubated and laid on a surgical table. The lower abdomen was shaved in preparation for the surgical placement of the laser and Luxtron fibre-optic thermal probes. During laparotomy, two sterile laser fibres were inserted approximately 25 mm into the right and left sides of the prostate gland at the superior-anterior surface (see Figure 6.4). The prostate glands of the two dogs were approximately 3.5 and 4.5 cm diameter. Care was taken to ensure that the laser fibres were oriented parallel with the long axis of the body which would be aligned with the main-magnetic field. Three or four Luxtron thermal probes were inserted into the prostate, approximately 5 to 10 mm away from and parallel to the laser fibres. A small sterile teflon holding device was fastened to the prostate and bladder with sutures to keep the laser and Luxtron fibres from being pulled out of the prostate. Upon completion of the placements of all fibres, a two-layer closure was made to facilitate a 24-hour recovery period following the application of the thermal lesions.

MR Localization, ILC Application, and Post-Treatment Imaging

At the MRI unit, the dog was placed supine in a specially-designed plexi-glass cradle and positioned feet first into the magnet, allowing for easier physiologic monitoring and intravenous access. A 5-inch surface coil was placed on the lower abdomen, centred on the prostate gland with a small gel-filled container in the centre of the coil to provide a reference MR signal for phase-shift thermometry. Prior to application of the laser heating, localizer images were acquired with a 3D-SPGR sequence (TE=15ms, TR=50ms, tip angle=30^o, 2 mm slice thickness) to determine the locations of the

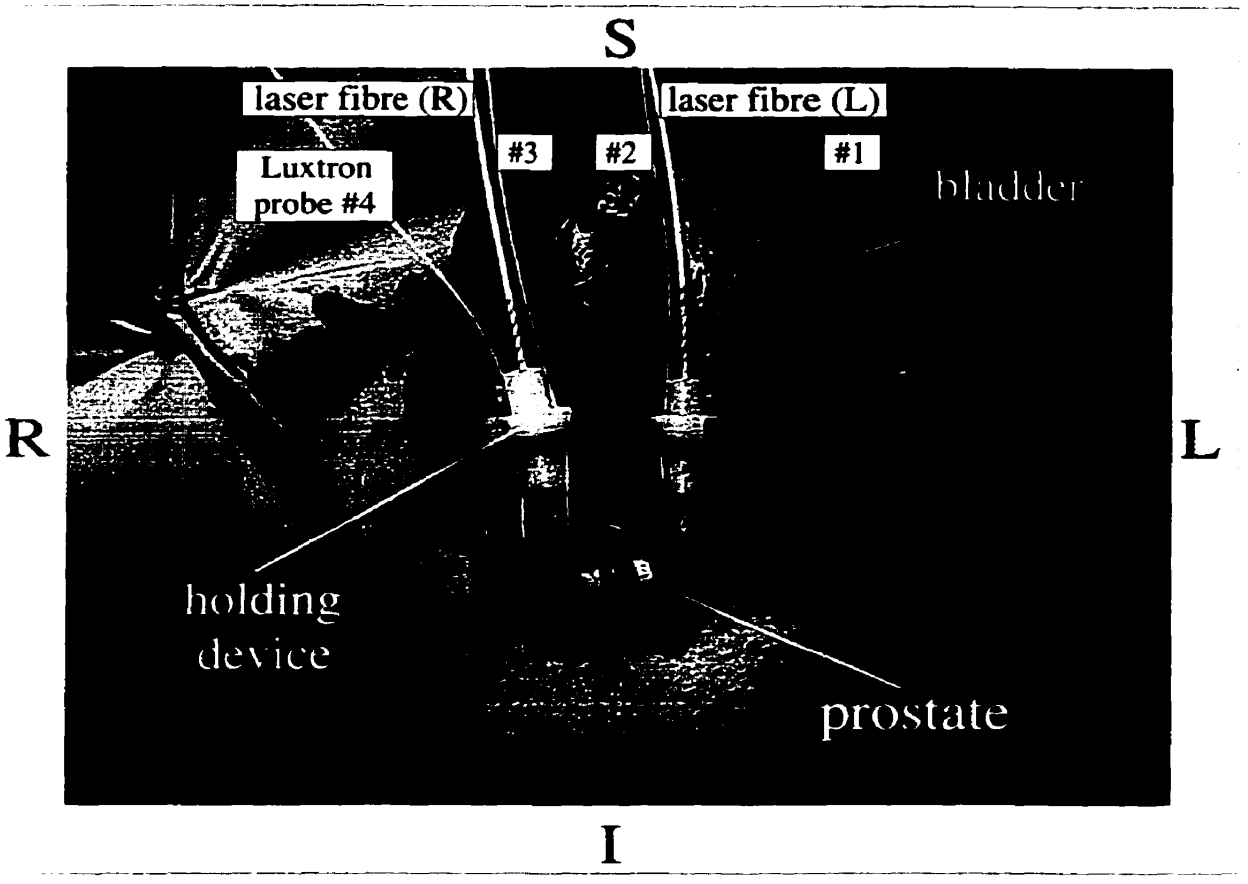

Figure 6.4: Surgical placement of the laser fibres within the canine prostate. Shown are the laser and Luxtron fibres for one of the canine studies. A teflon holding device is indicated which held the fibres firmly in place and was sutured to the bladder.

laser fibres within the prostate and to choose the position of the three 5 mm slices for the MR-thermal mapping. With the laser fibres positioned approximately parallel with the main-magnetic field, axial images were obtained with a field-of-view (FOV) of 160 mm. The frequency-encoding direction was chosen along the right-left direction to keep motion artifacts, originating from blood flow in the femoral vessels, from overlapping onto the prostate.

The two animals provided a total of four ILC applications from which a complete series of MR-thermal maps were obtained using the SPGR pulse sequence used in the gel-phantom experiments. A standard laser setting (3 min., Target T=85°C, 15 W) was used on two of the four lesions, with slight variations of this setting on the two remaining applications. This standard setting was based on a preset treatment protocol, developed specially with the Indigo laser system, that has been clinically demonstrated to be effective for the treatment of BPH [210,211]. Power was supplied

to only one laser fibre at a time. Thus for each ILC application, at least ten baseline images were obtained along with between 30 and 90 subsequent images during the heating and cooling periods. MR imaging was terminated once the entire prostate was restored to a uniform body temperature for at least five minutes. MR-thermal maps from the central 5 mm imaging slice were generated and displayed on a Sun SPARC Workstation (Sun Microsystems, Mountain View, CA) during each ILC application.

After laser heating, post-treatment images were obtained to assess the resultant thermal-coagulation volume. Approximately one hour after the laser heating, *T1*-weighted (*T1*-w: 2D spin echo, TE=20ms, TR=500ms with flow compensation) and *T2*-weighted (*T2*-w: 2D fast spin echo, TE=85ms with respiratory triggering and flow compensation) images were acquired, before and after a single-dose injection of gadodiamide (0.2 ml/kg, Omniscan, Nycomed Inc., Princeton, NJ). A second post-treatment series was obtained after a survival period of 24 hours for one of the canine studies.

Histological Examination of Thermal Damage

From the two canine studies, a four hour and 24-hour survival period was used for a host response to become manifest following the ILC. The animals were sacrificed with 20 ml of euthanyl and the prostate glands were removed *in toto* for histological examination. Each prostate was fixed in 10% buffered formalin for a minimum of 6 weeks and then axial distributed 3mm serial sections were cut. Tissue slices were then cut at 6μm for histology. The sections were whole mounted on 2-inch slides then stained with hematoxylin and eosin (H&E). Prior to sectioning, a 3D-SPGR image set was acquired of the fixed prostates to aid in choosing the correct section for comparison with the MR-thermal maps and post-treatment MR images.

Thermal-Damage Assessment from MR-Thermal Maps

MR-thermal maps were constructed from the phase-difference images using the PRF-thermal coefficient as measured in the gel-phantom experiments (parallel orientation). The thermal maps contain noise, originating from phase noise in the gradient-echo images which is inversely proportional to the magnitude signal-to-noise ratio (SNR) [176]. In the present experimental arrangement, the temperature noise level in the MR-thermal maps was approximately 2^{o}C, which was judged to be excessive and not amenable for subsequent analysis involving modelling of the onset of thermal

coagulation. Following the approach laid out in [199], the MR-thermal maps were masked to remove air and other non-relevant regions and spatially-Weiner filtered. The average Weiner-filter bandwidth was approximately 0.18 pixels^{-1} so that the spatial resolution was degraded to 3.5 mm from an initial pixel size of 0.6 mm. The temperature noise level after filtering was less than 0.5°C.

Three models of thermal damage were assessed using the available thermal data from the four ILC applications in the canine prostate. The first was based on a straight-forward critical temperature model. It was postulated that thermal-damage processes [17], such as thermal coagulation, occur rapidly over a narrow temperature range. With this model, thermal damage occurs if tissue exceeds a threshold temperature, with no damage below the threshold limit.

A second model included the effect of treatment time and was based on the Arrhenius-damage integral, which is a widely used model in conventional hyperthermia [47]. This model quantifies damage using temperature and time in a non-linear fashion and one way to express the damage integral is in the equivalent heating time at 43°C. In this analysis, the model took the form:

$$t_{43} = \sum_i K^{T_i - 43^\circ C} \Delta t \tag{6.2}$$

where T_i is the temperature (of each pixel) for image i, Δt is the time interval between adjacent thermal maps, and K has been determined to be approximately equal to 2 for temperatures above 43°C and equal to 4 for temperatures below 43°C. The summation in Equation 6.2 occurs over the entire available MR-thermal data set, which extended until the entire prostate was back to uniform-body temperature. Although all of the ILC applications were less than 5 minutes in duration, the above summation included between 30 and 90 MR-thermal maps which were acquired over a period of 10 to 30 minutes, respectively. The above calculation does not include the development of thermotolerance that is used with "step down heating" [47].

The third model treats both time and temperature exposure in a linear fashion, and consists of a temperature-time product (TTP):

$$TTP = \sum_i \Delta T_i \cdot \Delta t \tag{6.3}$$

where ΔT_i is the temperature elevation from baseline-body temperature (37 – 38°C) for image i. This hybrid model was explored primarily for its simplicity and because thermal treatments are often prescribed in the form of a target temperature and a duration, however it has been suggested

to be of little clinical value

In order to assess the three thermal-damage models, an indicator of the onset of thermal-coagulation was necessary. One indicator was provided by the thermal-lesion margins as seen in the post-treatment *T1*- and *T2*-weighted images. The second indicator came from the direct histological evidence, which was regarded as the only true margin of thermal damage. After digitizing and scaling the histological sections, the post-treatment and histology maps were registered to the Weiner-filtered MR-thermal maps via 2D translation and rotation. The thermal lesion margins were manually traced and used to assess the three thermal-damage model's ability to classify an isoeffect. For each ILC application, optimum model values were generated (eg. maximum T, t_{43}, and TTP) for each of the thermal-lesion margins (*T1*- and *T2*-weighted images and histology). The presence or lack of consistency in these results would indicate the predictability confidence of each model.

6.4 Results

6.4.1 PRF-Shift Thermometry Characterization of Laser Heating in a Gel Phantom

Annular regions-of-interest (ROIs) used in the phase-shift thermal calibration experiment are shown in representative magnitude and phase-difference images in Figure 6.5. Temperature-induced phase shifts at the four radial positions within the gel phantom are plotted in Figure 6.6 as a function of the temperature change, as measured by the Luxtron fibre-optic probes in the corresponding radial positions. The phase-shift measurements were extracted using annular regions-of-interest (ROI) at the four positions. At all four radial positions, there was good linear behavior between the phase shift and temperature change during both the heating and cooling portions of the experiment. A single thermal coefficient of -7.2 ± 0.1 (sd) °/°C was derived from the data of all four radii, and is shown as a straight line in Figure 6.6. With the TE setting of 30 ms, this corresponds to a spatially-independent PRF-shift thermal coefficient of -0.0104 ± 0.0001 (sd) ppm/°C for this particular experimental arrangement.

When the above calibration experiment was repeated using a single 10 mm slice thickness, a similar linear behavior was observed at all four radial positions. However, unlike the experiments performed with the 5 mm slice thickness, these phase-shift measurements had evidence of volume

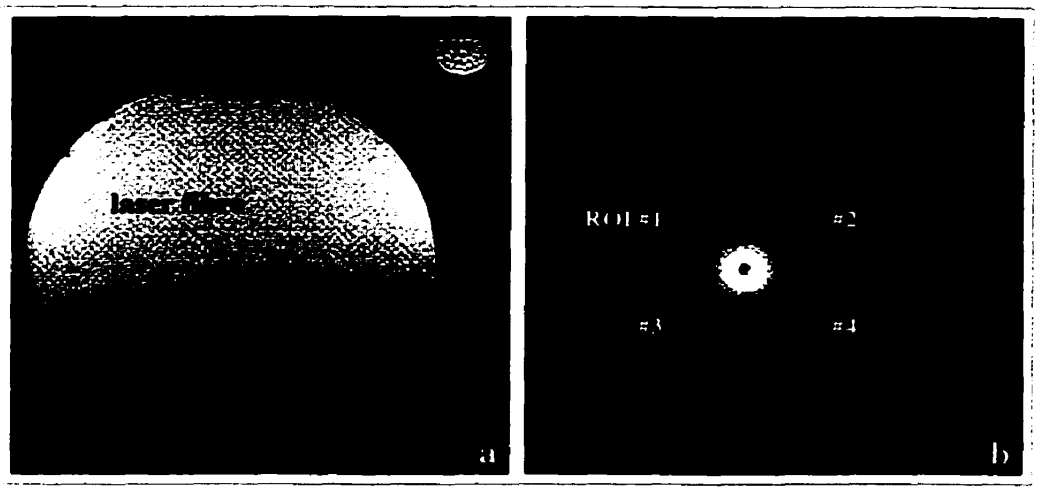

Figure 6.5: Magnitude and phase-difference images of the gel phantom. (*a*) The magnitude image at a uniform baseline temperature shows the relative positions of the laser fibre and the four Luxtron fibre-optic probes in a scan plane perpendicular to the laser fibre. (*b*) The phase-difference image indicates four annular ROIs that were used in the calibration. The measured radii of the Luxtron probes were 8.5, 10.1, 13.8, and 18.2 mm for probes 1 to 4, respectively.

averaging as there was a markedly different temporal response compared to the Luxtron thermal probe measurements. Such volume averaging is expected to occur as the slice thickness approaches the length of the diffuser region and thus the axial temperature distribution. While it was acknowledged that this experiment would not supply a meaningful PRF-thermal calibration, the data did allow for a reasonable linear fit that gave an apparent PRF-thermal coefficient of -0.0084 $\pm$ 0.0001 ppm/^{o}C. Ideally, the actual temperature distribution from the laser fibre will be most accurately determined with a thin slice thickness. A 5 mm slice centred on the diffuser region was considered an acceptable tradeoff with the canine studies.

6.4.2 Laser-Orientation Dependence in PRF-Shift Thermometry

The phase-difference images in Figure 6.7 demonstrate the effect of laser fibre orientation in PRF-shift thermometry. Shown are two phase-shift images of the gel phantom with the laser fibre oriented parallel (Figure 6.7*a*) and perpendicular (Figure 6.7*b*) to the main-magnetic field, after an equivalent duration of heating (90 sec.) and using a 5 mm slice thickness. While the image with the parallel orientation shows a circular, radially-symmetric phase-shift pattern, the image with the perpendicular orientation displays some noticeable eccentricity. Using the PRF-thermal coefficient of -0.0104 ppm/^{o}C, temperature profiles were obtained from the rectangular ROI's placed along the

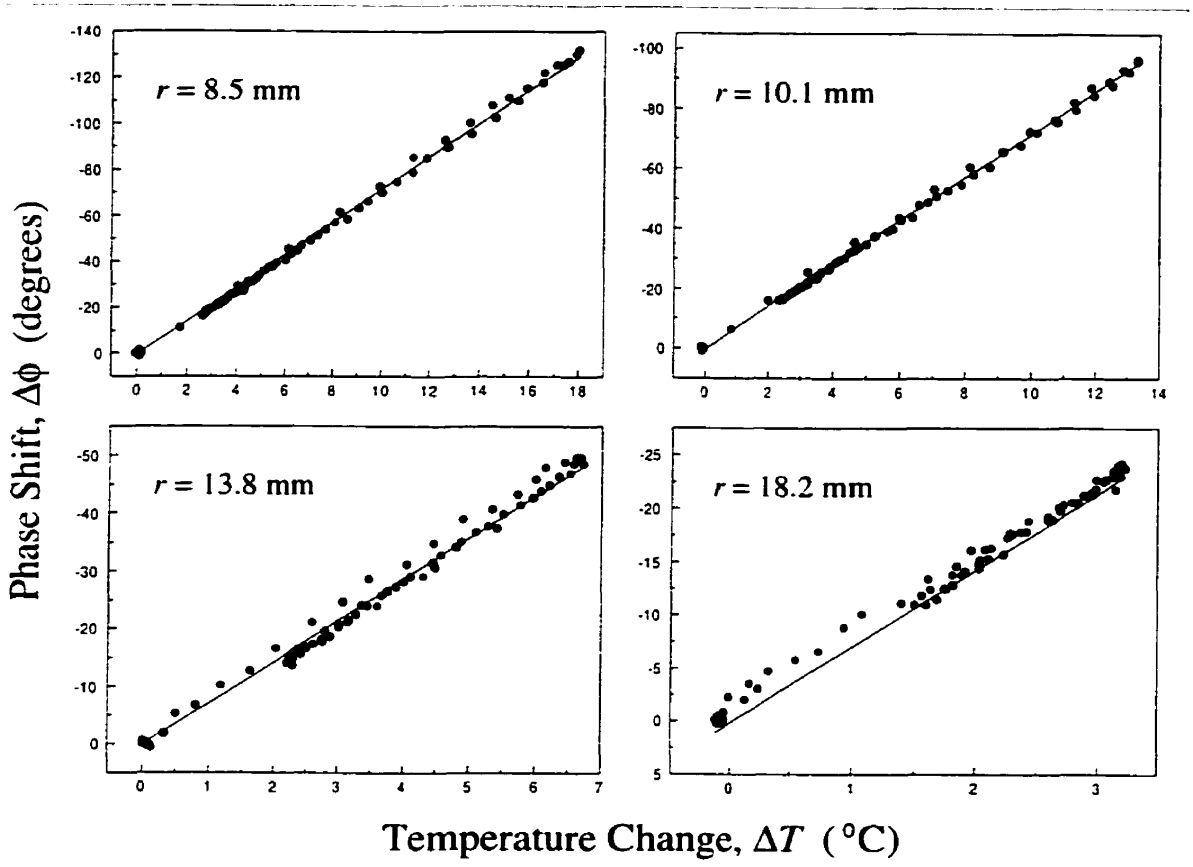

Figure 6.6: Phase shift ($\Delta\phi$) as a function of temperature change (ΔT) at four radial positions in the gel phantom. The straight line represents the derived average thermal coefficient of -7.18°/°C (-0.0104 ppm/°C). In this experiment, the laser fibre was oriented parallel to the main-magnetic field.

x-, y-, and z-directions (with z along the direction of the main-magnetic field). The temperature profiles were then subtracted from each other, yielding a measure of the temperature error due to eccentricity in the phase-shift patterns. The plot in Figure 6.7*c* and *e* confirms a radially-symmetric temperature distribution, with deviations of no more than ±1°C in the temperature-difference profile, resulting from random noise. Significant differences in the temperature profiles along the x- and z-directions are readily seen in Figure 6.7*d*, leading to discrepancies as large as 4°C as shown in Figure 6.7*f*. These findings show that at this point in the heating experiment, regions that were 5 mm from the laser fibre and in the direction of B_o had temperatures underestimated by approximately 2°C, and regions at right angles to B_o had temperatures overestimated by 2°C. To avoid this spatially-structured temperature error, the *in vivo* canine studies were performed with

the laser fibres oriented as parallel to B_o as possible.

6.4.3 MR-Temperature Profiles of the Laser Heating in Gel and Comparison with the Laser-Tip Temperature

A representative MR-thermal map of the relative heating pattern from the laser fibre is shown in Figure 6.8. Temperature profiles transverse and along the length of the fibre are shown in Figure 6.9. Generally, the laser fibre exhibits a relatively flat heating profile approximately 7–8 mm in length and centered on the diffuser region, as indicated in Figure 6.9 for both fibre versions. The transverse temperature profiles are similar to that shown in Figure 6.7*c*.

The temperature profiles in Figure 6.9 were obtained after approximately 96 seconds of laser heating within the gel and are compared with the laser-tip temperature reading, located at the $r = 0$ position. Notice that there is considerable discrepancy between the laser-tip reading and the transverse temperature profile in Figure 6.9*a*, with the laser-tip reading approximately 30°C *higher* than the MR-estimated temperature near the $r = 0$ position. There is markedly less discrepancy in Figure 6.9*b* with the low "self-heating" fibre. The results in Figure 6.9*a* are typical of all of the gel experiments that were undertaken. It is also noted that this discrepancy is only observed while the laser fibre is actively heating and once power is terminated to the fibre, the laser-tip temperature reading agrees with the MR-temperatures within temperature noise level of the images.

6.4.4 MR-Thermal Mapping of Laser Coagulation in the Canine Prostate Model

The pre-treatment multislice SPGR images provided an excellent visualization and localization of the laser and Luxtron fibres within the prostate gland as shown in Figure 6.10. With 2 mm slice thicknesses, it was possible to determine the distal tip of the laser fibre within ±1 mm in the axial images. The central of the three 5 mm slices for MR thermometry was chosen to be 8 mm from the distal tip of the laser fibre which corresponded to the middle of the diffuser region. Additionally, this pre-treatment image set allowed the angle the laser fibres made with the main-magnetic field to be determined. The laser fibres were oriented at 21° and 26° in one dog and 31° and 20° in the second dog. Although care was taken to keep the fibres parallel with the long axis of the body during the surgical placements, there was obviously some settling and rotation of the prostate within the abdomen upon surgical closure of the laparotomy. With these angles, the associated temperature error was estimated to be no larger than 0.5°C, which was approximately a

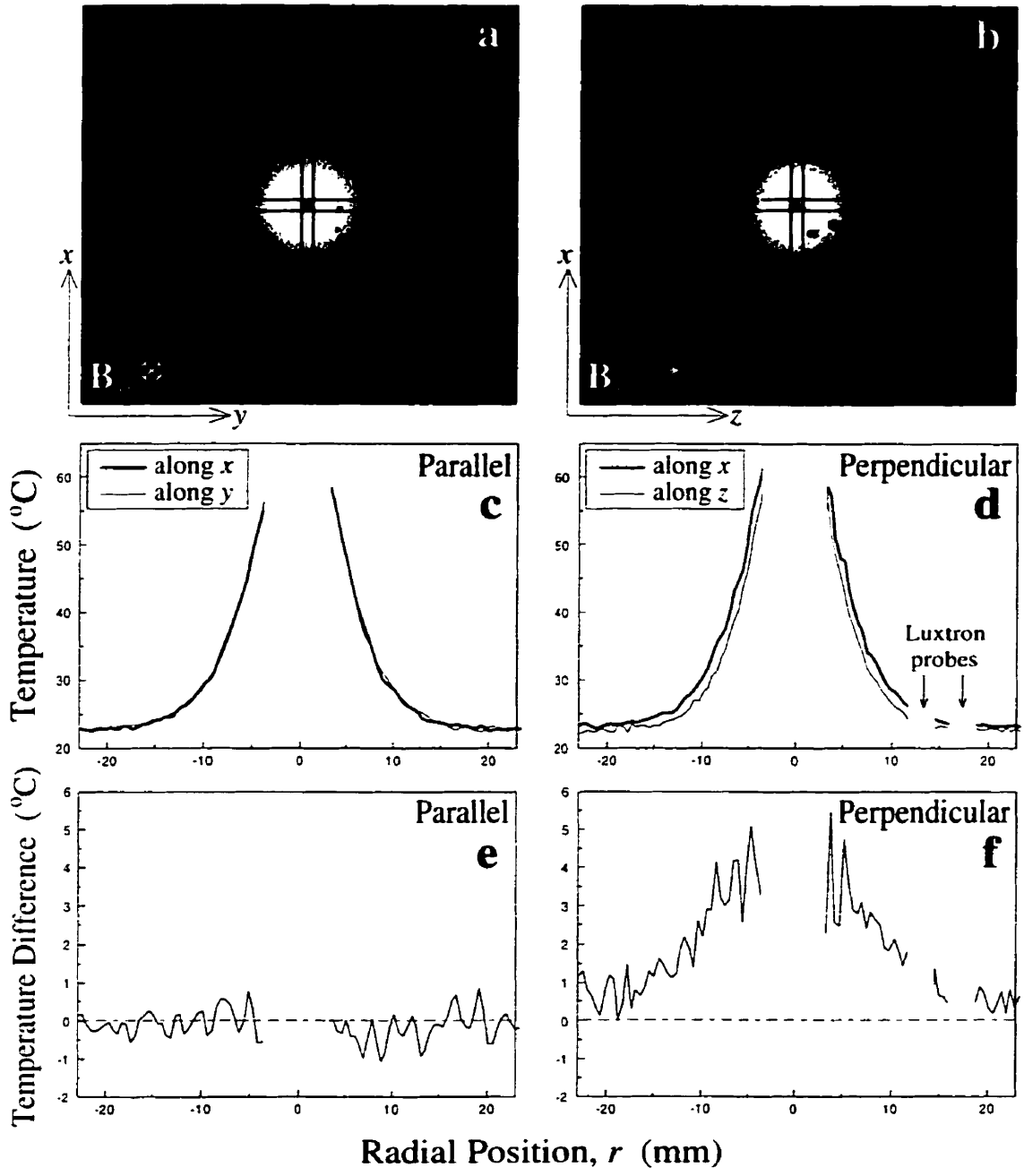

Figure 6.7: Orientation dependence of the laser fibre in PRF-shift thermometry. Shown are phase-difference images of the gel phantom with the laser fibre oriented (a) parallel and (b) perpendicular to the main-magnetic field, B_o. Also shown are (c,d) temperature profiles and (e,f) profiles of the temperature difference between the two directions. The above data was obtained after 90 seconds of heating with the laser fibre and the profiles in (c,d,e, and f) were averaged from ROI's that were 11 pixels (5.2 mm) in width which were carefully centred about the axis of the laser fibre. The region in the vicinity of the laser fibre (-4 mm $< r <$ 4 mm) was not considered reliable for phase-shift measurements due to local susceptibility artifacts

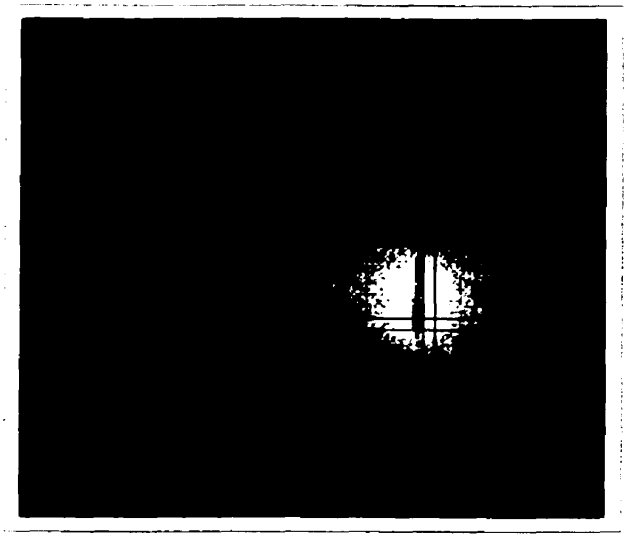

Figure 6.8: MR-thermal map of a gel phantom during laser heating. The thermal map was constructed from a 2 mm thick slice in the plane of and centered on the laser fibre. The laser fibre was oriented parallel to the direction of the main-magnetic field. Two ROIs are indicated that were used to extract temperature profiles transverse and along the length of the fibre. The thermal map was windowed and levelled to 30° and 25°C, respectively.

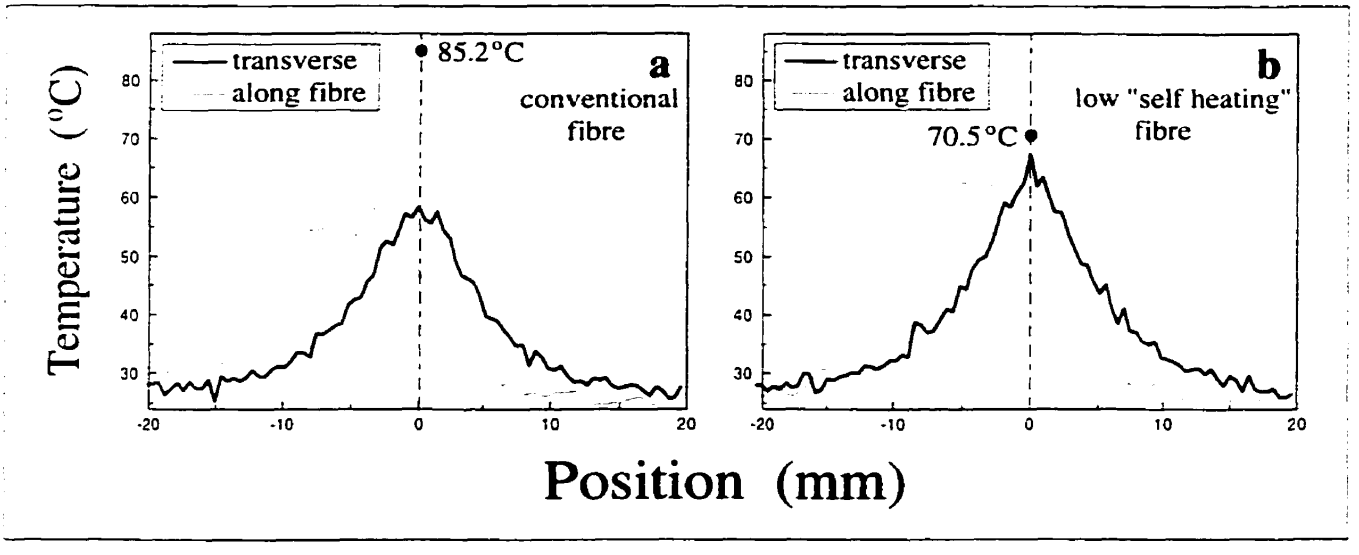

Figure 6.9: MR-derived temperature profiles of laser heating in a gel phantom. Shown are temperature profiles transverse and along the length of the laser fibre for (*a*) a conventional fibre and (*b*) low "self-heating" fibre. The symbol indicates the laser-tip temperature reading. The transverse profiles were obtained from an ROI passing through the center of the temperature sensing element and the temperature profiles along the fibre were obtained 2 mm from the edge of the laser fibre. All temperature profiles were averaged from a width of 3.3 mm.

quarter of the maximum error found in the gel-phantom experiments with the laser fibre oriented perpendicular (90°) to B_o. Consequently, non-radial phase-shift patterns were expected to reflect the true temperature distribution, which would be modified by anisotropic heat conduction and blood-flow cooling in the prostate.

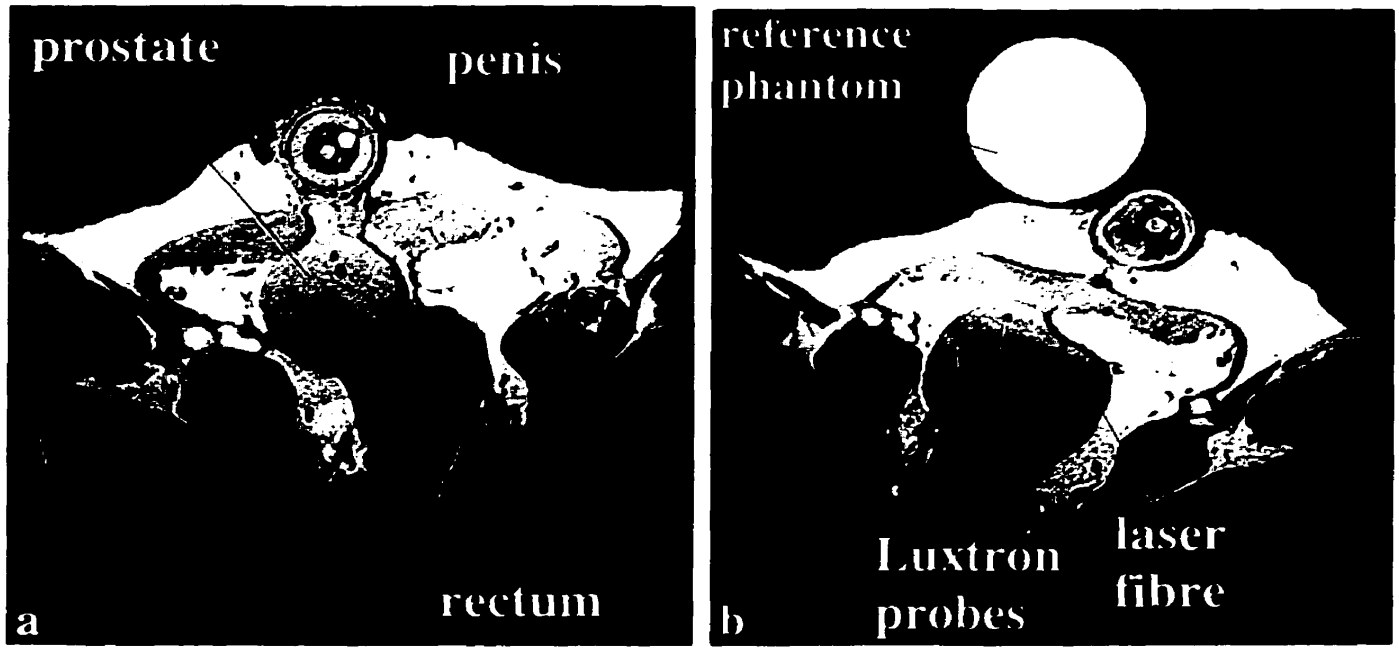

Figure 6.10: Pre-treatment localizer images from the two canine studies. The two laser fibres and Luxtron fibre-optic thermal probes were easily seen in the axial SPGR images within the canine prostate gland. Some motion artifacts are seen in the vertical direction in (*b*) due to respiratory motion and blood flow in the femoral vessels. The FOV is 160 mm.

The *T2** of the prostate tissue was also estimated in the pre-treatment images and was intended to choose the optimal *TE* setting for the PRF-shift thermometry [160]. In the two dog studies, the *T2** was estimated to be approximately 47 ms. However, prior experience from gel studies suggested that a *TE* setting this large would give rise to phase-wrapping artifacts due to excessive temperatures, as suggested in Equation 6.1 Instead, lower *TE* settings of either 20 ms or 30 ms were used in the PRF-shift thermometry pulse sequence. Pre-treatment SPGR images acquired with varying tip angles, keeping the *TR* fixed at 50 ms, also showed that optimal SNR in the prostate occurred with a tip angle of 30°.

The laser-fibre tip and Luxtron probes provided additional and independent measures of temperature within the prostate gland during laser heating. Although they were sparse, such measurements are usually used in human prostate treatments as they are considered to be accurate.

However, the temperature measurements shown in Figure 6.11 indicate an interaction between the laser and the Luxtron thermal probe readings. It was observed that on initial application of laser energy, the Luxtron temperature readings increased rapidly, especially when probes were within 6 - 7 mm of the laser fibre. Similar artifacts were observed in the gel-phantom experiments, Luxtron measurements with obvious errors were dismissed from the calibration data. The preliminary gel-phantom heating experiments also cast some doubt on the accuracy of the laser-tip temperature readings. In some instances, the laser-tip reading was as much as 20°C larger than temperatures in the vicinity of the fibre tip, as estimated in the MR-thermal maps. This is believed to be a result of internal self heating of the laser fibre. Fluctuations in the Luxtron readings (Figure 6.11*a*) correlate well with the variations in the laser power levels (Figure 6.11*c*), which operated in a feedback mode to regulate the temperature as measured on the fibre tip (Figure 6.11*b*). There are two possible explanations for this observed effect. First, some of the laser wavelength (median of 830 nm) may fall within the emission spectrum of the Luxtron probe's temperature-sensitive phosphor (magnesium fluorogermanate). This could cause an underestimation of the temperature-dependent fluorescent decay time constant and results in an overestimation of temperature. The greater the amplitude of the overlapping wavelength, the larger the artifact in the Luxtron temperature reading. Another possible explanation is that the black membrane covering the temperature-sensitive phosphor at the tip of the Luxtron probe is selectively absorbing the laser energy, thus causing preferential heating of the Luxtron probe. As the optical penetration depth in prostatic tissue for 850 nm wavelength light is approximately 3 mm, there could still be a significant amount of laser light at 2 - 3 optical depths [212]. Consistent with both explanations for interaction between the laser fibre and Luxtron thermal probes, artifacts were observed primarily when laser power levels were high or when Luxtron probes were close to the laser fibre. The laser settings and other useful information from the four ILC applications are shown in Table 6.1.

Some MR-thermal maps in the canine prostate gland are shown in Figure 6.12. The thermal maps clearly show the evolution of a non-radial temperature distribution within the prostate tissue that eventually disperses once laser power is terminated. In these unfiltered thermal maps, the standard deviation of temperature in the unheated region of the prostate was less than 1.5°C. Some spurious signals are seen in the thermal maps outside of the prostate and likely corresponded to phase artifacts from small motions in the abdomen.

One interesting observation that is evident from the thermal maps during the ILC appli-

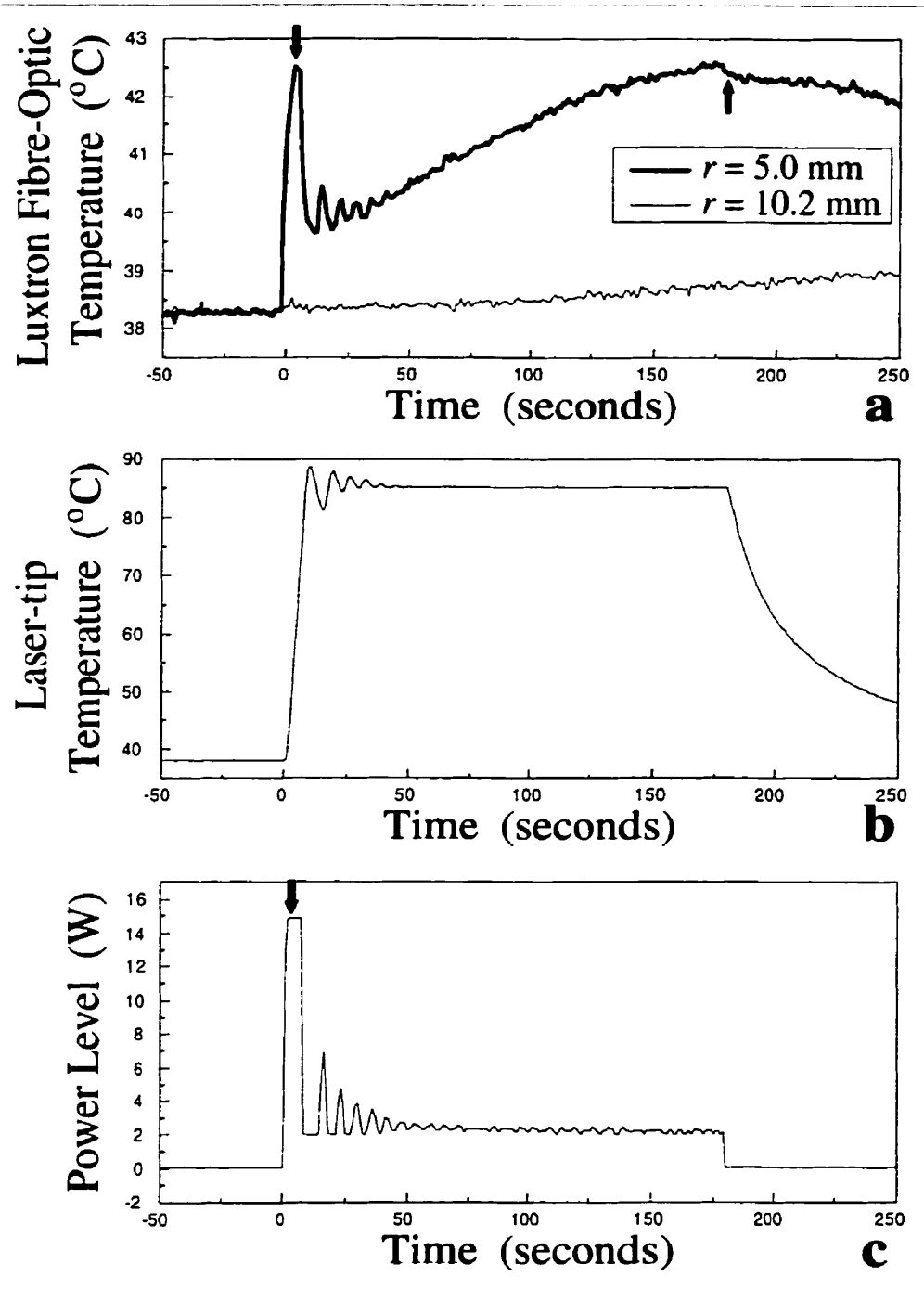

Figure 6.11: Representative Luxtron probe temperatures, laser-tip temperatures, and laser power levels during an ILC application in the canine prostate. Shown are the (*a*) Luxtron fibre-optic temperature at two radial positions relative to the laser fibre, (*b*) laser-tip temperature, and (*c*) laser power level for a three-minute heating duration. Measurement artifacts are seen in the Luxtron probe readings which correspond to fluctuations in the laser power level.

Table 6.1: Laser settings and resultant lesion volumes from the four ILC applications. The initial power level is shown as well as the total integrated energy delivered during the treatment. The lesion volume was measured from 3D images of the formalin-fixed prostate specimens and the maximum area is shown as measured from one of the 3 mm-thick slices. The uncertainties were estimated from repeat measurements.

	Lesion	Laser Setting	Total Energy (J)	Lesion Volume (cm^3)	Maximum Area (mm^2)
canine 1	1	3 min., 85°C, 15W	449	1.2 ± 0.3	79 ± 16
	2	5 min., 85°C, 10W	707	1.8 ± 0.1	112 ± 4
canine 2	3	3 min., 85°C, 15W	510	2.2 ± 0.2	117 ± 7
	4	4 min., 95°C, 15W	751	2.6 ± 0.6	127 ± 22

cations (Figure 6.12) is that the temperature distribution within the prostate gland terminates sharply at the prostatic capsule. One plausible explanation for this is that blood flow in the venous plexus, which forms the prostatic capsule, is simply cooling the prostatic tissue and thus providing a boundary condition on the temperature distribution. However, we acknowledge that this particular observation in these MR-thermal maps may, in fact, be artificial. The reason for this, is that the tissue immediately surrounding the prostate gland is fat, which has a PRF-thermal coefficient that is negligible compared to the water-containing prostatic tissue [164]. Consequently, even if this surrounding fat was heated, it may give a negligible phase shift and hence not appear as a temperature elevation in the MR-thermal maps. As there was no intentional or direct heating of the fat tissue, it is unclear which of the two explanations is the correct one. This effect, which appears usually at tissue interfaces, will likely be a point of future contention with PRF-shift thermometry.

6.4.5 Post-Treatment MR Images

The post-treatment images showed a lesion margin encircling the laser fibres (see Figure 6.13). With Gd-contrast enhancement, all lesions appeared hypointense in both the *T1*- and *T2*-weighted images. The images were registered with the MR-thermal maps and the lesion margins were manually traced for subsequent analysis of the thermal-damage models.

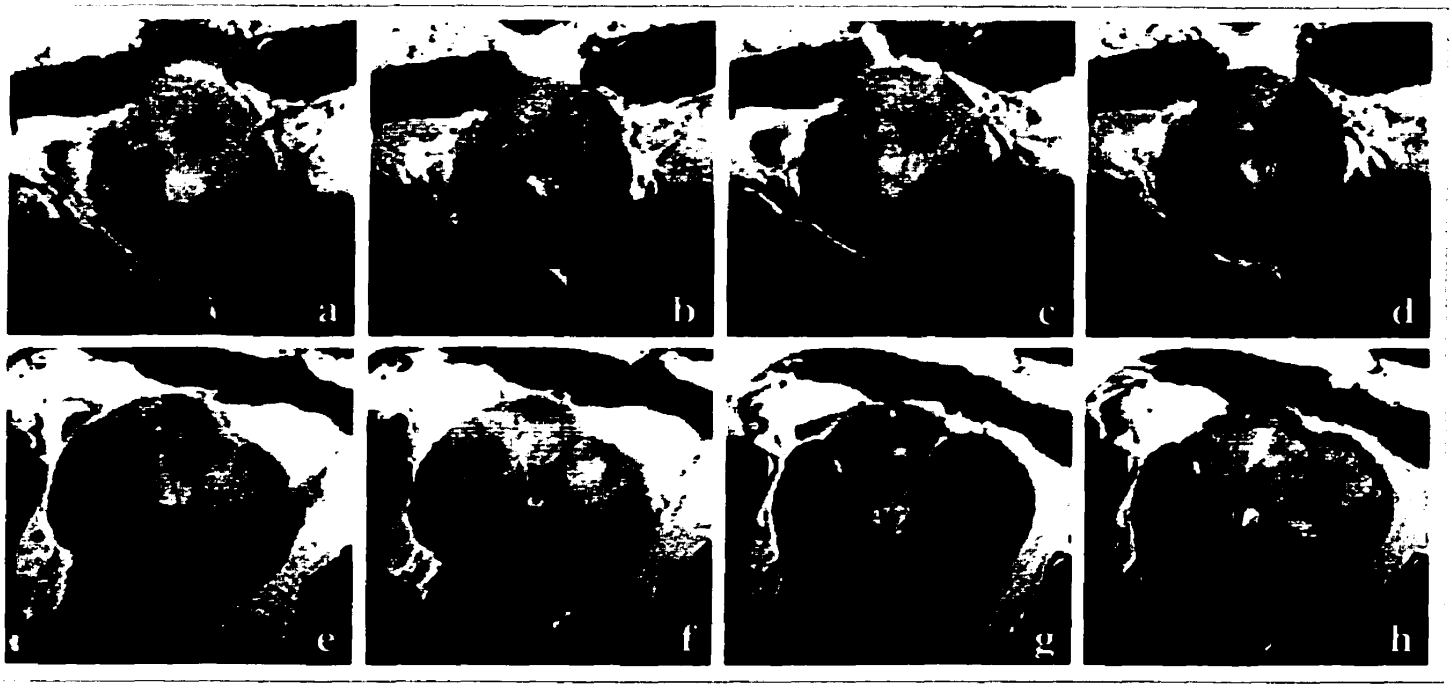

Figure 6.13: Post-treatment MR images of the four ILC applications in the canine prostate gland. Shown are (*a,c,e,g*) *T1*-weighted and (*b,d,f,h*) *T2*-weighted images from the two dog studies (*a-d*) and (*e-h*). The above images were obtained after Gd-contrast enhancement and approximately 1.5 hours after the applications. The above images have been cropped to show a FOV of 63 mm.

6.4.6 Histological Examination of Thermal Damage

Histological examination of the H&E stained sections from the two dog prostates revealed a region of necrosis that was sharply defined with an abrupt transition zone between the normal prostatic and necrotic tissue (Figure 6.14*a*). In the necrotic region the epithelial cells were necrotic and detached from the basement membrane, whereas stromal cells appeared viable. Hemorrhage and acute inflammation were present along the boundary of necrosis.

One interesting observation came from the prostate with the 4-hour survival period. Light microscopy of this H&E section showed the region of necrosis to appear annular with a region of intact viable cells immediately around the laser fibre tract (Figure 6.14*b*). In one ILC site, the radius of the central intact region was 2.8 mm surrounded by an annular necrotic region, 1.3 mm in width. However, as described by Thomsen [18], even though these cells within the necrosis region may appear to be viable under light microscopy, they are very likely necrotic. It generally takes from 24 hours to 5 days for the full extent of lethal thermal damage to be revealed by necrosis. The cells appear intact at this 4-hour time point, ie. did not undergo cellular and nuclear disintegration,

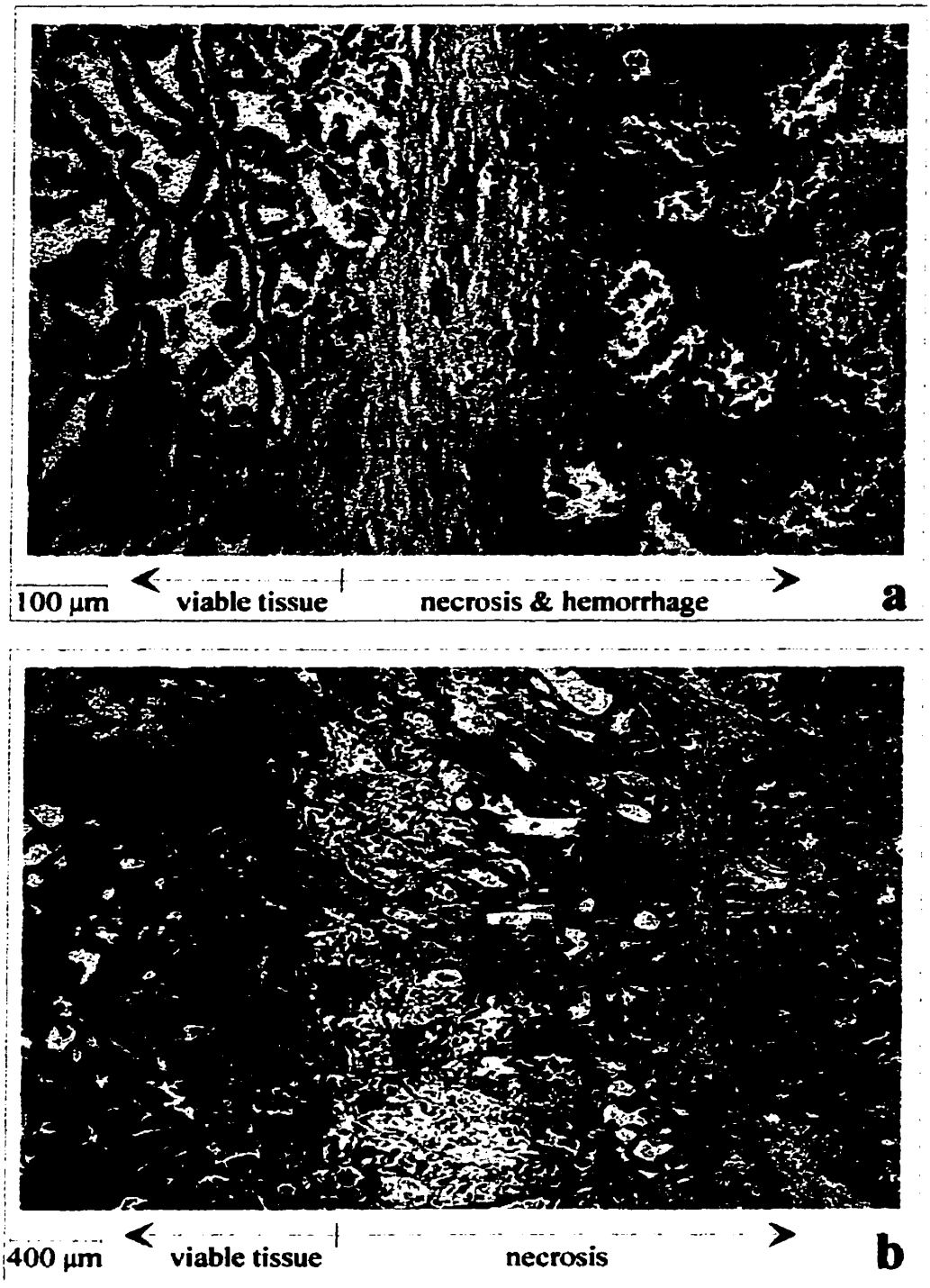

Figure 6.14: Histological sections of the canine prostate. Shown are H&E stained sections of the two prostates. The thermal necrosis margins are shown in the (a) 24-hour and (b) 4-hour survival periods, at two different magnifications. Evidence of hemorrhage can be seen in the necrotic region in (a) as a collection of red-blood cells.

because their intrinsic lytic enzymes had been thermally denatured and will likely persist until new blood vessels bring inflammatory cells to invade and digest the necrotic tissue. With the 24-hour survival period, there was no evidence of viable cells within the area of necrosis. In all thermal injury sites, the necrotic region was not found to reach the prostatic capsule. This finding lends support to the notion that the actual temperature distribution within the prostate was altered by blood flow in the prostatic capsule, which spared this tissue.

For each prostate, one axial histological section was used for the subsequent analysis of the thermal-damage models. Choice of the location of this section was aided with the 3D image set of the fixed prostate specimen that was obtained prior to slicing the prostates in 3 mm sections. These two histological sections contained the largest thermal-injury area from the ILC applications, and were judged to represent the axial location of the centre of the laser diffuser region.

6.4.7 Prediction of Thermal Damage from the MR-Thermal Maps

The three models of thermal damage were assessed using the Weiner-filtered MR-thermal maps from the four ILC applications in the canine prostate. The spatial onset of threshold of thermal damage was represented by the margins that were traced on the post-treatment *T1*- and *T2*-weighted images and the digitized histological sections. A second boundary, one pixel beyond this margin (0.6 mm), was also used to represent tissue regions that would be classified as normal.

The optimal model values that would best describe the onset of thermal coagulation were determined in the following way, similar to classification methods using discriminant analysis. In this analysis, an optimal threshold model value was chosen in which the fraction of pixels that equalled or exceeded this threshold value was *maximized* along the lesion margin and *minimized* along the outer boundary. These results are summarized in Table 6.2 and 6.3 for each of the four ILC applications, the three thermal-damage models, and three lesion margins. For example, an optimal threshold temperature of 50°C was determined from the histological section in lesion 1 (Table 6.3). In this case, 95% of the pixels along the thermal-damage margin equalled or exceeded 50°C, whereas only 38% of the pixels on the outer boundary (classified as normal tissue) did. A measure of uncertainty in the threshold model values was derived from lower and upper limits that provided half of the statistical confidence in the optimal model value. These estimates of uncertainty are shown in Table 6.3 for only the threshold model values from the histological lesion margin.

Table 6.2: Thermal-damage modelling results derived from the MR-thermal maps of the four ILC applications. Shown are the optimal threshold values of the three models: maximum temperature (max. T), t_{43}, and temperature-time product (TTP) as determined from the $T1$- and $T2$-weighted post-treatment MR images.

		***T1*-weighted contrast**			***T2*-weighted contrast**		
	Lesion	max. T (^{o}C)	t_{43} (min.)	TTP (min.^{o}C)	max. T (^{o}C)	t_{43} (min.)	TTP (min.^{o}C)
canine 1	1	61	1.8×10^5	96	64	1.8×10^6	108
	2	58	5.6×10^4	140	68	1.8×10^7	192
canine 2	3	73	5.6×10^8	124	83	5.6×10^{11}	168
	4	71	1.8×10^9	162	80	1.0×10^{11}	200

Table 6.3: Thermal-damage modelling results as determined from the digitized histological sections.

	Lesion	max. T (^{o}C)	t_{43} (min.)	TTP (min.^{o}C)
canine 1	1	50 ± 2	$1.8\times10^2 \pm$ 10-fold	62 ± 8
	2	49 ± 3	$1.0\times10^2 \pm$ 10-fold	80 ± 12
canine 2	3	56 ± 6	$1.0\times10^4 \pm$ 100-fold	74 ± 20
	4	49 ± 2	$1.8\times10^2 \pm$ 5-fold	118 ± 62

The lesion margins as derived from the $T1$- and $T2$-weighted post-treatment images did not provide uniform threshold values (maximum T, t_{43}, TTP) among the two canine studies, as shown in Table 6.2. For example, the $T1$-weighted lesion margins gave rise to threshold maximum T and t_{43} values of approximately 60^{o}C and 10^5 min., respectively, in the first canine study, and approximately 71^{o}C and 10^9 min. in the second study. These differences were well beyond the estimated uncertainties.

The threshold model values determined from the histology sections (Table 6.3) seemed to provide the only consistent findings among all four ILC applications (both canine studies). In particular, the average threshold temperature was 51 ± 2^oC and t_{43} was 200 $\pm$ 3-fold min., ie. 67 - 600 min. The threshold TTP model values were not found to provide results that were as consistent as the first two models did. Thermal-damage maps from the four ILC applications are shown in Figure 6.15 for the maximum-threshold temperature model, along with the histological

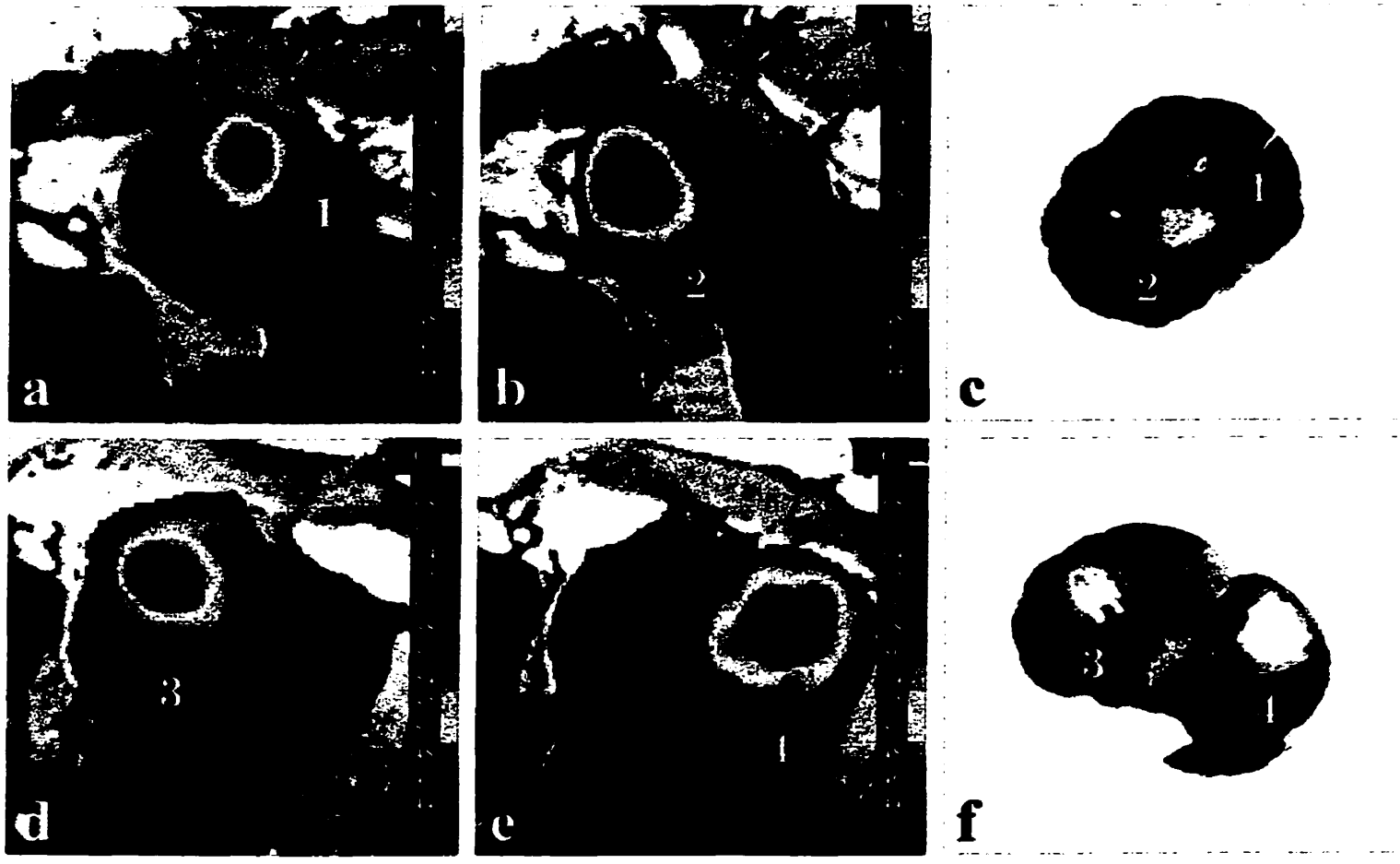

Figure 6.15: Critical-temperature maps from the four ILC applications in the two canine prostate studies. The ILC applications are numbered in the critical-temperature maps (a,b,d,e) and correspond to the lesions seen in the histological sections (c, f), which also shows an outline of the thermal-coagulation margin. The white spaces in (f) correspond to necrotic tissue that did not remain intact during routine processing.

sections.

6.5 Discussion

It seems reasonable that minimally-invasive practices of thermal therapy can be improved with real-time image guidance. Current MR-thermal mapping techniques are able to provide a 1°C temperature resolution with image update times as short as a few seconds to provide a dynamic visualization of the 3D deposition of heat energy in the tissues being treated. This represents a very significant improvement on the standard use of discrete, invasive temperature probes, such as thermal couples or the fibre-optic devices used in this study. The spatial-resolving ability, however, is easily appreciated by the fact that the laser-fibre heating produced non-radial temperature distributions in the perfused canine prostatic tissue.

Unfortunately, thermal-mapping modalities, such as MRI, must supply more than simple temperature measurements within tissue to ultimately realize their clinical importance or necessity. A better understanding of how temperature exposure relates to actual thermal damage is necessary in order to properly establish the predictive value of real-time MR-thermal mapping. In this report, three plausible thermal-damage models were assessed using the thermal data from four ILC applications in canine prostate, which is likely to have a thermal response that is similar to the human prostate. The only consistent results were obtained with histological evaluation of the thermal-injury boundary which was described by either a threshold-maximum temperature of 51°C or a t_{43} of approximately 200 minutes. However, these threshold values clearly need to be established from a much larger sample size and in a variety of different relevant tissues. Actually, there is much similarity between these two indicators of thermal damage. With a typical treatment period of 3 minutes, tissues that had reached the threshold maximum limit of 51°C would also have obtained a t_{43} of approximately 768 minutes, which is agreement with the modelling results. This finding, if valid over a much broader series of experiments, could change the way physicians regard high-temperature coagulation therapy. The onset of thermal damage may occur at a much lower temperature than what typical interstitial heating devices, such as laser fibres, are capable of. Further, such low threshold temperatures and t_{43} values are reminiscent of conventional hyperthermia biophysics, of which there is a larger body of empirical findings [155]. However, interstitial devices capable of high temperatures and large spatial-thermal gradients, are still necessary in order to create small lesion margins in perfusion-insensitive heating regimes.

The quantitative value of thermal-damage prediction from MR thermometry can be hindered by errors and misinterpretation in the temperature-sensitive MR signals. PRF-shift thermometry is particularly vulnerable to a number of factors that can give rise to errors in the MR-thermal maps. Among these contributing factors are the temperature sensitivity of the volume-magnetic susceptibility and electrical conductivity (Chapter 5) [209], as well as such experimental parameters as the heat-source geometry and orientation (Chapter 4) [184] and scan-slice thickness. With the same laser fibre used in the canine studies, we found the apparent PRF-shift thermal coefficient evaluated to be -0.0104 ppm/°C with a 5 mm-slice thickness and -0.0084 ppm/°C with a 10 mm slice from a well-controlled characterization of laser heating in a gel phantom. In retrospect, such a large discrepancy would not have allowed reliable interpretation of quantitative thresholds of thermal damage in the *in vivo* canine prostate model.

The observed discrepancy between the laser-tip temperature reading and the MR-thermal maps is troubling. The laser-fibre temperature reading tends to be regarded as an accurate measure of the temperature in the immediate surroundings of the laser fibre. Consequently, physicians will tend to rely on its accuracy more than the MR-thermal maps, which (in light of the previous chapters) can be subject to interpretation if certain precautions are not taken. As there is evidence that the laser-tip reading is *overestimating* the true temperature, it follows that the tissue may be left insufficiently treated. The findings from this and multiple previous investigations suggest that the conventional laser fibres are exhibiting some self heating effects and that the newer version of low "self-heating" fibres would be preferred in future clinical thermal-coagulation procedures. The MR-thermal mapping has been a valuable tool in this respect. Unfortunately, the conventional fibres were used in the present canine prostate study and, thus, the laser-tip temperature readings were not used in any of the subsequent analysis.

Without MR-thermal mapping, post-treatment MRI may be the only means available to assess the resultant thermal-damage boundary in tissue. Unfortunately, in the two canine studies, we found post-treatment *T1*- and *T2*-weighted images with Gd-enhancement to be of limited use. While margins were visible that appeared to represent the extent of the thermal injury, they were later found to be smaller than the direct histological finding. Also, post-treatment images often require a delay period for a host response to occur which places severe limitations on their prognostic value for thermal treatment since they only provide an estimate of the thermal-injury boundary after treatment has occurred.

Chapter 7

Summary, Future Directions, and Conclusion

7.1 Summary

One of the main themes of this thesis has been to investigate the capabilities and limitations of PRF-shift thermometry. The work has been motivated, in part, by the lack of agreement in the literature on value of the PRF-thermal coefficient. This apparent discrepancy has a direct consequence on the how well the PRF-shift method will be perceived by the scientific community, and eventually implemented clinically.

In **Chapter 3**, a simple and fundamental question was posed: is there an *ex vivo* tissue-type dependence on the PRF-thermal coefficient? The results showed that, within the experimental uncertainty of approximately 4%, there was no significant difference among the different tissues or with an agar-gel control. This finding showed that PRF-shift thermometry was simpler than previously thought. The calibration experiments allowed different tissues to be compared to each other in a well-controlled manner. However, it must be re-emphasized that the results only showed what the value of the PRF-thermal coefficient was (as defined in Chapter 2, Equation 12) for this particular experimental arrangement.

Finally, the experimental approach in Chapter 3 should not be considered as the definitive way to perform a thermal calibration experiment. Ideally, a well-controlled experiment that

emulates (as closely as possible) the actual clinical thermal-therapy application is preferable. Unfortunately, this is often not easily attained because most high-temperature thermal-coagulation therapies use point-like heating devices, such as laser fibres or focused ultrasound, which make accurate calibration difficult due to their rapid heating rates and large spatial-thermal gradients.

Chapter 4 continued from Chapter 3 in looking for potential sources of variation in the PRF-thermal thermometry. The main difference was that in this chapter, the experimental heating geometry was considered as a potential variable, rather than the actual material being heated.

Using a simple experimental model, it was demonstrated that temperature-induced changes in the volume-magnetic susceptibility perturb the macroscopic-magnetic field, which can give rise to a spatially-variable PRF-thermal coefficient. In this experiment, discrepancies in the value of the apparent thermal coefficient of $\pm 30\%$ were found.

The salient message in this chapter is that there should be some considerations on the heat-source geometry and orientation with the main-magnetic field when using PRF-shift thermometry to map the temperature distribution. The experimental model was purposely chosen to resemble clinical heating devices to show that they will also be prone to errors in MR-thermal mapping.

In **Chapter 5**, it was found that temperature-induced changes in the electrical conductivity caused a phase-retardation of the RF B_1 field which could cause errors in the MR-derived temperatures. This was noted through inconsistencies in the phase-shift data when using multiple TE settings.

Chapters 4 and 5 are quite similar, in that they both deal with a temperature-dependent property that can give rise to erroneous results in PRF-shift thermometry. There is an interesting symmetry that is worth noting. In Chapter 4, the relevant physical property was the volume-magnetic susceptibility that caused variations in the macroscopic-magnetic field and was most pronounced in heating devices that had large spatial-thermal gradients with a column-like temperature distribution, such as a laser fibre or focused ultrasound beam. On the other hand, in Chapter 5 it was the temperature-induced changes in the electrical conductivity that caused a phase retardation of the RF B_1 field, which presented an error when heating large volumes uniformly. This is believed to be problematic for thermal monitoring during hyperthermia, where generally large tissue volumes are heated.

	Chapter 4	**Chapter 5**
physical property:	volume-magnetic susceptibility (χ_v)	electrical conductivity (σ)
couples through:	macroscopic-magnetic field (B_{mac})	RF field (B_1)
problem with:	point-like, localized heating devices with large spatial-thermal gradients *eg.* laser fibres, microwave antennas, focused ultrasound	uniform heating of large volumes *eg.* hyperthermia applicators

Figure 7.1: Symmetry of errors in PRF-shift thermometry.

In **Chapter 6**, a practical implementation of MR-thermal mapping with laser heating in an *in vivo* canine prostate model was described. In this study, a number of considerations for thermal mapping were discussed, including the effect of slice thickness when using a localized heat source. An orientation dependence on the laser fibre was also verified, as predicted earlier in Chapter 4.

The utility of real-time thermal monitoring during thermal-coagulation therapy was also shown in Chapter 6. The canine prostate model provided an opportunity to examine if tissue damage, based on histological evidence, could be predicted from the MR-thermal maps. This limited study showed that the boundary of necrosis could be predicted by a critical-temperature model and underlined the importance of real-time thermal mapping for assessing the necrotic volume. Future similar studies that employ quantitatively accurate thermometry should prove valuable in elucidating the thermal dosimetry issue in human prostate and other living tissue.

7.2 Future Directions

There are two main areas in which further development of MR thermometry for monitoring thermal-coagulation therapy can be categorized. One area deals with MR-thermal monitoring of biological tissues, such as PRF-shift thermometry in the presence of fat, motion, and physiological responses. The other area involves other technical developments, such as SNR improvements at low-field strengths and the design of automated feedback-control mechanisms to provide real-time control from the thermal maps. Some of these issues are now briefly discussed.

7.2.1 PRF-Shift Thermometry in Fatty Tissues

The experiments that have been presented in this thesis have dealt exclusively with the ^{1}H resonance in water molecules which exhibit temperature dependence in both the electron-screening coefficient and volume-magnetic susceptibility, as described in Chapter 2. However, fat or lipid has a negligible PRF-thermal coefficient, which is dictated by changes in the magnetic susceptibility. Consequently, PRF-shift thermometry in fatty tissues pose a special challenge as the presence of lipid can lead to erroneous temperature measurements.

There are essentially two approaches to deal with the presence of fat. The first straightforward approach, is to visually identify fatty tissue from the target tissue using pre-treatment MR images. This approach was adequate for the canine prostate study of Chapter 6 where the prostate gland could be easily distinguished from the surrounding fat.

In cases where lipid is infiltrating to the extent where this approach is not feasible, the lipid MR signal can be removed or suppressed and thus its contribution to the phase-difference images removed [173, 213–216]. This approach has been demonstrated to provide more consistent temperature measurements in fat-infiltrating tissues and is likely to be a standard refinement to PRF-shift thermal mapping techniques especially in thermal applications in the breast and liver.

However, suppression or separation of the lipid signal only removes the lipid temperature induced phase-shift contribution from that of water. The temperature-induced changes in the magnetic susceptibility of lipid can be quite significant and will remain to cause perturbations in the macroscopic-magnetic field, which will affect the ^{1}H resonance of the surrounding tissue water. For example, the temperature dependence of the volume-magnetic susceptibility in fat tissue can be variable, depending on composition, and in two reports has been measured to be approximately -0.0097 $\times$ $10^{-6}/^oC$ and -0.0080 $\times$ $10^{-6}/^oC$ [164, 180]. Recall, in Chapter 2, it was shown that the susceptibility of water increased by only approximately 0.003 $\times$ $10^{-6}/^oC$. In short, lipid suppression from the MR phase-difference image, is a readily attainable correction, but susceptibility-related effects of lipid will remain. The significance of this effect will depend on the fractional volume and geometry of the fat relative to the tissue water.

7.2.2 The Effects of Motion

As described in the previous chapters, PRF-shift thermometry using the phase-shift mapping technique requires subtraction of phase images that are obtained during the course of heating from a

reference image that was obtained prior to heating. Therefore, it is important that there be no motion of the object during the heating application which would cause mis-registration and affect the image subtraction process. Such motion could cause phase shifts that could be mistaken for temperatures [217]. In the canine study of Chapter 6, the effects of motion were minimized by having the animal anesthetized and by immobilizing the animal's lower abdomen. While pulsatile blood flow in the femoral vessels were seen to cause phase-shift artifacts outside of the prostate gland, generally motion effects were not found to be problematic in this experiment. However, it is realized that such measures during clinical procedures in humans may not be possible. Also, motion effects will likely be more severe in tissues such as the liver or breast and less severe in tissues that can be easily immobilized, such as the brain.

Often when MR imaging is done over extended periods of time, re-registration of the MR images is performed. Image re-registration artificially moves objects in the images back into alignment with the reference image using digital-image processing techniques [218,219]. Re-registration can correct the anatomy shift in position, unfortunately, it does not address the movement of the patient within the inhomogeneous magnetic field, which will cause remnant phase-shifts to appear in the re-registered phase-shift images. Thus, with phase-shift mapping as described in this thesis, efforts should be made to try and restrict patient movements because although image re-registration procedures are a good first approximation, they do not provide a complete solution for MR-thermal mapping.

Ideally, the whole problem of motion could be circumvented if an internal reference were available for each image acquired during heating. This is the case with chemical-shift imaging techniques, where each voxel contains a reference peak (such as lipid) and a water peak, thus avoiding the need for a separate baseline image. There are some recent developments with the phase-shift mapping technique to extract phase separately from lipid and water, while maintaining the superior temporal and spatial resolution properties of phase-shift mapping. Developments of this nature will be an important contribution which will help make PRF-shift thermometry easier to implement and hence more clinically accessible.

7.2.3 Physiologic Effects in PRF-Shift Thermometry

Several potential contributors to discrepancy in PRF-shift thermometry have been discussed, such as the *ex vivo* tissue type and physical properties such as the volume-magnetic susceptibility and

electrical conductivity. However, one aspect that has not yet been sufficiently investigated are physiologic effects such as blood perfusion. While the *in vivo* canine prostate experiment in Chapter 6 showed the feasibility of MR-thermal mapping as a predictor of the eventual thermal damage, the limited study did not fully address the basic question of whether the temperature-induced PRF-shift is different among *in vivo* and *ex vivo* tissues.

At present, this has not been an active area of study in PRF-shift thermometry. A thorough investigation will necessarily require very careful and well-controlled thermal calibration experiments in living, perfused tissue and include parallel experiments on freshly excised or post-mortem tissue to rule out possible experimental effects.

From the few publications in the literature on potential physiologic effects, there appears to be two distinct views as to the significance in PRF-shift thermometry. One view is that *in vivo* tissue response is very complex such that a simple PRF-thermal calibration is simply not accessible. The second view is that physiological responses are present but are not significant enough to confound PRF-shift thermometry. Both opinions share one common ground which is that magnetic-susceptibility variations from deoxygenated and oxygenated blood are the likely primary physiologic response.

Young et al. [162] described an *in vivo* experiment where the calf muscle of a human volunteer was cooled with an external water bag. This was done while simultaneously measuring the peripheral muscle temperature with interstitial thermal probes and acquiring MR phase-difference images. The results from this study showed that the MR phase shifts exhibited a non-linear and irreversible behavior with temperature. In this report, it was suggested that this was a result of a thermal-induced change in the oxygenation of the blood flow. No other tissues were examined in this report and the authors acknowledged that the findings may be specific to the human calf muscle.

Representing the contrary view, Stollberger et al. [180, 220] recently provided a convincing argument on the expected magnetic-susceptibility variations in blood (limited to cerebral blood flow) which showed that such variations would be insignificant in PRF-shift thermometry. This report also provided direct experimental results which showed that the temperature-induced phase shift remained linear with temperature and that there was no significant difference between *in vivo* and post-mortem pig brain tissue.

Deoxygenated red blood cells are less diamagnetic (χ = -6.7 $\times$ 10^{-6}) than oxygenated blood

cells (χ = -9.2 × 10^{-6}) and it is plausible that temperature-regulated changes in the blood perfusion rate and blood oxygenation level may be significant factors in PRF-shift thermometry. Future studies in suitable animal models might include artificially clamping the blood flow to the tissue being heated in order to examine the basic effect of perfusion on the thermometry measurements, as well as varying the oxygenation saturation of the perfusing blood. Further, because heating is known to cause vasculature occlusion, the rate of heating might also be an important experimental variable. To investigate potential physiological effects, calibration experiments should be designed to examine changes in the linear behavior and reversibility of the MR-phase shift measurements with temperature as well as the value of the derived PRF-thermal coefficient.

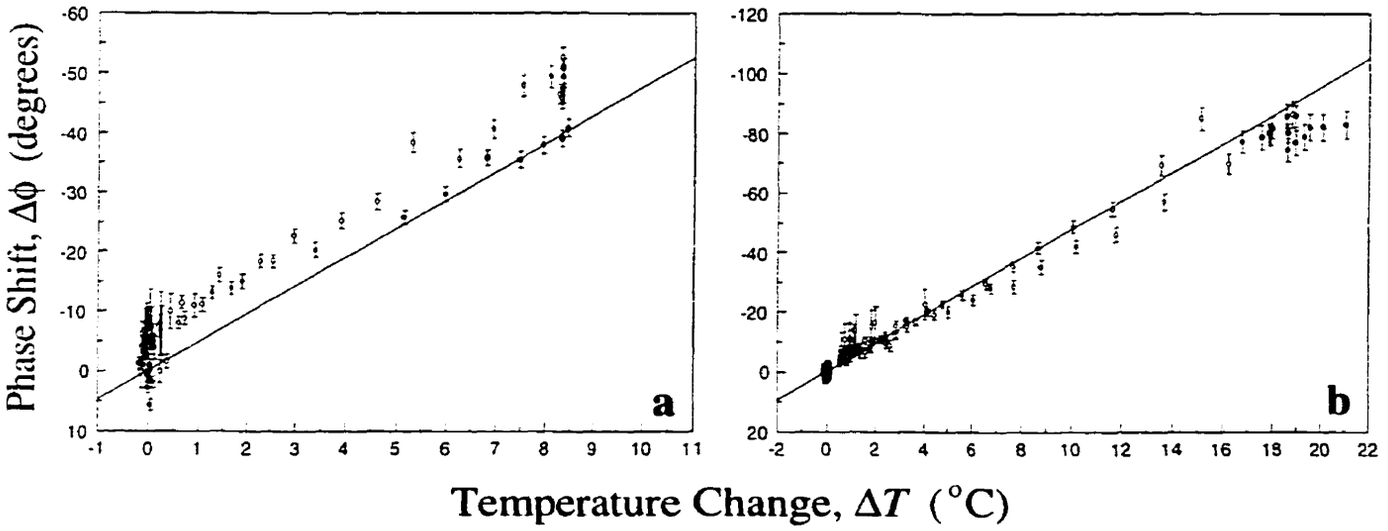

Figure 7.2: Phase shift as a function of temperature from *in vivo* canine prostate gland. Shown are results from the (*a*) first and (*b*) second canine study described in Chapter 6 in which the Luxtron thermal probes were within the imaging plane. The solid symbols represent the data points acquired during the heating portion, with the open symbols representing the cooling down portion. The solid line shows the -0.0104 ppm/°C calibration as derived from the gel-phantom experiments and was subsequently used in constructing the MR-thermal maps in the canine prostate experiments of Chapter 6.

As an aside, the *in vivo* canine prostate heating experiment in Chapter 6 was not designed as a calibration experiment, but rather to investigate the feasibility of predicting the eventual tissue thermal damage, as discussed. However, a limited data set was obtained in which phase-shift measurements in the prostate tissue could be confidently compared to the Luxtron temperature readings within the same imaging volume. These results (from both animals) are shown in Figure

7.2 which show the phase shift to vary linearly and reversibly with temperature, with the slope similar to what was measured in the gel-phantom studies that were included in Chapter 6. Although this experiment did not measure perfusion or blood oxygenation levels in the prostate gland, these limited results do seem to indicate that physiological responses did not confound the MR-thermal mapping in these two studies. The results shown in Figure 7.2 indicate that there may have been a maximum temperature discrepancy of approximately 2°C and hence lend support to the view taken by Stollberger et al.

7.2.4 PRF-Shift Thermometry in Low-Field MRI Systems

Most interventional MRI procedures, such as image-guided thermal-coagulation therapy, will likely be done in MR imaging systems that have improved patient accessibility compared with conventional whole-body systems [69, 70, 74]. At present, these interventional MRI systems operate with a main-magnetic field strength between 0.2 T – 0.5 T, but developments in magnet technology will soon increase this field strength beyond 1 T.

At low magnetic-field strengths, MR-derived temperature images have significantly lower signal-to-noise (SNR) properties compared to the results that have been presented in this thesis which were obtained in a 1.5 T conventional whole-body MRI system. For significance, consider the following illustrative example comparing the SNR property of phase-shift mapping at 1.5 T to 0.2 T. The minimum resolvable temperature in the MR-derived thermal maps will be determined by the amount of phase noise divided by the phase-shift thermal coefficient, $\Delta\phi/\Delta T$. The phase noise, or standard deviation in the phase angle, is inversely proportional to the SNR in the magnitude image [176]. The magnitude SNR, in turn, is approximately proportional to the strength of the main-magnetic field, B_o [119][1]. As described in the previous chapters, $\Delta\phi/\Delta T$, is also directly proportional to B_o and consequently, the minimum-resolvable temperature will be approximately inversely proportional to the square of B_o. This means, theoretically, that if a temperature-noise level of 1°C is attained in an experiment at 1.5 T, then (if all experimental variables are held constant) a noise level of approximately 56°C would be expected at 0.2 T.

To address this poor SNR performance at low-field strength, one approach that is easy to implement is to increase the phase-shift thermal coefficient, $\Delta\phi/\Delta T$ [168, 169, 173, 215, 221–223].

[1] This simple example does not consider such things as the $T1$ of tissue decreasing with B_o, which also affects the magnitude SNR.

This can be done by extending the *TE* setting into the next *TR* period using echo-shifting MR imaging pulse sequences, such as PRESTO as shown by DeZwart and Moonen et al. [173, 223], without increasing the total image-acquisition period. It should be noted, however, that the optimal *TE* setting for phase-shift mapping is the *T2** of the tissue, which can typically range from 20 – 60 ms [160, 161, 172, 173]. Another approach is to reduce the phase noise level by increasing the (magnitude) image SNR which can be readily achieved by prolonging the imaging time with multiple averages or reducing the spatial resolution [119].

One recently reported study at 0.2 T showed that a temperature resolution of 1 – 2.5°C is achievable using echo-shifting with an effective *TE* setting of 30 ms, an imaging acquisition time of 3 – 5 seconds, and a voxel volume of approximately $2 \times 2 \times 10$ mm^3 in a phantom material and excised tissue [169]. Similar temperature, spatial, and temporal resolutions have also been reported in a few studies performed at low-field strengths (0.2 – 0.3 T) [172, 224]. At present, however, most MR thermal-mapping implementations at low-field strengths are based on *T1*-weighted signal intensity changes which are less quantitative as discussed in Chapter 1, but have slightly higher SNR characteristics than the PRF-shift method.

7.2.5 Real-Time Feedback Control in MR-Thermal Mapping

A necessary component to implementing real-time thermal mapping in clinical thermal therapy is a method of incorporating the thermal measurements into the physician's decision-making process. This, in effect, represents the transition of MR-thermal mapping from a passive to an active role. Design and implementation of a feedback-control mechanism is an area that has not received a lot of attention at present which is probably because accurate thermometry has only become available during the last few years.

As discussed in Chapter 6, the utility in MR-thermal mapping is its real-time prediction of the eventual volume of necrosis. Confidence in this prediction will require quantitatively accurate thermometry and a reliable model of thermal damage (eg. critical temperature, Arrhenius integral, etc.). The general idea is that real-time thermal maps are translated into thermal-damage maps which are then used in an automated manner to control the delivery of heat energy. One way in which this can be implemented, is where a physician pre-selects a target volume boundary in the pre-treatment MR images and then begins heating within this volume. The delivery of heat is then either modulated or terminated based on the volume of the predicted thermal damage relative

to the pre-selected target volume. This approach can also be extended to include the physical translation of the heat-energy source to other spatial positions within the target volume, such as the steering of a high-intensity ultrasound focus.

In particular, a few implementations of automated feedback control have been described for use with external focused ultrasound transducers. Focused ultrasound differs from interstitial heating devices, such as laser fibres or microwave antennas, in that a narrow heating focus can be externally steered in three dimensions within tissue. One implementation as described by McDannold and Hynynen et al. showed how multiple focused ultrasound foci could be spatially arranged to cover a large target volume using MR-thermal mapping [225, 226]. Another report by De Zwart and Moonen et al. described the modulation of the intensity of an ultrasound transducer, based on MR thermal measurements, in order to maintain a constant, uniform temperature distribution in tissue [227, 228]. As in the above two examples, the overall goal of feedback control is to reduce the amount of operator dependence in controlling the thermal therapy. Computer-driven control will have a shorter response period than humans and thus be capable of making potentially critical decisions faster.

7.3 Conclusion

Medical-image guidance is becoming increasingly pervasive and is representative of how technology serves to advance the current practice of surgery and therapy. Quantitative MR thermometry is one tool of image guidance that may have a significant impact in the field of interventional radiology. In particular, the PRF-shift method of thermometry has the demonstrable ability to provide the necessary guidance for a novel class of minimally-invasive thermal therapies where the clinical goal is to induce thermal coagulation. This thesis has shown that quantitatively accurate MR-thermal mapping is within clinical reach, but requires the attention of many technical considerations. The developments made here mark only the mid-point in the application of clinical image-guided thermal-coagulation therapy. It now remains to use this tool of *in vivo* temperature visualization to gain a better understanding of the thermal-injury process. This will enhance the utility of MR-thermal mapping to more confidently predict the onset of necrosis in diseased tissue, while sparing the surrounding healthy tissue.

Bibliography

[1] S. Webb, "The Physics of Medical Imaging", Adam Hilger, Bristol, England, 1988.

[2] H. H. Holm, B. Skjoldbye, Interventional Ultrasound, *Ultrasound in Medicine and Biology* **22(7)**, 773–789 (1996).

[3] D. R. Uecker, C. Lee, Y. F. Wang, Y. Wang, Automated Instrument Tracking in Robotically Assisted Laparoscopic Surgery, *Journal of Image Guided Surgery* **1**, 308–325 (1995).

[4] K. R. Thomsen, Interventional Radiology, *Lancet* **350**, 354–358 (1997).

[5] K. Kandarpa, Future Directions in Vascular and Interventional Radiology Research: A Commentary, *Radiology* **209**, 19–21 (1998).

[6] K. Ouriel, R. M. Green, D. Waldman, R. Greenberg, C. K. Shortell, K. Illig, A Model for Merging Vascular Surgery and Interventional Radiology: Clinical and Economical Implications, *J. Vascular Surgery* **28**, 1006–1013 (1998).

[7] D. C. Levin, V. M. Rao, R. L. Bree, H. L. Neiman, Turf Battles in Radiology: How the Radiology Community Can Collectively Respond to the Challenge, *Radiology* **211**, 301–305 (1999).

[8] R. B. Schwartz, L. Hsu, D. F. Kacher, A. A. Zamani, P. M. Black, E. Alexander III, P. E. Stieg, T. M. Moriarty, C. A. Martin, R. Kikinis, F. A. Jolesz, Intraoperative MR Imaging Guidance for Intracranial Neurosurgery: Experience with the First 200 Cases, *Radiology* **211**, 477–488 (1999).

[9] V. Giles, The Historic Development and Modern Application of Artificial Fever, *New Orleans Med. Surg. J.* **91**, 655 (1938).

[10] G. M. Samaras, A. Y. Cheung, Microwave Hyperthermia for Cancer Therapy, *CRC Critical Reviews on Bioengineering* **February**, 123–184 (1981).

[11] S. A. Sapareto, The Biology of Hyperthermia *In Vitro*, *in* "Physical Aspects of Hyperthermia: (1981) AAPM Summer School Proceedings" (G. H. Nussbaum, Ed.), American Institute of Physics, New York, 1982.

[12] F. W. Hetzel, Hyperthermia *In Vivo*, *in* "Physical Aspects of Hyperthermia: (1981) AAPM Summer School Proceedings" (G. H. Nussbaum, Ed.), American Institute of Physics, New York, 1982.

[13] C. A. Perez, Rationale for Clinical Application of Hyperthermia: Alone or Combined iwth Irradation or Cytotoxic Drugs in Cancer Therapy, *in* "Physical Aspects of Hyperthermia: (1981) AAPM Summer School Proceedings" (G. H. Nussbaum, Ed.), American Institute of Physics, New York, 1982.

[14] G. H. Nussbaum, Conceptual Outline of Hyperthermia Physics, *in* "Physical Aspects of Hyperthermia: (1981) AAPM Summer School Proceedings" (G. H. Nussbaum, Ed.), American Institute of Physics, New York, 1982.

[15] C. W. Song, Physiological Factors in Hyperthermia of Tumors, *in* "Physical Aspects of Hyperthermia: (1981) AAPM Summer School Proceedings" (G. H. Nussbaum, Ed.), American Institute of Physics, New York, 1982.

[16] P. M. Corry, B. Barlogie, Clinical Application of High Frequency Methods for Local Tumor Hyperthermia, *in* "Physical Aspects of Hyperthermia: (1981) AAPM Summer School Proceedings" (G. H. Nussbaum, Ed.), American Institute of Physics, New York, 1982.

[17] S. Thomsen, Pathologic Analysis of Photothermal and Photomechanical Effects of Laser-Tissue Interactions, *Photochem. Photobiol.* **53**, 825–835 (1991).

[18] S. L. Thomsen, Mapping of Thermal Injury in Biologic Tissues using Quantitative Pathologic Techniques, *in* "Thermal Treatment of Tissue with Image Guidance" (T. P. Ryan, T. Z. Wong, Eds.), SPIE Press, Bellingham WA, Proceedings of SPIE Vol. 3594 edition, 1999.

[19] S. N. Goldberg, J. B. Kruskal, G. S. Gazelle, Thermal Ablation Therapy for Focal Malignancy: A Unified Approach to Underlying Principles, Techniques, and Dianostic Imaging Guidance, *in* "Thermal Treatment of Tissue with Image Guidance" (T. P. Ryan, T. Z. Wong, Eds.), SPIE Press, Bellingham WA, Proceedings of SPIE Vol. 3594 edition, 1999.

[20] J. W. Hand, Heat Delivery and Thermometry in Clinical Hyperthermia, *Recent Results in Cancer Research* **104**, 1–23 (1987).

[21] M. G. Skinner, M. N. Iizuka, M. C. Kolios, M. D. Sherar, A Theoretical Comparison of Energy Sources - Microwave, Ultrasound and Laser - for Interstitial Thermal Therapy, *Physics in Medicine and Biology* **43**, 3533–3547 (1998).

[22] E. C. Burdette, Electromagnetic and Acoustic Properties of Tissues, *in* "Physical Aspects of Hyperthermia: (1981) AAPM Summer School Proceedings" (G. H. Nussbaum, Ed.), American Institute of Physics, New York, 1982.

[23] M. F. Iskander, Physical Aspects and Methods of Hyperthermia Production by RF Currents and Microwaves, *in* "Physical Aspects of Hyperthermia: (1981) AAPM Summer School Proceedings" (G. H. Nussbaum, Ed.), American Institute of Physics, New York, 1982.

[24] R. W. Paglione, Power Deposition with Microwaves, *in* "Physical Aspects of Hyperthermia: (1981) AAPM Summer School Proceedings" (G. H. Nussbaum, Ed.), American Institute of Physics, New York, 1982.

[25] B. R. Paliwal, D. N. Buechler, Basics of Physical Parameters in Hyperthermia, *in* "Biological, Physical and Clinical Aspects of Hyperthermia: (1987) AAPM/NAHG Hyperthermia School Proceedings" (B. R. Paliwal, F. W. Hetzel, M. W. Dewhirst, Eds.), American Institute of Physics, New York, 1988.

[26] T. Seki, M. Wakabayashi, T. Nakagawa, T. Itho, T. Shiro, K. Kunieda, M. Sato, S. Uchiyama, K. Inoue, Ultrasonically Guided Percutaneous Microwave Coagulation Therapy for Small Hepatocellular Carcinoma, *Cancer* **74**, 817–825 (1994).

[27] H. Hyodoh, K. Hyodoh, K. Takahashi, M. Furuse, C. Kawamoto, N. Isoda, M. Hozumi, K. Ido, N. Hirota, Microwave Coagulation Therapyon Hepatomas: CT and MR Appearance after Therapy, *Journal of Magnetic Resonance Imaging* **8**, 451–458 (1998).

[28] H. Schwarzmaier, T. Kahn, Magnetic Resonance Imaging of Microwave Induced Tissue Heating, *Magnetic Resonance in Medicine* **33**, 729–731 (1995).

[29] B. S. Trembly, P. J. Hoopes, K. L. Moodie, A. S. Dvinsky, Microwave Antenna Array for Prostate Hyperthermia, *in* "Thermal Treatment of Tissue with Image Guidance" (T. P. Ryan, T. Z. Wong, Eds.), SPIE Press, Bellingham WA, Proceedings of SPIE Vol. 3594 edition, 1999.

[30] K. Ito, H. Yoshimura, K. Saito, L. Hamada, Heating Characteristics of Coaxial-Slot Antennas for Minimally Invasive Microwave Thermal Therapy, *in* "Thermal Treatment of Tissue with Image Guidance" (T. P. Ryan, T. Z. Wong, Eds.), SPIE Press, Bellingham WA, Proceedings of SPIE Vol. 3594 edition, 1999.

[31] P. R. Stauffer, Implantable Microwave Antennas for Thermal Therapy, *in* "Surgical Applications of Energy" (T. P. Ryan, Ed.), SPIE Press, Bellingham WA, Proceedings of SPIE Vol. 3249 edition, 1998.

[32] J. R. Oleson, T. C. Cetas, Clinical Hyperthermia with RF Currents, *in* "Physical Aspects of Hyperthermia: (1981) AAPM Summer School Proceedings" (G. H. Nussbaum, Ed.), American Institute of Physics, New York, 1982.

[33] Y. N. Cheng, R. W. Brown, Y. Chung, J. L. Duerk, H. Fujita, J. S. Lewin, D. Schuele, S. Shvartsman, Calculated RF Electric Field and Temperature Distributions in RF Thermal Ablation: Comparison with Gel Experiments and Liver Imaging, *Journal of Magnetic Resonance Imaging* **8**, 70–76 (1998).

[34] S. N. Goldberg, L. Solbiati, P. F. Hagn, E. Cosman, J. E. Conrad, R. Fogle, G. S. Gazelle, Large-Volume Tissue Ablation with Radio Frequency by Using a Clustered, Internally Cooled Electrode Technique: Laboratory and Clinical Experience in Liver Metastases, *Radiology* **209**, 371–379 (1998).

[35] L. Solbiati, S. N. Goldberg, T. Ierace, M. Dellanoce, T. Livraghi, G. S. Gazelle, Radiofrequency Ablation of Hepatic Metastases: Postprocedural Assessment with a US Microbubble Contrast Agent - Early Experience, *Radiology* **211**, 643–649 (1999).

[36] Q. Zhang, Y. Chung, J. S. Lewin, J. L. Duerk, A Method for Simultaneous RF Ablation and MRI, *Journal of Magnetic Resonance Imaging* **8**, 110–114 (1998).

[37] K. Hynynen, Focused Ultrasound Surgery Guided by MRI, *Scientific American: Science & Medicine* **Sept/Oct**, 62–71 (1996).

[38] D. Deardorff, C. J. Diederich, W. H. Nau, Air-Cooling of Direct-Couple Ultrasound Applicators for Interstitial Hyperthermia and Thermal Coagulation, *Medical Physics* **25(12)**, 2400–2409 (1998).

[39] H. Cline, K. Hynynen, R. D. Watkins, W. J. Adams, J. Schenck, R. H. Ettinger, W. R. Freund, J. P. Vetro, F. A. Jolesz, Focused US System for MR Imaging-guided Tumor Ablation, *Radiology* **194**, 731–737 (1995).

[40] C. R. Hill, G. R. ter Haar, Review Article: High Intensity focused Ultrasound - Potential for Cancer Treatment, *The British Journal of Radiology* **68**, 1296–1303 (1995).

[41] A. L. McKenzie, Physics of Thermal Processes in Laser-Tissue Interactions, *Physics in Medicine and Biology* **35(9)**, 1175–1209 (1990).

[42] D. J. Castro, R. E. Saxton, R. B. Lufkin, Interstitial Photoablative Laser Therapy Guided by Magnetic Resonance Imaging for the Treatment of Deep Tumors, *Seminars in Surgical Oncology* **8**, 233–241 (1992).

[43] R. Schober, M. Bettag, M. Sabel, F. Ulrich, S. Hessel, Fine Structure of Zonal Changes in Experimental Nd: YAG Laser-Induced Interstitial Hyperthermia, *Lasers in Surgery and Medicine* **12**, 234–241 (1993).

[44] S. A. Harries, Z. Amin, M. E. F. Smith, W. R. Lees, J. Cooke, M. G. Cook, J. H. Scurr, M. W. Kissin, S. G. Bown, Interstitial Laser Photocoagulation as a Treatment for Breast Cancer, *British J. of Surgery* **81**, 1617–1619 (1994).

[45] M. R. Gertner, A. Worthington, B. C. Wilson, M. D. Sherar, Ultrasound Imaging of Thermal Therapy in *In Vitro* Liver, *Ultrasound in Medicine and Biology* **24(7)**, 1023–1032 (1998).

[46] K. H. Cheng, M. Hernandez, Magnetic Resonance Diffusion Imaging Detects Structural Damage in Biological Tissues upon Hyperthermia, *Cancer Research* **52**, 6066–6073 (1992).

[47] S. A. Sapareto, W. C. Dewey, Thermal Dose Determination in Cancer Therapy, *Int. J. Radiat. Oncol. Biol. Phys.* **10**, 787–800 (1984).

[48] S. A. Sapareto, Thermal Dose, *in* "Biological, Physical and Clinical Aspects of Hyperthermia: (1987) AAPM/NAHG Hyperthermia School Proceedings" (B. R. Paliwal, F. W. Hetzel, M. W. Dewhirst, Eds.), American Institute of Physics, New York, 1988.

[49] M. C. Kolios, A. E. Worthington, M. D. Sherar, J. W. Hunt, Experimental Evaluation of Two Simple Thermal Models using Transient Temperature Analysis, *Physics in Medicine and Biology* **43**, 3325–3340 (1988).

[50] S. T. Clegg, S. K. Das, Y. Zhang, J. MacFall, E. Fullar, T. V. Samulski, Verification of a Hyperthermia Model using MR Thermometry, *International Journal of Hyperthermia* **11(5)**, 409–424 (1995).

[51] W. L. Nyborg, Solutions of the Bio-Heat Transfer Equation, *Physics in Medicine and Biology* **33(7)**, 785–792 (1988).

[52] J. J. W. Lagendijk, M. Scheliekens, J. Schipper, P. M. van der Linden, A Three-Dimensional Description of Heating Patterns in Vascularised Tissues during Hyperthermia Treatment, *Physics in Medicine and Biology* **29(5)**, 495–507 (1984).

[53] F. Reif, "Fundamentals of Statistical and Thermal Physics", McGraw-Hill Book Company, New York, NY, 1965.

[54] T. C. Cetas, Will Thermometric Tomography Become Practical for Hyperthermia Treatment Monitoring?, *Cancer Research (Suppl.)* **October**, 4805s–4808s (1984).

[55] T. C. Cetas, W. G. Connor, Thermometry Considerations in Localized Hyperthermia, *Medical Physics* **5(2)**, 79–91 (1978).

[56] D. A. Christensen, Current Techniques for Non-Invasive Thermometry, *in* "Physical Aspects of Hyperthermia: (1981) AAPM Summer School Proceedings" (G. H. Nussbaum, Ed.), American Institute of Physics, New York, 1982.

[57] E. S. Ebbini, C. Simon, Temperature Imaging using Diagnostic Ultrasound: Methods for Guidance and Monitoring of Thermal Treatments of Tissue, *in* "Thermal Treatment of Tissue with Image Guidance" (T. P. Ryan, T. Z. Wong, Eds.), SPIE Press, Bellingham WA, Proceedings of SPIE Vol. 3594 edition, 1999.

[58] W. L. Straube, R. M. Arthur, Theoretical Estimation of the Temperature Dependence of Backscattered Ultrasonic Power for Noninvasive Thermometry, *Ultrasound in Medicine and Biology* **20(9)**, 915–922 (1994).

[59] R. Nasoni, T. Bowen, W. Connor, R. Sholes, *In Vivo* Temperature Dependence of Ultrasound Speed in Tissue and its Application to Noninvasive Temperature onitoring, *Ultrasonic Imaging* **1(1)**, 34–43 (1979).

[60] J. C. Bamber, C. R. Hill, Ultrasonic Attenuation and Propagation Speed in Mammalian Tissues as a Function of Temperature, *Ultrasound in Medicine and Biology* **5**, 149–157 (1979).

[61] B. G. Fallone, P. R. Moran, E. B. Podgorsak, Noninvasive Thermometry with a Clinical X-Ray CT Scanner, *Medical Physics* **9(5)**, 715–721 (1982).

[62] G. A.Sandison, M. P.Loye, J. C. Rewcastle, L. J. Hahn, J. C. Saliken, J. G. McKinnon, B. J. Donnelly, X-Ray CT Monitoring of Iceball Growth and Thermal Distribution during Cryosurgery, *Physics in Medicine and Biology* **43**, 3309–3324 (1998).

[63] F. A. Jolesz, Interventional and Intraoperative MRI: A general Overview of the Field, *Journal of Magnetic Resonance Imaging* **8**, 3–6 (1998).

[64] G. M. Lamb, W. M. W. Gedroyc, Interventional Magnetic Resonance Imaging, *The British Journal of Radiology* **70**, S81–S88 (1997).

[65] F. A. Jolesz, Image-Guided Procedures and the Operating Room of the Future, *Radiology* **204**, 601–612 (1997).

[66] R. B. Lufkin, Interventional MR Imaging, *Radiology* **197**, 16–18 (1995).

[67] Y. Anzai, A. A. F. Desalles, K. L. Black, S. Sinha, K. Farahani, E. A. Behnke, D. J. Castro, R. B. Lufkin, Interventional MR Imaging, *RadioGraphics* **13**, 897–904 (1993).

[68] M. P. Fried, F. A. Jolesz, Image-Guided Intervention for Diagnosis and Treatment of Disorders of the Head and Neck, *Laryngoscope* **103**, 924–927 (1993).

[69] J. F. Schenck, F. A. Jolesz, P. B. Roemer, H. E. Cline, W. E. Lorensen, R. Kikinis, S. G. Silverman, C. J. Hardy, W. D. Barber, E. T. Laskaris, B. Dorri, R. W. Newman, C. E. Holley, B. D. Collick, D. P. Dietz, D. C. Mack, M. D. Ainslie, P. L. Jaskolski, M. Figueira, J. C. von Lehn, S. P. Souza, C. L. Dumoulin, R. D. Darrow, R. L. St Peters, K. W. Rohlin, R. D. Watkins, D. R. Eisner, S. M. Blumenfeld, K. G. Vosburgh, Superconducting Open-Configuration MR Imaging System for Image-Guided Therapy, *Radiology* **195**, 805–814 (1995).

[70] S. G. Silverman, B. D. Collick, M. R. Figueria, R. Khorasani, D. F. Adams, R. W. Newman, G. P. Topulos, F. A. Jolesz, Interactive MR-Guided Biopsy in an Open-Configuration MR Imaging System, *Radiology* **197**, 175–181 (1995).

[71] V. M. Tronnier, C. R. Wirtz, M. Knauth, G. Lenz, O. Pastyr, M. M. Bonsanto, F. K. Albert, R. Kuth, A. Staubert, W. Schlegel, K. Sartor, S. Kunze, Intraoperative Diagnostic and Interventional Magnetic Resonance Imaging in Neurosurgery, *Neurosurgery* **40(5)**, 891–902 (1997).

[72] F. A. Jolesz, P. R. Morrison, S. J. Koran, R. J. Kelley, S. G. Hushek, R. W. Newman, M. P. Fried, A. Melzer, R. M. M. Seibel, H. Jalahej, Compatible Instrumentation for Intraoperative MRI: Expanding Resources, *Journal of Magnetic Resonance Imaging* **8**, 8–11 (1998).

[73] E. K. Keeler, F. X. Casey, H. Engels, E. Lauder, C. A. Pirto, T. Reisker, J. Rogers, D. J. Schaefer, T. Tynes, Accessory Equipment Considerations with Respect to MRI Compatibility, *Journal of Magnetic Resonance Imaging* **8**, 12–18 (1998).

[74] R. S. Hinks, M. J. Bronskill, W. Kucharczyk, M. Bernstein, B. D. Collick, R. M. Henkelman, MR Systems for Image-Guided Therapy, *Journal of Magnetic Resonance Imaging* **8**, 19–25 (1998).

[75] N. Bloembergen, E. M. Purcell, R. V. Pound, Relaxation Effects in Nuclear Mangetic Resonance Absorption, *Physical Review* **73(7)**, 679–712 (1948).

[76] R. L. Conger, P. W. Selwood, Proton Relaxation in Paramagnetic Solutions, *Journal of Chemical Physics* **20(3)**, 383–387 (1952).

[77] P. A. Bottomley, T. H. Foster, R. E. Argersinger, L. M. Pfeifer, A Review of Normal Tissue Hydrogen NMR Relaxation Times and Relaxation Mechanisms from 1 – 100 MHz: Dependence on Tissue Type, NMR Frequency, Temperature, Species, Excision, and Age, *Medical Physics* **11(4)**, 425–448 (1984).

[78] C. J. Lewa, Z. Majewska, Temperature Relationships of Proton Spin-Lattice Relaxation Time T1 in Biological Tissues, *Bulletin du Cancer (Paris)* **67(5)**, 525–530 (1980).

[79] R. Jayasundar, S. Ayyar, P. Raghunathan, Proton Resonance Imaging and Relaxation in Raw and Cooked Hen Eggs, *Magnetic Resonance Imaging* **15(6)**, 709–717 (1997).

[80] D. L. Parker, V. Smith, P. Sheldon, L. E. Crooks, L. Fussell, Temperature Distribution Measurements in Two-Dimensional NMR Imaging, *Medical Physics* **10(3)**, 321–325 (1983).

[81] D. L. Parker, Applications of NMR Imaging in Hyperthermia: An Evaluation of the Potential for Localized Tissue Heating and Noninvasive Temperature Monitoring, *IEEE Transactions on Biomedical Engineering* **BME-31(1)**, 161–167 (1984).

[82] B. D. Youl, C. P. Hawkins, J. K. Morris, E. P. G. H. DuBoulay, P. S. Tofts. *In Vivo T1* Values from Guinea Pig Brain Depend on Body Temperature, *Magnetic Resonance in Medicine* **24**, 170–173 (1992).

[83] Y. Baba, M. M. Lerch, D. D. Stark, A. Tanimoto, B. P. Kreft, L. Zhao, A. K. Saluja, M.Takahashi, Time After Excision and Temperature Alter Ex Vivo Tissue Relaxation Time Measurements, *Journal of Magnetic Resonance Imaging* **4**, 647–651 (1994).

[84] C. J. Lewa, J. D. de Certaines, Measurements of the Effect of Storage Temperature at Various Temperatures on the T1 of *Ex Vivo* Tissues, *Medical Physics* **22(6)**, 831–834 (1995).

[85] E. Moser, E. Winklmayr, P. Holzmuller, M. Krssak, Temperature and pH-Dependence of Proton Relaxation Rates in Rat Liver Tissue, *Magnetic Resonance Imaging* **13(3)**, 429–440 (1995).

[86] T. R. Nelson, S. M. Tung, Temperature Dependence of Proton Relaxation Times In Vitro, *Magnetic Resonance Imaging* **5**, 189–199 (1987).

[87] M. Aso, Y. Yui, M. Kakishita, Effects of Thermal Denaturation on the Longitudinal Relaxation Time (T1) of Water Protons in Protein Solutions: Study of the Factors Determining the T1 of Water Protons, *Magnetic Resonance Imaging* **6**, 17–25 (1988).

[88] R. J. Dickinson, A. S. Hall, A. J. Hind, I. R. Young, Measurement of Changes in Tissue Temperature Using MR Imaging, *Journal of Computer Assisted Tomography* **10(3)**, 468–472 (1986).

[89] C. Schwarzbauer, J. Zange, H. Adolf, R. Deichmann, U. Noth, A. Haase, Fast Measurement of Temperature Distributions by Rapid T1 Mapping, *Journal of Magnetic Resonance, Series B* **106**, 178–180 (1995).

[90] A. S. Hall, M. V. Prior, J. W. Hand, I. R. Young, R. J. Dickinson, Observation by MR Imaging of In Vivo Temperature Changes Induced by Radio Frequency Hyperthermia, *Journal of Computer Assisted Tomography* **14(3)**, 430–436 (1990).

[91] R. Matsumoto, K. Oshio, F. A. Jolesz, Monitoring of Laser and Freezing-Induced Ablation in the Liver with T1-weighted MR Imaging, *Journal of Magnetic Resonance Imaging* **2**, 555–562 (1992).

[92] R. Matsumoto, R. V. Mulkern, S. G. Hushek, F. A. Jolesz, Tissue Temperature Monitoring for Thermal Interventional Therapy: Comparison of T1-Weighted MR Sequences, *Journal of Magnetic Resonance Imaging* **4**, 65–70 (1994).

[93] C. Bohris, W. G. Schreiber, J. Jenne, I. Simiantonakis, R. Rastert, H. Zabel, P. Huber, R. Bader, G. Brix, Quantitative MR Temperature Monitoring of High-Intensity Focused Ultrasound Therapy, *Magnetic Resonance Imaging* **17(4)**, 603–610 (1999).

[94] I. R. Young, J. W. Hand, A. Oatridge, M. V. Prior, G. R. Forse, Further Observations on the Measurements of Tissue T1 to Monitor Temperature *In Vivo* by MRI, *Magnetic Resonance in Medicine* **31**, 342–345 (1994).

[95] I. R. Young, J. W. Hand, A. Oatridge, M. V. Prior, Modeling and Observation of Temperature Changes *In Vivo* Using MRI, *Magnetic Resonance in Medicine* **32**, 358–369 (1994).

[96] K. Hynynen, W. R. Freund, H. E. Cline. A. H. Chung, R. D. Watkins, J. P. Vetro, F. A. Jolesz, A Clinical, Noninvasive, MR Imaging-Monitored Ultrasound Surgery Method, *RadioGraphics* **16**, 185–195 (1996).

[97] J. H. Simpson, Diffusion and Nuclear Spin Relaxation in Water, *Physical Review* **111**, 1201–1202 (1958).

[98] D. Le Bihan, J. Delannoy, R. L. Levin, Temperature Mapping with MR Imaging of Molecular Diffusion: Application to Hyperthermia, *Radiology* **171**, 853–857 (1989).

[99] E. O. Stejskal, J. E. Tanner, Spin Diffusion Measurements: Spin Echoes in the Presence of a Time-Dependent Field Gradient, *J. Chem. Phys.* **42**, 288–292 (1965).

[100] D. Morvan, A. Leroy-Willig, P. Jehenson, C. A. Cuenod, A. Syrota, Temperature Changes Induced in Human Muscle by Radio-Frequency H-1 Decoupling: Measurement with an MR Imaging Diffusion Technique, *Radiology* **185**, 871–874 (1992).

[101] T. V. Samulski, S. T. Clegg, S. Das, J. MacFall, D. M. Prescott, Application of New Technology in Clinical Hyperthermia, *International Journal of Hyperthermia* **10(3)**, 389–394 (1994).

[102] D. Morvan, A. Leroy-Willig, A. Malgouyres, C. A. Cuenod, P. Jehenson, A. Syrota, Simultaneous Temperature and Regional Blood Volume Measurements in Human Muscle Using an MRI Fast Diffusion Technique, *Magnetic Resonance in Medicine* **29**, 371–377 (1993).

[103] T. V. Samulski, J. MacFall, Y. Zhang, W. Grant, C. Charles, Non-invasive Thermometry using Magnetic Resonance Diffusion Imaging: Potential for Application in Hyperthermia Oncology, *International Journal of Hyperthermia* **8(6)**, 819–829 (1992).

[104] K. A. Il'yasov, J. Hennig, Single-Shot Diffusion-Weighted RARE Sequence: Application for Temperature Monitoring During Hyperthermia Session, *Journal of Magnetic Resonance Imaging* **8**, 1296–1305 (1998).

[105] W. Wlodarczyk, M. Hentschel, P. Wust, R. Noeske, N. Hosten, H. Rinneberg, R. Felix, Comparison of Four Magnetic Resonance Methods for Mapping Small Temperature Changes, *Physics in Medicine and Biology* **44**, 607–624 (1999).

[106] J. MacFall, D. M. Prescott, E. Fullar, T. V. Samulski, Temperature Dependence of Canine Brain Tissue Diffusion Coefficient Measured *In Vivo* with Magnetic Resonance Echo-Planar Imaging, *International Journal of Hyperthermia* **11(1)**, 73–86 (1995).

[107] J. F. Schenck, The Role of Magnetic Susceptibility in Magnetic Resonance Imaging: MRI Magnetic Compatibility of the First and Second Kinds, *Medical Physics* **23(6)**, 815–850 (1996).

[108] A. Abragam, "The Principles of Nuclear Magnetism", Clarendon Press, Oxford, UK, 1961.

[109] H. Tanaka, K. Eno, H. Kato, T. Ishida, Possible Application of Non-Invasive Thermometry for Hyperthermia using NMR, *Nippon Acta Radiologica* **41(9)**, 897–899 (1981).

[110] Y. Kamimura, Y. Amemiya, An NMR Technique for Non-Invasive Thermometry using M_o as the Temperature-Sensitive Parameter, *Automedica* **8**, 295–313 (1987).

[111] W. G. Schneider, H. J. Bernstein, J. A. Pople, Proton Magnetic Resonance Chemical Shift of Free (Gaseous) and Asociated (Liquid) Hydride Molecules, *J. Chemical Physics* **28(4)**, 601–607 (1958).

[112] J. C. Hindman, Proton Resonance Shift of Water in Gas and Liquid States, *J. Chem. Phys.* **44(12)**, 4582–4592 (1966).

[113] Y. Ishihara, A. Calderon, H. Watanabe, K. Mori, K. Okamoto, Y. Suzuki, K. Sato, A Precise and Fast Temperature Mapping Method using Water Proton Chemical Shift, *in* "Proc. SMRM, 11th Annual Meeting", p. 4803, 1992.

[114] W. Wlodarczyk, R. Boroschewski, M. Hentschel, P. Wust, G. Monich, R. Felix, 3D Monitoring of Small Temperature Changes for Therapeutic Hyperthermia using Magnetic Resonance, *Journal of Magnetic Resonance Imaging* **8**, 165–174 (1998).

[115] F. Bertsch, J. Mattner, M. K. Stehling, U. Mueller-Lisse, M. Peller, R. Loeffler, J. Weber, K. Member, W. Wilmanns, R. issels, M. Reiser, Non-Invasive Temperature Mapping using MRI: comparison of Two Methods Based on Chemical Shift and $T1$-Relaxation, *Magnetic Resonance Imaging* **16(4)**, 393–404 (1998).

[116] J. DePoorter, C. DeWagter, Y. DeDeene, C. Thomsen, F. Stahlberg, E. Achten, The Proton-Resonance-Frequency-Shift Method Compared with Molecular Diffusion for Quantitative measurement of Two-Dimensional Time-Dependent Temperature Distributionin a Phantom, *Journal of Magnetic Resonance, Series B* **103**, 234–241 (1994).

[117] F. Bloch, Nuclear Induction, *Physical Review* **70**, 460–473 (1946).

[118] E. M. Purcell, H. C. Torrey, R. V. Pound, Resonance Absorption in Nuclear Magnetic Moments in a Solid, *Physical Review* **69**, 37–38 (1946).

[119] D. G. Nishimura, "Introduction to Magnetic Resonance Imaging", Dept. of Electrical Engineering, Stanford University, 1996.

[120] P. C. Lauterbur, Image Formation by Induced Local Interactions: Examples Employing Nuclear Magnetic Resonance, *Nature* **242**, 190–191 (1973).

[121] H. E. Duckworth, "Electricity and Magnetism", MacMillan Company of Canada Ltd, Toronto, Canada, 1960.

[122] A. D. Buckingham, T. Schaefer, W. G. Schneider, Solvent Effects in Nuclear Magnetic Resonance Spectra, *J. Chemical Physics* **32(4)**, 1227–1233 (1960).

[123] W. C. Dickinson, The Time Average Magnetic Field at the Nucleus in Nuclear Magnetic Resonance Experiments, *Physical Review* **81(5)**, 717–731 (1951).

[124] J. R. Zimmerman, M. R. Foster, Standardization of NMR High Resolution Spectra, *J. Phys. Chem.* **61**, 282–289 (1957).

[125] J. Ronayne, D. J. Williams, Solvent Effects in Proton Magnetic Resonance Spectroscopy, *Annu. Reports NMR Spectroscopy* **2**, 83–124 (1969).

[126] S. C. K. Chu, Y. Xu, J. A. Balschi, C. S. Springer, Bulk Magnetic Susceptibility Shifts in NMR Studies of Compartmentalied Samples: Use of Paramagnetic Reagents, *Magnetic Resonance in Medicine* **13**, 239–262 (1990).

[127] M. Gerstein, M. Levitt, Simulating Water and the Molecules of Life, *Scientific American* **November**, 100–105 (1998).

[128] E. D. Isaacs, A. Shukla, P. M. Platzman, D. R. Hamann, B. Barbiellini, C. A. Tulk, Covalency of the Hydrogen Bond in Ice: A Direct X-Ray Measurement, *Physical Review Letters* **82(3)**, 600–603 (1999).

[129] S. H. Koenig, R. D. Brown, The Importance of the Motion of Water for Magnetic Resonance Imaigng, *Investigative Radiology* **20**, 297–305 (1985).

[130] A. P. Wills, G. F. Boeker, The Dependence of the Diamagnetism of Water upon Its Temperature, *Physical Review* **46**, 907–909 (1934).

[131] S. Seely, The Variation of the Diamagnetism of Water with Temperature, *Physical Review* **52**, 662 (1937).

[132] G. P. Arrighini, M. Maestro, R. Moccia, Magnetic Properties of Polyatomic Molecules. I. Magnetic Susceptibility of H_2O, NH_3, CH_4, H_2O_2, *J. Chemical Physics* **49(2)**, 882–889 (1968).

[133] R. Cini, M. Torrini, Temperature Dependence of the Magnetic Susceptibility of Water, *J. Chemical Physics* **49(6)**, 2826–2830 (1968).

[134] H. Taft, B. P. Dailey, Magnetic Susceptibility of the H_2O Molecule, *J. Chemical Physics* **51(3)**, 1002–1007 (1969).

[135] Y. C. Pan, H. F. Hameka, Calculation of the Diamagnetic Susceptibility of the Water Molecule, *J. Chemical Physics* **53(3)**, 1265–1269 (1970).

[136] T. H. Crawford, J. Swanson, Temperature Dependent Magnetic Measurements and Structural Equilibria in Solution, *J. Chemical Education* **48**, 382–386 (1971).

[137] J. S. Philo, W. M. Fairbank, Temperature Dependence of the Diamagnetism of Water, *J. Chemical Physics* **72(8)**, 4429–4433 (1980).

[138] E. P. Day, Equation for the Magnetic Susceptibility of Water, *J. Chemical Physics* **72(8)**, 4434–4436 (1980).

[139] R. C. Weast, M. J. Astle, "CRC Handbook of Chemistry and Physics", CRC Press, Boca Raton, Florida, 1981.

[140] N. Muller, R. C. Reiter, Temperature Dependence of Chemical Shifts of Protons in Hydrogen Bonds, *J. Chemical Physics* **42(9)**, 3265–3269 (1965).

[141] N. Muller, Concerning Structural Models for Water and Chemical-Shift Data, *J. Chemical Physics* **28**, 2555–2556 (1965).

[142] L. D. Hall, S. L. Talagala, Mapping of pH and Temperature Distribution Using Chemical-Shift-Resolved Tomography, *Journal of Magnetic Resonance Imaging* **65**, 501–505 (1985).

[143] N. W. Lutz, A. C. Kuesel, W. E. Hull, A ^{1}H-NMR Method for Determining Temperature in Cell Culture Perfusion Systems, *Magnetic Resonance in Medicine* **29**, 113–118 (1993).

[144] E. B. Cady, P. C. D'Souza, J. Penrice, A. Lorek, The Estimation of Local Brain Temperature by *in Vivo* ^{1}H Magnetic Resonance Spectroscopy, *Magnetic Resonance in Medicine* **33**, 862–867 (1995).

[145] K. Kuroda, Y. Suzuki, Y. Ishihara, K. Okamoto, Y. Suzuki, Temperature Mapping using Water Proton Chemical Shift Obtained with 3D-MRSI: Feasibility *In Vivo*, *Magnetic Resonance in Medicine* **35**, 20–29 (1996).

[146] K. J. Franklin, R. J. Buist, J. den Hartog, G. A. McRae, D. P. Spencer, Encapsulated Liquid Crystals as Probes for Remote Thermometry, *International Journal of Hyperthermia* **8(2)**, 253–262 (1992).

[147] A. G. Webb, M. Wong, M. Neisman, K. J. Kolbeck, L. J. Wilmes, R. L. Magin, K. S. Suslick, *In-vivo* NMR Thermometry with Liposomes Containing ^{59}Co Complexes, *International Journal of Hyperthermia* **11(6)**, 821–827 (1995).

[148] S. N. Sarkar, H. W. Dodgen, J. P. Hunt, Multinuclear MR Frequency Shifts of Hydrated Ions as a Function of Applicated Pressure and Temperature, *Journal of Magnetic Resonance, Series B* **112**, 197–199 (1996).

[149] A. G. Webb, E. C. Wiener, Measurement of Microwave-Induced Heating of Mammary Tumors in Animal Models Using Cobalt NMR, *Journal of Magnetic Resonance, Series B* **111**, 90–93 (1996).

[150] C. S. Zuo, J. L. Bowers, K. R. Metz, T. Nosaka, A. D. Sherry, M. E. Clouse, $TmDOTP^{5-}$: A Substance for NMR Temperature Measurements *in Vivo*, *Magnetic Resonance in Medicine* **36**, 955–959 (1996).

[151] S. Aime, M. Botta, M. Fasano, E. Terreno, P. Kinchesh, A New Ytterbium Chelate as Contrast Agent in Chemical Shift Imaging and Temperature Sensitive Probe for MR Spectroscopy, *Magnetic Resonance in Medicine* **35**, 648–651 (1996).

[152] T. Frenzel, K. Roth, S. Kossler, B. Raduchel, H. Bauer, J. Platzek, H. J. Weinmann, Noninvasive Temperature Measurement *in Vivo* Using a Temperature-Sensitive Lanthanide Complex and ^{1}H Magnetic Resonance Spectroscopy, *Magnetic Resonance in Medicine* **35**, 364–369 (1996).

[153] C. S. Zuo, K. R. Metz, Y. Sun, A. D. Sherry, NMR Temperature Measurements using a Paramagnetic Lanthanide Complex, *Journal of Magnetic Resonance* **133**, 53–60 (1998).

[154] M. Hentschel, W. Dreher, P. Wust, S. Roll, D. Leibfritz, R. Felix, Fast Spectroscopic Imaging for Non-Invasive Thermometry using the Pr[MOE-DO3A] Complex, *Physics in Medicine and Biology* **44**, 2397–2408 (1999).

[155] Biological, Physical, and Clinical Aspects of Hyperthermia, *in* "AAPM Monograph No. 16" (B. Paliwal, F. Hetzel, M. Dewhirst, Eds.), American Institute of Physics, New York, 1988.

[156] J. R. Lepock, H. E. Frey, G. A. Senisterra, M. L. P. Heynen, Mechanisms of Thermal Damage, *in* "Radiation Research 1895-1995" (U. Hagen, D. Harder, H. Jung, C. Streffer, Eds.), Universitatsdruckerei H. Sturtz AG, Wurzburg, vol.2 edition, 1995.

[157] U. G. Mueller-Lisse, A. F. Hueck, P. Schneede, R. Muschter, J. Scheidler, A. G. Hofstetter, M. F. Reiser, Postoperative MRI in Patients Undergoing Interstitial Laser Coagulation Thermotherapy of Benign Prostatic Hyperplasia, *Journal of Computer Assisted Tomography* **20(2)**, 273–278 (1996).

[158] J. J. Phillips, G. E. Kopchok, S. K. Peng, M. P. Mueller, R. A. White, MR Imaging of Ho:YAG Laser Diskectomy with Histologic Correlation, *Journal of Magnetic Resonance Imaging* **3**, 515–520 (1993).

[159] J. Delannoy, C. Chen, R. Turner, R. L. Levin, D. LeBihan, Noninvasive Temperature Imaging Using Diffusion MRI, *Magnetic Resonance in Medicine* **19**, 333–339 (1991).

[160] A. H. Chung, K. Hynynen, V. Colucci, K. Oshio. H. E. Cline, F. A. Jolesz, Optimization of Spoiled Gradient-Echo Phase Imaging for *In Vivo* Localization of a Focused Ultrasound Beam, *Magnetic Resonance in Medicine* **36**, 745–752 (1996).

[161] J. MacFall, D. Prescott, H. Charles, T. Samulski, ^{1}H MRI Phase Thermometry *In Vivo* in Canine Brain, Muscle, and Tumor Tissue, *Medical Physics* **23(10)**, 1775–1782 (1996).

[162] I. R. Young, J. Hagnal, I. Roberts, J. Ling, R. Hill-Cottingham, A. Oatridge, J. A. Wilson, An Evaluation of the Effects of Susceptibility Changes on the Water Chemical-Shift Method of Temperature Measurement in Human Peripheral Muscle, *Magnetic Resonance in Medicine* **36**, 366–374 (1996).

[163] Y. Ishihara, A. Calderon, H. Watanabe, K. Okamoto, Y. Suzuki, K. Kuroda, Y. Suzuki, A Precise and Fast Temperature Mapping using Water, *Magnetic Resonance in Medicine* **34**, 814–823 (1995).

[164] J. DePoorter, Noninvasive MRI Thermometry with the Proton Resonance Frequency Method: Study of Susceptibility Effects, *Magnetic Resonance in Medicine* **34**, 359–367 (1995).

[165] J. DePoorter, C. D. Y. De Deene, C. Thomsen, F. Stahlberg, E. Achten, Noninvasive MRI Thermometry with the Proton Resonance Frequency (PRF) Method : *In Vivo* Results in Human Muscle, *Magnetic Resonance in Medicine* **33**, 74–81 (1995).

[166] K. Hynynen, N. I. Vykhodtseva, A. H. Chung, V. Sorrentino, V. Colucci, F. A. Jolesz, Thermal Effects of Focused Ultrasound of the Brain: Determination with MR imaging, *Radiology* **204**, 247–253 (1997).

[167] R. V. Mulkern, A. H. Chung, F. A. Jolesz, K. Hynynen, Temperature Monitoring of Ultrasonically Heated Muscle with RARE Chemical Shift Imaging, *Medical Physics* **24(12)**, 1899–1906 (1997).

[168] T. Harth, T. Kahn, M. Rassek, B. Schwabe, H. J. Schwarzmaier, J. S. Lewin, U. Modder, Determination of Laser-Induced Temperature Distributions using Echo-Shifted TurboFLASH, *Magnetic Resonance in Medicine* **38**, 238–245 (1997).

[169] Y. C. Chung, J. L. Duerk, A. Shankaranarayanan, M. Hampke, E. M. Merkle, J. S. Lewin, Temperature Measurement using Echo-Shifted FLASH at Low Field for Interventional MRI, *Journal of Magnetic Resonance Imaging* **9**, 138–145 (1999).

[170] H. E. Cline, K. Hynynen, E. Schneider, C. J. Hardy, S. E. Maier, R. D. Watkins, F. A. Jolesz, Simultaneous Magnetic Resonance Phase and Magnitude Temperature Maps in Muscle, *Magnetic Resonance in Medicine* **35**, 309–315 (1996).

[171] P. M. Jakob, C. Hendrich, T. Breitling, A. Schafer, A. Berden, A. Haase, Real Time Monitoring of Laser-Induced Thermal Changes in Cartilage in Vitro by Using Snapshot FLASH, *Magnetic Resonance in Medicine* **37**, 805–808 (1997).

[172] S. Sinha, T. Oshiro, U. Sinha, R. Lufkin, Phase Imaging on a 0.2 T MR Scanner: Application to Temperature Monitoring During Ablation Procedures, *Journal of Magnetic Resonance Imaging* **7**, 918–928 (1997).

[173] J. A. De Zwart, P. Van Gelderen, D. J. Kelly, C. T. Moonen, Fast Magnetic-Resonance Temperature Imaging, *J. Magnetic Resonance, Series B* **112**, 86–90 (1996).

[174] M. J. Bronskill, S. J. Graham, *in* "The Physics of MRI: (1992) AAPM Summer School Proceedings" (P. Sprawls, M. J. Bronskill, Eds.), American Institute of Physics, New York, 1993.

[175] G. K. Bhattacharyya, R. A. Johnson, "Statistical Concepts and Methods", John Wiley and Sons, New York, 1977.

[176] T. E. Conturo, G. D. Smith, Signal-to-Noise in Phase Angle Reconstruction: Dynamic Range Extension using Phase Reference Offsets, *Magnetic Resonance in Medicine* **15**, 420–437 (1990).

[177] F. A. Jolesz, Interventional and Intraoperative MRI: A General Overview of the Field, *Journal of Magnetic Resonance Imaging* **8**, 3–7 (1998).

[178] K. Kuroda, K. Abe, S. Tsutsumi, Y. Ishihara, Y. Suzuki, K. Satoh, Water Proton Magnetic Resonance Spectroscopic Imaging, *Biomed. Thermol* **13**, 43–62 (1993).

[179] R. D. Peters, R. S. Hinks, R. M. Henkelman, *Ex Vivo* Tissue-Type Independence in Proton-Resonance Frequency Shift MR Thermometry, *Magnetic Resonance in Medicine* **40**, 454–459 (1998).

[180] R. Stollberger, P. W. Ascher, D. Huber, W. Renhart, H. Radner, F. Ebner, Temperature Monitoring of Interstitial Thermal Tissue Coagulation using MR Phase Images, *Journal of Magnetic Resonance Imaging* **8**, 188–196 (1998).

[181] D. R. Croft, J. A. R. Stone, "Heat Transfer Calculations using Finite Difference Equations", Applied Science Publishers Ltd, 1977.

[182] I. A. Vitkin, J. A. Moriarty, R. D. Peters, M. C. Kolios, A. Gladman, J. C. Chen, R. S. Hinks, J. W. Hunt, B. C. Wilson, A. Easty, M. J. Bronskill, W. Kucharczyk, M. D. Sherar, R. M. Henkelman, Magnetic Resonance Imaging of Temperature Changes During Interstitial Microwave Heating: A Phantom Study, *Medical Physics* **24(2)**, 269–277 (1997).

[183] J. A. Moriarty, J. C. Chen, C. M. Purcell, L. Ang, R. S. Hinks, R. D. Peters. R. M. Henkelman, D. B. Plewes, M. J. Bronskill, W. Kucharczyk, MRI Monitoring of Interstitial Microwave-Induced Heating and Thermal Lesions in Rabbit Brain *in-vivo*, *Journal of Magnetic Resonance Imaging* **8**, 128–135 (1998).

[184] R. D. Peters, R. S. Hinks, R. M. Henkelman, Heat-Source Orientation and Geometry Dependence in Proton-Resonance Frequency Shift MR Thermometry, *Magnetic Resonance in Medicine* **41**, 909–918 (1999).

[185] P. A. Bottomley, E. R. Andrew, RF Magnetic Field Penetration, Phase Shift and Power Dissipation in Biological Tissue: Implications for NMR Imaging, *Physics in Medicine and Biology* **23(4)**, 630–643 (1978).

[186] R. M. Henkelman, M. J. Bronskill, P. R. Goebel, Absorption of NMR Signals at High Frequencies in Physiological Phantoms, *SPIE Medical Imaging and Instrumentation* **486**, 192–197 (1984).

[187] J. M. Jin, "Electromagnetic Analysis and Design in Magnetic Resonance Imaging", CRC Press, Boca Raton, Florida, 1998.

[188] J. D. Bronzino, "The Biomedical Engineering Handbook", CRC Press, Boca Raton, Florida, 1995.

[189] R. D. Stoy, K. Foster, H. Schwan, Dielectric Properties of Mammalian Tissues from 0.1 to 100 MHz: A Summary of Recent Data, *Physics in Medicine and Biology* **27(4)**, 501–513 (1981).

[190] M. A. Stuchly, T. W. Athey, S. S. Stuchly, G. M. Samaras. G. Taylor, Dielectric Properties of Animal Tissues *In Vivo* at Frequencies 10 MHz - 1 GHz, *Bioelectromagnetics* **2**, 93–103 (1981).

[191] H. P. Schwan, Electrical Properties of Tissue and Cell Suspensions, *Advances in Biological and Medical Physics* **5**, 147–209 (1957).

[192] H. P. Schwan, K. Li, Capacity and Conductivity of Body Tissues at Ultrahigh Frequencies, *in* "Proc. of the I.R.E. December", pp. 1735–1740, 1953.

[193] G. H. Haggis, J. B. Hasted, T. J. Buchanan, The Dielectric Properties of Water in Solutions, *J. Chem. Phys.* **20(9)**, 1452–1465 (1952).

[194] C. Chen, D. I. Hoult, "Biomedical Magnetic Resonance Technology", Adam-Hilger, Bristol, 1989.

[195] E. R. McVeigh, M. J. Bronskill, R. M. Henkelman, Phase and Sensitivity of Receiver Coils in Magnetic Resonance Imaging, *Medical Physics* **13(6)**, 806–814 (1986).

[196] D. I. Hoult, R. Richards, The Signal-to-Noise Ratio of the Nuclear Magnetic Resonance Experiment, *Journal of Magnetic Resonance Imaging* **24**, 71–85 (1976).

[197] D. I. Hoult, The Sensitivity of the High Field Imaging Experiment Involving Human Samples, *in* "Proc. ISMRM, 7th Annual Meeting", p. 416, 1999.

[198] J. G. Sled, G. B. Pike, Quantitative Experimental Validation of an Analytic Model fo Intensity Non-Uniformity in MRI, *in* "Proc. ISMRM, 7th Annual Meeting", p. 2140, 1999.

[199] S. J. Graham, L. Chen, M. Leitch, R. D. Peters, M. J. Bronskill, S. Foster, R. M. Henkelman, D. B. Plewes, Quantifying Tissue Damage due to Focused Ultrasound Heating Observed by MRI, *Magnetic Resonance in Medicine* **41**, 321–328 (1999).

[200] N. McDannold, R. L. King, F. A. Jolesz, K. Hynynen, The Usefulness of Temperature Sensitive MRI-Derived Thermal Dose for Determining the Threshold for Tissue Damage, *in* "Proc. ISMRM, 7th Annual Meeting", p. 1936, 1999.

[201] S. Sinha, T. Oshiro, K. Ong, U. Sinha, A. L. Daniell, D. S. Lu, R. Lufkin, *In-Vivo* Laser Ablation of a Porcine Model: Real-Time Temperature Monitoring and Tissue Damage Modeling, *in* "Proc. ISMRM, 7th Annual Meeting", p. 1940, 1999.

[202] U. G. Mueller-Lisse, M. Thoma, S. Faber, A. Heuck, R. Muschter, P. Schneede, E. Weninger, A. Hofstetter, M. Reiser, Coagulative Interstitial Laser-induced Thermotherapy of Benign Prostatic Hyperplasia: Online Imaging with a T2-weighted Fast Spin-Echo MR Sequence - Experience in Six Patients, *Radiology* **210**, 373–379 (1999).

[203] U. G. Mueller-Lisse, A. F. Hueck, M. Thoma, R. Muschter, P. Schneede, E. Weninger, S. Faber, A. Hofstetter, M. Reiser, Predictability of the Size of Laser-Induced Lesions in T1-Weighted MR Images Obtained during Interstitial Laser-Induced Thermotherapy of Benign Prostatic Hyperplasia, *Journal of Magnetic Resonance Imaging* **8**, 31–39 (1998).

[204] R. H. Boni, T. Sulser, W. Jochum, B. Romanowski, J. F. Debatin, G. Krestin, Laser Ablation-induced Changes in the Prostate: Findings at Endorectal MR Imaging with Histologic Correlation, *Radiology* **202**, 232–236 (1997).

[205] U. G. Mueller-Lisse, A. Heuck, P. Schneede, R. Muschter, J. Scheidler, A. Hofstetter, M. Reiser, Postoperative MRI in Patient Undergoing Interstitial Laser Coagulation Thermotherapy of Benign Prostatic Hyperplasia, *Journal of Computer Assisted Tomography* **20(2)**, 273–278 (1996).

[206] S. N. Goldberg, P. Hagn, F. McGovern, R. M. Fogle, P. Mueller, G. Gazelle, Benign Prostate Hyperplasia: US-guided Transrectal Urethral Enlargement with Radio Frequency - Initial Results in a Canine Model, *Radiology* **208**, 491–498 (1998).

[207] A. Terai, Y. Arai, I. Yamamoto, H. Onishi, K. Oishi, O. Yoshida, Newly Developed Transurethral Radiofrequency Thermotherapy Device for Benign Prostatic Hyperplasia: A Pilot Study in Canine Prostate, *Int. J. Hyperthermia* **11(5)**, 627–635 (1995).

[208] J. Olsrud, R. Wirestam, S. Brockstedt, A. M. K. Nilsson, K. Tranberg, F. Stoahlberg, B. R. R. Persson, MRI Thermometry in Phantoms by use of the Proton Resonance Frequency Shift Method: Application to Interstitial Laser Thermotherapy, *Physics in Medicine and Biology* **43**, 2597–2613 (1998).

[209] R. D. Peters, R. M. Henkelman, Proton-Resonance Frequency Shift MR Thermometry is Affected by Changes in the Electrical Conductivity of Tissue, *Magnetic Resonance in Medicine* **43**, 62–71 (2000).

[210] J. C. Williams, Interstitial Laser Coagulation of the Prostate: Introduction of a Volume Based Treatment Formula with 12-month Follow-up, *World Journal of Urology* **15(6)**, 392–395 (1999).

[211] M. Greenberger, M. S. Steiner, The University of Tennesee Experience with the Indigo 830e Laser Device for the Minimally Invasive Treatment of Benign Prostatic Hyperplasia, *World Journal of Urology* **15(6)**, 386–391 (1999).

[212] A. Roggan, K. Dorschel, O. Minet, D. Wolff, G. Muller, The Optical Properties of Biological Tissue in the NIR Range - Review and Measurements, *in* "Laser Induced Interstitial Thermotherapy" (G. Muller, A. Roggan, Eds.), SPIE Press, Bellingham WA, 1995.

[213] K. Kuroda, K. Oshio, A. H. Chung, K. Hynynen, F. A. Jolesz, Temperature Mapping using the Water Proton Chemical Shift: A Chemical Shift Selective Phase Mapping Method, *Magnetic Resonance in Medicine* **38**, 845–851 (1997).

[214] R. V. Mulkern, L. P. Panych, N. J. McDannold, F. A. Jolesz, K. Hynynen, Tissue Temperature Monitoring with Multiple Gradient-Echo Imaging Sequences, *Journal of Magnetic Resonance Imaging* **8**, 493–502 (1998).

[215] J. A. De Zwart, F. C. Vimeux, C. Delalande, P. Canioni, C. T. W. Moonen, Fast Lipid-Suppressed MR Temperature Mapping with Echo-Shifted Gradient-Echo Imaging and Spectral-Spatial Excitation, *Magnetic Resonance in Medicine* **42**, 53–59 (1999).

[216] K. Kuroda, R. V. Mulkern, K. Oshio, L. P. Panych, T. Nakai, T. Moriya, S. Okuda, K. Hynynen, F. A. Jolesz, Temperature Mapping using the Water Proton Chemical Shift: Self-Referenced Method with Echo-Planar Spectroscopic Imaging, *Magnetic Resonance in Medicine* **43**, 220–225 (2000).

[217] T. Harth, B. Schwabe, T. Kahn, Motion Corrected Proton-Resonance-Frequency Method for MR-Thermometry using Navigator Echos, *in* "Proc. ISMRM, 5th Annual Meeting", p. 1956, 1997.

[218] J. Hajnal, N. Saeed, A. Oatridge, E. Soar, I. Young, G. Bydder, A Registration and Interpolation Procedure for Subvoxel Matching of Serially Acquired MR Images, *Journal of Computer Assisted Tomography* **19**, 289–296 (1995).

[219] N. Saeed, J. Hajnal, A. Oatridge, I. Young, Regions of Interest Tracking in Temporal Scans Based on Statistical Analysis of Gray Scale and Edge Properties and Registration of Images, *Journal of Magnetic Resonance Imaging* **8**, 182–187 (1998).

[220] R. Stollberger, P. W. Ascher, K. Leber, F. Ebner, G. Fuchs, A. Baumgartner, G. Litscher, M. Hubmer, Assessment of the Influence of In Vivo Thermal Response to Interstitial Laser Coagulation on MR-Temperature Quantification using the Phase Method, *in* "Proc. ISMRM, 7th Annual Meeting", p. 400, 1999.

[221] G. Liu, G. Sobering, J. Duyn, C. T. W. Moonen, A Functional MRI Technique Combining Principles of Echo-shifting with a Train of Observations (PRESTO), *Magnetic Resonance in Medicine* **30**, 764–768 (1993).

[222] G. Liu, G. Sobering, A. W. Olson, P. van Gelderen, C. T. W. Moonen, Fast Echo-Shifted Gradient-Recalled MRI: Combining a Short Repetition Time with Variable T2* Weighting, *Magnetic Resonance in Medicine* **30**, 68–75 (1993).

[223] C. T. W. Moonen, G. Liu, P. van Gelderen, G. Sobering, A Fast Gradient-Recalled MRI Technique with Increased Sensitivity to Dynamic Susceptibility Effects, *Magnetic Resonance in Medicine* **26**, 184–189 (1992).

[224] T. Takahashi, K. Komura, M. Dohi, J. Harada, Stabilized Temperature Mapping on a 0.3 T Open MRI System, *in* "Proc. ISMRM, 8th Annual Meeting", p. 1339, 2000.

[225] N. McDannold, K. Hynynen, D. Wolf, G. Wolf, F. Jolesz, MRI Evaluation of Thermal Ablation of Tumors with Focused Ultrasound, *Journal of Magnetic Resonance Imaging* **8**, 91–100 (1998).

[226] K. Hynynen, N. McDannold, K. Mahoney, F. A. Jolesz, MRI Thermal Dosimetry During Focused Ultrasound Surgery with Multiple Sonications, *in* "Proc. ISMRM, 8th Annual Meeting", p. 1357, 2000.

[227] J. A. De Zwart, F. C. Vimeux, J. Palussiere, C. Delalande, C. T. W. Moonen, Rapid MR Temperature Imaging for Real-Time Visualization and Control of Focused Ultrasound Tissue Heating, *in* "Proc. ISMRM, 7th Annual Meeting", p. 401, 1999.

[228] R. Salomir, J. A. De Zwart, F. C. Vimeux, N. Grenier, J. Palussiere, C. T. W. Moonen, MR Guided FUS Hyperthermia: Automatic Temperature Control based on a Physical Model of Energy Deposit and Heat Diffusion, *in* "Proc. ISMRM, 8th Annual Meeting", p. 1359, 2000.